Broadband Green's Function and Applications to Fast Electromagnetic Analysis of High-Speed Interconnects

Shaowu Huang

A dissertation
submitted in partial fulfillment of the
requirements for the degree of

Doctor of Philosophy

University of Washington

2015

Reading Committee:

Leung Tsang, Chair

Henning Braunisch

Kung-Hau Ding

Yasuo Kuga

Program Authorized to Offer Degree:

Electrical Engineering

University of Washington

Abstract

Broadband Green's Function and Applications to Fast Electromagnetic Analysis of High-Speed Interconnects

Shaowu Huang

Chair of the Supervisory Committee

Professor Leung Tsang

Department of Electrical Engineering

This dissertation is focused on research and development of an innovative Broadband Green's Function method and the applications to fast electromagnetic modeling and simulations of high-speed interconnects. Innovative solutions based on proposed broadband Green's function method are presented and demonstrated to solve the challenging problems in signal integrity, power integrity, and electromagnetic compatibility and interference for computer system designs. The main contents of this dissertation are twofold: to overcome the fundamental restrictions in the conventional Green's function methods through introducing the broadband Green's function method, to explore the applications of the broadband Green's function to modeling of high-speed interconnects in modern electronic devices and systems. In the first project, the method of broadband Green's function with low wavenumber extraction (BBGFL) is proposed for arbitrary shaped waveguide. The methodologies of BBGFL are derived for both Neumann and Dirichlet boundary conditions. In the second project, we combine the BBGFL with method of moment (MoM) for fast full wave modeling and simulations of scattering in arbitrary shaped waveguides. The method is applied to solve the problem of vias inside PCB power/ground plane waveguide. In the third project, a number of applications are investigated, including modeling of vias in arbitrary shaped power/ground planes, modeling of emissions from printed circuit boards, modeling of stripline connecting transition vias in power/ground planes, modeling of arbitrary shaped waveguide structures in microwave components. The proposed methods are compared to in-house method of moment program and commercial HFSS tool. Simulation results of various problems are illustrated. The present methods are verified by comparing the resonant frequencies, Green's functions, S-parameters, surface fields, and/or radiated emission for different problems. BBGFL has good agreement with MoM and/or HFSS on the numerical results. The computational efficiency is checked by comparing the CPU time. BBGFL is about two or three orders faster than MoM and HFSS for most cases in modeling of high-speed interconnects.

TABLE OF CONTENTS

ACKNOWLEDGEMENTS

First, I want to express my deep gratitude to my advisor, Prof. Leung Tsang, for his guidance, encouragement, trust and support during the entire course of my Ph.D. study and research at University of Washington. His immense knowledge, passion and expertise in research and innovation help me conquer the challenges in my Ph.D. research. I have learned a lot from him on various areas of electromagnetics. He is my eminent role model as a real scholar.

Second, I would like to thank the members of my Ph.D. committee: Dr. Henning Braunisch, Dr. Kung-Hau Ding, Prof. Yasuo Kuga, Prof. Akira Ishimaru, and Prof. Charles Barrack, for their generous help and valuable suggestions.

Third, I wish to thank the graduate students and visiting scholars in LACEO at UW for their discussion and companionship: Haogang Wang, Il-Suek Koh, Ding Liang, Boping Wu, Ruihua Ding, Xiaolan Xu, Jeremy Quinn Bagley, Wenmo Chang, Xin Chang, Tien Hao Liao, Xudong Li, Shurun Tan, Chenxin Su, Tianlin Wang, Huanting Huang, Tai Qiao.

Fourth, I am grateful for my colleagues and managers of Intel Corporation for their support and help. I own a debt of gratitude to Larry Bethurum, Beomtaek Lee, Xiaoning Ye, Kai Xiao, Richard Kunze, Jeff Loyer, Chunfei Ye, Gong Ouyang, John J Abbott, Lounsbery Darrell.

Finally, I want to sincerely thank my family – my parents Miaoxi Huang and Yijie Huang, my wife Linda Bai, and my son Edwin Huang. Without their support, I will not be to finish this work.

DEDICATION

To my family for their love and support.

LIST OF FIGURES

LIST OF TABLES

Table Number Page

Chapter 1 Introduction

1.1 Research Background

Waveguides or cavities are common structures in modern electronic devices and systems. Effects of waveguide or cavity structures are critical for the electrical performance of electronic components and systems. In computer system design, harmful electromagnetic signal noises or interferences are usually generated and amplified at the resonant frequencies due to the waveguide or cavity structures in electronic devices. In radio frequency (RF) and microwave circuits and components, the functional operation may rely on the resonant modes of the waveguide structures. This causes problems in terms of signal integrity (SI), power integrity (PI), electromagnetic interference (EMI), electromagnetic compatibility (EMC), and others. The issue deteriorates when the electronic devices or systems operate at higher frequency or faster speed, which have been the trend in industry.

Particularly in printed circuited boards (PCBs), two adjacent power/ground planes form a waveguide/cavity structure. The propagating mode in satisfy the Neumann boundary condition on the edges of PCB power/ground plane structures, which is typically the transverse electromagnetic (TE) case. These power/ground plane structures are the key in many SI/PI and EMI/EMC problems. Vias are used for vertical interconnect for multilayer PCBs. Under the resonant frequencies of the power/ground plane pair, the propagating electromagnetic waves along vias may excite strong resonant modes, which can result in strong edge radiation and cause EMI/EMC problems; the switching noises induced by voltage regulator module (VRM) can generate voltage fluctuations and lead to PI problems; the high frequency power noise can also couple into signal vias and cause SI/PI coupling issues. Therefore, modeling of PCB cavity with vias is critical for EMI/EMC and SI/PI analysis in practical designs and applications of high-speed PCBs and packages. Fast and accurate modeling technique is desired for broadband simulations in electronic design and application. Various methods have been developed to calculate the resonant frequencies and modes of the waveguide and cavity structures. For example, analytical method is developed for rectangular structure [1] and boundary integral resonant mode expansion (BI-RME) method [2] was developed for arbitrarily shaped waveguide structure. In practical electronic design and application, it is usually in need to characterize not only the waveguide structures, but also the coupling between vias and power/ground boundary. 3D commercial tools such as HFSS provide solutions for accurate analysis the via-cavity coupling problem. But, existing 3D full wave simulators need too much CPU times and memory, they may not be suited for fast broadband analysis.

Green's function has played a critical role in various techniques used in modeling electronic devices and components. For example, boundary integral equation method with free space Green's function is used to model the power/ground planes in printed circuit boards (PCBs) [3] [4] [5] [6]. One key advantage of Green's functions is it can be used for compute the complex structures including waveguide/cavity, vias, and other components in PCB. But, conventional Green's function needs separate computation for different frequencies points. This is a fundamental restriction in broadband modeling and simulations. Hence, it is desired to develop fast techniques for computing the Green's function.

1.2 Research Methodology

In this dissertation, the broadband Green's function method is proposed for fast and accurate modeling of electronic devices and components with arbitrarily shaped waveguide/cavity structures. The broadband Green's function with low frequency extraction (BBGFL) is developed and its various applications is investigated. Systematic methodologies are derived for both TE and TM cases. Different applications are investigated. For TE case, particularly the high-speed interconnects. The method, instead of computing the Green's function at every frequency point directly, it uses three steps to accelerate the computation: first, expand the original Green's function using modal expansion; then compute the modes with a reference Green's function; finally use the modes to quickly construct the Green's function at all the frequency points of interest. In addition, it also uses low wavenumber extraction to further accelerate the convergence of the modal expansion. The low wavenumber part is calculated directly and stored in memory. One key merit of the proposed method is that, it needs only one time computation of Green's function at a single wavenumber, and the results of other frequencies can be quickly derived. This overcomes the restriction of conventional Green's function methods due to repeating same amount of computation for every frequency point of waveguide problems. In particular, it is suited for fast computer-aided design (CAD) in high-speed interconnects.

Besides of TE case, in this dissertation the BBGFL is also applied for the transverse magnetic (TM) case with Dirichlet boundary condition. It is applied to fast and accurate modeling of electronic devices and components with arbitrarily shaped conducting waveguide/cavity structures. Integrated Green's function defined at small patch is introduced to accelerate the convergence of modal expansion series. The broadband Green's function consists of modal expansion of modes that are frequency independent. To accelerate convergence of the Green's function, two low frequency extractions are performed. The first low frequency extraction is done by integrating the modal expansion series of Green's function for the rectangular waveguide over small patches. There are two motivations to introduce the integrated Green's function: (1) in many applications, the integrated Green's function defined at small patch is needed, not the point Green's function; (2) the convergence of integrated Green's function is one order faster than that of conventional point Green's function. In model expansion series, the terms of source are independent with those of observation. In addition, all the terms are frequency independent. Thus, the model expansion series terms are simply pre-computed once, and used for all points and all frequencies. In the second low frequency extraction, we calculate the final Green's function for arbitrarily shaped waveguide at a single low frequency using MoM. The singularity of the Green's function is extracted by such low frequency extraction. These are readily computed once and used for all frequencies. Computation results are presented for TM case. Results show BBGLF and direct MoM are in good agreement. The substantial improvement in computational efficiency enables the BBGFL for fast computer-aided design (CAD) in applications of TM case.

1.3 Organization of the Dissertation

In Chapter 2, we developed the method of broadband Green's function with low wavenumber extraction (BBGFL) for arbitrary shaped waveguide of Neumann case. The bounded medium Greens function has the advantage that when using it to solve boundary value problems, the boundary conditions for a large part of the boundary, such as the boundary of a waveguide, have been satisfied already. To facilitate modeling over a wide range of frequency, we develop the broadband bounded medium Green's function that consists of modal expansion of modes that are frequency independent. To accelerate convergence of the Green's function, low wavenumber extraction is performed by calculating the Green's function at a single low wavenumber. The singularity of the Green's function is also extracted by such low wavenumber extractions. In applying BBGFL, only a small set of field points and source points are usually needed. These are readily computed once and used for all frequencies. Numerical results show BBGLF and direct MoM are in good agreement. We illustrate the application of BBGFL for broadband simulations of vias in arbitrarily shaped power-ground planes by combining with the method of Foldy-Lax multiple scattering equation. The present method is compared with method of moment (MoM) and commercial tool HFSS. Results show that BBGFL has good comparisons with MoM and HFSS on S-parameters, but BBGFL is many times faster than direct MoM and HFSS in CPU.

In chapter 3, we present the application of broadband Green's function with low wavenumber extraction (BBGFL) to fast modeling of the radiated emissions from printed circuit boards (PCBs). The studies are for power bus structure for electromagnetic interference/compatibility (EMI/EMC). We use the BBGFL to compute the Green's function over broadband frequencies along the boundary walls of arbitrarily shaped power/ground planes. The broadband Green's function is based on modal expansions with low wavenumber extraction. Because the modal expressions are independent of frequencies, they are computed once and used for all frequencies. Then the radiated fields are readily derived from the fields on boundary walls using the equivalent principle. Results are illustrated up to 10 GHz and for arbitrary shaped PCB up to 5 inches in sizes. The accuracy and computational efficiency of the present method are compared with the method of moment (MoM) and commercial tool HFSS. The results of radiated emission of BBGFL are in good agreement with MoM and HFSS. In CPU, the method of BBGFL is several hundred times faster than direct MoM and HFSS for broadband simulations. The significant improvement in computational efficiency makes this technique useful for electronic design automation (EDA) to EMI/EMC applications. In this chapter, we present the application of broadband Green's function with low wavenumber extraction (BBGFL) to fast modeling of the radiated emissions from printed circuit boards (PCBs). The studies are for power bus structure for electromagnetic interference/compatibility (EMI/EMC). We use the BBGFL to compute the Green's function over broadband frequencies along the boundary walls of arbitrarily shaped power/ground planes. The broadband Green's function is based on modal expansions with low wavenumber extraction. Because the modal expressions are independent of frequencies, they are computed once and used for all frequencies. Then the radiated fields are readily derived from the fields on boundary walls using the equivalent principle. Results are illustrated up to 10 GHz and for arbitrary shaped PCB up to 5 inches in sizes. The accuracy and computational efficiency of the present method are compared with the method of moment (MoM) and commercial tool HFSS. The results of radiated emission of BBGFL are in good agreement with MoM and HFSS. In CPU, the method of BBGFL is several hundred times faster than direct MoM and HFSS for broadband simulations. The significant improvement in computational efficiency makes this technique useful for electronic design automation (EDA) to EMI/EMC applications.

In chapter 4, we combine the broadband Green's function with low wavenumber extraction (BBGFL) with MoM to study scattering problem in arbitrary shaped waveguide. The technique is applied to broadband modeling and simulation of the scattering by multiple vias in arbitrary shaped waveguide. The BBGFL is used to formulate surface integrals on the surfaces of the vias which are then solved with MoM. By using BBGFL instead of free space Green's functions, we have a drastic reduction of the number of surface unknowns in the integral equations. Since the BBGFL utilize modal expansions that are frequency independent, the method is suitable for broadband simulations. The mixed boundary conditions with external PMC waveguide boundary conditions and internal PEC boundary conditions are studied in this chapter. Results are case of compared with the MoM method of free space Green's function and that of HFSS. It is shown that the results are accurate and the BBGFL/MoM method is much faster than MoM and that of HFSS for broadband simulations.

In chapter 5, we extend the method of broadband Green's function with low frequency extraction (BBGFL) for the transverse magnetic (TM) case with Dirichlet boundary condition. Small patch integrated Green's function is introduced to accelerate the convergence of modal expansion. The BBGFL is applied to fast modeling of Dirichlet boundary value problems, such as the boundary of an arbitrarily shaped conducting waveguide. The broadband Green's function consists of modal expansion of modes that are frequency independent. To accelerate convergence of the Green's function, two low frequency extractions are performed. The first low frequency extraction is done by integrating the Green's function over small patch, which has two advantages: (1) in many applications, the integrated Green's function defined at small patch is needed, not the point Green's function; (2) the convergence of integrated Green's function is one order faster than that of conventional point Green's function. In model expansion series, the terms for source are independent with the terms for observation. In addition, all the terms are frequency independent. Thus, the model expansion series terms are pre-computed once, and used for all points and all frequencies. The second low frequency extraction is performed by calculating the final Green's function for arbitrarily shaped waveguide at a single low frequency using MoM. The singularity of the Green's function is extracted by such low frequency extraction. These are readily computed once and used for all frequencies. Computation results are presented for TM case. Results show BBGLF and direct MoM are in good agreement. The substantial improvement in computational efficiency enables the BBGFL for fast computer-aided design (CAD) in applications of TM case.

In Chapter 6, the proposed Broadband Green's function with low wavenumber extraction (BBGFL) is applied to modeling of traces connecting vias in printed circuit boards, particularly arbitrarily shaped power/ground planes. The proposed method is a hybrid technique based on mode decomposition: BBGFL is used to fast compute the vias in power/ground planes, MoM is used to calculate the impedance matrix of the traces, and then physical circuit model is applied to cascade the vias and traces in the power/ground planes. The present method is compared to method of moment (MoM) and commercial tool HFSS. Results show the present technique has good agreement with MoM and HFSS on the radiated emissions from printed circuit board (PCB) power/ground planes. But it is several hundred times faster than HFSS in CPU time for broadband simulations. The technique provides a fast technique for system level high speed interconnect design and applications.

Chapter 2 Broadband Green's Function with Low Wavenumber Extraction Method for Arbitrary Shaped Waveguides: TE case and Application to Modelling of Vias in Finite Power/Ground Plane

2.1 Summery

In this chapter we developed the method of broadband Green's function with low wavenumber extraction (BBGFL) for arbitrary shaped waveguide. The case of Neumann boundary condition is treated. The Greens function has the advantage that when using it to solve boundary value problems, such as the boundary of a waveguide, the boundary conditions have been satisfied already. To facilitate broadband modeling the broadband Green's function is expressed in modal expansion of modes that are frequency independent. To accelerate convergence of the Green's function, a low wavenumber extraction is performed. The singularity of the Green's function is also extracted by such low wavenumber extractions. Numerical results show that BBGLF and direct MoM are in good agreement. We next illustrate the application of BBGFL for broadband simulations of vias by combining with the method of Foldy-Lax multiple scattering equation. The Results show that BBGFL are in good agreement with MoM and HFSS. It is also shown that BBGFL is many times faster than direct MoM and HFSS. The computational efficiency makes this technique useful for fast computer-aided design (CAD).

2.2 Introduction

The effects of waveguide or cavity structures are critical for the electrical performance of electronic devices and components in signal integrity (SI), power integrity (PI), electromagnetic interference (EMI), and electromagnetic compatibility (EMC). Harmful electromagnetic signal noises or interferences are often generated and amplified at the resonant frequencies due to the waveguide or cavity structures. The issues deteriorate when the electronic devices or computer systems operate at higher frequency or faster speed. In printed circuited boards (PCBs), two adjacent power/ground planes form a waveguide/cavity structure. The propagating modes satisfy the PMC (Neumann boundary conditions) at the edges of PCB power/ground plane structures. These power/ground plane structures are the key root causes in SI/PI and EMI/EMC problems. Vias are used for vertical interconnect for multilayer PCBs. At near the resonant frequencies of the power/ground plane pair, the propagating electromagnetic waves along vias excite strong resonant modes, which can result in strong edge radiation and cause EMI/EMC problems. The switching noises induced by voltage regulator module (VRM) can generate voltage fluctuations and lead to PI problems. The high frequency power noise can also couple into signal vias and cause SI/PI coupling issues. Therefore, modeling of PCB cavity with vias is critical in practical designs and applications of high-speed PCBs and packages. Fast and accurate modeling technique is desired for broadband simulations in electronic design and application. The parallel power/ground planes are finite making them waveguide/cavity structures. They are also of arbitrary shape. Commercial tools such as HFSS provide solutions for accurate analysis the via-cavity coupling problem with much CPU times and memory. They may not be suited for fast broadband analysis. Various methods have been developed to calculate the resonant frequencies and modes of the waveguide and cavity structures. The physical problem is TM mode in a cavity with PMC boundary conditions on the side walls. For example, analytical methods were developed for rectangular structure [1] and boundary integral resonant mode expansion (BI-RME) method [2] [7] [8] [9] [10] [11] [12] was used to calculate the modes of arbitrarily shaped waveguide structures.

Green's function has played an important in modeling electronic devices and components with waveguide/cavity structures. For example, boundary integral equation method with free space Green's function is used to model the power/ground planes in printed circuit boards (PCBs) [3] [13] [4] [6]. In references [13] [4] [6], the free space Green's function is used to formulate the integral equation. However, the disadvantage of the conventional free space Green's function method is that, one solves the boundary value problem with a dense MoM matrix equation for each frequency. For broadband simulations, MoM has to be solved for many times. This leads to low computational efficiency. In this chapter a novel technique, the broadband Green's function with low wavenumber extraction (BBGFL), is proposed for fast and accurate modeling of electronic devices and components with arbitrarily shaped waveguide/cavity structures. It is applied also to the problem of high-speed interconnects. Broadband Green's functions exist for rectangular waveguide and circular waveguide [2] [14]. In this chapter we develop the broadband Green's function for waveguide of arbitrary shape. Unlike the MoM method in [13] [4], in BBGFL, the MoM is used only once for low wavenumber extraction.

In the BBGFL method, we compute the modes of the arbitrary shape waveguide with a reference Green's function. Then we use the modes to construct the broadband Green's function In addition, a low wavenumber extraction is introduced to accelerate the convergence of the modal expansion of the broadband Green's function. The merits of the methodology of BBGFL are: (1) to develop a novel fast technique for computing the broadband Green's functions, which can be used in broadband modeling of electronic devices, components, and interconnects with waveguide structures; (2) to accelerate the convergence of Green's function modal expansion using low wavenumber extractions; (3) with the low wavenumber extraction, the singularity of the broadband Green's function is also extracted, (4) to combine the method with Foldy-Lax multiple scattering equations [3] [13] [4] [6] [15] [16] [17] [18] [19] [5] for fast field simulation of vias in arbitrarily shaped PCB power/ground planes.

2.3 Methodology

In this section, we describe the theorem and derive the equations for the presented BBGFL technique.

2.3.1 Broadband Bounded Green's Function with Low Frequency Extractions for Neumann Case

In this section we derive the equations for the BBGFL technique and illustrate it for the L-shape waveguide. The methodology applies to waveguide of arbitrary shape. In Figure 2.1a, and 1b, we show respectively rectangular waveguide with domain Ω and L shape waveguide with domain$S$. The boundaries are $\partial\Omega$ and $\partial\mathrm{S}$ respectively. The boundary σ in Figures 1a and 1b is the part of $\partial\mathrm{S}$ that is not in$\partial\Omega$.

The signal integrity problem consists of multiple vias in the L-shaped waveguideS. In Figure 2.1b, we showed two vias one centered at$\bar{\rho}_p$ and the other centered at $\bar{\rho}_q$. The goal is to solve the problem in Figure 2.1b for a broad range of frequencies. The Green's function $g_H^{\Omega}(k,\bar{\rho},\bar{\rho}')$ for rectangular waveguide Ω has been used in the BI-RME method [2, 3, 7]. The Green's function is at wavenumber. In this chapter, we develop the Green's function $g_H^{\mathrm{S}}(k,\bar{\rho},\bar{\rho}')$ for the L-shape waveguide$S$. The subscript H is to denote the Neumann boundary condition on the boundary $\partial\Omega$ and$\partial\mathrm{S}$. A reason for using the H subscript is that traditionally, Neumann boundary condition is associated with the magnetic field.

The physical problem in Figure 2.1b is that of TM modes with PMC on the boundary ∂S and PEC on the boundary of the vias. In waveguide problems with PEC side walls, the Neumann boundary condition corresponds to the TE case. For the present problem, the wave function ψ represents the E_z component of the TM wave.

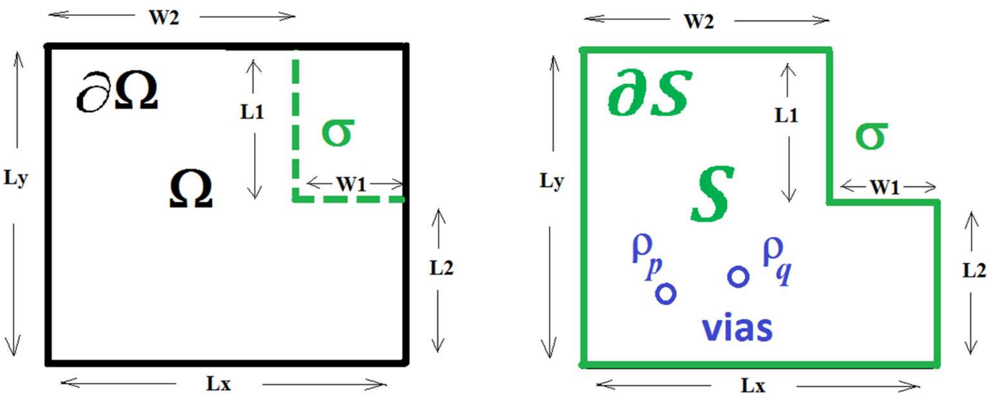

(a) (b)

Figure 2.1 (a). Rectangle cavity Ω with boundary $\partial\Omega$. $g_H^{\Omega}(k,\bar{\rho},\bar{\rho}')$ is Green's function with wavenumber k for Ω, $g_H^{\Omega}(k_L^{\Omega},\bar{\rho},\bar{\rho}') = g_0(k_L^{\Omega},\bar{\rho},\bar{\rho}') + g_{HR}^{\Omega}(k_L^{\Omega},\bar{\rho},\bar{\rho}')$ is Green's function at low wavenumber k_L^{Ω}; (b). L-shaped cavity S with boundary ∂S. $g_H^{S}(k,\bar{\rho},\bar{\rho}')$ is Green's function with general wavenumber k for S, $g_H^{S}(k_L^{S},\bar{\rho},\bar{\rho}') = g_0(k_L^{S},\bar{\rho},\bar{\rho}') + g_{HR}^{S}(k_L^{S},\bar{\rho},\bar{\rho}')$ is Green's function at low wavenumber k_L^{S}.

2.3.1.1 Broadband Green's Function $\mathbf{g_H^{\Omega}(k,\bar{\rho},\bar{\rho}')}$ and $\mathbf{g_H^{S}(k,\bar{\rho},\bar{\rho}')}$ with Low Wavenumber Extraction.

Consider a rectangular waveguide Ω of dimensions $\mathrm{L_x}$ and $\mathrm{L_y}$, $-\frac{\mathrm{L_x}}{2} < x < \frac{\mathrm{L_x}}{2}$, $-\frac{\mathrm{L_y}}{2} < y < \frac{\mathrm{L_y}}{2}$.

The modal solutions are

$$\Psi_{mn}^{\Omega}(\bar{r}) = \sqrt{\frac{\xi_m \xi_n}{L_x L_y}} \cos\frac{m\pi}{L_x}\left(x + \frac{L_x}{2}\right) \cos\frac{n\pi}{L_y}\left(y + \frac{L_y}{2}\right) \tag{1}$$

where $m, n = 0,1,2, \cdots\cdots$; $\xi_m = 2$ if $m \neq 0$; and $\xi_m = 1$ if $m = 0$. Let $k_{mn} = \sqrt{(k_{xm})^2 + \left(k_{yn}\right)^2}$ be the resonant wavenumber of the rectangular waveguide Ω with $k_{xm} = \frac{m\pi}{L_x}$, $k_{yn} = \frac{n\pi}{L_y}$.

If we use α as the combined index of (m, n), then

$$g_H^{\Omega}(k, \bar{\rho}, \bar{\rho}') = \sum_{\alpha} \frac{\psi_{\alpha}^{\Omega}(\bar{\rho})\psi_{\alpha}^{\Omega}(\bar{\rho}\prime)}{k_{\alpha}^2 - k^2} \tag{2}$$

In the BIRME method [2] [7] [11], the convergence of the modal expansion is accelerated by extraction at DC. In the following, we use a low wavenumber extraction to accelerate the convergence. Let the low wavenumber be k_L^{Ω}, which is much lower than the wavenumber of interest. That is$k_L^{\Omega} \ll k = \omega\sqrt{\mu\varepsilon}$.

We calculate $g_H^{\Omega}\left(k_L^{\Omega}, \bar{\rho}, \bar{\rho}'\right)$ as the sum of the free space Green's function and the response

$$g_H^{\Omega}\left(k_L^{\Omega}, \bar{\rho}, \bar{\rho}'\right) = g_0\left(k_L^{\Omega}, \bar{\rho}, \bar{\rho}'\right) + g_{HR}^{\Omega}\left(k_L^{\Omega}, \bar{\rho}, \bar{\rho}'\right) \tag{3}$$

where

$$g_0\left(k_L^{\Omega}, \bar{\rho}, \bar{\rho}'\right) = \frac{1}{4j} H_0^{(2)}\left(k_L^{\Omega}, \bar{\rho}, \bar{\rho}'\right) \tag{4}$$

In equation (4) $H_0^{(2)}$ is the 0th order Hankel function of the second kind, and $g_{HR}^{\Omega}\left(k_L^{\Omega}, \bar{\rho}, \bar{\rho}'\right)$ is the response a single low wavenumber k_L^{Ω}. In the appendix, we describe the calculations of the impedance matrix elements associated with the free space Green's function and the response Green's function.

Then

$$g_H^\Omega(k,\bar{\rho},\bar{\rho}') = g_0\left(k_L^\Omega,\bar{\rho},\bar{\rho}'\right) + g_{HR}^\Omega\left(k_L^\Omega,\bar{\rho},\bar{\rho}'\right) + \sum_\alpha \frac{k^2-\left(k_L^\Omega\right)^2}{\left(k_\alpha^2-k^2\right)\left(k_\alpha^2-\left(k_L^\Omega\right)^2\right)} \psi_\alpha^\Omega(\bar{\rho})\psi_\alpha^\Omega(\bar{\rho}') \tag{5}$$

Note that the modal expansion now converges as $1/k_\alpha^4$. Also $g_H^\Omega(k,\bar{\rho},\bar{\rho}')$ needs only be calculated for $\bar{\rho},\bar{\rho}'$ on the L part of the boundary which is denoted as σ in Figure 2.1b.

2.3.1.2 Calculation of $\mathbf{g_H^S(k,\bar{\rho},\bar{\rho}')}$ Modal Solution $\boldsymbol{\psi_\beta^S}$ and Resonant Wavenumber $\mathbf{k_\beta^S}$

The Green's function for the L-shaped waveguide S is

$$g_H^S(k,\bar{\rho},\bar{\rho}') = \sum_\beta \frac{\psi_\beta^S(\bar{\rho})\psi_\beta^S(\bar{\rho}')}{\left(\mathrm{k}_\beta^S\right)^2-k^2} \tag{6}$$

where $\psi_\beta^S(\bar{\rho})$ is the modal solution of S and k_β^S is the corresponding resonant wavenumber. Following a procedure similar to BI-RME [2] [7] [11] an integral equation approach can be formulated to calculate $\psi_\beta^S(\bar{\rho})$ by using the $g_H^\Omega(k,\bar{\rho},\bar{\rho}')$ with low wavenumber extraction and equivalent sources onσ. There are some differences from BI-RME in the final matrix equation because we use of low wavenumber extraction instead of DC extraction. The wave function ψ_H^S obeys the wave equation

$$(\nabla_t^2 + k^2)\psi_H^S = 0 \tag{7}$$

with Neumann boundary condition $\hat{n}_t \cdot \psi_H^{\mathrm{S}} = 0$ on ∂S. Applying the Green's theorem to domain S for the two functions ψ_H^{S}, and g_H^{Ω} , there is a contribution from σ because g_H^{Ω} does not obey boundary condition on σ. The result integral equation is

$$-\psi_H^s(\bar{\rho}) = \int_\sigma dl' \left(\psi_H^s(\bar{\rho}')\hat{n}_t' \cdot \nabla_{\mathrm{t}}' g_H^{\Omega}(k,\bar{\rho},\bar{\rho}')\right) \tag{8}$$

Substitute the low wavenumber extraction result of $g_H^{\Omega}(k,\bar{\rho},\bar{\rho}')$ from (5) into (8), we obtain

$$\psi_H^s(\bar{\rho}) = -\int_\sigma dl' \, \psi_H^s(\bar{\rho}')\hat{n}_t' \cdot \nabla'_{\mathrm{t}} \, g_0\left(k_L^{\Omega},\bar{\rho},\bar{\rho}'\right)$$
$$-\int_\sigma dl' \, \psi_H^s(\bar{\rho}')\hat{n}_t' \cdot \nabla_{\mathrm{t}}' g_{HR}^{\Omega}\left(k_L^{\Omega},\bar{\rho},\bar{\rho}'\right) - \sum_\alpha b_\alpha \frac{\psi_\alpha(\bar{\rho})}{k_\alpha^2 - \left(k_L^{\Omega}\right)^2} \tag{9}$$

with

$$b_\alpha = \frac{k^2 - \left(k_L^{\Omega}\right)^2}{k_\alpha^2 - k^2} \int_\sigma dl' \, \psi_H^s(\bar{\rho}')\hat{n}_t' \cdot \nabla_{\mathrm{t}}' \psi_\alpha(\bar{\rho}') \tag{10}$$

Equation (9) can be solved by the method of moments with point matching and pulse basis functions. Note that the singularity is only in the term containing the free space low wavenumber Green's function $\hat{n}_t' \cdot \nabla_{\mathrm{t}}' g_0\left(k_L^{\Omega},\bar{\rho},\bar{\rho}'\right)$. We discretizing σ into N patches of Δt length each. Let the unknown be

$$\psi_{Hn}^{\mathrm{S}} = \frac{q_n}{\Delta t} \tag{11}$$

on σ_n, where σ_n is the nth patch on σ . Let the truncation of the modal expansion be M terms, $\alpha = 1,2,\cdots\cdots,M$.

Define matrix elements,

$$P_{mn} = \left(\frac{1}{2}\right)\frac{1}{\Delta t} + \frac{1}{\Delta t}\int_{\sigma_m} dl'\hat{n}'_t \cdot \nabla'_t g^{\Omega}_{HR}\left(k^{\Omega}_L, \bar{\rho}_m, \bar{\rho}'\right) \tag{12.a}$$

for $n = m$;

$$P_{mn} = \frac{1}{\Delta t}\int_{\sigma_n} dl'\hat{n}'_t \cdot \nabla'_t g^{\Omega}_{H}\left(k^{\Omega}_L, \bar{\rho}_m, \bar{\rho}'\right) \tag{12.b}$$

for $n \neq m$, and

$$S_{m\alpha} = \left(\frac{1}{k^2_{\alpha} - \left(k^{\Omega}_L\right)^2}\right)\psi_{\alpha}(\,\bar{\rho}_m) \tag{13}$$

In the Appendix, we describe the method that we used to calculate P_{mn} which is at a single low wavenumber k^{Ω}_L.

In matrix notations

$$\bar{\bar{S}}\bar{b} + \bar{\bar{P}}\bar{q} = 0 \tag{14}$$

where $\bar{\bar{S}}$ is of dimension $N \times M$ with matrix elements described in (12), $\bar{\bar{P}}$ is of dimension $N \times N$ with matrix elements described in (13), $\bar{b}$ is unknown eigenvector of dimension $M \times 1$, and $\bar{q}$ is of dimension $N \times 1$ with elements defined in (11).

Let

$$Q_{\alpha n} = \left(\frac{1}{k^2_{\alpha} - \left(k^{\Omega}_L\right)^2}\right)\left[\hat{n}'_t \cdot \nabla'_t \psi_{\alpha}(\bar{\rho}')\right]_{\bar{\rho}' = \bar{\rho}_n} \tag{15}$$

Then

$$b_\alpha = \frac{k^2 - \left(k_L^\Omega\right)^2}{k_\alpha^2 - k^2} \left(k_\alpha^2 - \left(k_L^\Omega\right)^2\right) \sum_{n=1}^{N} Q_{\alpha n} q_n \tag{16}$$

Let

$$D_{\alpha\beta} = \left(\frac{1}{k_\alpha^2 - \left(k_L^\Omega\right)^2}\right) \delta_{\alpha\beta} \tag{17}$$

Then in matrix notations

$$\bar{\bar{D}}\bar{b} + \bar{\bar{Q}}\bar{q} = \frac{1}{k^2 - \left(k_L^\Omega\right)^2} \bar{b} \tag{18}$$

where $\bar{\bar{D}}$ is of dimension $M \times M$ and $\bar{\bar{Q}}$ is of dimension $M \times N$. Combining the two matrix equations (14) and (17) gives the eigenvalue problem

$$\left(\bar{\bar{D}} - \bar{\bar{Q}}\bar{\bar{P}}^{-1}\bar{\bar{S}}\right)\bar{b} = \frac{1}{\tilde{k}^2} \bar{b} \tag{19}$$

with $\tilde{k}^2 = k^2 - \left(k_L^\Omega\right)^2$. Solving the eigenvalue problem gives the resonant wavenumber k and the associated eigenvector $\bar{b}$.

2.3.1.3 Normalization of Modes for Neumann Case

The size of the matrix eigenvalue equation in (19) is$M$. Let β be the eigenvalue index, k_β^S be the resonant wavenumber and $b_{\alpha\beta}$ be the eigenvector. After solving (19), we next normalize the modes $\psi_\beta^S(\bar{\rho})$.

Let

$$\tilde{\psi}_\beta^S(\bar{\rho}) = \sum_{\alpha=1}^{M} b_{\alpha\beta} \frac{\psi_\alpha(\bar{\rho})}{k_\alpha^2 - \left(k_L^\Omega\right)^2} \tag{20}$$

Substitute (20) into (9) and apply ∇^2. Then

$$\nabla^2 \tilde{\psi}_\beta^s(\bar{\rho}) = -\nabla^2 \psi_H^s(\bar{\rho}) + \left(k_L^\Omega\right)^2 \int_\sigma dl' \, \psi_H^s(\bar{\rho}') \hat{n}_t' \cdot \nabla_{\mathrm{t}}' g_H^\Omega\left(k_L^\Omega, \bar{\rho}, \bar{\rho}'\right) \tag{21}$$

Discretizing the L-shaped boundaryσ, using the discretized unknowns q_n and (20) give

$$\left(k_\beta^{\mathrm{S}}\right)^2 \psi_\beta^s(\bar{\rho}) = \sum_{\alpha=1}^M b_{\alpha\beta} \frac{k_\alpha^2 \psi_\alpha(\bar{\rho})}{k_\alpha^2 - \left(k_L^\Omega\right)^2} + \left(k_L^\Omega\right)^2 \sum_{n=1}^N q_n \left[\hat{n}_t' \cdot \nabla_{\mathrm{t}}' g_H^\Omega\left(k_L^\Omega, \bar{\rho}, \bar{\rho}'\right)\right]_{\bar{\rho}' = \bar{\rho}_n} \tag{22}$$

i) Case of $k_\beta \neq 0$:

Let the nth element of the column vector $\bar{\zeta}(\bar{\rho})$ be

$$[\bar{\zeta}(\bar{\rho})]_n = \left[\hat{n}_t' \cdot \nabla_{\mathrm{t}}' g_H^\Omega\left(k_L^\Omega, \bar{\rho}, \bar{\rho}'\right)\right]_{\bar{\rho}' = \bar{\rho}_n} \tag{23}$$

Then

$$\left(k_\beta^{\mathrm{S}}\right)^2 \psi_\beta^s(\bar{\rho}) = \sum_{\alpha=1}^M b_{\alpha\beta} \frac{k_\alpha^2 \psi_\alpha(\bar{\rho})}{k_\alpha^2 - \left(k_L^\Omega\right)^2} + \left(k_L^\Omega\right)^2 [\bar{\zeta}^t(\bar{\rho})] \bar{q} \tag{24}$$

where t denotes transpose of the matrix.

Then the normalization is

$$\iint_{\mathrm{S}} dxdy \left(\psi_\beta^s(\bar{\rho})\right)^2 = \frac{1}{\left(k_\beta^{\mathrm{S}}\right)^4} \iint_{\mathrm{S}} dxdy \sum_\alpha \sum_{\alpha'} \left[\frac{b_{\alpha\beta} k_\alpha^2 \psi_\alpha(\bar{\rho})}{k_\alpha^2 - \left(k_L^\Omega\right)^2} \frac{b_{\alpha'\beta} k_{\alpha'}^2 \psi_{\alpha'}(\bar{\rho})}{k_{\alpha'}^2 - \left(k_L^\Omega\right)^2}\right]$$

$$+\frac{1}{\left(k_\beta^{\mathrm{S}}\right)^2}\iint_{\mathrm{S}} dxdy \sum_{\alpha'}\left[\frac{b_{\alpha'\beta}k_{\alpha'}^2\psi_{\alpha'}(\bar{\rho})}{k_{\alpha'}^2-\left(k_L^\Omega\right)^2}\right]\frac{\left(k_L^\Omega\right)^2}{\left(k_\beta^{\mathrm{S}}\right)^2}[\bar{\zeta}^t(\bar{\rho})]\bar{q}$$

$$+\frac{1}{\left(k_\beta^{\mathrm{S}}\right)^2}\iint\limits_{\mathrm{S}} dxdy \sum_{\alpha}\left[\frac{b_{\alpha\beta}k_{\alpha}^2\psi_{\alpha}(\bar{\rho})}{k_{\alpha}^2-\left(k_L^\Omega\right)^2}\right]\frac{\left(k_L^\Omega\right)^2}{\left(k_\beta^{\mathrm{S}}\right)^2}[\bar{\zeta}^t(\bar{\rho})]\bar{q}$$

$$+\iint_{\mathrm{S}} dxdy\left[\frac{\left(k_L^\Omega\right)^2}{\left(k_\beta^{\mathrm{S}}\right)^2}[\bar{\zeta}^t(\bar{\rho})]\bar{q}\right]^2 \tag{25}$$

We use the property $k_\alpha^2\iint_{\mathrm{S}} dxdy\,\psi_\alpha(\bar{\rho}) = 0$. Then

$$\iint_{\mathrm{S}} dxdy\left(\psi_\beta^s(\bar{\rho})\right)^2 = \frac{1}{\left(k_\beta^{\mathrm{S}}\right)^4}\sum_\alpha\left(b_{\alpha\beta}\right)^2\left(\frac{k_\alpha^2}{k_\alpha^2-\left(k_L^\Omega\right)^2}\right)^2$$

$$+\iint_{\mathrm{S}} dxdy\left[\frac{\left(k_L^\Omega\right)^2}{\left(k_\beta^{\mathrm{S}}\right)^2}[\bar{\zeta}^t(\bar{\rho})]\bar{q}\right]^2 \tag{26}$$

Since $\iint_{\mathrm{S}} dxdy\left(\psi_\beta^s(\bar{\rho})\right)^2 = 1$ and $k_L^\Omega \ll k_\beta^S$, the normalization condition for the eigenvector is

$$\sum_{\alpha=1}^{M}\left(b_{\alpha\beta}\right)^2 = \left(k_\beta^{\mathrm{S}}\right)^4 \tag{27}$$

ii) Case of $k_\beta^S = 0$

The constant is a solution for the arbitrary waveguide with Neumann boundary condition. The constant mode for the L-shaped waveguide is

$$\psi_0^S(\bar{\rho}) = \sqrt{\frac{1}{A_S}} \tag{28}$$

where A_S = area of L-shaped waveguide.

2.3.1.4 Broadband Green's Function for L-shaped Waveguide and Low Wavenumber Extraction

After the normalized modal functions are calculated, the Green's function for Neumann problem of the L-shaped waveguide is as given in equation (6) with the modal functions and eigenvalues as calculated by (19) for $k_\beta^S \neq 0$ and by (28) for $k_\beta^S = 0$. We will also use low wavenumber extraction for g_H^{S} of the arbitrary waveguide. Note that we use low wavenumber extraction, twice, with k_L^{Ω} for the rectangular waveguide and k_L^{S} for the waveguide with arbitrary shape. Let the solution be denoted by$g_H^{\mathrm{S}}\left(k_L^{\mathrm{S}}, \bar{\rho}, \bar{\rho}'\right)$. When calculating the solution by MoM at k_L^{S}, the solution is readily separated into the sum of the primary $g_0\left(k_L^{\mathrm{S}}, \bar{\rho}, \bar{\rho}'\right)$ and the response $g_{HR}^{\mathrm{S}}\left(k_L^{\mathrm{S}}, \bar{\rho}, \bar{\rho}'\right)$.

$$g_H^{\mathrm{S}}\left(k_L^{\mathrm{S}}, \bar{\rho}, \bar{\rho}'\right) = g_0\left(k_L^{\mathrm{S}}, \bar{\rho}, \bar{\rho}'\right) + g_{HR}^{\mathrm{S}}\left(k_L^{\mathrm{S}}, \bar{\rho}, \bar{\rho}'\right) \tag{29}$$

With the subtraction of $g_H^{\mathrm{S}}\left(k_L^{\mathrm{S}}, \bar{\rho}, \bar{\rho}'\right)$ the Green's function $g_H^{\mathrm{S}}(k, \bar{\rho}, \bar{\rho}')$ for arbitrary k is

$$\begin{aligned} g_H^{\mathrm{S}}(k, \bar{\rho}, \bar{\rho}') = {} & g_0\left(k_L^{\mathrm{S}}, \bar{\rho}, \bar{\rho}'\right) + g_{HR}^{\mathrm{S}}\left(k_L^{\mathrm{S}}, \bar{\rho}, \bar{\rho}'\right) \\ & + \sum_\beta \frac{k^2 - \left(k_L^{\mathrm{S}}\right)^2}{\left(\left(k_\beta^{\mathrm{S}}\right)^2 - k^2\right)\left(\left(k_\beta^{\mathrm{S}}\right)^2 - \left(k_L^{\mathrm{S}}\right)^2\right)} \psi_\beta^{\mathrm{S}}(\bar{\rho}) \psi_\beta^{\mathrm{S}}(\bar{\rho}') \end{aligned} \tag{30}$$

Equation (30) is the result of the Broadband Green's function. Note that:

i) The modal summation in (30) has convergence of $\left(k_\beta^S\right)^{-4}$;

ii) The singularity of the Green's function in (30) has been subtracted and resides in the primary Green's function of the single low wavenumber, $g_0\left(k_L^{\mathrm{S}}, \bar{\rho}, \bar{\rho}'\right)$;

iii) $\psi_\beta^{\mathrm{S}}(\bar{\rho})$, $\psi_\beta^{\mathrm{S}}(\bar{\rho}')$ and k_β^S only depends on geometry and are computed once and used for all frequencies;

iv) The part of the expression that depends on frequencies and material properties are in k^2 in (30); and

v) The broadband Green's function $g_H^{\mathrm{S}}(k, \bar{\rho}, \bar{\rho}')$ are usually only needed for a small set of points $\bar{\rho}$ and $\bar{\rho}'$ since the Neumann boundary conditions on ∂S.

2.3.1.5 Summary Procedure for Computing $\mathbf{g}_{\mathbf{H}}^{\mathbf{S}}(\mathbf{k}, \overline{\boldsymbol{\rho}}, \overline{\boldsymbol{\rho}}')$

In summary, there are 5 steps in the procedure as follows:

Step 1: At a single low wavenumberk_L^{Ω}, calculate the impedance matrix elements of P_{mn} of equation (12) as given in Appendix A.

Step 2: Use equation (18) to solve for eigenmodes $\psi_\beta^{\mathrm{S}}(\bar{\rho})$ and resonant wavenumbers k_β^S.

Step 3: Normalization of modes $\psi_\beta^{\mathrm{S}}(\bar{\rho})$ are performed by equations (27) and (28).

Step 4: At a single low wavenumberk_L^S, solve MoM for L-shaped waveguide to get$g_H^{\mathrm{S}}\left(k_L^{\mathrm{S}}, \bar{\rho}, \bar{\rho}'\right)$. Decompose into primary and response as in (29).

Step 5: Construct broadband Green's function $g_H^{\mathrm{S}}(k, \bar{\rho}, \bar{\rho}')$ from low wavenumber extraction of$g_H^{\mathrm{S}}\left(k_L^{\mathrm{S}}, \bar{\rho}, \bar{\rho}'\right)$, and normalized modal solutions $\psi_\beta^{\mathrm{S}}(\bar{\rho})$ as in equation (30).

With the $g_H^{\mathrm{S}}(k, \bar{\rho}, \bar{\rho}')$, then the response Green's function at arbitrary, $g_{HR}^{\mathrm{S}}(k, \bar{\rho}, \bar{\rho}')$ is given by subtracting the primary at k

$$g_{HR}^{\mathrm{S}}(k, \bar{\rho}, \bar{\rho}') = g_0\left(k_L^{\mathrm{S}}, \bar{\rho}, \bar{\rho}'\right) + g_{HR}^{\mathrm{S}}\left(k_L^{\mathrm{S}}, \bar{\rho}, \bar{\rho}'\right) - g_0(k, \bar{\rho}, \bar{\rho}')$$

$$+\sum_{\beta}\frac{k^2-\left(k_L^{S}\right)^2}{\left(\left(k_\beta^{S}\right)^2-k^2\right)\left(\left(k_\beta^{S}\right)^2-\left(k_L^{S}\right)^2\right)}\psi_\beta^{S}(\bar{\rho})\psi_\beta^{S}(\bar{\rho}') \qquad (31)$$

The above is the broadband expression and is useful since the primary is always known. The procedure thus includes one MoM solution at low wavenumber k_L^{S} for arbitrarily shaped waveguide (L-shaped waveguide). The result in equation (31) is labelled as broadband because the dependence of the expression on frequency/wavenumber is merely the factor $\frac{\left(k^2-\left(k_L^{S}\right)^2\right)}{\left(\left(k_\beta^{S}\right)^2-k^2\right)}$ and the rest of the expression is independent of wavenumber/frequency.

The method of DC extraction is used in BI-RME [2] [7] [8] [9] [10] [11] [12] for the case of rectangular waveguide and circular waveguide. In such cases, closed form analytical expressions were obtained for the DC extraction. Analytical expressions do not exist for DC for arbitrary waveguide. We find it convenient to use low wavenumber extraction because it is general and can be implemented numerically for rectangular waveguide and arbitrary shape waveguide rather than relying on closed form analytical expressions. Another reason is because DC extraction needs to deal with the mode at kmn=0, while low wavenumber extraction circumvents the problem. We also use a modal series representation in the Appendix for low wavenumber extraction of the rectangular waveguide.

In addition to using low wavenumber extraction, it is to be noted that the BIRME [2] [7] [8] [9] [10] [11] [12] was only used to construct modes for arbitrary waveguide. It had not been used to construct the Green's function. In this chapter, we use the modes of arbitrary waveguide to construct the broad band Green's function (BBGFL). The expression of BBGFL is convenient for broadband simulations. We next use BBGFL for broadband simulations of the multiple vias problem.

2.3.2 Application of Broadband Green’s Function of Arbitrary Waveguide to Foldy Lax Multiple Scattering Equation for Scattering by Vertical Vias

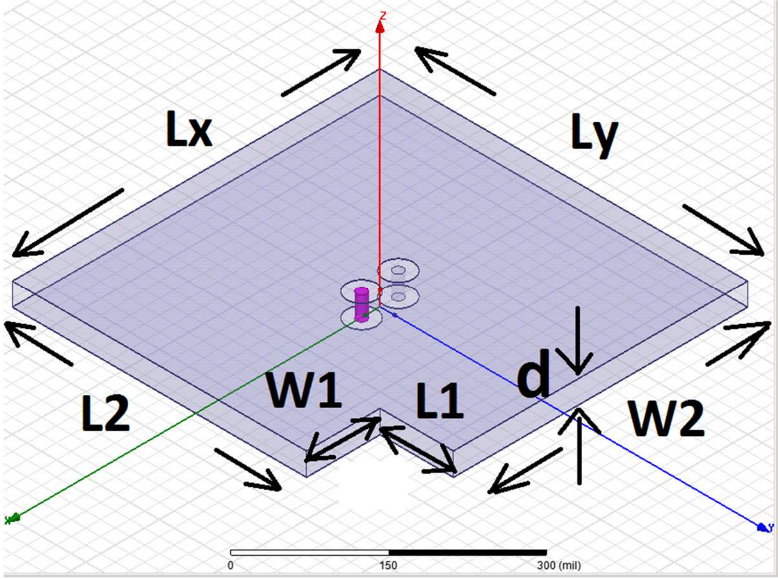

Figure 2.2 3D geometry of the L-shaped power/ground plane pair with small cut out and 2 vias.

We next consider multiple vias in the arbitrary shaped waveguide$S$. The Green's function at an arbitrary k can be separated into the primary Green's function and the wall Green's function$g_W^S(k,\bar{\rho},\bar{\rho}')$. The wall Green’s function is the same as the response Green’s function $g_{HR}^S(k,\bar{\rho},\bar{\rho}')$ of equation (31). We used the name wall Green's function to be consistent with the previous chapter in which we combined MoM with the Foldy Lax equation [6]. In this section, we combine the BBGFL with Foldy Lax multiple scattering solutions. The results are expressed in terms of the wall Green’s function$g_W^S(k,\bar{\rho},\bar{\rho}')$.

In the multiple scattering using Foldy Lax equations, we treat the TM modes with

$$k_{zl} = \frac{l\pi}{d};\ k_{\rho l} = \sqrt{k^2 - k_{zl}^2} \tag{32}$$

where $l = 0,1,2,\cdots\cdots$. The separation between the two plates isd, and k is the wavenumber. In the problem of PCB power/ground plane pair, $kd \ll 1$. Thus modes with $l \neq 0$ are evanescent and will not propagate to the wall and have little reflection from the boundary walls. To include the boundary effects of waveguide of arbitrary shape, we consider only the $l = 0$ mode. The modes with $l \neq 0$ are included in the results but follow the same treatment of Foldy Lax equations as that of infinite ground plane [16] [17] [18]. In the $l \neq 0$ modes, the near field interactions are included among the vias and between the antipad source and the vias. The $l = 0$ mode solutions are modified by including the wall effects. For TM_0 mode, the electric field only has the E_z component which is represented by the wave function ψ. The "z" subscript in E_z will be suppressed. For the $l = 0$ mode, $k_{zl} = 0$ and$k_{\rho l} = k$. Since there is no variation with z; we use only the 2-dimensional ∇_t and the two dimensional position vector$\bar{\rho}$. The power/ground planes have perfect magnetic conductor (PMC) on the boundary walls. Thus the wave functions obey Neumann boundary conditions.

In the following we suppress the k dependence in g_W and g_0, since in solving Foldy Lax equations, we solve the equations for each k.

Consider a via centered at $\bar{\rho}_p$ (left circle in Figure 2.3). From the via, the E_z component of the outgoing mth cylindrical wave of the TM_0 mode is

$$E_m(\bar{\rho} - \bar{\rho}_p) = kH_m^{(2)}(k|\bar{\rho} - \bar{\rho}_p|)e^{-jm\phi_{\overline{\rho\rho_p}}} \tag{33}$$

where $\phi_{\overline{\rho\rho_p}}$ is the angle between the vector $\bar{\rho} - \bar{\rho}_p$ and the x axis. To obtain $E_m(\bar{\rho} - \bar{\rho}_p)$ from $g_0(\bar{\rho}, \bar{\rho}_a)$ we use the relation

$$g_0(\bar{\rho},\bar{\rho}_a) = \frac{1}{4j} H_0^{(2)}(k|\bar{\rho}-\bar{\rho}_a|)$$

$$= \sum_m \frac{1}{4jk} J_m\left(k\left|\bar{\rho}_a - \bar{\rho}_p\right|\right) exp\left(jm\phi_{\overline{\rho_a\rho_p}}\right) E_m\left(\bar{\rho}-\bar{\rho}_p\right) \tag{34}$$

Consider $\bar{\rho}_a$ to be points on a circular cylinder of radius R_1 about the via center $\bar{\rho}_p$ (left circle in Figure 2.3), then

$$E_m\left(\bar{\rho}-\bar{\rho}_p\right) = \frac{4jk}{2\pi J_m(kR_1)} \int_0^{2\pi} d\,\phi_{\overline{\rho_a\rho_p}} exp\left(-jm\phi_{\overline{\rho_a\rho_p}}\right) g_0(\bar{\rho},\bar{\rho}_a) \tag{35}$$

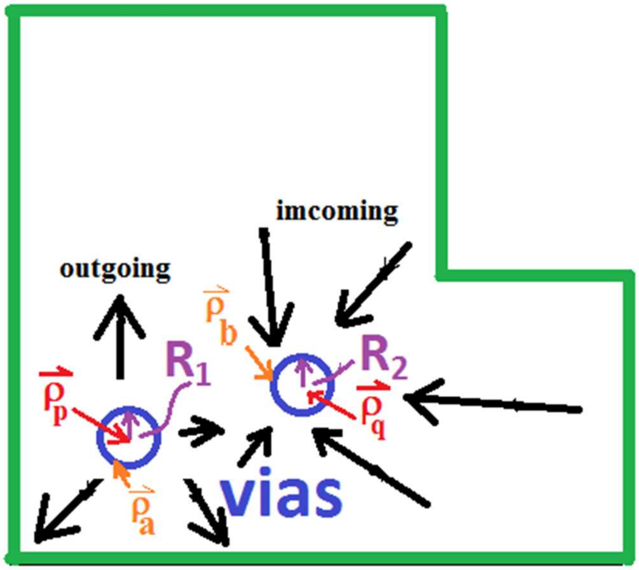

Figure 2.3 Calculation of X_{nm}^{qpW} by integration over two circles of radii R_1 and R_2 around $\bar{\rho}_p$ and $\bar{\rho}_q$ respectively.

The electric field of the *m*th cylindrical wave from via *p* is incident on the wall. The scattered field from the wall, $E_s^{Wpm}(\bar{\rho})$, is expressed in terms of the wall Green's function $g_W(\bar{\rho},\bar{\rho}_a)$.

$$E_s^{Wpm}(\bar{\rho}) = \frac{4jk}{2\pi J_m(kR_1)} \int_0^{2\pi} d\,\phi_{\overline{\rho_a\rho_p}} exp\left(-jm\phi_{\overline{\rho_a\rho_p}}\right) g_W(\bar{\rho},\bar{\rho}_a) \tag{36}$$

Next we consider the wall reflected field $E_s^{Wpm}(\bar{\rho})$ to be incident on via q. The via q can be the same as via, in which case $q = p$, or not the same via, in which case, $q \neq p$. The scattered field from the wall onto via q is expanded into regular wave functions, $RgE_n(\bar{\rho} - \bar{\rho}_q)$, about via q

$$E_s^{Wpm}(\bar{\rho}) = \sum_n RgE_n(\bar{\rho} - \bar{\rho}_q) X_{nm}^{qpW} \tag{37}$$

where

$$RgE_n(\bar{\rho} - \bar{\rho}_q) = kJ_n(k|\bar{\rho} - \bar{\rho}_q|) exp(-jn\overline{\rho\rho_q}) \tag{38}$$

In (37), X_{nm}^{qpW} is the coefficient, due to the wall reflection that couples the *m*th cylindrical outgoing wave of via p to the *n*th incident cylindrical wave onto via q. The X_{nm}^{qpW} coefficients are obtained by

$$X_{nm}^{qpW} = \frac{1}{2\pi k J_n(kR_2)} \int_0^{2\pi} d\,\phi_{\overline{\rho_b\rho_q}} exp\left(jn\phi_{\overline{\rho_b\rho_q}}\right) E_s^{Wpm}(\bar{\rho}_b) \tag{39}$$

where $\bar{\rho}_b$ are points on a circular cylinder of radius R_2 about the via $\bar{\rho}_q$ (right circle in Figure 2.3). Substituting (36) into (39),

$$X_{nm}^{qpW} = \frac{1}{2\pi k J_n(kR_2)} \int_0^{2\pi} d\,\phi_{\overline{\rho_b\rho_q}} exp\left(jn\phi_{\overline{\rho_b\rho_q}}\right) \frac{4jk}{2\pi J_m(kR_1)}$$
$$\int_0^{2\pi} d\,\phi_{\overline{\rho_a\rho_p}} exp\left(-jm\phi_{\overline{\rho_a\rho_p}}\right) g_W(\bar{\rho}_b, \bar{\rho}_a) \tag{40}$$

The above equation calculates X_{nm}^{qpW} in terms of the wall Green's function $g_W(\bar{\rho}_b, \bar{\rho}_a)$ by carrying out integrations over two circles (left and right circles in Figure 2.3). In the previous paper [6] combining MoM with Foldy-Lax multiple scattering, the coefficients X_{nm}^{qpW} were obtained by solving the surface integral equation by MoM for each wavenumber$k$. After the X_{nm}^{qpW}coefficientsn were obtained, the Foldy Lax equations of multiple scattering in the presence of the wall can be solved [6]. We use matrix notations of dimension $(2M+1), n = -M, -(M-1), \cdots\cdots, (M-1), M,$ where M is the maximum harmonic index. Let superscript t be used to denote transpose. Then

$$\bar{E}^t(\bar{\rho}-\bar{\rho}_q) = \left[E_{-M}(\bar{\rho}-\bar{\rho}_q) \;\; E_{-(M-1)}(\bar{\rho}-\bar{\rho}_q) \;\; \cdots\cdots \;\; E_M(\bar{\rho}-\bar{\rho}_q)\right] \tag{41}$$

$\bar{\bar{X}}^{qpW}$ is a matrix of dimension $(2M+1)\times(2M+1)$. Consider N vias in the waveguide. The via index is q, $q = 1,2,3,\cdots\cdots,N$.

The T-matrix coefficient in the absence of the wall is

$$T_m = -\frac{J_m(ka)}{H_m^{(2)}(ka)}; \quad m = 0, \pm 1, \cdots, \pm M \tag{42}$$

In matrix notations, the T matrix in the absence of the wall, $\bar{\bar{T}}^q$, is a $(2M+1)\times(2M+1)$ diagonal matrix, with diagonal element equal to T_m. Let $\bar{\bar{\tau}}^q$ be the T-matrix of single qth via, $q = 1,2,\cdots,N$, including the wall effect. It is calculated by

$$\bar{\bar{\tau}}^q = \left(\bar{\bar{I}} - \bar{\bar{T}}^q \bar{\bar{X}}^{qqW}\right)^{-1} \bar{\bar{T}}^q \tag{43}$$

where $\bar{\bar{\tau}}^q$ relates $\bar{A}^q$, the scattered coefficient of via q, to the $\bar{w}^q$ the, the exciting coefficient on via q by

$$\bar{A}^q = \bar{\bar{\tau}}^q \bar{w}^q \tag{44}$$

$\bar{A}^q$ and $\bar{w}^q$ are both of dimension $(2M+1)\times 1$.

Using the scattered field coefficients $\bar{A}^q$ and the $\bar{\bar{\tau}}^q$, we have the Foldy Lax multiple scattering equations

$$\bar{w}^q = \bar{a}^{q,inc} + \sum_{p\neq q}^{N} \left[\bar{\bar{\alpha}}_{qp}^{+} + \bar{\bar{X}}^{qpW}\right] \bar{A}^p \tag{45}$$

where the nm element of the matrix $\bar{\bar{\alpha}}^{+}_{qp}$ is

$$\left[\bar{\bar{\alpha}}^{+}_{qp}\right]_{nm} = H^{(2)}_{n-m}\left(k\left|\bar{\rho}_p - \bar{\rho}_q\right|\right) e^{j(n-m)\phi_{\overline{\rho_p \rho_q}}} \tag{46}$$

$\bar{\bar{\alpha}}^{+}_{qp}$ is of dimension $(2M+1) \times (2M+1)$.

Substituting (44) into (45), the Foldy Lax multiple scattering equations are

$$\bar{w}^{q} = \bar{a}^{q,inc} + \sum_{p\neq q}^{N}\left[\bar{\bar{\alpha}}^{+}_{qp} + \bar{\bar{X}}^{qpW}\right]\bar{\bar{\tau}}^{p}\,\bar{w}^{p} \tag{47}$$

and $\bar{a}^{q,inc}$ are the incident field coefficients for sources on the antipad [3] [6] [18] [5].

In summary, the procedure of modeling of vias in arbitrarily shaped power/ground planes using BBGFL and Foldy-lax equation is as follows.

Step 1: solve the broadband wall Green's function $g^{S}_{W}(k,\bar{\rho},\bar{\rho}')$ for the cavity structure of power/ground planes using BBGFL as described in previous section.

Step 2: calculates X^{qpW}_{nm} by equation (40) using values of the wall Green's function $g_W(\bar{\rho}_b,\bar{\rho}_a)$ on the circles in Figures 3.

Step 3: solve the $\bar{\bar{\tau}}^{q}$ matrix for each via $q = 1, \dots N$ by equation (43) using$\bar{\bar{X}}^{qqW}$.

Step 4: solve the combined problem of vias and power/ground planes using Foldy-Lax multiple scattering equations (47).

Step 5: after the Foldy-Lax multiple scattering equations are solved, we then follow the equations given in [6] to calculate the currents on the vias. The admittance matrices and the scattering matrices are then calculated as in [3] [16].

2.3.3 Small Patch Green's Function for TE Case

2.3.3.1 Small Patch Integrated Green's Function for TE Case

The conventional point Green's function for rectangular waveguide can be written in modal expansion series as

$$g_H^{\Omega}(k_L,\bar{\rho},\bar{\rho}') = \sum_{m=0}^{\infty}\sum_{n=0}^{\infty}\frac{A_{mn}A_{mn}}{(k_{mn})^2-(k_L)^2}\cos\frac{m\pi}{L_x}\left(x+\frac{L_x}{2}\right)$$

$$\cos\frac{n\pi}{L_y}\left(y+\frac{L_y}{2}\right)\cos\frac{m\pi}{L_x}\left(x'+\frac{L_x}{2}\right)\cos\frac{n\pi}{L_y}\left(y'+\frac{L_y}{2}\right) \qquad (2.41)$$

As $(m,n)\to\infty$, then

$$\frac{A_{mn}A_{mn}}{(k_{mn})^2-(k_L)^2}\to\frac{1}{(k_{mn})^2}=\frac{1}{\left(\frac{m\pi}{L_x}\right)^2+\left(\frac{n\pi}{L_y}\right)^2} \qquad (2.42)$$

Thus, the series (2.41) slowly converges when $\bar{\rho}\neq\bar{\rho}'$. How many terms depend on how close $\bar{\rho}$ is close to $\bar{\rho}'$. But it have no convergence when $\bar{\rho}=\bar{\rho}$. Since $g_H^{\Omega}(k_L,\bar{\rho},\bar{\rho}')=g_0(k_L,\bar{\rho},\bar{\rho}')+g_{HR}^{\Omega}(k_L,\bar{\rho},\bar{\rho}')$, the free space Green's function $g_0(k_L,\bar{\rho},\bar{\rho}')$ and response Green's function $g_{HR}^{\Omega}(k_L,\bar{\rho},\bar{\rho}')$. Note, $g_0(k_L,\bar{\rho},\bar{\rho})=\ln\infty$, which is not that "bad" because $\log\infty$ is a small ∞.

Small patch integrated Green's function for rectangular waveguide $\boldsymbol{\int_{\sigma_{oj'}} dl'\, g_E^{\Omega}(k_L,\bar{\rho},\bar{\rho}')}$ for TE case can be written as

$$\int_{\sigma_{oj'}} dl'\, g_E^{\Omega}(k_L,\bar{\rho},\bar{\rho}') = -\Delta\mathrm{l}\frac{A_{00}A_{00}}{(k_L)^2}$$

$$+\Delta l\sum_{m=1}^{\infty}\frac{A_{m0}A_{m0}}{(\mathrm{k_{xm}})^2-(k_L)^2}\cos\frac{m\pi}{L_x}\left(x+\frac{L_x}{2}\right)\cos\frac{m\pi}{L_x}\left(x'+\frac{L_x}{2}\right)$$

$$+\Delta l\sum_{n=1}^{\infty}\frac{A_{0n}A_{0n}}{\left(\mathrm{k_{yn}}\right)^2-(k_L)^2}\cos\frac{n\pi}{L_y}\left(y+\frac{L_y}{2}\right)\cos\frac{n\pi}{L_y}\left(y'+\frac{L_y}{2}\right)$$

$$+\Delta l\sum_{m=1}^{\infty}\sum_{n=1}^{\infty}2\,\frac{A_{mn}A_{mn}}{(k_{mn})^2-(k_L)^2}\left[\frac{\tau_{x'}\sin\frac{m\pi}{L_x}\left(\frac{\Delta x'}{2}\right)}{\frac{m\pi}{L_x}}+\frac{\tau_{y'}\sin\frac{n\pi}{L_y}\left(\frac{\Delta y'}{2}\right)}{\frac{n\pi}{L_y}}\right]$$

$$\cos\frac{m\pi}{L_x}\left(x+\frac{L_x}{2}\right)\cos\frac{n\pi}{L_y}\left(y+\frac{L_y}{2}\right)$$

$$\cos\frac{m\pi}{L_x}\left(x'+\frac{L_x}{2}\right)\cos\frac{n\pi}{L_y}\left(y'+\frac{L_y}{2}\right) \tag{2.43}$$

The first term is constant. The second term has fast convergence as $m \to \infty$ when $\bar{\rho} \neq \bar{\rho}'$ or $\bar{\rho} = \bar{\rho}'$. The third term has fast convergence as $n \to \infty$ when $\bar{\rho} \neq \bar{\rho}'$ or $\bar{\rho} = \bar{\rho}'$. As $(m, n) \to \infty$, then

$$\frac{A_{mn}A_{mn}}{(k_{mn})^2-(k_L)^2}\left[\frac{\tau_{x'}\sin\frac{m\pi}{L_x}\left(\frac{\Delta x'}{2}\right)}{\frac{m\pi}{L_x}}+\frac{\tau_{y'}\sin\frac{n\pi}{L_y}\left(\frac{\Delta y'}{2}\right)}{\frac{n\pi}{L_y}}\right] \rightarrow \frac{1}{\left(\frac{m\pi}{L_x}\right)^2+\left(\frac{n\pi}{L_y}\right)^2}\left[\frac{1}{\frac{m\pi}{L_x}}+\frac{1}{\frac{n\pi}{L_y}}\right] \tag{2.44}$$

Hence, the fourth term has fast converges when $\bar{\rho} \neq \bar{\rho}'$. And it slowly but still converges when $\bar{\rho} = \bar{\rho}'$. Overall, patch integrated Green's function (2.43) is one order faster than point Green's function (2.41) on convergence. With pre-computed $\int_{\sigma_{oj'}} dl'\, g_E^{\Omega}(k_L, \bar{\rho}, \bar{\rho}')$ in place, the point Green's function $g_E^{\Omega}(k_L, \bar{\rho}, \bar{\rho}')$ can be calculated from small patch integrated Green's function using $g_E^{\Omega}(k_L, \bar{\rho}, \bar{\rho}') = \frac{\int_{\sigma_{oj'}} dl'\, g_E^{\Omega}(k_L, \bar{\rho}, \bar{\rho}')}{\Delta l}$.

2.3.3.2 Derivative of Small Patch Integrated Green's Function for TE Case

The derivative of conventional point Green's function for TE case can be written in modal expansion series as

$$\hat{n}_t' \cdot \nabla_t' g_H^{\Omega}(k_L, \bar{\rho}, \bar{\rho}')$$

$$= -\sum_{m=0}^{\infty}\sum_{n=0}^{\infty}\frac{A_{mn}A_{mn}}{(k_{mn})^2-(k_L)^2}\,cos\,\frac{m\pi}{L_x}\left(x+\frac{L_x}{2}\right)cos\,\frac{n\pi}{L_y}\left(y+\frac{L_y}{2}\right)$$

$$\left[n_{x'}\frac{m\pi}{L_x}sin\,\frac{m\pi}{L_x}\left(x'+\frac{L_x}{2}\right)cos\,\frac{n\pi}{L_y}\left(y'+\frac{L_y}{2}\right)+\right.$$

$$+n_{y'}\frac{n\pi}{L_y}cos\frac{m\pi}{L_x}\left(x'+\frac{L_x}{2}\right)sin\frac{n\pi}{L_y}\left(y'+\frac{L_y}{2}\right)\Big] \tag{2.45}$$

As $(m,n) \to \infty$, then

$$\frac{A_{mn}A_{mn}}{(k_{mn})^2-(k_L)^2}\left[n_{x'}\frac{m\pi}{L_x}+n_{y'}\frac{n\pi}{L_y}\right]$$

$$\to \frac{1}{(k_{mn})^2}\left[\frac{m\pi}{L_x}+\frac{n\pi}{L_y}\right]=\frac{\left[\frac{m\pi}{L_x}+\frac{n\pi}{L_y}\right]}{\left(\frac{m\pi}{L_x}\right)^2+\left(\frac{n\pi}{L_y}\right)^2} \tag{2.46}$$

Thus, the series (2.45) has no convergence for $\bar{\rho} \neq \bar{\rho}'$ or $\bar{\rho} = \bar{\rho}$.

Small patch integrated Green's function for rectangular waveguide $\int_{\sigma_{oj'}} dl'\, g_H^{\Omega}(k_L,\bar{\rho},\bar{\rho}')$ for TE case can be written as

$$\int_{\sigma_{oj'}} dl'\, \hat{n}_t' \cdot \nabla_t' g_H^{\Omega}(k_L,\bar{\rho},\bar{\rho}') =$$

$$-\Delta l\sum_{m=1}^{\infty}\frac{A_{m0}A_{m0}}{(k_{m0})^2-(k_L)^2}\cos\frac{m\pi}{L_x}\left(x+\frac{L_x}{2}\right)\left[n_{x'}\frac{m\pi}{L_x}\sin\frac{m\pi}{L_x}\left(x'+\frac{L_x}{2}\right)\right]$$

$$-\Delta l\sum_{n=1}^{\infty}\frac{A_{0n}A_{0n}}{(k_{0n})^2-(k_L)^2}\cos\frac{n\pi}{L_y}\left(y+\frac{L_y}{2}\right)\left[n_{y'}\frac{n\pi}{L_y}\sin\frac{n\pi}{L_y}\left(y'+\frac{L_y}{2}\right)\right]$$

$$+Third\ Term\ (m \neq 0,\ n \neq 0)$$

(2.47)

when $\bar{\rho} \neq \bar{\rho}'$,

the third term $(m \neq 0,\ n \neq 0)$

$$= -\sum_{m=1}^{\infty}\sum_{n=1}^{\infty}\frac{2A_{mn}A_{mn}}{(k_{mn})^2-(k_L)^2}\cos\frac{m\pi}{L_x}\left(x+\frac{L_x}{2}\right)\cos\frac{n\pi}{L_y}\left(y+\frac{L_y}{2}\right)$$

$$\left[\begin{array}{c}
\tau_{x'}n_{x'}\sin\frac{m\pi}{L_x}\left(\frac{\Delta x'}{2}\right)\sin\frac{m\pi}{L_x}\left(x'+\frac{L_x}{2}\right)\cos\frac{n\pi}{L_y}\left(y'+\frac{L_y}{2}\right)\\
+\tau_{x'}n_{y'}\frac{nL_x}{mL_y}\sin\frac{m\pi}{L_x}\left(\frac{\Delta x'}{2}\right)\cos\frac{m\pi}{L_x}\left(x'+\frac{L_x}{2}\right)\sin\frac{n\pi}{L_y}\left(y'+\frac{L_y}{2}\right)\\
+\tau_{y'}n_{x'}\frac{mL_y}{nL_x}\sin\frac{n\pi}{L_y}\left(\frac{\Delta y'}{2}\right)\sin\frac{m\pi}{L_x}\left(x'+\frac{L_x}{2}\right)\cos\frac{n\pi}{L_y}\left(y'+\frac{L_y}{2}\right)\\
+\tau_{y'}n_{y'}\sin\frac{n\pi}{L_y}\left(\frac{\Delta y'}{2}\right)\cos\frac{m\pi}{L_x}\left(x'+\frac{L_x}{2}\right)\sin\frac{n\pi}{L_y}\left(y'+\frac{L_y}{2}\right)
\end{array}\right]$$

(2.48)

As $(m,n)\to\infty$,

$$\frac{2A_{mn}A_{mn}}{(k_{mn})^2-(k_L)^2}\left[\begin{array}{c}
\tau_{x'}n_{x'}\sin\frac{m\pi}{L_x}\left(\frac{\Delta x'}{2}\right)+\tau_{x'}n_{y'}\frac{nL_x}{mL_y}\sin\frac{m\pi}{L_x}\left(\frac{\Delta x'}{2}\right)\\
+\tau_{y'}n_{x'}\frac{mL_y}{nL_x}\sin\frac{n\pi}{L_y}\left(\frac{\Delta y'}{2}\right)+\tau_{y'}n_{y'}\sin\frac{n\pi}{L_y}\left(\frac{\Delta y'}{2}\right)
\end{array}\right]$$

$$\to\frac{1}{(k_{mn})^2}=\frac{1}{\left(\frac{m\pi}{L_x}\right)^2+\left(\frac{n\pi}{L_y}\right)^2} \qquad (2.49)$$

Hence, this series fast converge when $\bar{\rho}\neq\bar{\rho}'$

when $\bar{\rho}=\bar{\rho}'$,

the third term $(m\neq 0,\ n\neq 0)$

$=\sum_{m=1}^{\infty}\sum_{n=1}^{\infty}\frac{1}{4}\frac{A_{mn}A_{mn}}{(k_{mn})^2-(k_L)^2}$

$$\left[\begin{array}{c}
\tau_{x'} n_{x'} \sin\frac{m\pi}{L_x}(\Delta x') \sin 2\frac{m\pi}{L_x}\left(x' + \frac{L_x}{2}\right) \\
+\tau_{y'} n_{y'} \sin\frac{n\pi}{L_y}(\Delta y') \sin 2\frac{n\pi}{L_y}\left(y' + \frac{L_y}{2}\right) \\
+\tau_{x'}\begin{pmatrix} n_{x'} \sin\frac{m\pi}{L_x}(\Delta x') \\ +\frac{L_y m}{L_x n} n_{y'} \sin\frac{n\pi}{L_y}(\Delta y') \end{pmatrix} \sin 2\frac{m\pi}{L_x}\left(x' + \frac{L_x}{2}\right) \cos 2\frac{n\pi}{L_y}\left(y' + \frac{L_y}{2}\right) \\
+\tau_{y'}\begin{pmatrix} \frac{L_x n}{L_y m} n_{x'} \sin\frac{m\pi}{L_x}(\Delta x') \\ +n_{y'} \sin\frac{n\pi}{L_y}(\Delta y') \end{pmatrix} \cos 2\frac{m\pi}{L_x}\left(x' + \frac{L_x}{2}\right) \sin 2\frac{n\pi}{L_y}\left(y' + \frac{L_y}{2}\right)
\end{array}\right]$$

(2.50)

As $(m, n) \to \infty$

$$\frac{A_{mn}A_{mn}}{(k_{mn})^2 - (k_L)^2}\tau_{x'} n_{x'} \to \frac{1}{(k_{mn})^2} = \frac{1}{\left(\frac{m\pi}{L_x}\right)^2 + \left(\frac{n\pi}{L_y}\right)^2} \qquad (2.51.a)$$

$$\frac{A_{mn}A_{mn}}{(k_{mn})^2 - (k_L)^2}\tau_{y'} n_{y'} \to \frac{1}{(k_{mn})^2} = \frac{1}{\left(\frac{m\pi}{L_x}\right)^2 + \left(\frac{n\pi}{L_y}\right)^2} \qquad (2.51.b)$$

$$\frac{A_{mn}A_{mn}}{(k_{mn})^2 - (k_L)^2}\tau_{x'}\begin{pmatrix} n_{x'} \sin\frac{m\pi}{L_x}(\Delta x') \\ +\frac{L_y m}{L_x n} n_{y'} \sin\frac{n\pi}{L_y}(\Delta y') \end{pmatrix} \to \frac{1}{(k_{mn})^2} = \frac{1}{\left(\frac{m\pi}{L_x}\right)^2 + \left(\frac{n\pi}{L_y}\right)^2} \qquad (2.51.c)$$

$$\frac{A_{mn}A_{mn}}{(k_{mn})^2 - (k_L)^2}\tau_{x'} n_{y'}\begin{pmatrix} \frac{L_x n}{L_y m} n_{x'} \sin\frac{m\pi}{L_x}(\Delta x') \\ +n_{y'} \sin\frac{n\pi}{L_y}(\Delta y') \end{pmatrix}$$

$$\to \frac{1}{(k_{mn})^2} = \frac{1}{\left(\frac{m\pi}{L_x}\right)^2 + \left(\frac{n\pi}{L_y}\right)^2} \qquad (2.51.d)$$

Hence, the fourth term converge when $\bar{\rho} = \bar{\rho}'$. With pre-computed $\int_{\sigma_{oj'}} dl'\, \hat{n}_t' \cdot \nabla_t' g_H^{\Omega}(k_L, \bar{\rho}, \bar{\rho}')$ in place, the point Green's function $\hat{n}_t' \cdot \nabla_t' g_H^{\Omega}(k_L, \bar{\rho}, \bar{\rho}')$ can be calculated from small patch integrated Green's function using $\hat{n}_t' \cdot \nabla_t' g_H^{\Omega}(k_L, \bar{\rho}, \bar{\rho}') = \frac{\int_{\sigma_{oj'}} dl' \hat{n}_t' \cdot \nabla_t' g_H^{\Omega}(k_L, \bar{\rho}, \bar{\rho}')}{\Delta l}$.

2.4 Numerical Results

The L-shaped waveguide in Figure 2.1b is used. The dimension parameters are: Lx=Ly=500mils, L1=250mils, and W1=100mils. We show first the results of resonance wavenumber and the eigenmode solutions. Then we show results for the Green's functions. Note that the resonance wavenumbers only depend on geometry and are independent of frequencies nor material properties. The dependence of the broadband Green's function on frequency and materials properties are through $k^2 = \omega^2 \mu_0 \varepsilon_0 \varepsilon_r$ where ε_r is the relative permittivity. We only need to specify k for the modal solution and the Green's functions.

In calculating the field solution of the modal solutions and the Green's function, the field points are located at y=20mils, x=[-245mils, 245mils]. In calculating the broadband Green's function, the source point is located at (25mils, 20mils).

We compare the results with that of MoM. In calculating resonant wavenumber and resonant mode with MoM, we set up the integral equation using the free space Green's function$g_0(k, \bar{\rho}, \bar{\rho}') = H_0^{(2)}(k|\bar{\rho} - \bar{\rho}'|)/(4j)$. We then search the real k that obeys the surface integral equation.

2.4.1 Computation of Green's Functions for Neumann Case

2.4.1.1 Resonant Wavenumber Comparison

In Table I, we compare the resonant wavenumbers k as computed by BBGFL and MoM. The eigenmatrix equation of the present approach can give nonphysical modes in addition to physical modes. The nonphysical modes can be quickly identified because the eigenfunction of a physical mode, for the Neumann case, is constant outside the original solution boundary. In Table 1, there is 1 nonphysical mode (the 9th mode) in the BBGFL solution. Thus the 9th mode of MoM is compared with the 10th mode of BBGF. Results in Table 1 show that BBGFL and MoM are in good agreement.

Table 2-1 Comparison of MoM and BBGFL for resonant frequencies of Neumann case

MoM Mode Number	MoM resonant wave number in inverse meter	BBGFL Mode Number Total/physical	BBGFL resonant wave number In inverse meter
0 (constant mode)	2.638	0 (constant mode)	0
1	229.5	1/1	228.7
2	277.0	2/2	276.9
3	371.5	3/3	371.7
4	495.0	4/4	494.8
5	513.9	5/5	513.7
6	561.8	6/6	561.3
7	641.0	7/7	646.0
8	674.4	8/8	661.2
NA	NA	9/NA	674.2 (nonphysical

			mode)
9	750.9	10/9	750.6
10	757.5	11/10	757.5

2.4.1.2 Modal Solution Comparison

In the BBGFL, the eigenmatrix equations and the resonant wavenumbers are real. Thus the modal solutions are real. On the other hand, in using MoM to calculate the modes, the Hankel functions is complex. Thus the MoM results have small imaginary parts in the solutions depending on the accuracy of the nonlinear search in applying MoM. In Figure 2.4, we compare the modal solutions of BBGFL and MoM. The eigenfunctions from MoM are normalized to the same scale as BBGFL. Four of the modes listed in Table I are compared. Results are in good agreement.

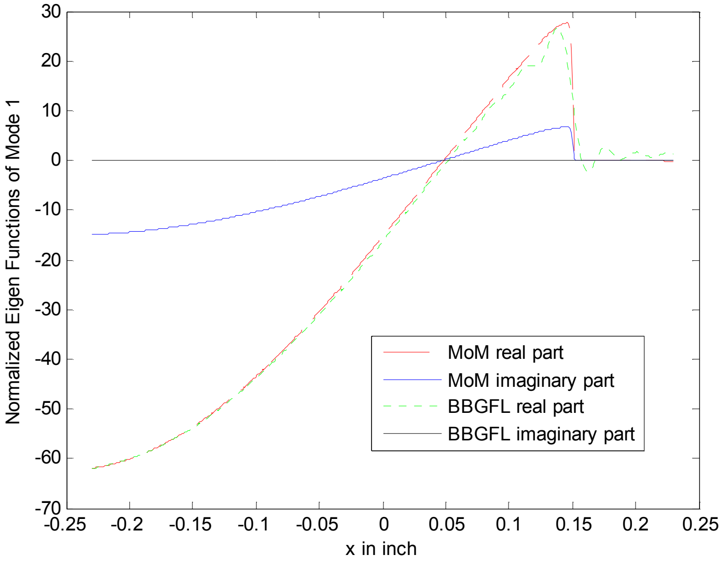

(a) Mode #1 at k=228.7

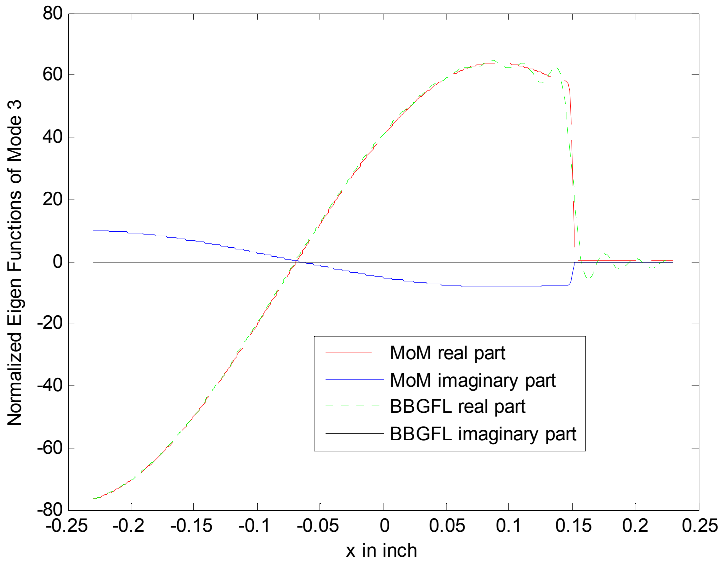

(b) Mode #3 at k=371.7

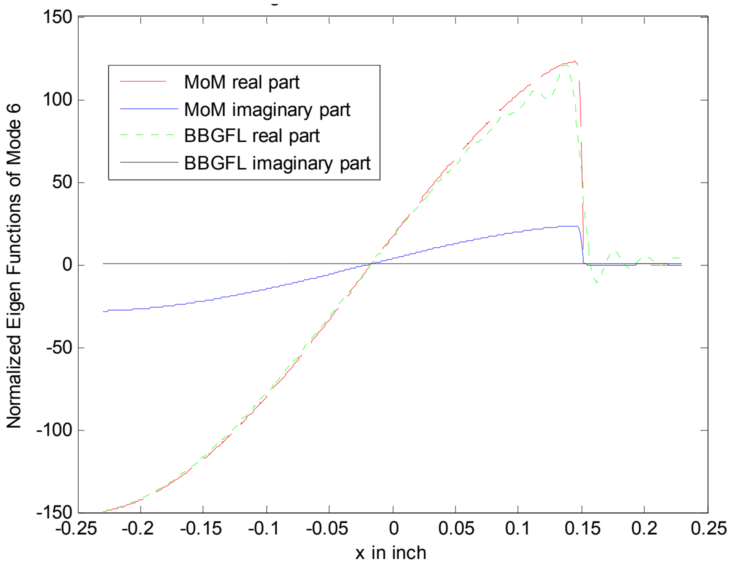

s

(c) Mode #6 at k=561.3

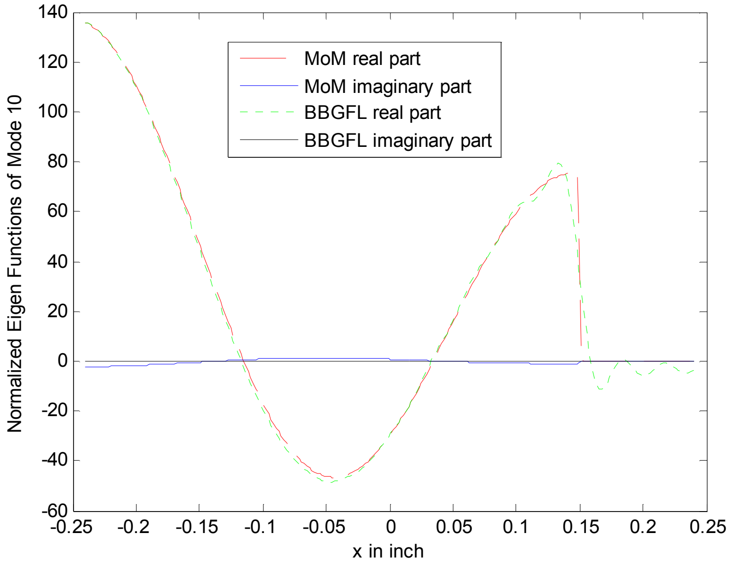

(d) Mode #10 at k=575.5

Figure 2.4 Comparison of MoM and BBGFL for modal solutions of Neumann case

2.4.1.3 Comparison of Green's Function $\mathbf{g}_{\mathbf{H}}^{\mathbf{S}}$

In Figure 2.5, we compare the Green's function computed by BBGFL and MoM for various real wavenumbers k. In the low wavenumber extractions, we use $k_L^{\Omega} = 0.044$, and $k_L^{S} = 220$. The results of BBGFL and MoM are in good agreement

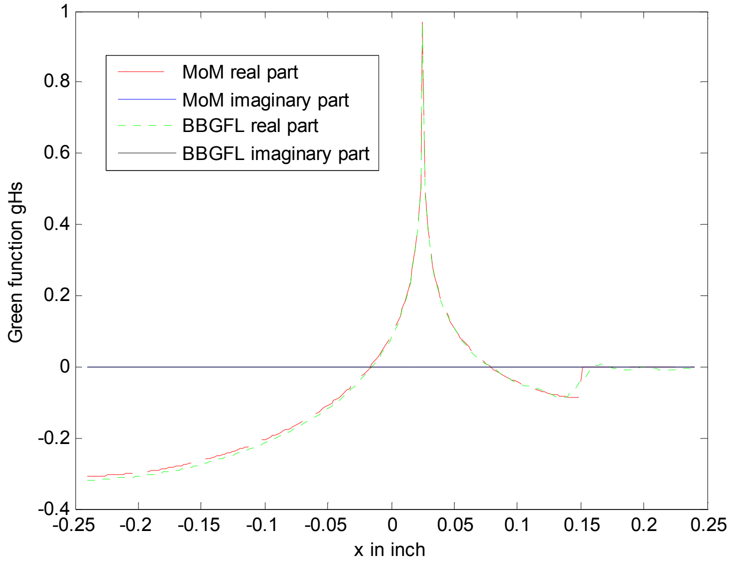

(a) Neumann gHs at k=175.8

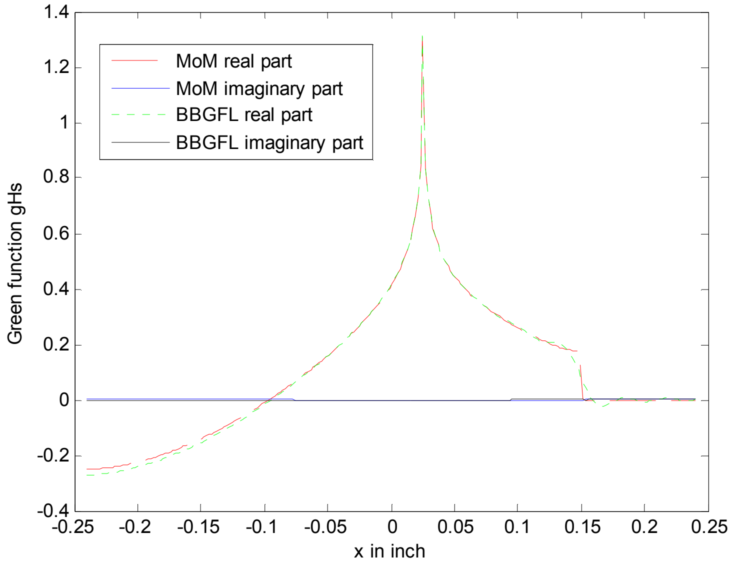

(b) Neumann gHs at k=351.7

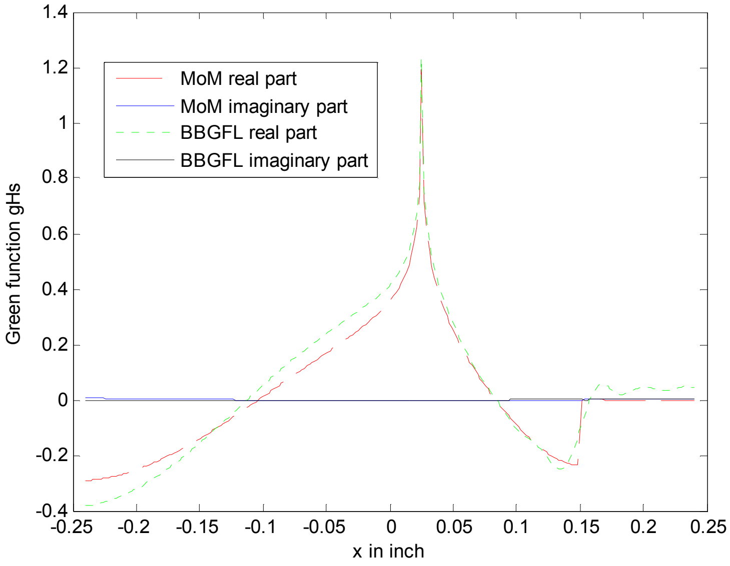

(c) Neumann gHs at k=615.5

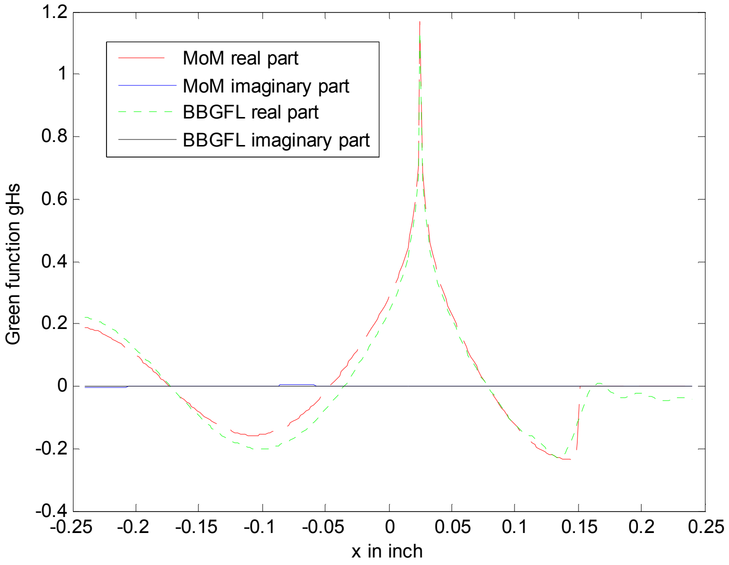

(d) Neumann gHs at k=879.2

Figure 2.5 Comparison between MoM and BBGFL for final total Green's function of Neumann case.

2.4.1.4 Comparison of CPU Times

In Table II, we compare the CPU time of BBGFL and MoM for computing the Green's function. In the comparison, the input simulation parameters are: the discretization spacing is 2mils for both MoM and BBGFL, the BBGFL uses $M_o = 30$ for both kxm and kyn with total $M_\alpha = (1 + M_o) \times (1 + M_o) = 961$ modes. For each frequency point, the Green's function is calculated with 1 source point and 240 observation points combined. Note, for BBGFL, the CPU time consists two parts: the first part is for computing eigenfunctions and eigenvalues, and second part is to calculate Green's function with the pre-computed eigenfunctions and eigenvalues. In the Table II, for 1000 wavenumber points, the first part takes 40.28 seconds, while the second part is only 180 seconds for computing the final g_H of 240 observation points. This indicates that, even for computation of 240 observation points, the CPU of second part is still negligible. For broadband modeling with 1000 wavenumber points, the proposed method is more than 162 times faster. The Green's functions are at many wavenumber points. The method of calculating a few wavenumber points followed by interpolation is not accurate because of the multiple resonances.

Table 2-2 Comparison of BBGFL and direct MoM for CPU times

Methods	1 wavenumber point	10 wavenumber points	100 wavenumber points	1000 wavenumber points
BBGFL	40.28s + 0.18 =40.46 sec	40.28s + 0.18*10 =42.08 sec	40.28s + 0.18*100 =58.28 sec	40.28s + 0.18*1000 =220.28 sec
Direct MoM	36.01 sec	36.01*10 =360.1 sec	36.01*100 =3601 sec	36.01*1000 =36010 sec

2.4.2 Application of BBGFL to the Simulation of Vias in Arbitrarily Shaped PCB Power/Ground Plane Pair

We next model the scattering matrices for the problem of multiple vias in the L-shaped PCB/power ground plane for the frequency up to 20GHz. . The dielectric thickness d between the two parallel plates is 30 mils. Thus $kd \ll 1$. For the sake of simplicity in combining BBGFL with the Foldy Lax approach, we only use the zeroth harmonic for the $l = 0$ mode in the Foldy Lax approach. We included higher order harmonics for $l > 0$ modes. This simplification does not deal with the cases when the vias are close together which presently are under study.

2.4.2.1 Modeling of Two Signal Vias in a Rectangular Power/Ground Plane Pair with Small Cut Out

Consider a power/ground plane pair with two signal vias as showed in Figure 2.2. Lx=Ly=500mils, L1=100mils, W1=100mils. The relative permittivity is complex and is set at $\varepsilon_r = 3.4(1 - j0.02)$. Via 1 and Via 2 are located at (-25, 0) mil and (25, 0) mil, respectively. Using notations as in reference [6] [5]. The via radius is a=6.75 mils, and the antipad radius is b= 20 mils.

In Figure 2.6, we compare the results of the 4 methods for the s-parameters of insertion loss, return loss, near end crosstalk (NEXT), and far end crosstalk 1(FEXT). The red curves are results obtained by using BBGFL with Foldy-Lax. The blue curves are results from HFSS. We also consider the case with $\ell = 0$ only and also the case with higher order $\ell \geq 1$ Included. The green curves are results from direct MoM solution with signal vias and plane pair, with ℓ =0 mode. Direct MoM means solving, at every frequency, the surface integral equation of arbitrary ground plane and vias formulated with free space Green's function. The black curves are results combining direct MoM solution with $\ell = 0$ mode, and Foldy-Lax solution with $\ell \geq 1$ modes. The results of BBGFL/Foldy-Lax (red) are in good agreement with HFSS (blue) and MoM/Foldy-Lax (black). It can be seen that all the methods capture the resonance frequencies, which are caused by the reflections by the PMC walls of the finite power/ground plane. However, the green results with only $\ell = 0$ has large difference compared to other methods. This means the $\ell > 0$ modes are important for the coupling effects caused by the dense vias (small pitch between two vias). Because the vias are small and are not near the boundary, the $(n, m) = (0,0)$ in the wall coupling coefficients X_{nm}^{qpW} has the dominant effects. In our simulations, we used $R_1 = R_2 = a$ (Figure 2.3).

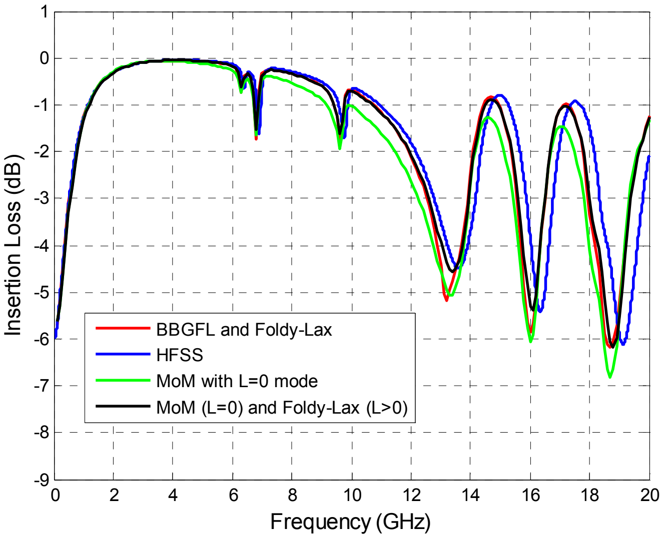

(a) Insertion Loss

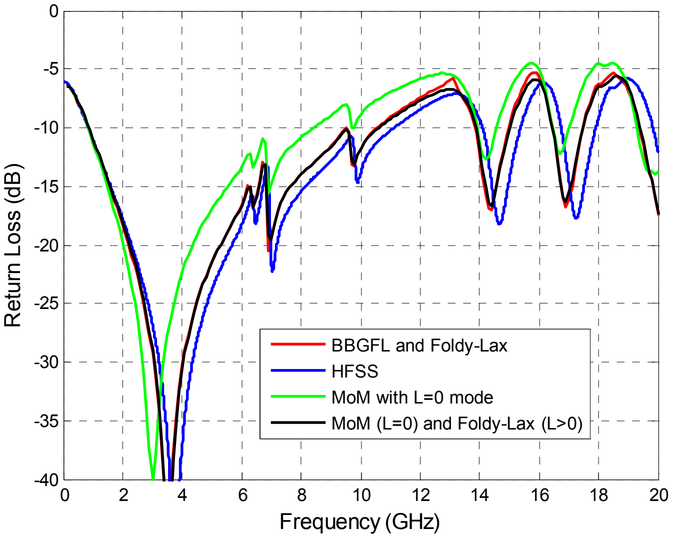

(b) Return Loss

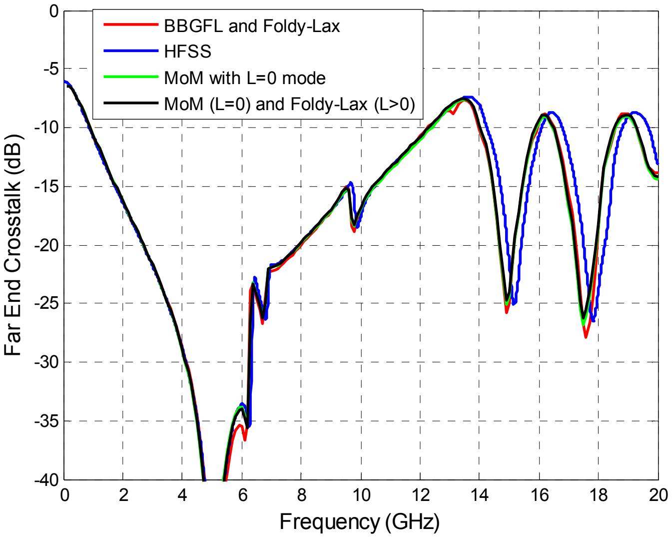

(c) Far End Crosstalk

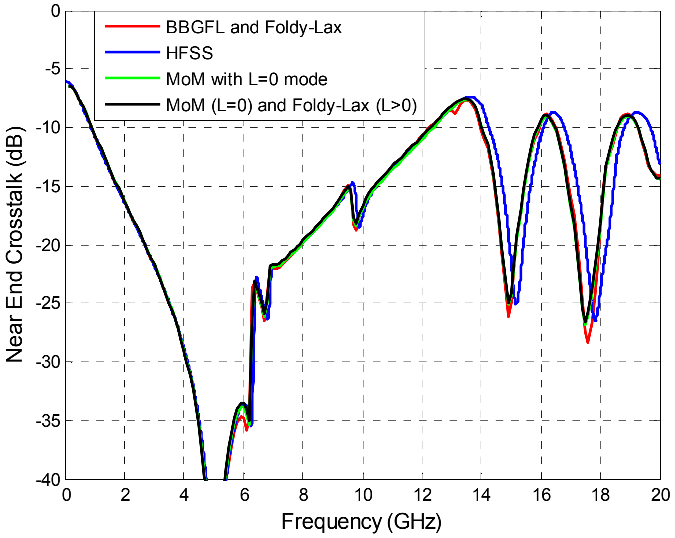

(d) Near End Crosstalk

Figure 2.6 Comparison of BBGFL and different methods for s-parameters from simulations with Figure 2.6: Red –BBGFL/Foldy-Lax, Blue – HFSS, Green – direct MoM with L=0 mode, Black - combine direct MoM with L=0 mode and Foldy-Lax with L>0 modes.

2.4.2.2 Modeling of Two Signal Vias in A Rectangular Power/Ground Plane Pair with Large Cut Out

Consider a power/ground plane pair with two signal vias as showed in Figure 2.2. Lx=Ly=500mils, L1=100mils, W1=200mils. The relative permittivity is real and is $\varepsilon_r = 3.4$. Via 1 and Via 2 are located at (-25, 0) mil and (25, 0) mil, respectively. The via radius is 6.75 mils, and the antipad radius is 20 mils.

In Figure 2.6, BBGFL is compared with three different methods. The results of the s-parameters of insertion loss, return loss, near end crosstalk (NEXT), and far end crosstalk (FEXT) are shown. The red curves are results obtained by using BBGFL with Foldy-Lax. The blue curves are results from HFSS. The green curves are results from direct MoM solution with $\ell = 0$ mode. The black curves are results combining direct MoM solution with $\ell = 0$ mode, and Foldy-Lax solution with $\ell > 0$ modes. The BBGFL/Foldy-Lax (red) results are in good agreement with HFSS (blue) and MoM/Foldy-Lax (black). It can be seen that all the methods can capture the resonance frequencies, which are caused by reflections from the walls of the finite plane. The results also show that higher order modes $\ell > 0$ modes are important.

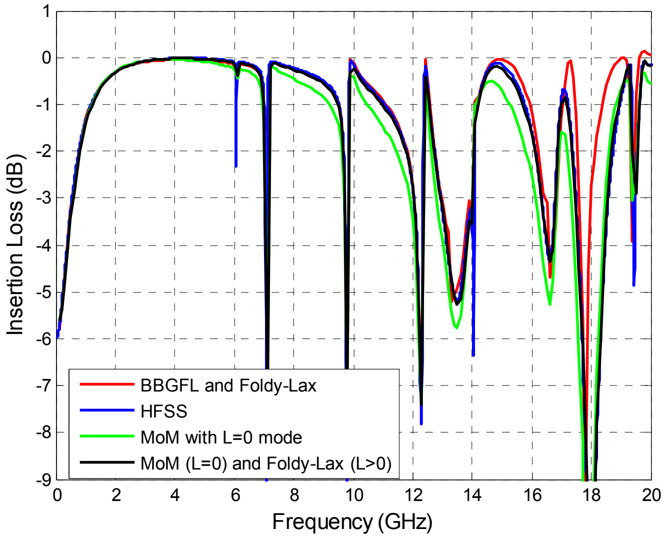

(a) Insertion Loss

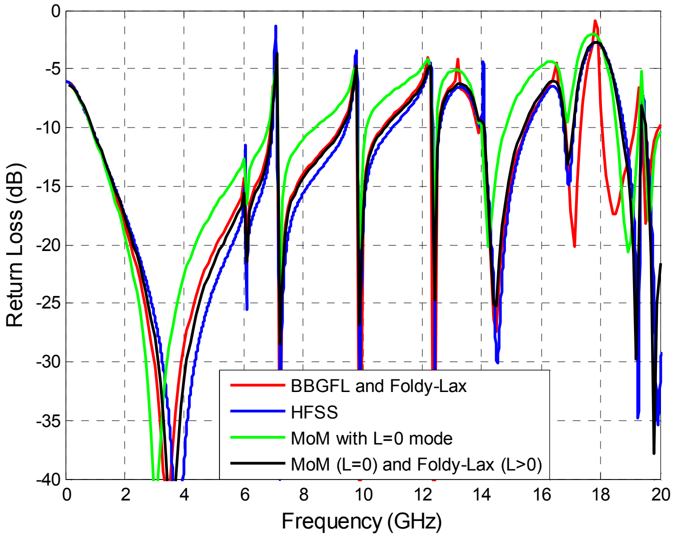

(b) Return Loss

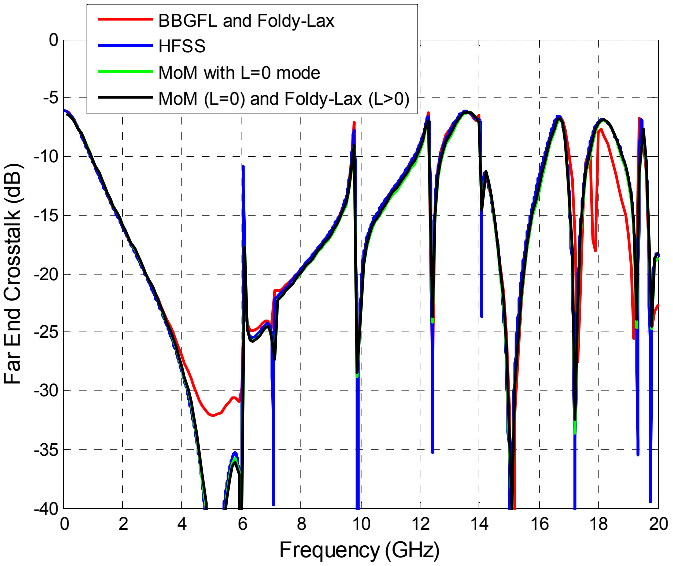

(c) Far End Crosstalk

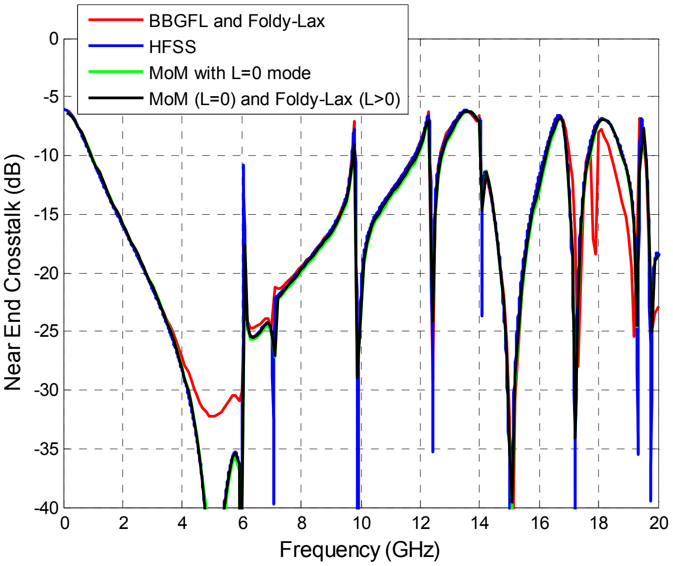

(d) Near End Crosstalk

Figure 2.7 Comparison of BBGFL and different methods for s-parameters: Red – BBGFL/Foldy-Lax, Blue – HFSS, Green – direct MoM with L=0 mode, Black - combine direct MoM with L=0 mode and Foldy-Lax with L>0 modes.

2.4.2.3 Modeling of Two Signal Vias and Two Shorting Vias in a Rectangular Power/Power (or Ground/Ground) Plane Pair with Large Cut Out

Consider a power/power or ground/ground plane pair with two signal vias and two shorting as shown in Figure 2.8. Lx=Ly=500mils, L1=200mils, W1=100mils. The relative permittivity $\varepsilon_r = 3.4(1 - j0.02)$. Via 1 and Via 2 are signal vias, and they are located at (-25, 0) mil and (25, 0) mil respectively. Two shorting vias are located at (0, -25) mil and (0, 25) mil, respectively. The via radius is 6.75 mils, and the antipad radius is 20 mils.

In Figure 2.9, the s-parameters of insertion loss, return loss, near end crosstalk (NEXT), and far end crosstalk (FEXT) are shown. The results are in good agreement.

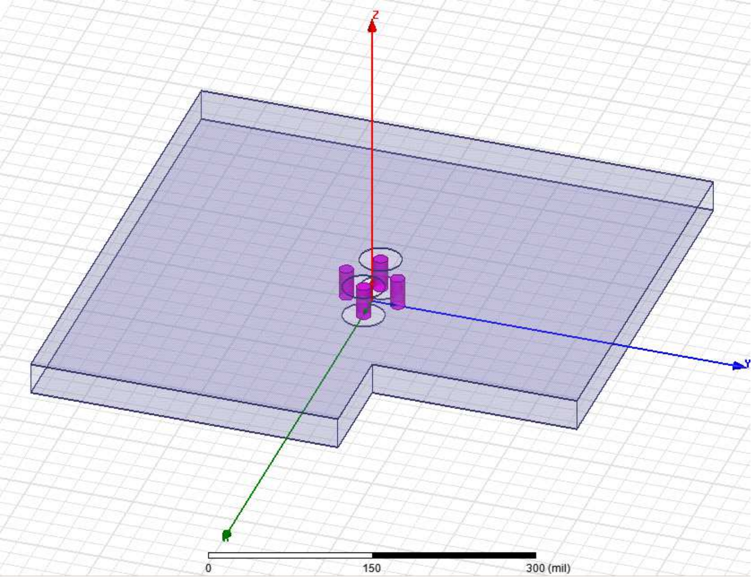

Figure 2.8 3D geometry of the simulation with 2 signal vias and 2 shorting vias in an irregular shaped plate pair with large cut out.

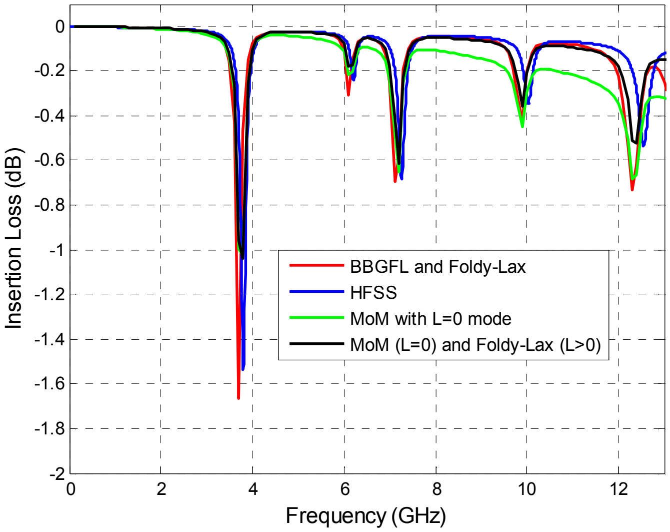

(a) Insertion Loss

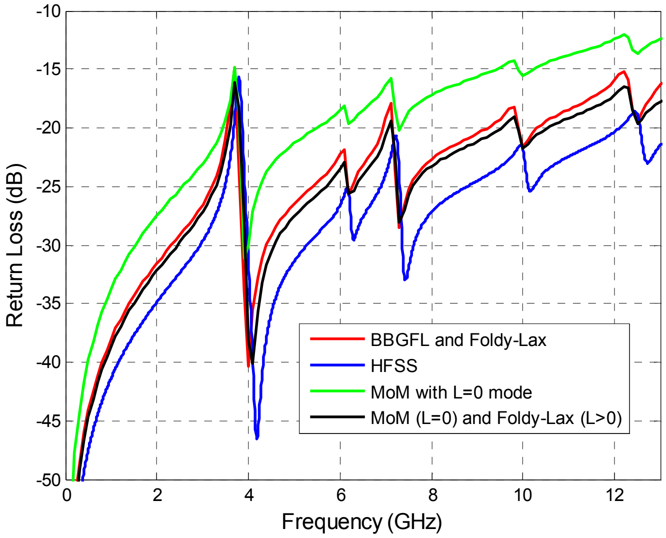

(b) Return Loss

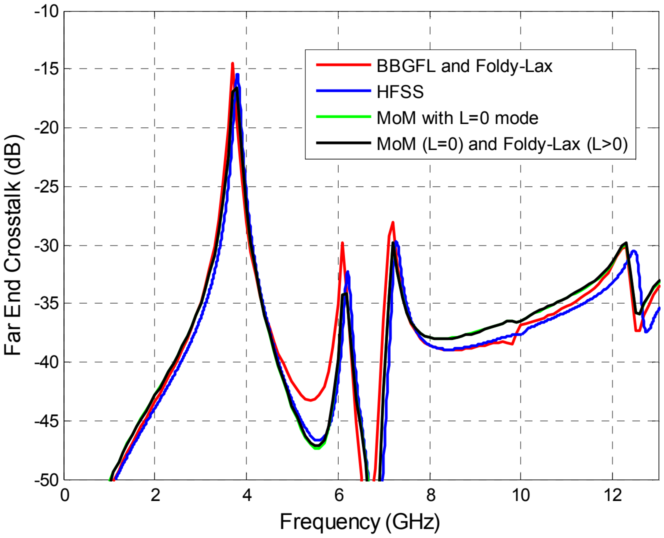

(c) Far End Crosstalk

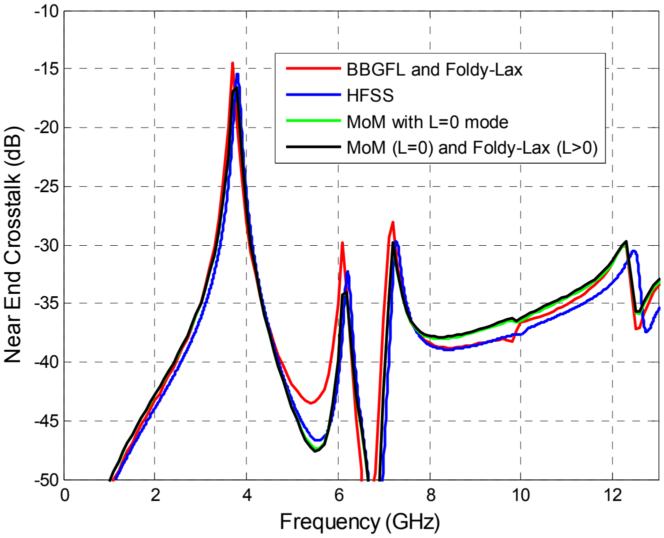

(d) Near End Crosstalk

Figure 2.9 Comparison of BBGFL and different methods for s-parameters from simulations with Figure 2.8: Red –BBGFL/Foldy-Lax, Blue – HFSS, Green – direct MoM with L=0 mode, Black - combine direct MoM with L=0 mode and Foldy-Lax with L>0 modes.

2.4.2.4 Modeling of 8 Vias: Four Signal Vias and Four Shorting Vias in a Rectangular Power/Power (or Ground/Ground) Plane Pair with Large Cut Out

Consider a power/power or ground/ground plane pair with 4 signal vias and 4 shorting as showed in Figure 2.10. Lx=Ly=500mils, L1=200mils, W1=100mils. The relative permittivity $\varepsilon_r = 3.4(1 - j0.02)$. Signal Vias 1, 2, 3 and 4 are located at (-25, 50), (25, 50), (-25, -50), and (25, 50) mils, respectively. Shorting vias are located at (0, 75), (0, 25), (0,-25), and (0,-75) mils, respectively. Two shorting vias are located at (0, -25) mil and (0, 25) mil, respectively. The via radius is 6.75 mils, and the antipad radius is 20 mils. The results are shown in Figure 2.11.

The results from the various methods are in good agreement.

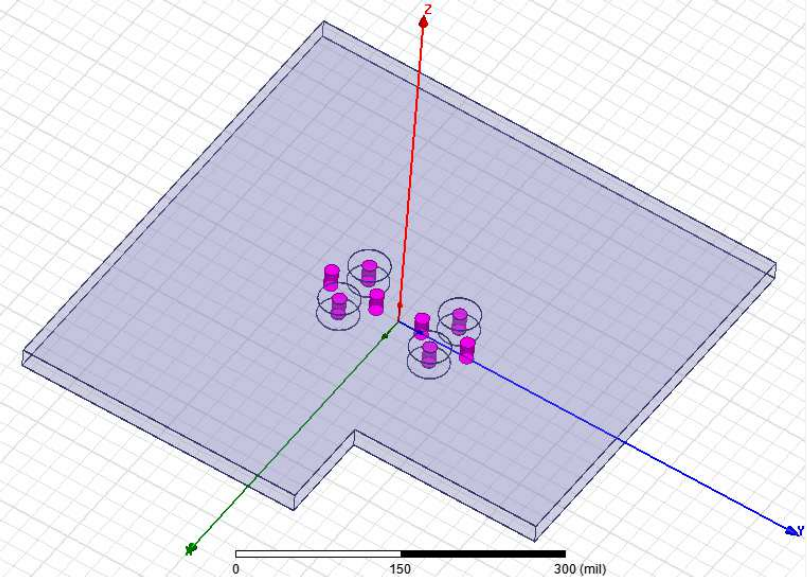

Figure 2.10 3D geometry of the simulation with 4 signal vias and 4 shorting vias in an irregular shaped plate pair with large cut out.

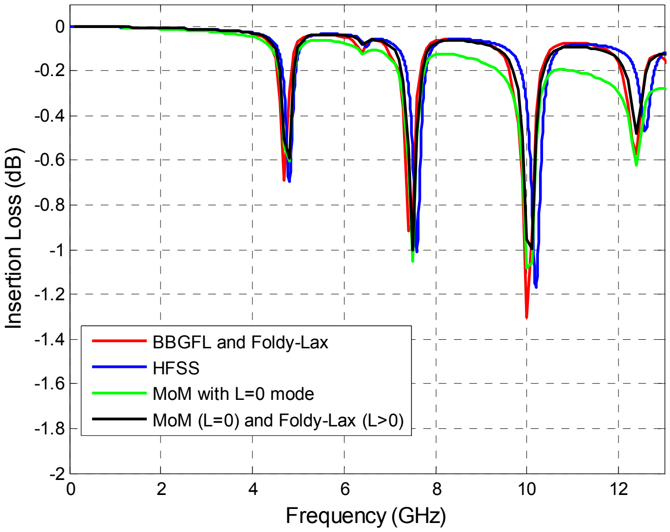

(a) Insertion Loss

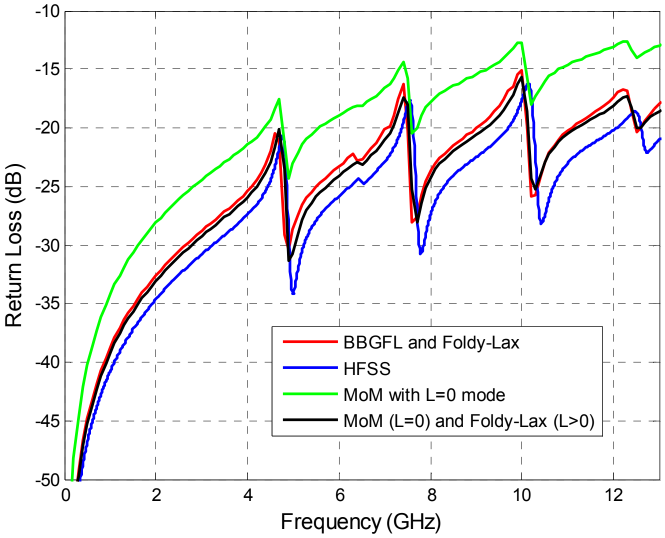

(b) Return Loss

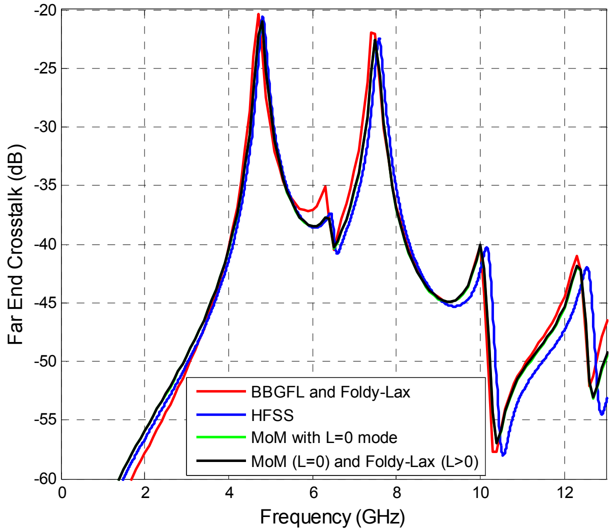

(c) Far End Crosstalk

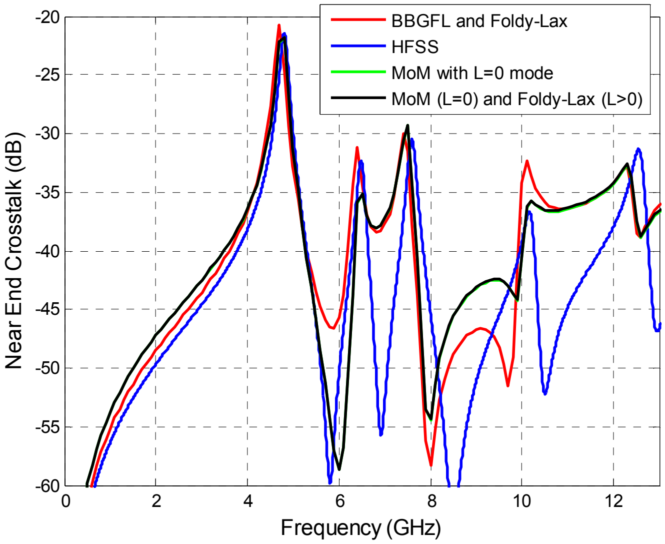

(d) Near End Crosstalk

Figure 2.11 Comparison of BBGFL and different methods for s-parameters from simulations with Figure 2.10: Red –BBGFL/Foldy-Lax, Blue – HFSS, Green – direct MoM with L=0 mode, Black - combine direct MoM with L=0 mode and Foldy-Lax with L>0 modes.

2.4.2.5 Comparison of CPU Time for Vias Simulations

In Table III, we compare the CPU time used in the simulations of Figure 2.8. In the comparison, the input parameters are: the discretization spacing is 4 mils for both MoM and BBGFL, the BBGFL uses $M_o = 20$ for both kxm and kyn. For BBGFL, the CPU time consists three parts. The first part is for computation of eigenfunctions and values. The second part is for creating response Green's function with the computed eigenfunctions and values. The third part is solve the Foldy-Lax equations with the response Green's function. We show the sum of the 3 parts. The CPU time of HFSS contains two parts. The first part is for simulation setup (CAD meshing, etc) which is done only once, and the second part is for FEM simulation which needs to be repeated for all frequency points. For the simulation of 1000 frequency points, BBGFL takes 4.7 seconds for first part, 2 seconds for the second part, and 5 seconds for the third part. For total CPU time used for 100 frequency points, the proposed method is 59 times faster than direct MoM, and is 103 times faster than HFSS. For total CPU time used for 1000 frequency points, the proposed method is 273 times faster than direct MoM, and is 447 times faster than HFSS. This shows that the BBGFL, combined with Foldy-Lax, is much more efficient than MoM and HFSS for broadband simulations. It is to be noted that large number of frequency points are necessary for multiple resonances for the cavity.

Table 2-3 Comparison of CPU times using different methods: BBGFL/Foldy-Lax, direct MoM, and HFSS.

Methods	1 frequency point	10 frequency points	100 frequency points	1000 frequency points
BBGFL/Foldy-Lax	4.7 + 0.002+0.005 =4.707	4.7 + 0.002*10+0.005*10 =4.77 sec	4.7 + 0.002*100+0.005*100 =5.4 sec	4.7 + 0.002*1000+0.005*1000 =11.7 sec

	sec			
Direct MoM	3.2 sec	3.2*10 =32 sec	3.2*100 =320 sec	3.2*1000 =3200 sec
HFSS	35+5.2 =40.2 sec	35+5.2*10 =87 sec	35+5.2*100 =555 sec	35+5.2*1000 =5235 sec

2.5 Conclusion

In this chapter, we present a new technique, BBGFL, for fast broadband modeling and simulations of scattering problems in arbitrarily shaped waveguides or cavities. Results show BBGFL and direct MoM are in good agreement on resonance frequencies, modes, and Green's function. The proposed method is also implemented for practical PCB applications. We combined BBGFL with Foldy-Lax multiple scattering equation, to simulate vias in arbitrarily shaped power/ground plane pairs. Simulation results show BBGFL/Foldy-Lax results are in good agreement with MoM and HFSS in S-parameters. BBGFL/Foldy-Lax are many times faster than MoM and HFSS for broadband simulation. We are presently extending the approach to more complicated cases. With fast broadband simulations at many frequencies, the results in the time domain can also be obtained from the frequency domain results.

Chapter 3 Fast Electromagnetic Analysis of Emissions from Printed Circuit Board Using Broadband Green's Function

3.1 Summary

In this chapter, we present the application of broadband Green's function with low wavenumber extraction (BBGFL) to fast modeling of the radiated emissions from printed circuit boards (PCBs). The studies are for power bus structure for electromagnetic interference/compatibility (EMI/EMC). We use the BBGFL to compute the Green's function over broadband frequencies along the boundary walls of arbitrarily shaped power/ground planes. The broadband Green's function is based on modal expansions with low wavenumber extraction. Because the modal expressions are independent of frequencies, they are computed once and used for all frequencies. Then the radiated fields are readily derived from the fields on boundary walls using the equivalent principle. Results are illustrated up to 10 GHz and for arbitrary shaped PCB up to 5 inches in sizes. The accuracy and computational efficiency of the present method are compared with the method of moment (MoM) and commercial tool HFSS. The results of radiated emission of BBGFL are in good agreement with MoM and HFSS. In CPU, the method of BBGFL is several hundred times faster than direct MoM and HFSS for broadband simulations. The significant improvement in computational efficiency makes this technique useful for electronic design automation (EDA) to EMI/EMC applications.

3.2 Introduction

The power/ground plane bus is an important structure in modern electronic devices [1] [20] [21] [22] [23]. In computer systems, the power distribution network (PDN) consists of power/ground plane structure on printed circuit boards (PCBs). In electronic packages, the PDN is also often realized as power/ground plane structure.

Fast and accurate analysis of electromagnetic emissions from power/ground plane structure are for the studies of the electromagnetic compatibility (EMC) and electromagnetic interference (EMI). The non-ideal switching behavior of chip (e.g. a packaged integrated circuit) induces short current pulses on the PDN. Because of the nonzero impedance of the PDN, the current pulses can lead to voltage fluctuations, that are known as delta-I noise, switching noise, or power noise [1] [20] [21] [22] [23].

In high-speed electronic systems, the power noise can have wideband spectral harmonics up to multi-GHz. In addition to signal and power integrity problems, the power noise can be the source of considerable radiated emissions [1] [20] [21] [22] [23]. The power noise and radiated emission can be significantly amplified near the resonance frequencies of the power/ground plane cavity and become serious EMC/EMI problems. Thus, accurate and fast modeling of radiated emission from power/ground bus is critical for EMC/EMI.

Various methods have been used to analyze the radiated emissions from power/ground planes [22]. For rectangular power/ground structure, the cavity model theory provides simple analytical solutions [1] [20] [24]. For irregular shaped power/ground planes, full wave methods were used. The full wave techniques include the Method of Moment (MoM) [21] [23] [25] [26], the partial element equivalent circuit method (PEEC) [27], the finite difference time domain method (FDTD) [28], the finite differential method (FDM) [29]. Commercial EM simulation tools for PCB EMC/EMI analysis are based on these full wave methods. However, the full wave methods are expensive in terms of CPU time and memory cost. In particular, the MoM method based on free space Green's function requires the solution of a dense matrix equation of irregular ground plane at every frequency [4]. This methodology is not suited for broadband modeling of emissions from power bus.

In this chapter, a recently developed fast technique based on broadband Green's function with low wavenumber extraction [30] [31] [32] is proposed for broadband simulations of the radiated emissions from power bus structure. In [30] [31] [32], we show accurate simulation results for scattering matrices of vertical interconnects in finite ground planes for broadband modeling in irregular shaped power/ground planes. The method is several hundred times faster than MoM [3] [5] [6] and HFSS. In this chapter, we apply the method for broadband simulations of radiated emissions from arbitrary shaped PCB.

The key approach of BBGFL is that the modal expansions of the arbitrary waveguides are used and the modes are independent of frequencies. A low wavenumber extraction is used to accelerate the convergence of the modal expansion. Thus the expansions are used for all frequencies making BBGFL a fast approach for broadband modelling. On the other hand, in the usual MoM formulation, the free space Green's function used in the formulation of the surface integral equation [4] and the matrix equation for the arbitrary shape has to be solved for every frequency. This explains the present BBGFL is much more efficient than the MoM approach of using free space Green's function.

We compare the present method with MoM and commercial tool HFSS. Results show that BBGFL agrees with MoM and HFSS on surface fields and radiated emission, but BBGFL is several hundred times faster than direct MoM and HFSS in CPU for broadband simulations.

The improvement in computational efficiency will make this technique useful for electronic design automation (EDA) to EMI/EMC applications.

The chapter is organized as follows. In Section II, we present the methodology for the proposed method. In Section III, we show the simulation results for PCB up to 10GHz and sizes of PCB up to 5 inches. In Section IV, we make conclusions on this work.

3.3 Methodology

In this section the methodology of the proposed technique is described.

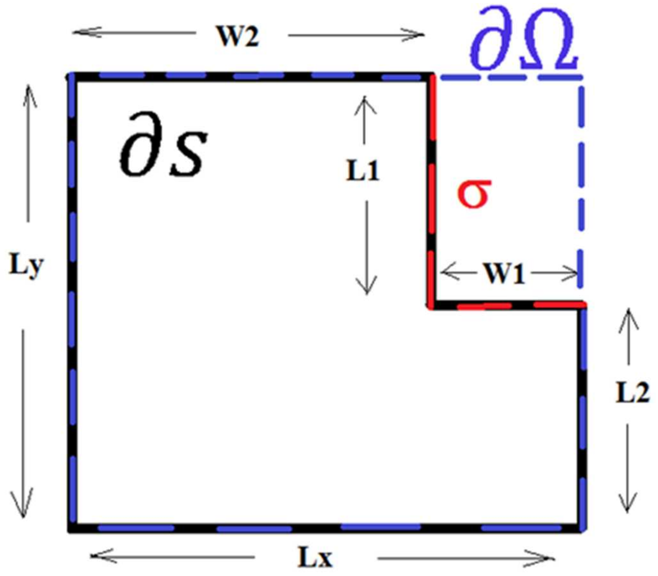

Figure 3.1 Arbitrary shaped waveguide with Neumann boundary condition.

The thickness of PCB in electronic designs and applications is small. The power/ground planes can be modeled as TM mode in a cavity with PMC boundary conditions on the side walls. Consider an irregular shaped waveguide with Neumann boundary condition (PMC) as showed in Figure 3.1. The approach is illustrated for an L-shaped waveguide. The Green's functions along the boundary wall of the waveguide are calculated using the recent developed method BBGFL [31]. The details of formulation are presented in [31]. In this section, we briefly summarize the key steps as follows.

3.3.1 Broadband Green's Function with Low Wavenumber Extraction for Calculation of Fields on Boundary Walls of Power/Ground Plane

Step 1: Constructing $g_H^{\Omega}(k,\bar{\rho},\bar{\rho}')$ with low wavenumber extraction be the boundary of the L-shaped waveguide

The boundary σ is the boundary ∂S that does not overlap with the rectangular boundary. Neumann boundary conditions hold for the boundary walls for TM modes with PMC walls. Let $\Psi_\alpha(\bar{\rho})$ be the modal functions of the rectangular waveguide with k_α the resonant wavenumber. Let $g_H^{\Omega}(k,\bar{\rho},\bar{\rho}')$ be the Green's function for the rectangular waveguide where subscript H stands for Neumann boundary condition. $g_H^{\Omega}(k,\bar{\rho},\bar{\rho}')$ can be expanded in model expansions of $\Psi_\alpha(\bar{\rho})$ and $\Psi_\alpha(\bar{\rho}')$. It is the sum of the free space Green's function g_0 and the response g_{HR}^{Ω}

$$g_H^{\Omega}(k,\bar{\rho},\bar{\rho}') = g_0(k,\bar{\rho},\bar{\rho}') + g_{HR}^{\Omega}(k,\bar{\rho},\bar{\rho}')$$

$$=g_0\left(k_L^{\Omega},\bar{\rho},\bar{\rho}'\right) + g_{HR}^{\Omega} + \sum\nolimits_\alpha \frac{k^2-\left(k_L^{\Omega}\right)^2}{\left(k_\alpha^2-k^2\right)\left(k_\alpha^2-\left(k_L^{\Omega}\right)^2\right)}\psi_\alpha^{\Omega}(\bar{\rho})\psi_\alpha^{\Omega}(\bar{\rho}')\left(k_L^{\Omega},\bar{\rho},\bar{\rho}'\right) \tag{1}$$

The convergence of the modal expansion of $g_H^{\Omega}(k,\bar{\rho},\bar{\rho}')$ at k is accelerated by using the result for a single low wavenumber $g_H^{\Omega}\left(k_L^{\Omega},\bar{\rho},\bar{\rho}'\right)$ where k_L^{Ω} is the low wavenumber.

Step 2: For the L-shaped waveguide, calculation of modal solution ψ^{S} and resonant wavenumber k_{β}^{S}

Using the Green's function from the rectangular waveguide, the modes of the L-shaped waveguide are solved discretizing the boundary σ into N intervals, σ_n, $n = 1,2,\cdots,N$. The center point of the mth interval is at $\bar{\rho}_m$. The value of the eigenmode is $\psi_{Hn}^{\mathrm{S}} = q_n/\Delta t$ on σ_n.

The rectangular waveguide modal expansions are truncated at $\Psi_\alpha(\bar{\rho})$, $\alpha = 1,2,\cdots,M$. The result matrix equation for the eigenvalue problem is

$$\left(\bar{\bar{D}} - \bar{\bar{Q}}\bar{\bar{P}}^{-1}\bar{\bar{S}}\right)\bar{b} = \frac{1}{\left(k^2 - \left(k_L^{\Omega}\right)^2\right)}\bar{b} \tag{2}$$

where k^2 are the modal wavenumber squared to be solved. The results $\left(k_{\beta}^{\mathrm{S}}\right)^2$, $\beta = 1,2,3\cdots\cdots$. where β is the mode index

In equation (1) $\bar{\bar{P}}$ and $\bar{\bar{S}}$ are $N \times N$ matrix and $N \times M$ matrices respectively and the elements are

$$P_{mn}$$

$$= \left(\frac{1}{2}\right)\frac{1}{\Delta t} + \frac{1}{\Delta t}\int_{\sigma_m} dl'\hat{n}_t' \cdot \nabla_t' g_{HR}\left(k_L^{\Omega}, \bar{\rho}_m, \bar{\rho}'\right) \qquad \text{for } n = m \tag{3.a}$$

$$= \frac{1}{\Delta t}\int_{\sigma_n} dl'\left[\hat{n}_t' \cdot \nabla_t' g_H^{\Omega}\left(k_L^{\Omega}, \bar{\rho}_n, \bar{\rho}'\right)\right]_{\bar{\rho}=\bar{\rho}_m} \qquad \text{for } n \neq m \tag{3.b}$$

$$S_{m\alpha} = \frac{1}{\left(k_\alpha^2 - \left(k_L^{\Omega}\right)^2\right)}\Psi_\alpha(\bar{\rho}_m) \tag{4}$$

The matrix $\bar{\bar{Q}}$ is a $M \times N$ matrix and $\bar{\bar{D}}$ is a $M \times M$ diagonal matrix. The elements are

$$Q_{\alpha n} = \frac{[\hat{n}_t' \cdot \nabla_t' \Psi_\alpha(\bar{\rho}')]_{\bar{\rho}'=\bar{\rho}_n}}{k_\alpha^2 - \left(k_L^\Omega\right)^2} \tag{5}$$

$$D_{\alpha\beta} = \frac{1}{k_\alpha^2 - \left(k_L^\Omega\right)^2} \delta_{\alpha\beta} \tag{6}$$

After the eigenvalue and eigenvectors are solved, the modal wave functions on σ are calculated by $q_n, n = 1,2,\cdots,N$.

$$\bar{q} = -\bar{\bar{P}}^{-1}\bar{\bar{S}}\bar{b} \tag{7}$$

Then the modal functions are calculated by the integral over σ

$$-\psi_H^S(\bar{\rho}) = \int_\sigma dl' \left(\psi_H^S(\bar{\rho}')\hat{n}_t' \cdot \nabla_t' g_H^\Omega(k, \bar{\rho}, \bar{\rho}')\right) \tag{8}$$

Step 3: Normalization of modes $\psi_\beta^S(\bar{\rho})$

The normalization of modes are such that

$$\sum_{\alpha=1}^{M} \left(b_{\alpha\beta}\right)^2 = \left(k_\beta^S\right)^4 \text{ for } k_\beta^S \neq 0 \tag{9.a}$$

$$\psi_0^S(\bar{\rho}) = \frac{1}{\sqrt{A_S}} \quad \text{for } k_\beta^S = 0 \tag{9.b}$$

Where A_S= area of L-shaped waveguide.

Step 4: Construct broadband Green's function $g_H^{\mathrm{S}}(k, \bar{\rho}, \bar{\rho}')$ with low wavenumber extraction of $g_H^{\mathrm{S}}\left(k_L^{\mathrm{S}}, \bar{\rho}, \bar{\rho}'\right)$

Using the modes of the L-shaped waveguide, $\psi_\beta^S(\bar{\rho})$, the Green's function $g_H^{\mathrm{S}}(k, \bar{\rho}, \bar{\rho}')$ of the L-shaped waveguide can be expressed. However, the series expansion converges slowly. To accelerate the convergence, we use MoM to solve the Green's function $g_H^S(k_L^S, \bar{\rho}, \bar{\rho}')$ at a single wavenumber k_L^S which is separated into primary free space and response

$$g_H^S(k_L^S, \bar{\rho}, \bar{\rho}') = g_0(k_L^S, \bar{\rho}, \bar{\rho}') + g_{HR}^S(k_L^S, \bar{\rho}, \bar{\rho}') \tag{10}$$

With the subtraction of $g_H^S(k_L^S, \bar{\rho}, \bar{\rho}')$, the Green's function for arbitrary waveguide k is

$$g_H^S(k, \bar{\rho}, \bar{\rho}') = g_0(k_L^S, \bar{\rho}, \bar{\rho}') + g_{HR}^S(k_L^S, \bar{\rho}, \bar{\rho}') + \sum_\beta \left[\frac{\left(k^2-\left(k_L^S\right)^2\right)\psi_\beta^S(\bar{\rho})\psi_\beta^S(\bar{\rho}')}{\left(\left(k_\beta^S\right)^2-k^2\right)\left(\left(k_\beta^S\right)^2-\left(k_L^S\right)^2\right)}\right] \tag{11}$$

Note that the dependence of the expression in (11) on frequency is merely the factor $\frac{\left(k^2-\left(k_L^S\right)^2\right)}{\left(\left(k_\beta^S\right)^2-k^2\right)}$ and the rest of the expression is independent of frequency. Hence we use the name of Broadband Green's function. Note that we use low wavenumber extraction, twice , with k_L^Ω for the rectangular waveguide and k_L^S for the waveguide with arbitrary shape The advantages of the methodology of BBGFL are: (1) the modal functions $\psi_\beta^S(\bar{\rho})$ are independent of frequency so that they can be used for broadband modeling, (2) the convergence of Green's function modal expansion using low wavenumber extractions, (3) with the low wavenumber extraction, the singularity of the broadband bounded medium Green's function is also extracted.

3.3.2 Calculation of Radiated Emissions From Power/Ground Plane with Green's Functions

In this section we study the radiation of power/ground plane cavity in PCB and packages. Based on Huygens' principle, the radiated fields can be computed by the integral of the surface fields on the outer surfaces of the power/ground plane cavity [33] [14]. The contribution from the top and bottom surfaces are negligible, because, (1) the induced surface fields on the outer top/bottom cavity surface are much smaller than those on the inner top/bottom cavity surface; (2) the thickness of the computer PCB is usually much small than the wavelength of frequency of interest, so that the contributions of top and bottom surface fields, which are of opposite side, cancel out. The radiated field is determined by the tangential electric field on the edges, i.e. the side walls of the power/ground planes.

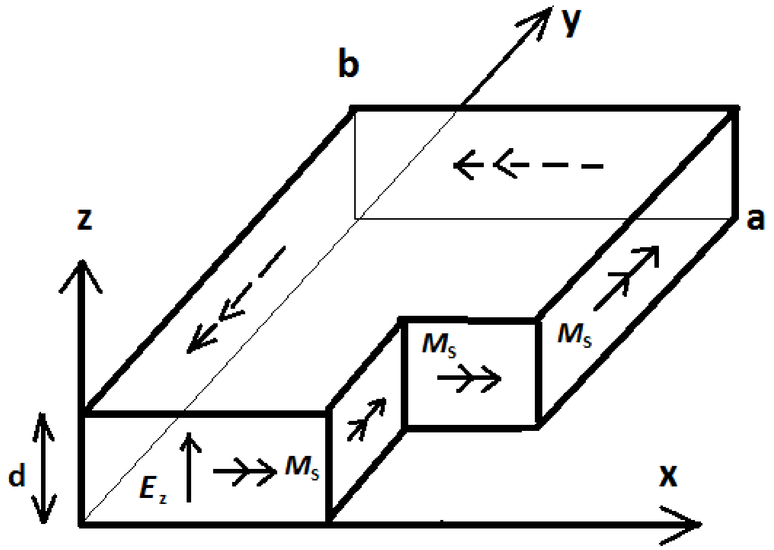

Figure 3.2 Equivalent magnetic current on periphery of the planes.

The equivalent magnetic surface current on the side walls $\bar{\rho}'$ are

$$\bar{M}_s(\bar{\rho}') = -\hat{n}' \times \bar{E}_z(\bar{\rho}') \tag{12}$$

where $\bar{E}_z(\bar{\rho}')$ is the z component of electric field on the side wall, and $\hat{n}'$ is the normal vector pointing out from the side walls. The equivalent magnetic current is shown in Figure 3.2. If we consider a point excitation at inside the waveguide, then $\bar{E}_z(\bar{\rho}') = g_H^S(k, \bar{\rho}', \bar{\rho}'')$ which is calculated by equation (11) using BBGFL method. Since the PCB is thin, only TEM mode can propagate to the walls with all other modes being evanescent waves. We can set $z' = z'' = 0$. The excitation source can be a signal via located at $\bar{\rho}''$.

Using the equivalent magnetic current as the radiation source, the radiation field can be calculated using free space Green's function as [33] [14] and [15], page 295

$$\bar{E} = -\frac{d}{4\pi}\nabla\times\int_C dl'\bar{M}_s(\bar{\rho}')\frac{e^{-jk_0|\bar{r}-\bar{r}'|}}{|\bar{r}-\bar{r}'|} \tag{13}$$

where the integral path C extends over the periphery of the board and $\bar{r}$, and $\bar{r}'$ are observation and source point vectors, respectively, expressed in spherical coordinates.

In far-zone $\bar{r} \gg \bar{r}'$, the above formula can be approximated as

$$\bar{E} = j\frac{k_0 d}{4\pi}\frac{e^{-jk_0 r}}{r}\int_C dl'\hat{r}\times\bar{M}_s(\bar{\rho}')\,e^{jk_0\hat{r}\cdot\bar{r}'} \tag{14}$$

Then $\bar{M}_s(\bar{\rho}') = \bar{E}_z(\bar{\rho}') = \hat{l}'g_H^S(k,\bar{\rho}',\bar{\rho}'')$, where $\hat{l}'$ is counterclockwise along the boundary wall. For simplicity, consider the horizontal boundary to be consisting of straight lines. Let $\hat{l}' = \hat{\tau}' = \tau'_x\hat{x} + \tau'_y\hat{y}$. Then $\hat{l}'dl' = \tau'_x dx'\hat{x} + \tau'_y dy'\hat{y}$. Thus

$$\bar{E} = j\frac{k_0 d}{4\pi}\frac{e^{-jk_0 r}}{r}$$

$$\int_C \hat{r}\times\left(\tau'_x dx'\hat{x} + \tau'_y dy'\hat{y}\right)g_H^S\,(k,\bar{\rho}',\bar{\rho}'')e^{jk_0\hat{r}\cdot\bar{r}'} \tag{15}$$

In the far field there are only E_θ and E_ϕ components. Let $\hat{r} = \hat{x}\sin\theta\cos\phi + \hat{y}\sin\theta\sin\phi + \hat{z}\cos\theta$, then

$$E_\theta = j\frac{k_0 d}{4\pi}\frac{e^{-jk_0 r}}{r}$$

$$\int_C \left(-\hat{\phi}\right)\cdot\left\{\tau_x' dx'\hat{x} + \tau_y' dy'\hat{y}\right\} g_H^{\mathrm{S}}\left(k,\bar{\rho}',\bar{\rho}''\right) e^{jk_0\hat{r}\cdot\bar{r}'} \tag{16}$$

Simplifying,

$$E_\theta = -j\frac{k_0 d}{4\pi}\frac{e^{-jk_0 r}}{r}\int_C g_H^{\mathrm{S}}\left(k,\bar{\rho}',\bar{\rho}''\right)$$

$$\left(-\sin\phi\,\tau_x' dx' + \cos\phi\,\tau_y' dy'\right)e^{jk_0\left(x'\sin\theta\cos\phi + y'\sin\theta\sin\phi\right)} \tag{17}$$

Similarly

$$E_\phi = j\frac{k_0 d}{4\pi}\frac{e^{-jk_0 r}}{r}\cos\theta\int_C g_H^{\mathrm{S}}\left(k,\bar{\rho}',\bar{\rho}''\right)$$

$$\left(\cos\phi\,\tau_x' dx' + \sin\phi\,\tau_y' dy'\right)e^{jk_0\left(x'\sin\theta\cos\phi + y'\sin\theta\sin\phi\right)} \tag{18}$$

The magnitude of the radiated electric field is given by

$$|E_{total}| = \sqrt{|E_\theta|^2 + \left|E_\phi\right|^2}. \tag{19}$$

3.4 Simulation

In this section, we present simulation results to investigate the computational accuracy and efficiency of the proposed technique. The results are shown as a function of frequency as well as selected frequencies to show the usefulness of the BBGFL technique in broadband simulations.

In using equation (11), we note that $k = k_0\sqrt{\varepsilon_r}$, where ε_r is the relative permittivity of the dielectric substrate and k_0 is the wavenumber in air. In the simulations, we choose $\varepsilon_r = 4.4(1 - j0.02)$, and use discretization step = 10mils for both MoM and BBGFL. By MoM in this chapter, we mean solving the irregular shape waveguide with surface integral equation formulated with the free space Green's function [25].

Figure 3.3 shows the 3D view of a power/ground plane waveguide with a cut out used in the simulations. The excitation is located in $\bar{\rho}'' = (-25\text{mils}, 0\text{mil})$.

As discussed earlier, once $\psi_{\beta}^{S}(\bar{\rho})$, the modes are determined, $g_{H}^{S}(k, \bar{\rho}, \bar{\rho}')$ at all frequencies are computed by the summations in (11).

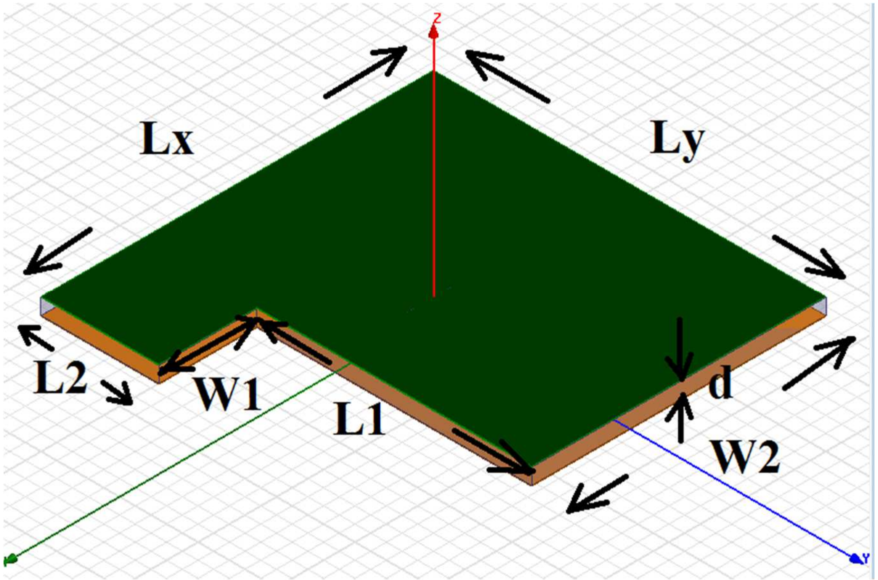

Figure 3.3 3D geometry of the L-shaped power/ground plane pair with cut out.

3.4.1 Case A: 0.5 by 0.5 Square-inch Rectangular Power/Ground Plane Pair with 0.125 by 0.35 Square-inch Cut-out

The dimension parameters are: Lx=Ly=0.5inch, L1=0.125inch, W1=0.350inch, d=20mils. For this case, the number of modes chosen is $M_{\alpha} = (1 + M_{o}) \times (1 + M_{o}) = 6 \times 6 = 36$. In Figure 3.4a, we plot the real and imaginary parts of $g_{H}^{S}(k, \bar{\rho}', \bar{\rho}'')$ as a function of frequency from 1GHz to 10GHz. The $\bar{\rho}'$ is chosen at

(0.1*Lx, -0.5*Ly) on the side wall. A total of 100 frequency points are used. We see the resonances. The results are in good agreement. In figures 4b and 4c, we show the fields on the wall respectively at 2GHz and 10GHz.

In Figure 3.5a, we plot the radiation field at $(\theta, \phi) = (135^{o}, 45^{o})$, as a function of frequency from 1GHz to 10GHz.

In figures 5b and 5c we show the comparison of BBGFL, MoM, and HFSS for the radiated field 2GHz and 10GHz respectively. Results show BBGFL agree with HFSS 3D solution.

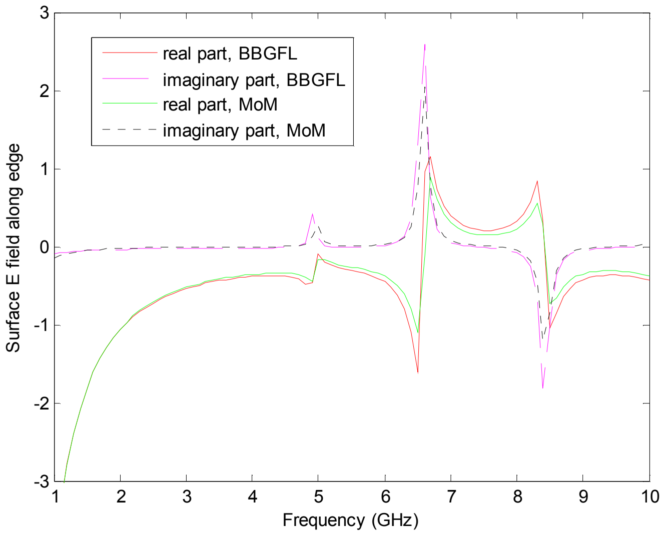

(a) Surface E-field as function of frequency

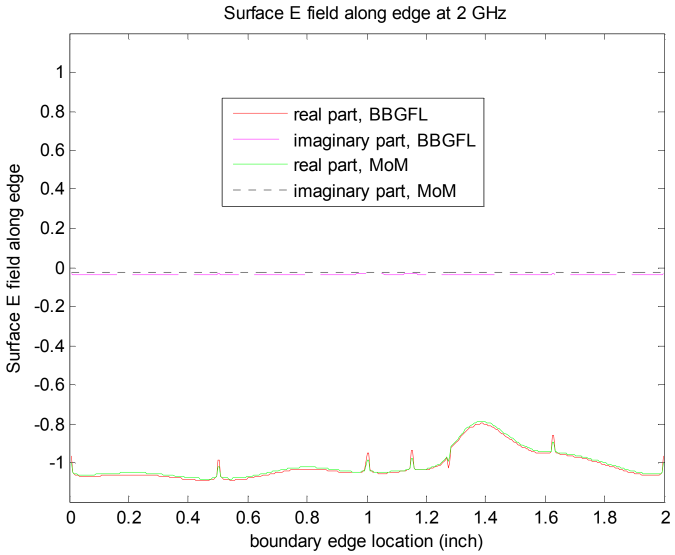

(b) Surface E-field along edge at 2GHz

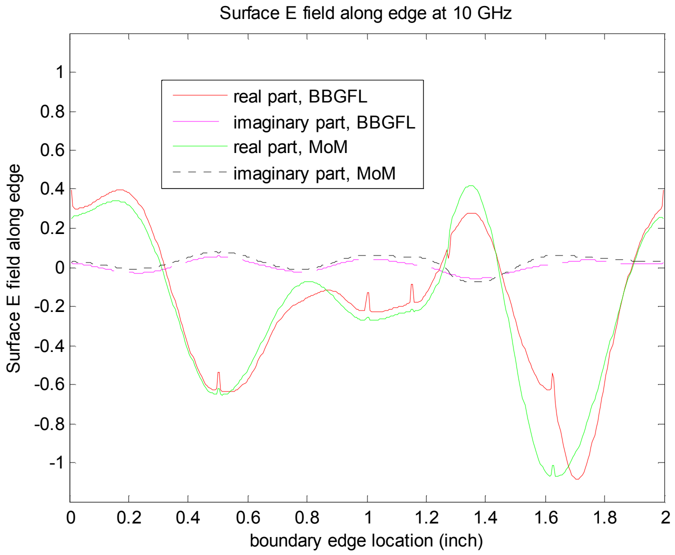

(c) Surface E-field along edge at 10GHz

Figure 3.4 Surface electric field along boundary edge for Case A at different frequencies: (a) surface field at $(\theta, \phi) = (0.1 * Lx, -0.5 * Ly)$ as a function of frequency, (b) comparison at 2GHz, (c) comparison at 10GHz.

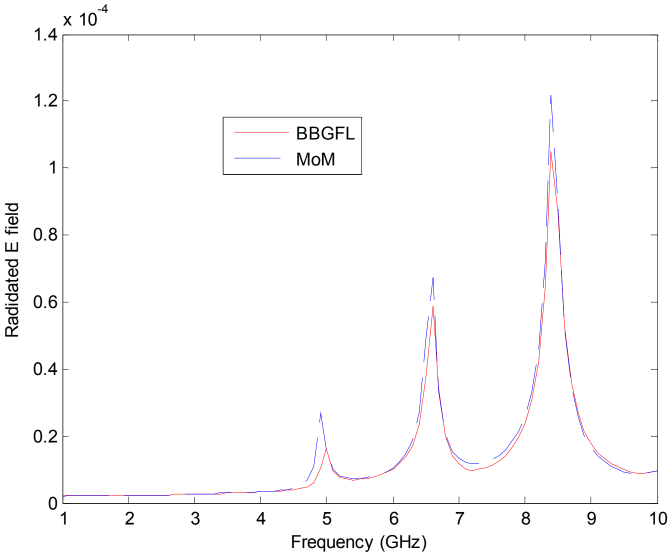

(a) Radiated E-field as function of frequency

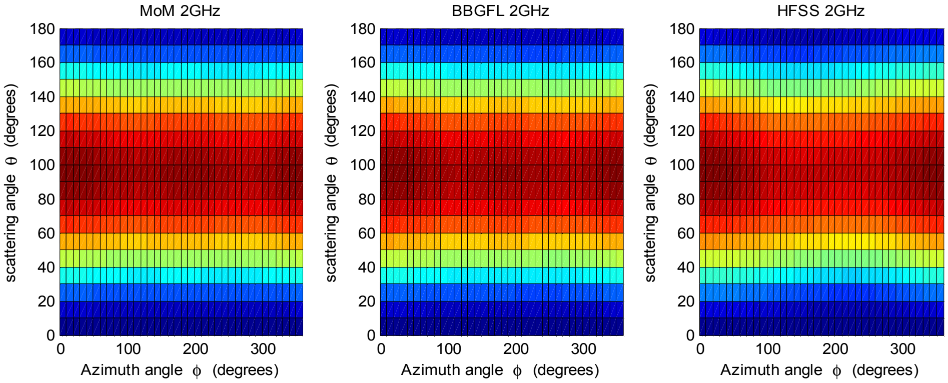

(b) Radiated E-field at 2GHz

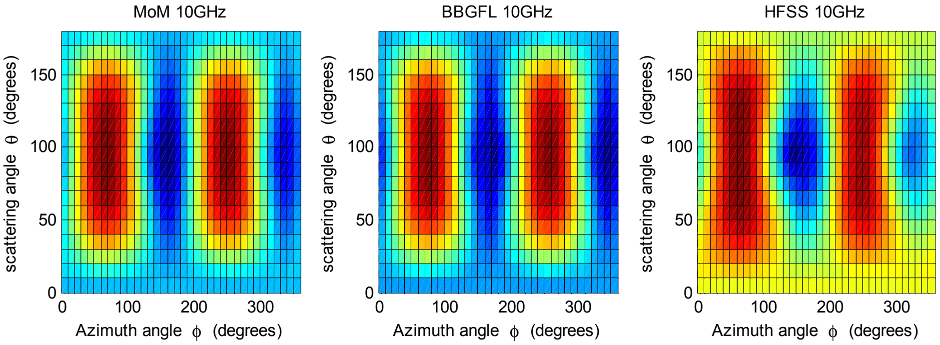

(c) Radiated E-field at 10GHz

Figure 3.5 Far-zone Radiated electric field along boundary edge for Case A at different frequencies: (a) radiation field at $(\theta, \phi) = (135^o, 45^o)$ as a function of frequency, (b) comparison at 2GHz, (c) comparison at 10GHz.

3.4.2 Case B: 1.5 by 1.5 Square-inch Rectangular Power/Ground Plane Pair with 0.125 by 0.35 Square-inch Cut-out

The dimension parameters are: Lx=Ly=1.5inch, L1=0.125inch, W1=0.350inch, d=20mils. For this case, the number of modes chosen is $M_\alpha = (1 + M_o) \times (1 + M_o) = 11 \times 11 = 121$. In Figure 3.6a, we plot the real and imaginary parts of $g_H^S(k, \bar{\rho}', \bar{\rho}'')$ as a function of frequency from 1GHz to 10GHz. The $\bar{\rho}'$ is chosen at (0.1*Lx, -0.5*Ly) on the side wall. A total of 100 frequency points are used. We see the resonances. The results are in good agreement. In figures 6b and 6c, we show the fields on the wall respectively at 2GHz and 10GHz.

In Figure 3.7a, we plot the radiation field at $(\theta, \phi) = (135^o, 45^o)$, as a function of frequency from 1GHz to 10GHz.

In figures 7b and 7c we show the comparison of BBGFL, MoM, and HFSS for the radiated field 2GHz and 10GHz respectively. Results show BBGFL agree with HFSS 3D solution.

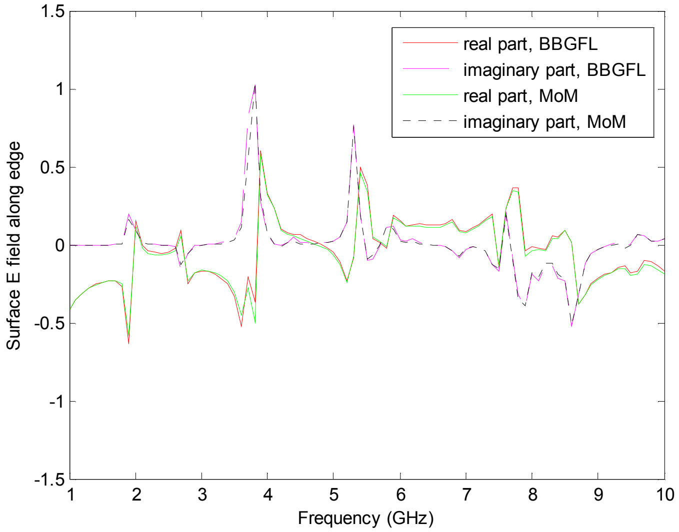

(a) Surface E-field as function of frequency

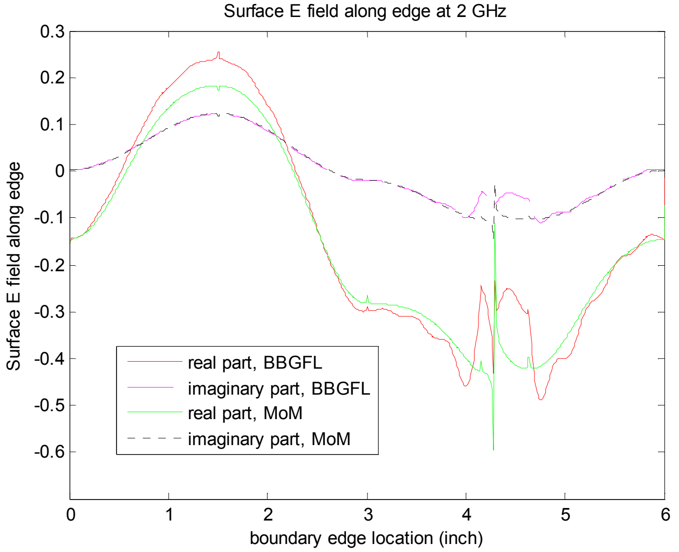

(b) Surface E-field along edge at 2GHz

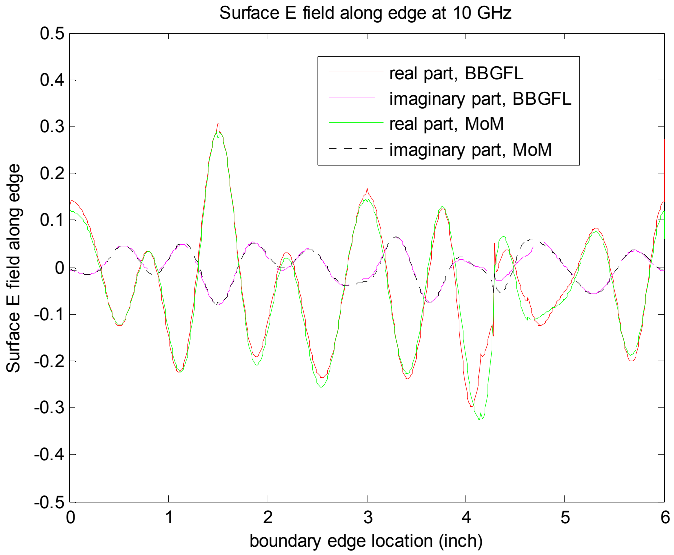

(c) Surface E-field along edge at 10GHz

Figure 3.6 Surface electric field along boundary edge for Case B at different frequencies: (a) surface field at $(\theta, \phi) = (0.1 * Lx, -0.5 * Ly)$ as a function of frequency, (b) comparison at 2GHz, (c) comparison at 10GHz.

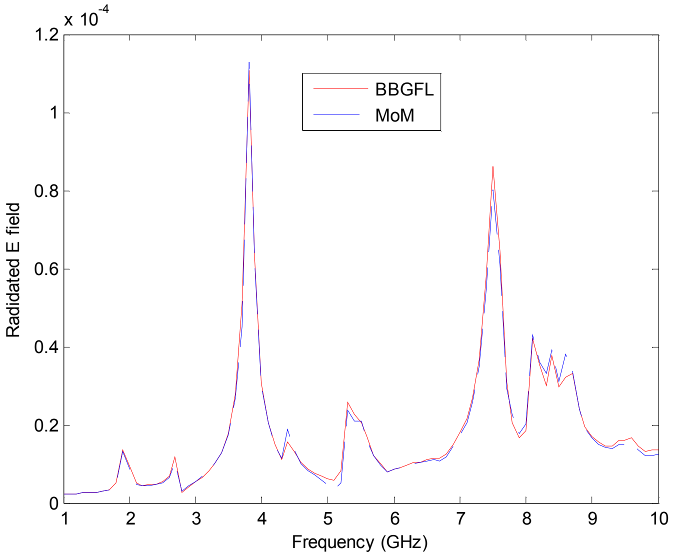

(a) Radiated E-field as function of frequency

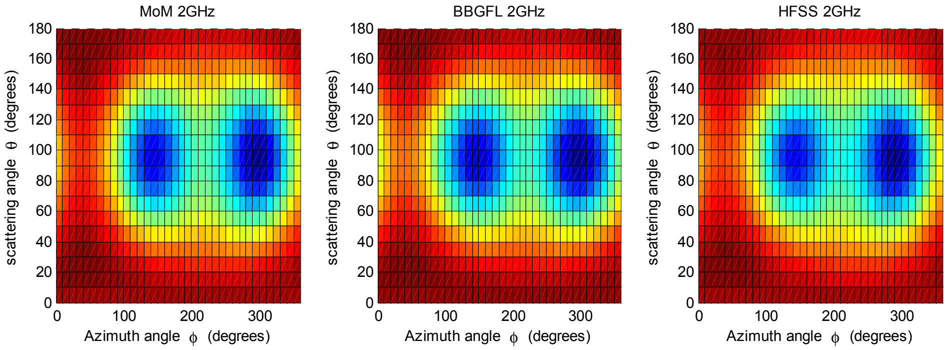

(b) Radiated E-field at 2GHz

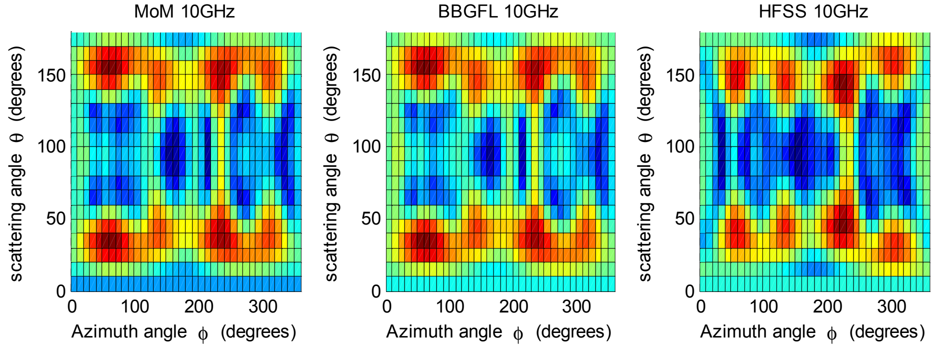

(c) Radiated E-field at 10GHz

Figure 3.7 Far-zone Radiated electric field along boundary edge for Case B at different frequencies: (a) radiation field at $(\theta, \phi) = (135^o, 45^o)$ as a function of frequency, (b) comparison at 2GHz, (c) comparison at 10GHz.

3.4.3 Case C: 5 by 5 Square-inch Rectangular Power/Ground Plane Pair with 0.125 by 0.35 Square-inch Cut-out

The dimension parameters are: Lx=Ly=5inch, L1=0.125inch, W1=0.350inch, d=20mils. For this case, the number of modes chosen is $M_\alpha = (1 + M_o) \times (1 + M_o) = 21 \times 21 = 441$. In Figure 3.8a, we plot the real and imaginary parts of $g_H^S(k, \bar{\rho}', \bar{\rho}'')$ as a function of frequency from 0.1GHz to 10GHz. The $\bar{\rho}'$ is chosen at (0.1*Lx, -0.5*Ly) on the side wall. A total of 100 frequency points are used. We see the resonances. The results are in good agreement. In figures 8b and 8c, we show the fields on the wall respectively at 2GHz and 10GHz.

In Figure 3.9a, we plot the radiation field at $(\theta, \phi) = (135^{o}, 45^{o})$, as a function of frequency from 0.1GHz to 10GHz. In figures 9b and 9c we show the comparison of BBGFL, MoM, and HFSS for the radiated field 2GHz and 10GHz respectively. Results show BBGFL agree with HFSS 3D solution.

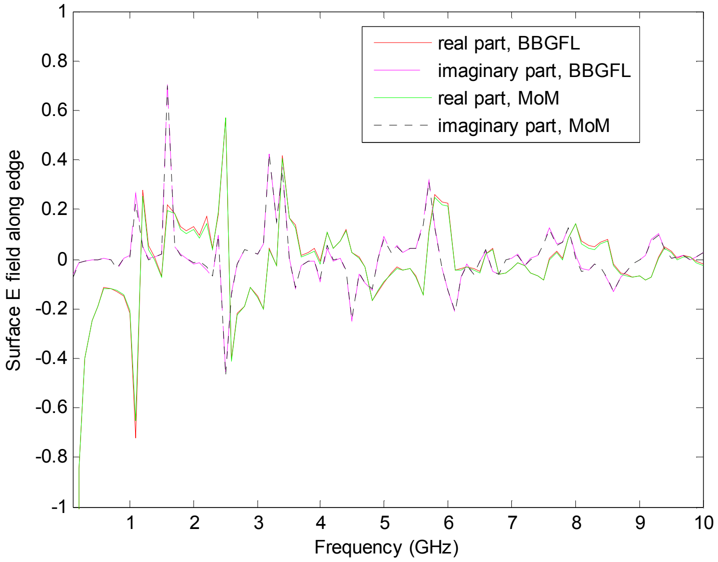

(a) Surface E-field as function of frequency

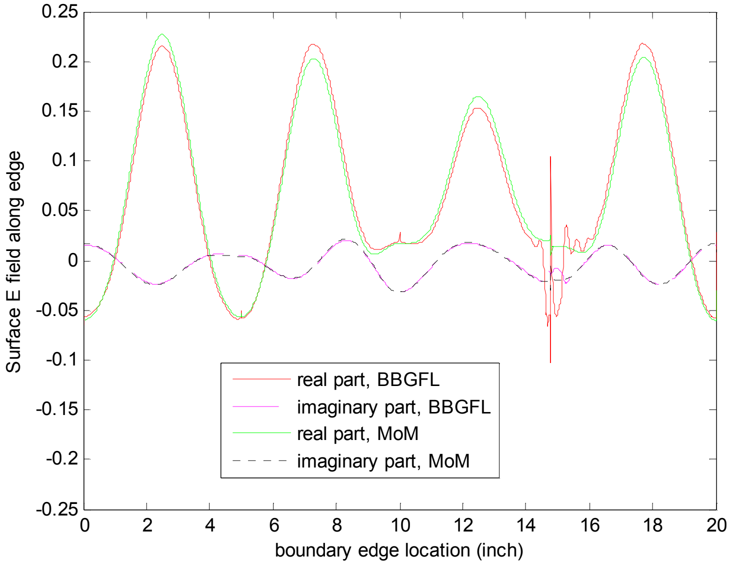

(b) Surface E-field along edge at 2GHz

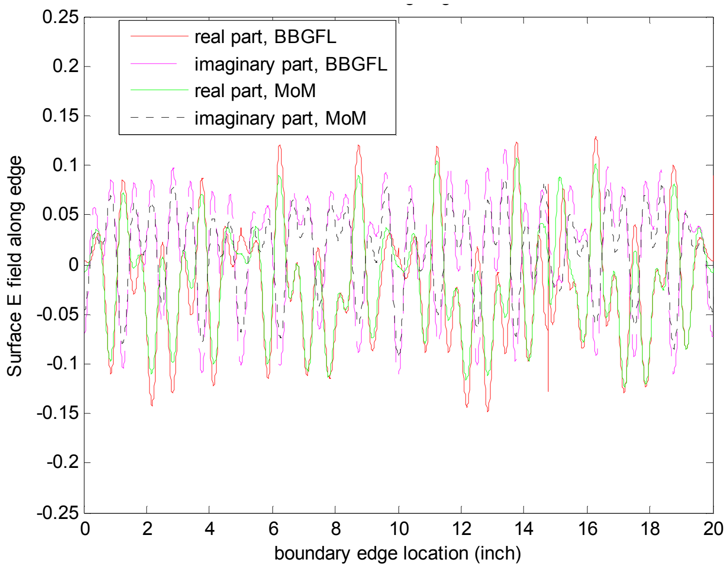

(c) Surface E-field along edge at 10GHz

Figure 3.8 Surface electric field along boundary edge for Case C at different frequencies: (a) surface field at $(\theta, \phi) = (0.1 * Lx, -0.5 * Ly)$ as a function of frequency, (b) comparison at 2GHz, (c) comparison at 10GHz.

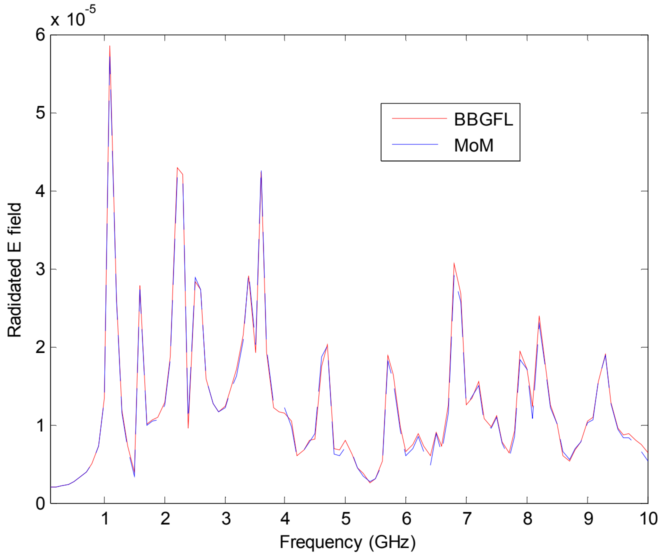

(a) Radiated E-field as function of frequency

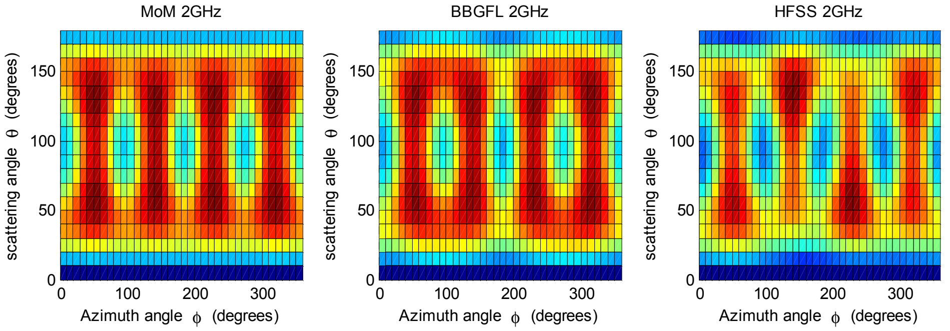

(b) Radiated E-field at 2GHz

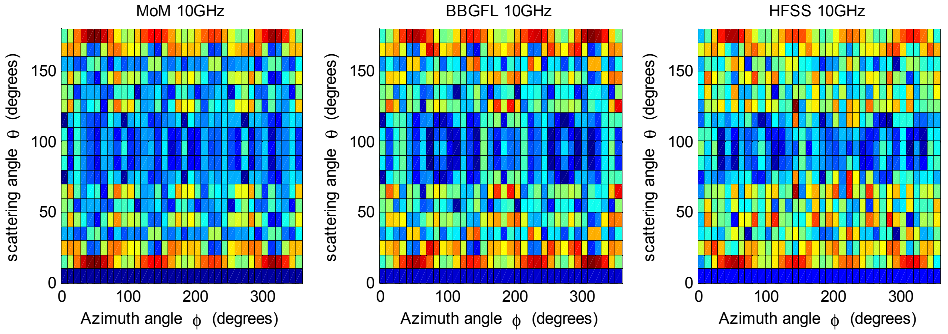

(c) Radiated E-field at 10GHz

Figure 3.9 Far-zone Radiated electric field along boundary edge for Case C at different frequencies: (a) radiation field at $(\theta, \phi) = (135^o, 45^o)$ as a function of frequency, (b) comparison at 2GHz, (c) comparison at 10GHz.

3.4.4 Case D: 5 by 5 Square-inch Rectangular Power/Ground Plane Pair with 1.25 by 3.5 Square-inch Cut-out

The dimension parameters are: Lx=Ly=5inch, L1=1.25inch, W1=3.5inch, d=20mils. For this case, the number of modes chosen is $M_\alpha = (1 + M_o) \times (1 + M_o) = 21 \times 21 = 441$. In Figure 3.10a, we plot the real and imaginary parts of $g_H^S(k, \bar{\rho}', \bar{\rho}'')$ as a function of frequency from 0.1GHz to 10GHz. The $\bar{\rho}'$ is chosen at (0.1*Lx, -0.5*Ly) on the side wall. A total of 100 frequency points are used. We see the resonances. The results are in good agreement. In figures 10b and 10c, we show the fields on the wall respectively at 2GHz and 10GHz.

In Figure 3.11a, we plot the radiation field at $(\theta, \phi) = (135^o, 45^o)$, as a function of frequency from 0.1GHz to 10GHz. In figures 11b and 11c we show the comparison of BBGFL, MoM, and HFSS for the radiated field 2GHz and 10GHz respectively. Results show BBGFL agree with HFSS 3D solution.

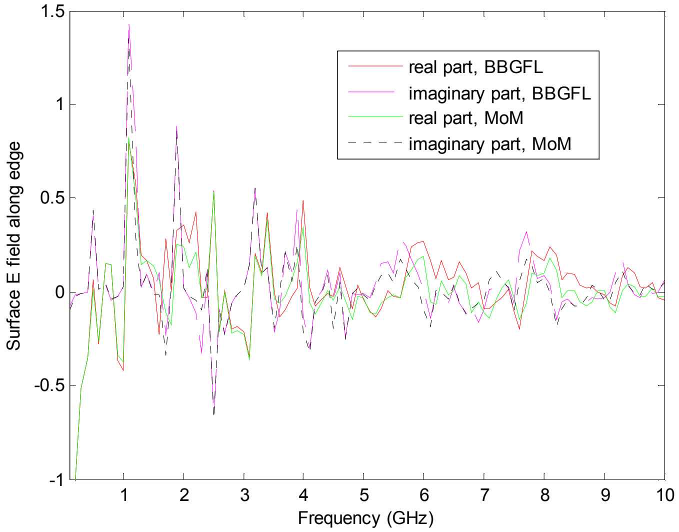

(a) Surface E-field as function of frequency

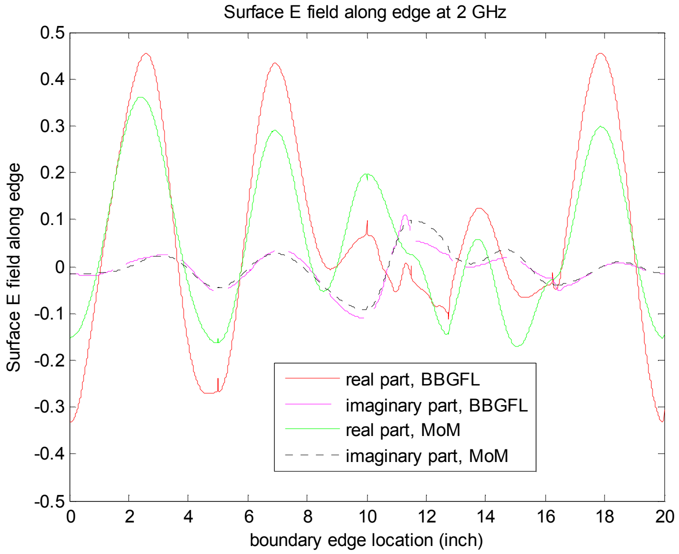

(b) Surface E-field along edge at 2GHz

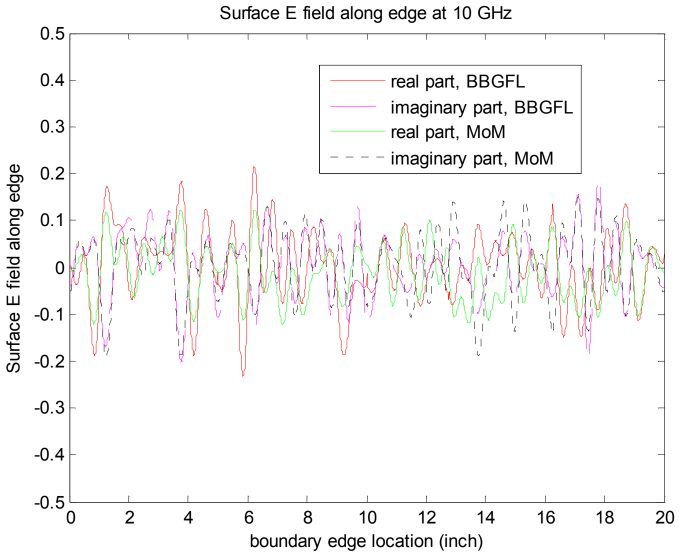

(c) Surface E-field along edge at 10GHz

Figure 3.10 Surface electric field along boundary edge for Case D at different frequencies: (a) surface field at $(\theta, \phi) = (0.1 * Lx, -0.5 * Ly)$ as a function of frequency, (b) comparison at 2GHz, (c) comparison at 10GHz.

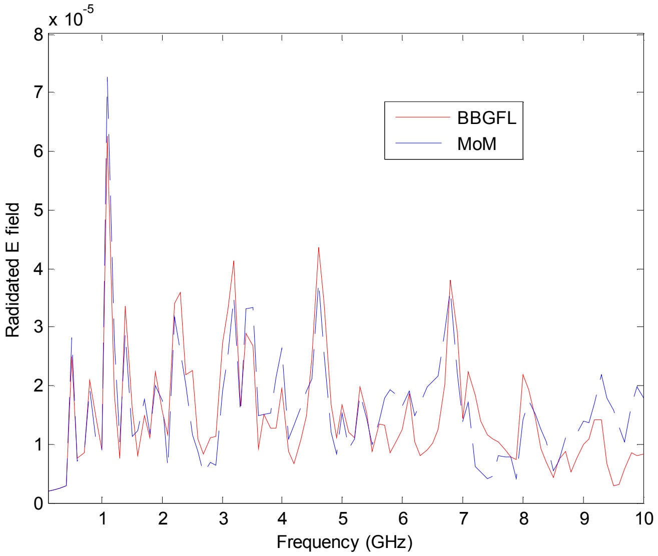

(a) Radiated E-field as function of frequency

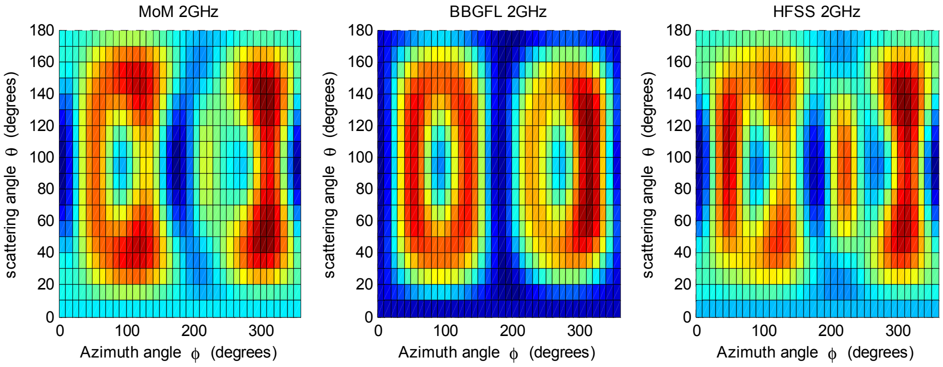

(b) Radiated E-field at 2GHz

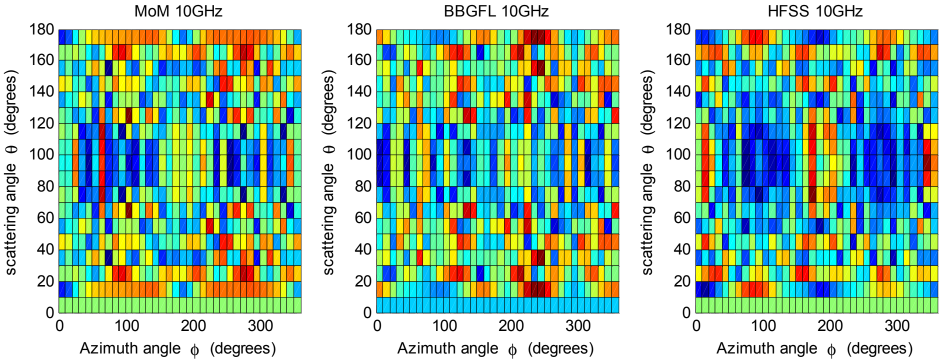

(c) Radiated E-field at 10GHz

Figure 3.11 Far-zone Radiated electric field along boundary edge for Case D at different frequencies: (a) radiation field at $(\theta, \phi) = (135^{o}, 45^{o})$ as a function of frequency, (b) comparison at 2GHz, (c) comparison at 10GHz.

3.4.5 Case E: 0.5 by 0.5 Square-inch Rectangular Power/Ground Plane Pair with 0.1 by 0.1 Square-inch Cut-out

The dimension parameters are: Lx=Ly=0.5inch, L1=W1=0.1inch, d=20mils. For this case, the number of modes chosen is $M_\alpha = (1 + M_o) \times (1 + M_o) = 6 \times 6 = 36$. In Figure 3.12a, we plot the real and imaginary parts of $g_H^{\mathrm{S}}(k, \bar{\rho}', \bar{\rho}'')$ as a function of frequency from 1GHz to 10GHz. The $\bar{\rho}'$ is chosen at (0.1*Lx, -0.5*Ly) on the side wall. A total of 100 frequency points are used. We see the resonances. The results are in good agreement between BBGFL and MoM. In figures 12b and 12c, we show the fields on the wall respectively at 2GHz and

10GHz.

In Figure 3.13a, we plot the radiation field at $(\theta, \phi) = (135^{o}, 45^{o})$, as a function of frequency from 1GHz to 10GHz. Results over this broad frequency range are in good agreement between BBGFL and MoM.

In figures 13b and 13c we show the comparison of BBGFL, MoM, and HFSS for the radiated field 2GHz and 10GHz respectively. Results show BBGFL agree with HFSS 3D solution.

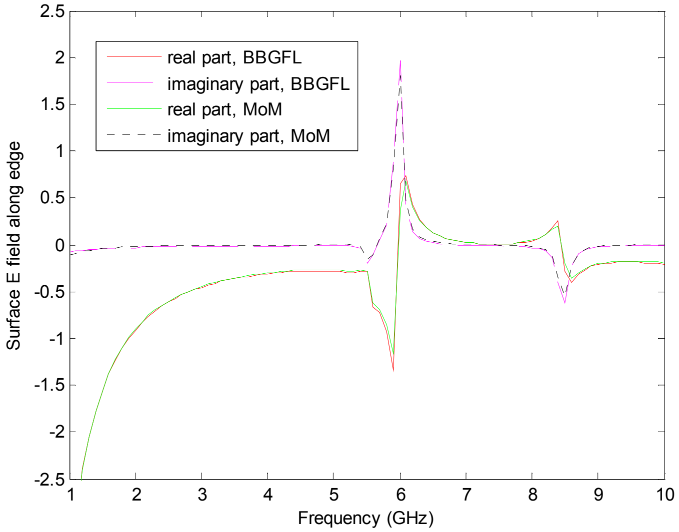

(a) Surface E-field as function of frequency

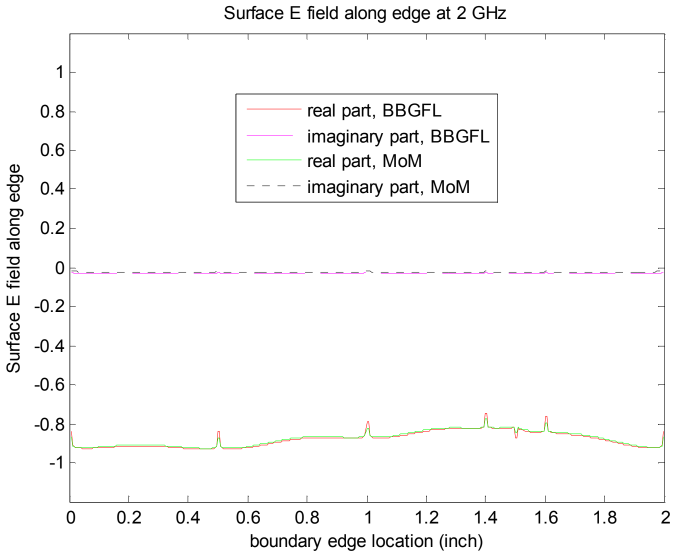

(b) Surface E-field along edge at 2GHz

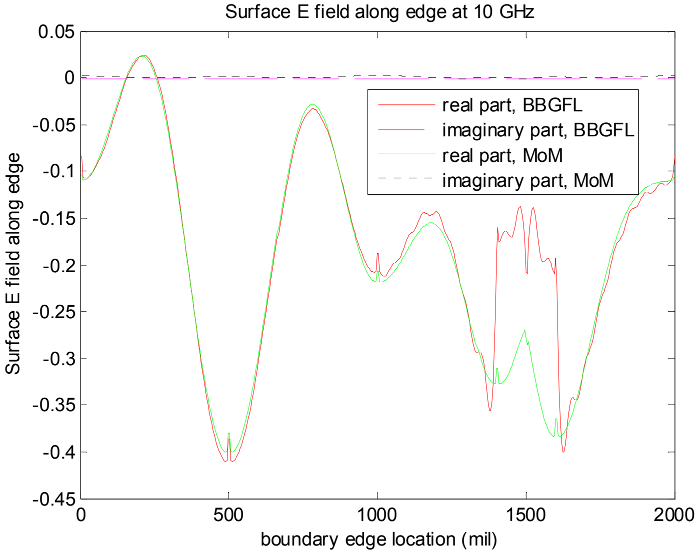

(c) Surface E-field along edge at 10GHz

Figure 3.12 Surface electric field along boundary edge for Case E at different frequencies: (a) surface field at $(\theta, \phi) = (0.1 * Lx, -0.5 * Ly)$ as a function of frequency, (b) comparison at 2GHz, (c) comparison at 10GHz.

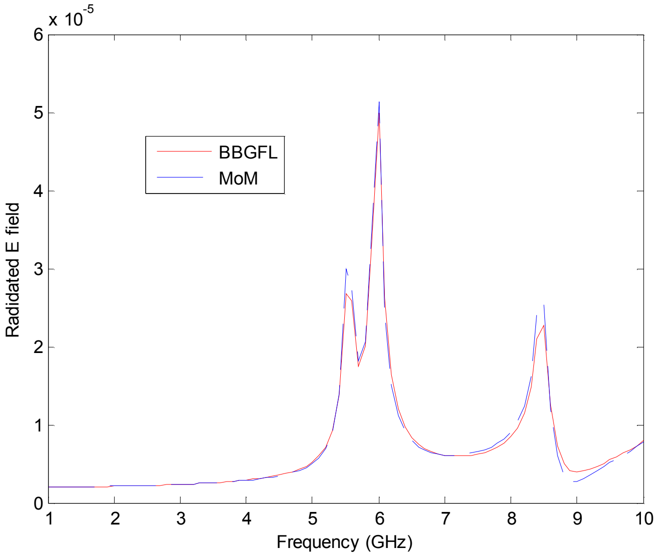

(a) Radiated E-field as function of frequency

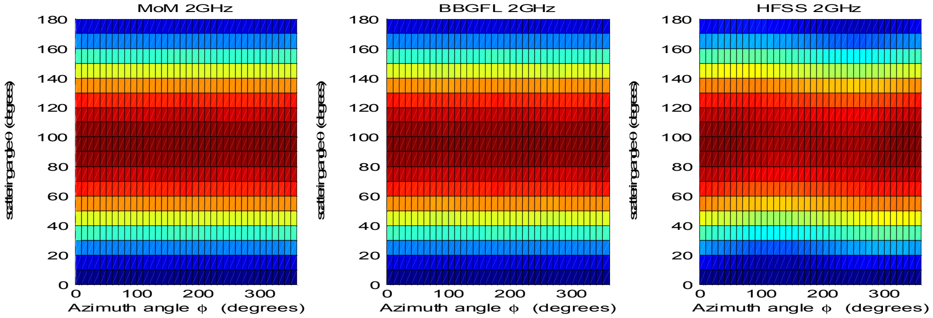

(b) Radiated E-field at 2GHz

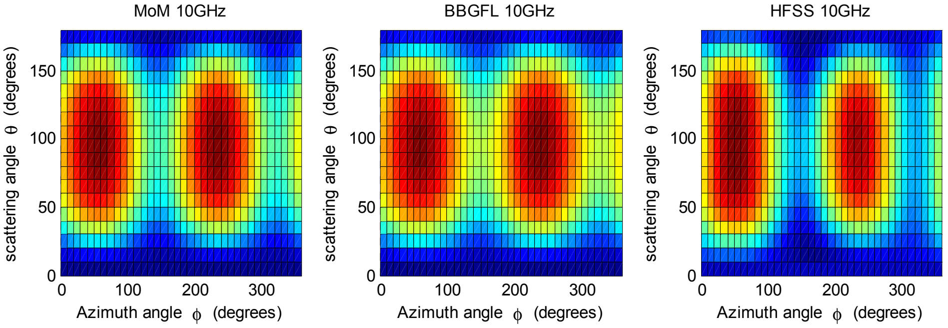

(c) Radiated E-field at 10GHz

Figure 3.13 Far-zone Radiated electric field along boundary edge for Case E at different frequencies: (a) radiation field at $(\theta, \phi) = (135^o, 45^o)$ as a function of frequency, (b) comparison at 2GHz, (c) comparison at 10GHz.

3.4.6 Case F: 1 by 1 Square-inch Rectangular Power/Ground Plane Pair with 0.125 by 0.35 Square-inch Cut-out

The dimension parameters are: Lx=Ly=1inch, L1=0.125inch, W1=0.350inch, d=20mils. For this case, the number of modes chosen is $M_\alpha = (1 + M_o) \times (1 + M_o) = 9 \times 9 = 81$. In Figure 3.14a, we plot the real and imaginary parts of $g_H^S(k, \bar{\rho}', \bar{\rho}'')$ as a function of frequency from 1GHz to 10GHz. The $\bar{\rho}'$ is chosen at (0.1*Lx, -0.5*Ly) on the side wall. A total of 100 frequency points are used. We see the resonances. The results are in good agreement. In figures 14b and 14c, we show the fields on the wall respectively at 2GHz and 10GHz.

In Figure 3.15a, we plot the radiation field at $(\theta, \phi) = (135^o, 45^o)$, as a function of frequency from 1GHz to 10GHz.

In figures 3.15b and 3.15c we show the comparison of BBGFL, MoM, and HFSS for the radiated field 2GHz and 10GHz respectively. Results show BBGFL agree with HFSS 3D solution.

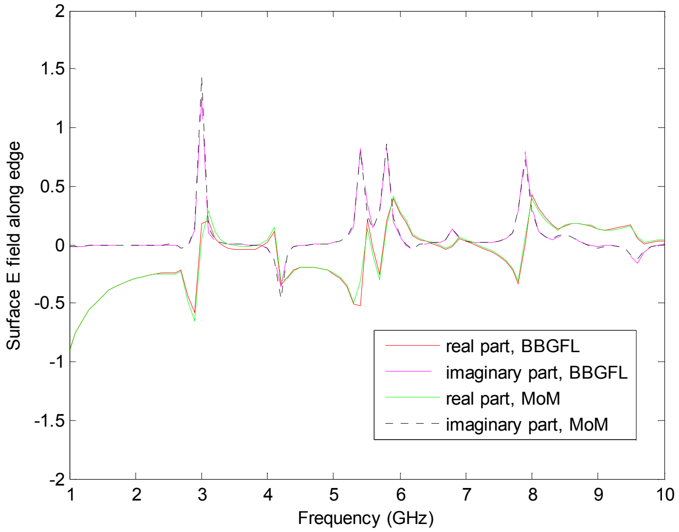

(a) Surface E-field as function of frequency

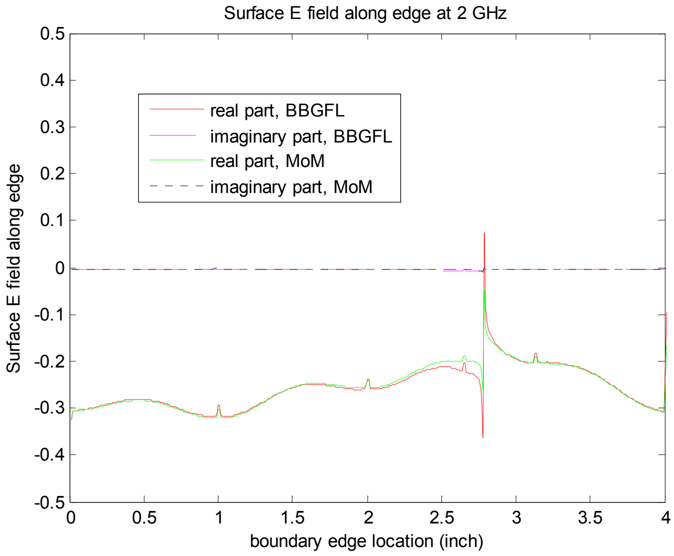

(b) Surface E-field along edge at 2GHz

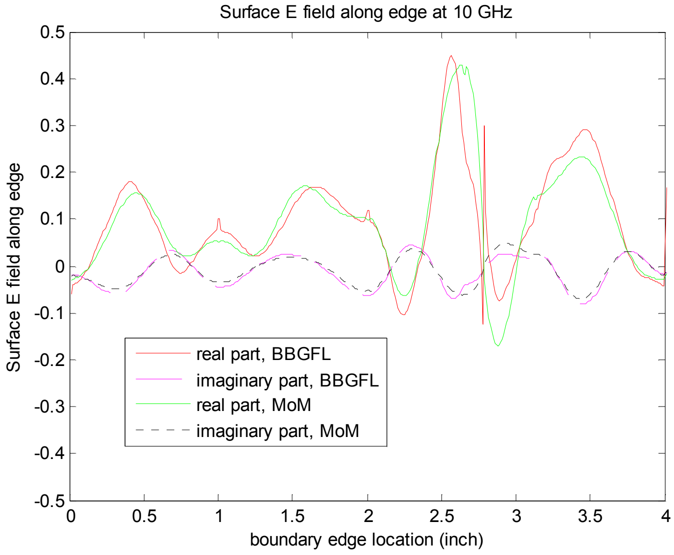

(c) Surface E-field along edge at 10GHz

Figure 3.14 Surface electric field along boundary edge for Case F at different frequencies: (a) surface field at $(\theta, \phi) = (0.1 * Lx, -0.5 * Ly)$ as a function of frequency, (b) comparison at 2GHz, (c) comparison at 10GHz.

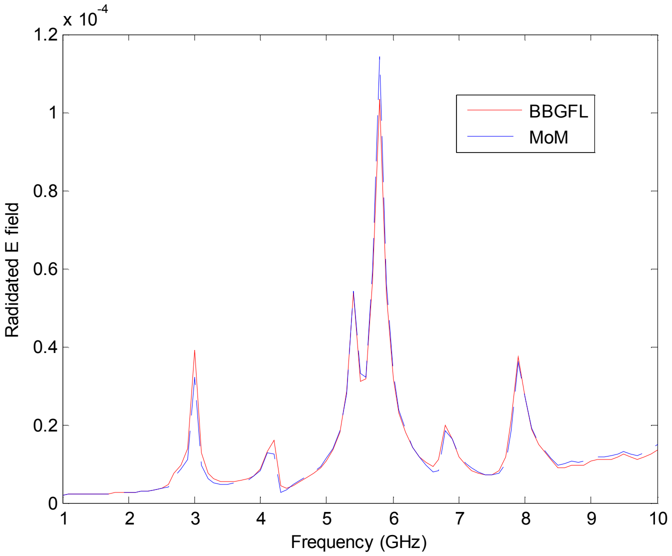

(a) Radiated E-field as function of frequency

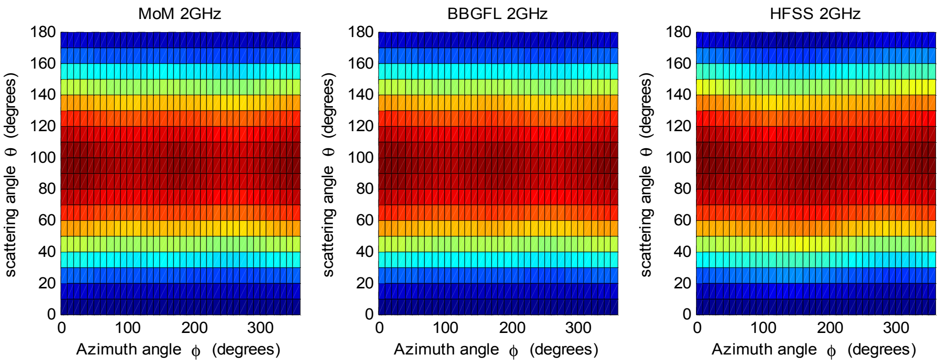

(b) Radiated E-field at 2GHz

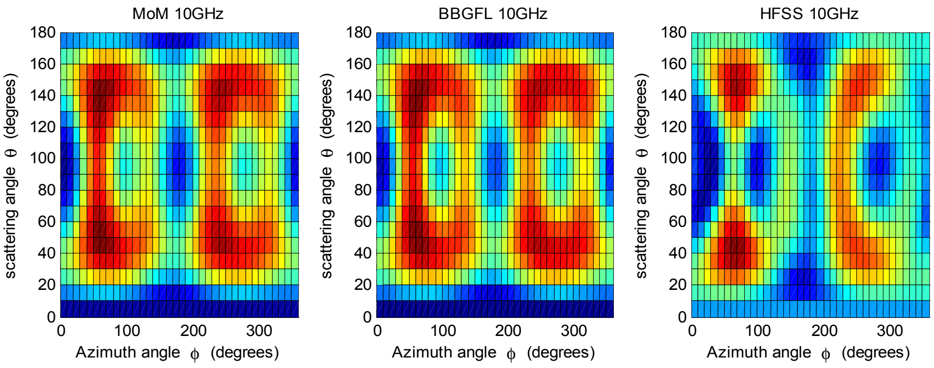

(c) Radiated E-field at 10GHz

Figure 3.15 Far-zone Radiated electric field along boundary edge for Case F at different frequencies: (a) radiation field at $(\theta, \phi) = (135^{o}, 45^{o})$ as a function of frequency, (b) comparison at 2GHz, (c) comparison at 10GHz.

3.4.7 Comparison of CPU Time for Vias Simulations

In Table 3.1-3.3, we compare three different methods (BBGFL, MoM, HFSS) for modeling EMC radiation from the irregular shaped power/ground planes waveguides in Case A-D. The thickness of dielectric substrate is 60mils. In the simulations, the discretization spacing is 10mils for both MoM and BBGFL. The BBGFL uses a number of M_o modes for both kxm and kyn, with a total number of $M_\alpha = (1 + M_o) \times (1 + M_o)$ in two dimensions. In Case A (Table I), $M_o = 5$. In Case B (Table II), $M_o = 11$. In Case C (Table III), $M_o = 20$. In Case D (Table IV), $M_o = 20$. The cpu time of BBGFL consists of 3 parts: the first part is for one time of MoM solution at low frequency, the second part is for pre-computing the modes, and the third part is for post-processing the final Green's functions. In the Table I and II, for broadband modeling with 100 frequency points, the proposed method is more than 100 times faster than HFSS. For the Case C (Table III) and the Case D (Table IV) with 5 by 5 square inches, the BBGFL is several hundred times faster than MoM and HFSS.

Table 3-1 Comparison of CPU time between BBGFL, MoM, and HFSS for Case A. Dimension parameters: Lx=Ly=0.5inch, L1=0.125inch, W1=0.35inch.

Methods	1 frequency point	10 frequency points	100 frequency points	1000 frequency points
BBGFL	1.27+0.2 +0.01*1 =1.48 sec	1.27+0.2 +0.01*10 =1.57 sec	1.27+0.2 +0.01*100 =2.47 sec	1.27+0.2 +0.01*1000 =11.47 sec
MoM	1.27*1 = 1.27 sec	1.27*10 = 12.7 sec	1.27*100 = 127 sec	1.27*1000 = 1270 sec
HFSS	15+2.4*1 = 17.4 sec	15+2.4*10 = 39 sec	15+2.4*100= 255 sec	15+2.4*1000= 2415 sec

Table 3-2 Comparison of CPU time between BBGFL, MoM, and HFSS for Case B. Dimension parameters: Lx=Ly=1.5inches, L1=0.125inch, W1=0.35inch.

Methods	1 frequency point	10 frequency points	100 frequency points	1000 frequency points
BBGFL	6.6+1.2 +0.04*1 =7.84 sec	6.6+1.2 +0.04*10 =8.2 sec	6.6+1.2 +0.04*100 =11.8 sec	6.6+1.2 +0.04*1000 =47.8 sec
MoM	6.6*1 = 6.6 sec	6.6*10 = 66 sec	6.6*100 = 660 sec	6.6*1000 = 6600 sec
HFSS	137+20*1 = 157 sec	137+20*10= 337 sec	137+20*100= 2137 sec	137+20*1000= 20137 sec

Table 3-3 Comparison of CPU time between BBGFL, MoM, and HFSS for Case C. Dimension parameters: Lx=Ly=5inches, L1=0.125inch, W1=0.35inch.

Methods	1 frequency point	10 frequency points	100 frequency points	1000 frequency points
BBGFL	1057+16 +0.2*1 =1073.2sec	1057+16 +0.2*10 =1075sec	1057+16 +0.2*100 =1093sec	1057+16 +0.2*1000 =1273 sec
MoM	1057*1 = 1057sec	1057*10 = 10570 sec	1057*100 = 105700 sec	1057*1000 = 1057000 sec
HFSS	2932 +508*1 =3440sec	2932 +508*10 = 8012 sec	2932 +508*100 = 53732 sec	2932 +508*1000 = 510932 sec

Table 3-4 Comparison of CPU time between BBGFL, MoM, and HFSS for Case D. Dimension parameters: Lx=Ly=5inches, L1=1.25inch, W1=3.5inch.

Methods	1 frequency point	10 frequency points	100 frequency points	1000 frequency points
BBGFL	1057+139 +0.4*1 =1196.4 sec	1057+139 +0.4*10 =1200sec	1057+139 +0.4*100 =1236 sec	1057+139 +0.4*1000 =1596 sec
MoM	1057*1 = 1057 sec	1057*10 = 10570 sec	1057*100 = 105700 sec	1057*1000 = 1057000 sec
HFSS	3409+552*1 = 4492sec	531+3961*10 = 40141sec	531+3961*100 = 396631sec	531+3961*1000 = 3961531sec

3.5 Conclusion

In this chapter, we introduce the application of BBGFL to fast modeling of the radiated emissions from power buses in printed circuit boards (PCBs) and packages. The BBGFL is used in fast calculation of the Green's function along the edge of arbitrarily shaped power/ground planes at broadband frequencies. Then the radiated fields are quickly derived from the pre-computed surface fields terms of Green's functions based on the equivalent principle. The present method is compared with method of moment (MoM) and commercial tool HFSS. Results show that BBGFL has good comparisons with MoM and HFSS on S-parameters, but BBGFL is several hundred times faster than direct MoM and HFSS in CPU. The substantial improvement in computational efficiency enables this technique for EDA solutions to EMI/EMC applications.

Chapter 4 Combining Broadband Green's Function with Low Wavenumber Extraction and Method of Moment for Fast Broadband Simulations of Scattering in Arbitrary Shaped Waveguides

4.1 Summary

In this chapter, we combine the broadband Green’s function with low wavenumber extraction (BBGFL) with MoM to study scattering problem in arbitrary shaped waveguide. The technique is applied to broadband modeling and simulation of the scattering by multiple vias in arbitrary shaped waveguide. The BBGFL is used to formulate surface integrals on the surfaces of the vias which are then solved with MoM. By using BBGFL instead of free space Green’s functions, we have a drastic reduction of the number of surface unknowns in the integral equations. Since the BBGFL utilize modal expansions that are frequency independent, the method is suitable for broadband simulations. The mixed boundary conditions with external PMC waveguide boundary conditions and internal PEC boundary conditions are studied in this chapter. Results are case of compared with the MoM method of free space Green’s function and that of HFSS. It is shown that the results are accurate and the BBGFL/MoM method is much faster than MoM and that of HFSS for broadband simulations.

4.2 Introduction

The effects of waveguide or cavity structures are critical for the electrical performance of electronic devices and components in terms of signal integrity (SI), power integrity (PI), electromagnetic interference (EMI), electromagnetic compatibility (EMC), and more [1] [34] [35] [22]. Harmful electromagnetic signal noises or interferences are usually generated and amplified at the resonant frequencies due to the waveguide or cavity structures in electronic devices. The issue deteriorates when the electronic devices or computer systems operate at higher frequency or faster speed, which have been the trend in industry.

In integrated circuit (IC) packages and printed circuited boards (PCBs), two adjacent power/ground planes form a waveguide/cavity structure [1] [34] [35] [22]. The propagating modes satisfy the PMC (Neumann boundary conditions) on the edges of package power/ground plane structures. These power/ground plane structures are the key root cause in many SI/PI and EMI/EMC problems. Vias are used for vertical interconnect for multilayer packages. Under the resonant frequencies of the power/ground plane pair, the propagating electromagnetic waves along vias may excite strong resonant modes, which can result in strong edge radiation and cause EMI/EMC problems; the switching noises induced by voltage regulator module (VRM) can generate voltage fluctuations and lead to PI problems; the high frequency power noise can also couple into signal vias and cause SI/PI coupling issues. Therefore, modeling of package cavity with vias is critical for EMI/EMC and SI/PI analysis in practical designs and applications of high speed microelectronic packaging. Fast and accurate modeling technique is desired for broadband simulations in package design and application.

Green's function has played an important role in various techniques used in modeling electronic devices and components [1] [35] [3] [4] [5] [6] [31] [30] [36] [37] [38] [15] [26] [32]. For example, boundary integral equation method with free space Green's function and MoM is used to model the power/ground planes in printed circuit boards (PCBs) [1] [35] [3] [4] [5] [6]. One key advantage of Green's functions is it can be used for compute the complex structures including waveguide/cavity, vias, and other components in PCB. But, the use of free space Green's function in formulating the integral equation needs separate computation for different frequencies points. If the free space Green's function is used, then there are large number of unknowns in the dense matrix equation at every frequency. This is a fundamental restriction of using MoM in broadband modeling and simulations.

In [31] [30] we presented the broadband Green's function with low frequency extraction (BBGFL) for the PMC case (Neumann boundary condition). In [36], we showed the application of BBGFL to fast modeling of the radiated emissions from printed circuit boards (PCBs), in particular the power bus structure for electromagnetic interference/compatibility (EMI/EMC). To accelerate convergence of the Green's function, two low frequency extractions are performed. The first low frequency extraction is done by integrating the modal expansion series of Green's function for the rectangular waveguide over small patches. In the second low frequency extraction, we calculate the final Green's function for arbitrarily shaped waveguide at a single low frequency using MoM. The singularity of the Green's function is extracted by such low frequency extraction.

In this chapter, we used the BBGFL to formulate surface integral equations which are then solved with MoM. We consider the multiple scattering of vias in the arbitrary shaped waveguide. Although the solution of the problem of BBGFL/MoM still need to solve the dense matrix equation at every frequency, however, there is a drastic reduction of surface unknowns compared with the usual MoM with free space Green's function.

Since the BBGFL utilize modal expansions that are frequency independent, the method is suitable for broadband simulations. Results are case of compared with the MoM method of free space Green's function and that of HFSS. It is shown that the results of combining BBGFL with MoM are accurate and the BBGFL/MoM method is much faster than MoM and that of HFSS for broadband simulations. The substantial improvement in computational efficiency enables the BBGFL for fast computer-aided design (CAD).

The chapter is organized as follows. In Section II, we present the methodology for the proposed method of BBGFL. In Section III, we combine BBGFL with MoM by using BBGFL to formulate the surface integral equations. In Section IV, we show the simulation results. In Section V, we make conclusions on this work.

4.3 Methodology

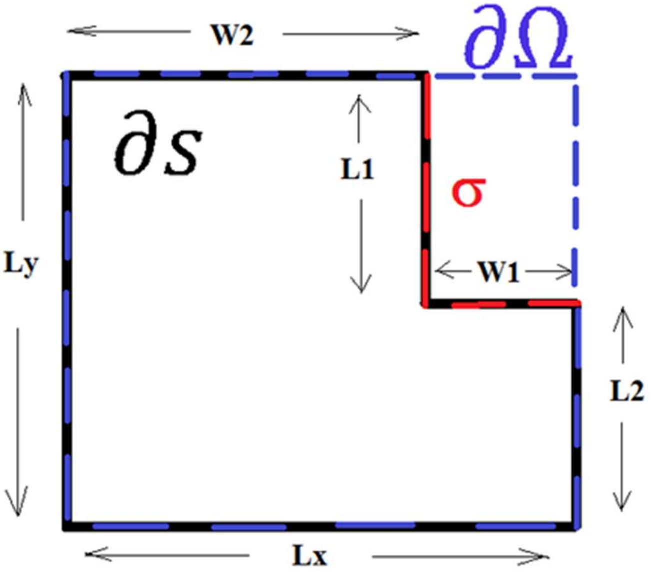

Figure 4.1 Arbitrary shaped waveguide with Neumann boundary condition

The thickness of PCB in electronic designs and applications is small. The power/ground planes can be modeled as TM mode in a cavity with PMC boundary conditions on the side walls. Consider an irregular shaped waveguide with Neumann boundary condition (PMC) as showed in Figure 1. The approach is illustrated for an L-shaped waveguide. The Green's functions along the boundary wall of the waveguide are calculated using the recent developed method

BBGFL [31]. The details of formulation are presented in [31]. In this section, we briefly summarize the key steps as follows.

4.3.1 Broadband Green's Function with Low Wavenumber Extraction for Calculation of Fields on Boundary Walls of Power/Ground Plane

Step 1: Constructing $g_H^{\Omega}(k,\bar{\rho},\bar{\rho}')$ with low wavenumber extraction be the boundary of the L-shaped waveguide

The boundary σ is the boundary ∂S that does not overlap with the rectangular boundary. Neumann boundary conditions hold for the boundary walls for TM modes with PMC walls. Let $\Psi_\alpha(\bar{\rho})$ be the modal functions of the rectangular waveguide with k_α the resonant wavenumber. Let $g_H^{\Omega}(k,\bar{\rho},\bar{\rho}')$ be the Green's function for the rectangular waveguide where subscript H stands for Neumann boundary condition. $g_H^{\Omega}(k,\bar{\rho},\bar{\rho}')$ can be expanded in model expansions of $\Psi_\alpha(\bar{\rho})$ and $\Psi_\alpha(\bar{\rho}')$. It is the sum of the free space Green's function g_0 and the response g_{HR}^{Ω}

$$g_H^{\Omega}(k,\bar{\rho},\bar{\rho}') = g_0(k,\bar{\rho},\bar{\rho}') + g_{HR}^{\Omega}(k,\bar{\rho},\bar{\rho}')$$

$$= g_0\left(k_L^{\Omega},\bar{\rho},\bar{\rho}'\right) + g_{HR}^{\Omega} + \sum_\alpha \frac{k^2-\left(k_L^{\Omega}\right)^2}{\left(k_\alpha^2-k^2\right)\left(k_\alpha^2-\left(k_L^{\Omega}\right)^2\right)} \psi_\alpha^{\Omega}(\bar{\rho})\psi_\alpha^{\Omega}(\bar{\rho}')\left(k_L^{\Omega},\bar{\rho},\bar{\rho}'\right) \qquad (1)$$

The convergence of the modal expansion of $g_H^{\Omega}(k,\bar{\rho},\bar{\rho}')$ at k is accelerated by using the result for a single low wavenumber $g_H^{\Omega}\left(k_L^{\Omega},\bar{\rho},\bar{\rho}'\right)$ where k_L^{Ω} is the low wavenumber.

Step 2: For the L-shaped waveguide, calculation of modal solution ψ^S and resonant wavenumber k_β^S

Using the Green's function from the rectangular waveguide, the modes of the

L-shaped waveguide are solved discretizing the boundary σ into N intervals, σ_n, $n = 1,2,\cdots,N$. The center point of the mth interval is at $\bar{\rho}_m$. The value of the eigenmode is $\psi_{Hn}^{\mathrm{S}} = q_n/\Delta t$ onσ_n.

The rectangular waveguide modal expansions are truncated at $\Psi_\alpha(\bar{\rho})$, $\alpha = 1,2,\cdots,M$. The result matrix equation for the eigenvalue problem is

$$\left(\bar{\bar{D}} - \bar{\bar{Q}}\bar{\bar{P}}^{-1}\bar{\bar{S}}\right)\bar{b} = \frac{1}{\left(k^2-\left(k_L^{\Omega}\right)^2\right)}\bar{b} \tag{2}$$

where k^2 are the modal wavenumber squared to be solved. The results$\left(k_\beta^{\mathrm{S}}\right)^2$, $\beta = 1,2,3\cdots\cdots$. where β is the mode index

In equation (1) $\bar{\bar{P}}$ and $\bar{\bar{S}}$ are $N \times N$ matrix and $N \times M$ matrices respectively and the elements are

$$P_{mn}$$

$$= \left(\frac{1}{2}\right)\frac{1}{\Delta t} + \frac{1}{\Delta t}\int_{\sigma_m} dl'\hat{n}_t' \cdot \nabla_t' g_{HR}\left(k_L^{\Omega}, \bar{\rho}_m, \bar{\rho}'\right) \qquad \text{for } n = m \tag{3.a}$$

$$= \frac{1}{\Delta t}\int_{\sigma_n} dl'\left[\hat{n}_t' \cdot \nabla_t' g_H^{\Omega}\left(k_L^{\Omega}, \bar{\rho}_n, \bar{\rho}'\right)\right]_{\bar{\rho}=\bar{\rho}_m} \qquad \text{for } n \neq m \tag{3.b}$$

$$S_{m\alpha} = \frac{1}{\left(k_\alpha^2-\left(k_L^{\Omega}\right)^2\right)}\Psi_\alpha(\bar{\rho}_m) \tag{4}$$

The matrix $\bar{\bar{Q}}$ is a $M \times N$ matrix and $\bar{\bar{D}}$ is a $M \times M$ diagonal matrix. The elements are

$$Q_{\alpha n} = \frac{\left[\hat{n}_t' \cdot \nabla_t' \Psi_\alpha(\bar{\rho}')\right]_{\bar{\rho}'=\bar{\rho}_n}}{k_\alpha^2-\left(k_L^{\Omega}\right)^2} \tag{5}$$

$$D_{\alpha\beta} = \frac{1}{k_\alpha^2-\left(k_L^{\Omega}\right)^2}\delta_{\alpha\beta} \tag{6}$$

After the eigenvalue and eigenvectors are solved, the modal wave functions on σ are calculated by q_n, $n = 1,2,\cdots,N$.

$$\bar{q} = -\bar{\bar{P}}^{-1}\bar{\bar{S}}\bar{b} \tag{7}$$

Then the modal functions are calculated by the integral over σ

$$-\psi_H^S(\bar{\rho}) = \int_\sigma dl' \left(\psi_H^S(\bar{\rho}')\hat{n}_t' \cdot \nabla_t' g_H^\Omega(k,\bar{\rho},\bar{\rho}')\right) \tag{8}$$

Step 3: Normalization of modes $\psi_\beta^S(\bar{\rho})$

The normalization of modes are such that

$$\sum_{\alpha=1}^{M}\left(b_{\alpha\beta}\right)^2 = \left(k_\beta^S\right)^4 \qquad \text{for } k_\beta^S \neq 0 \tag{9.a}$$

$$\psi_0^S(\bar{\rho}) = \frac{1}{\sqrt{A_S}} \qquad \text{for } k_\beta^S = 0 \tag{9.b}$$

where A_S= area of L-shaped waveguide.

Step 4: Construct broadband Green's function $g_H^{\mathrm{S}}(k,\bar{\rho},\bar{\rho}')$ with low wavenumber extraction of $g_H^{\mathrm{S}}\left(k_L^{\mathrm{S}},\bar{\rho},\bar{\rho}'\right)$

Using the modes of the L-shaped waveguide, $\psi_\beta^S(\bar{\rho})$, the Green's function $g_H^{\mathrm{S}}(k,\bar{\rho},\bar{\rho}')$ of the L-shaped waveguide can be expressed. However, the series expansion converges slowly. To accelerate the convergence, we use MoM to solve the Green's function $g_H^{\mathrm{S}}(k_L^S,\bar{\rho},\bar{\rho}')$ at a single wavenumber k_L^S which is separated into primary free space and response

$$g_H^{\mathrm{S}}(k_L^S,\bar{\rho},\bar{\rho}') = g_0(k_L^S,\bar{\rho},\bar{\rho}') + g_{HR}^{\mathrm{S}}(k_L^S,\bar{\rho},\bar{\rho}') \tag{10}$$

This is the one time MoM matrix inversion for the entire L shaped boundary. With the subtraction of $g_H^S(k_L^S, \bar{\rho}, \bar{\rho}')$, the Green's function for arbitrary waveguide k is

$$g_H^S(k, \bar{\rho}, \bar{\rho}') = g_0(k_L^S, \bar{\rho}, \bar{\rho}') + g_{HR}^S(k_L^S, \bar{\rho}, \bar{\rho}') + \sum_\beta \left[\frac{\left(k^2 - \left(k_L^S\right)^2\right) \psi_\beta^S(\bar{\rho}) \psi_\beta^S(\bar{\rho}')}{\left(\left(k_\beta^S\right)^2 - k^2\right)\left(\left(k_\beta^S\right)^2 - \left(k_L^S\right)^2\right)} \right] \tag{11}$$

Note that the dependence of the expression in (11) on frequency is merely the factor $\frac{\left(k^2 - \left(k_L^S\right)^2\right)}{\left(\left(k_\beta^S\right)^2 - k^2\right)}$ and the rest of the expression is independent of frequency. Hence we use the name of Broadband Green's function. Note that we use low wavenumber extraction, twice, with k_L^Ω for the rectangular waveguide and k_L^S for the waveguide with arbitrary shape. The advantages of the methodology of BBGFL are: (1) the modal functions $\psi_\beta^S(\bar{\rho})$ are independent of frequency so that they can be used for broadband simulations, (2) the accelerated convergence of Green's function modal expansion using low wavenumber extractions, (3) with the low wavenumber extraction, the singularity of the broadband Green's function is also extracted.

4.3.2 **Combine BBGFL and MoM**

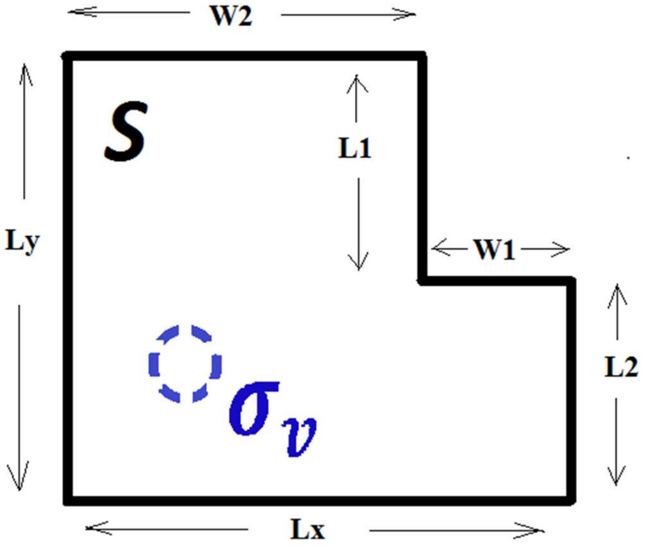

Figure 4.2 Mixed boundary conditions: external arbitrary shaped waveguide with Neumann boundary condition and internal vias with Dirichlet boundary conditions.

Next we formulate the surface integral equation with BBGFL. Rewrite (11) as (12)

$$g_H^{\mathrm{S}}(k,\bar{\rho},\bar{\rho}') = g_H^{\mathrm{S}}(k_L^S,\bar{\rho},\bar{\rho}') + \sum_\beta \left[\frac{\left(k^2-\left(k_L^{\mathrm{S}}\right)^2\right)\psi_\beta^S(\bar{\rho})\psi_\beta^S(\bar{\rho}')}{\left(\left(k_\beta^{\mathrm{S}}\right)^2-k^2\right)\left(\left(k_\beta^{\mathrm{S}}\right)^2-\left(k_L^{\mathrm{S}}\right)^2\right)}\right] \tag{11}$$

Note

$$\nabla^2 g_H^{\mathrm{S}}(k,\bar{\rho},\bar{\rho}') + k^2 g_H^{\mathrm{S}}(k,\bar{\rho},\bar{\rho}') = -\delta(\bar{\rho}-\bar{\rho}') \tag{12}$$

Boundary Condition for $\bar{\rho}$ on S is

$$\hat{n}\cdot\nabla g_H^{\mathrm{S}}(k,\bar{\rho},\bar{\rho}') = 0 \tag{13}$$

Physical Problem of via in L-shaped waveguide (Figure 2). Consider a point source at $\bar{\rho}_0$ in the L shaped cavity with a via centered at $\bar{\rho}_v$. Let σ_v be the surface of the via of radius a. Then the problem is to calculate the wave function ψ that obeys the wave equation with point source at $\bar{\rho}_0$

$$\nabla^2\psi + k^2\psi = -\delta(\bar{\rho} - \bar{\rho}_0) \tag{14}$$

$\hat{n}\cdot\nabla\psi = 0$ on $S, and\ \psi = 0$ on σ_v

Then consider Green's theorem taking over the inside of the cavity and outside the via. As shown in the figure 2

$$\iint_A dxdy\left[\psi\nabla_t^2 g_H^{\mathrm{S}} - g_H^{\mathrm{S}}\nabla_t^2\psi\right] = \int_S dl\left[\psi\hat{n}\cdot\nabla_t g_H^{\mathrm{S}} - g_H^{\mathrm{S}}\hat{n}\cdot\nabla_t\psi\right] - \int_{\sigma_v} dl\left[\psi\hat{n}\cdot\nabla_t g_H^{\mathrm{S}} - g_H^{\mathrm{S}}\hat{n}\cdot\nabla_t\psi\right] \tag{15}$$

Where $\hat{n}$ be the normal the via pointing out of the via and out of S

The integral over Svanishes because

$$\hat{n}\cdot\nabla\psi = 0 \tag{16.a}$$

$$\hat{n}\cdot\nabla_t g_H^{\mathrm{S}} = 0 \tag{16.b}$$

Thus

$$\iint_A dxdy\left[\psi\nabla_t^2 g_H^{\mathrm{S}} - g_H^{\mathrm{S}}\nabla_t^2\psi\right] = -\int_{\sigma_v} dl\left[\psi\hat{n}\cdot\nabla_t g_H^{\mathrm{S}} - g_H^{\mathrm{S}}\hat{n}\cdot\nabla_t\psi\right] \tag{17}$$

On $\sigma_v, \psi = 0$. Thus

$$\iint_A dxdy\left[\psi\nabla_t^2 g_H^{\mathrm{S}} - g_H^{\mathrm{S}}\nabla_t^2\psi\right] = \int_{\sigma_v} dl\left[g_H^{\mathrm{S}}\hat{n}\cdot\nabla_t\psi\right] \tag{18}$$

Thus substitution of the wave equation into the integral over A, and exchange $\bar{\rho} \leftrightarrow \bar{\rho}'$, we have, using also symmetry of $g_H^{\mathrm{S}}(\bar{\rho},\bar{\rho}')$,

$$-\psi(\bar{\rho}) + g_H^{\mathrm{S}}(\bar{\rho},\bar{\rho}_0) = \int_{\sigma_v} dl\left[g_H^{\mathrm{S}}(\bar{\rho},\bar{\rho}')\hat{n}\cdot\nabla_t\psi(\bar{\rho}')\right] \tag{19}$$

Next let $\bar{\rho} \rightarrow \sigma_v, \psi = 0$. Then

$$g_H^{\mathrm{S}}(\bar{\rho}, \bar{\rho}_0) = \int_{\sigma_v} dl' \left[g_H^{\mathrm{S}}(\bar{\rho}, \bar{\rho}') \hat{n}' \cdot \nabla_t' \psi(\bar{\rho}') \right] \tag{20}$$

This is the surface integral equation to calculate$\hat{n}' \cdot \nabla_t' \psi(\bar{\rho}')$. Let

$$\hat{n}' \cdot \nabla_t' \psi(\bar{\rho}') = J(\bar{\rho}') \tag{21}$$

$$g_H^{\mathrm{S}}(\bar{\rho}, \bar{\rho}_0) = \psi_{inc}(\bar{\rho}) \tag{22}$$

$$\int_{\sigma_v} dl' \left[g_H^{\mathrm{S}}(\bar{\rho}, \bar{\rho}') J(\bar{\rho}') \right] = \psi_{inc}(\bar{\rho}) \tag{23}$$

To solve the surface integral equation, we use pulse basis function and point matching

$$\sum_n Z_{mn} J_n = \psi_{inc,n} \tag{24}$$

For non self-patch, $n \neq m$

$$Z_{mn} = g_H^{\mathrm{S}}(\bar{\rho}_m, \bar{\rho}_n) \Delta t_n \tag{25}$$

For the self-patch, we examine the expressions in (10) and (11).

All three terms on the right hand side of the equation can be calculated. As noted in equation (10) $g_0(k_L^S, \bar{\rho}, \bar{\rho}') + g_{HR}^{\mathrm{S}}(k_L^S, \bar{\rho}, \bar{\rho}')$ are calculated by 1 time MoM at k_L^S and the two terms are kept separate. Second, the last term which is summation over modal solution is not singular even at$\bar{\rho} = \bar{\rho}'$ and can be calculated.

Define on the self-patch

$$C(\bar{\rho}) = g_{HR}^{\mathrm{S}}\left(k_L^S, \bar{\rho}, \bar{\rho} \quad\right) + \sum_\beta \left[\frac{\left(k^2 - \left(k_L^{\mathrm{S}}\right)^2\right) \psi_\beta^S(\bar{\rho}) \psi_\beta^S(\bar{\rho} \quad)}{\left(\left(k_\beta^{\mathrm{S}}\right)^2 - k^2\right)\left(\left(k_\beta^{\mathrm{S}}\right)^2 - \left(k_L^{\mathrm{S}}\right)^2\right)} \right] \tag{26}$$

Thus on the self-patch, we have approximately

$$g_H^{\mathrm{S}}(k,\bar{\rho},\bar{\rho}') \cong g_0(k_L^S,\bar{\rho},\bar{\rho}') + C(\bar{\rho}) \tag{27}$$

Then [13]-[15],

$$g_0\left(k_L^{\mathrm{S}},\bar{\rho},\bar{\rho}'\right) = \frac{1}{4j}\left[1 - j\frac{2}{\pi}\ln\left(\frac{\gamma k_L^S t'}{2}\right)\right] \tag{28}$$

Thus, for the self-patch, for $m = n$

$$Z_{mm} = \int_{-\frac{\Delta t_m}{2}}^{\frac{\Delta t_m}{2}} dt'\, g_H^{\mathrm{S}}(t_m,t')$$

$$= \int_{-\frac{\Delta t_m}{2}}^{\frac{\Delta t_m}{2}} dt'\left[g_0\left(k_L^{\mathrm{S}},\bar{\rho},\bar{\rho}'\right) + C(\bar{\rho})\right]$$

$$= -\frac{\Delta t_m}{2\pi}\left[-\frac{\pi}{2j} + \ln\left(\frac{\gamma k_L^S}{4e}\Delta t_m\right)\right] + C(\bar{\rho}_m)\Delta t_m \tag{29}$$

where $\gamma = 1.78107$ is Euler's number.

4.3.3 3D problem of multiple vias in the arbitrary waveguide

We next study the 3D problem of multiple vias in the L-shaped PCB power/ground plane.

We treat the TM modes with $k_{zl} = \frac{l\pi}{d}$, where $l = 0,1,2,3,\cdots$. In the problem of PCB power/ground plane pair, $kd \ll 1$. Thus modes with $l \neq 0$ are evanescent and will not propagate to the wall and have little reflection from the boundary walls.

For the $l = 0$ mode, we include the boundary effects of the L-shaped wall. We use BBGFL/MoM to calculate the results.

For the $l \geq 1$ modes, we use the Foldy Lax Equations [5] [6] [31] [30]. The final results of scattering matrices include all modes $l \geq 0$.

4.4 Simulations

In this section, we present the simulation results of proposed method compared with the cases of free space green functions and that of HFSS.

We model the scattering matrices for the problem of multiple vias in the L-shaped PCB/power ground plane for the broadband simulations. The dielectric thickness d between the two parallel plates is 20 and 30 mils. Thus $kd \ll 1$.

4.4.1 Comparison between BBGFL/MoM with MoM Using L=0 Mode Only

We first compare the results between BBGFL/MoM and MoM. We also compare the surface current on the vias calculated as a function of frequency between BBGFL/MoM with MoM.

4.4.1.1 Modeling of Two Signal Vias in a Rectangular Power/Ground Plane Pair with Small Cut Out

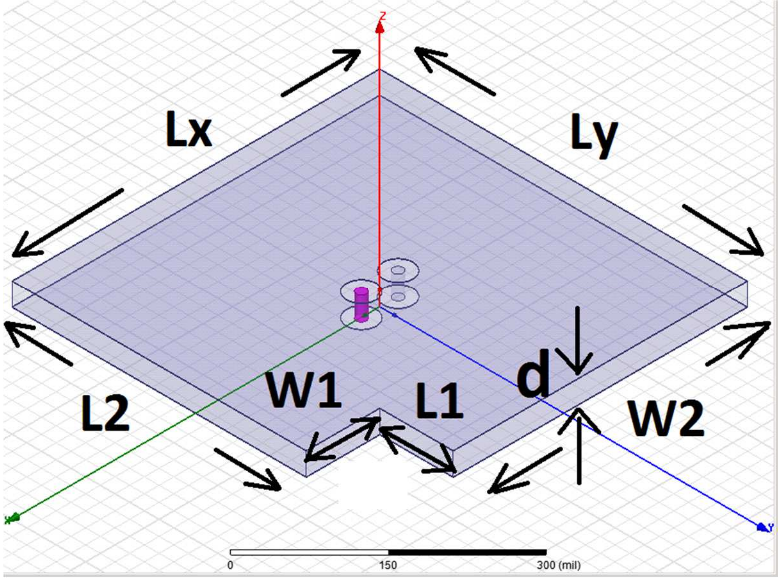

Figure 4.3 3D geometry of the L-shaped power/ground plane pair with small cut out and 2 vias.

Consider a power/ground plane pair with two signal vias as showed in Figure 4.3. Lx=Ly=500mils, L1=100mils, W1=100mils. The relative permittivity is complex and is set at$\varepsilon_r = 3.4(1 - j0.02)$. Via 1 and Via 2 are located at (-25, 0) mil and (25, 0) mil, respectively. Thickness d = 30mils. Using notations as in reference [2] [3] [4] [5] [6]. The via radius is a=6.75 mils, and the antipad radius is b= 20 mils.

In Figure 4.4, we compare the results of BBGFL/MoM and direct MoM for the surface currents on the Via 1 and Via 2. The red/black curves are the real/imaginary part of surface currents obtained by the method combining BBGFL and MoM with ℓ =0 mode respectively. The blue/green curves are the real/imaginary part of surface currents obtained by direct MoM with ℓ =0 mode respectively. Figure 4a show the currents on Via 1, and Figure 4b show the currents on Via 2. The excitation is on Via 1. The BBGFL/MoM and direct MoM have good agreement.

In Figure 4.5, we compare the results of the 4 methods for the s-parameters of insertion loss, return loss, near end crosstalk (NEXT), and far end crosstalk 1 (FEXT). The blue curves are results obtained by the hybrid method combining BBGFL and MoM with ℓ =0 mode. The green curves are results from direct MoM solution, with ℓ =0 mode. Direct MoM means solving, at every frequency, the surface integral equation of arbitrary ground plane and vias formulated with free space Green's function. The results of BBGFL/MoM (blue) are in good agreement direct MoM (green). It can be seen that two methods capture the resonance frequencies, which are caused by the reflections by the PMC walls of the finite power/ground plane.

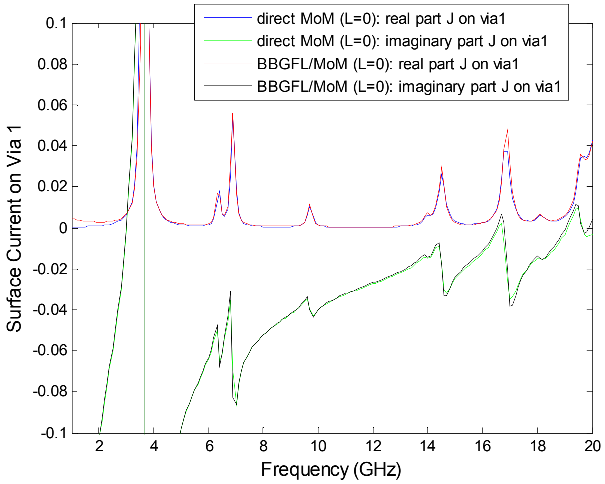

(a) Surface Currents on Via 1

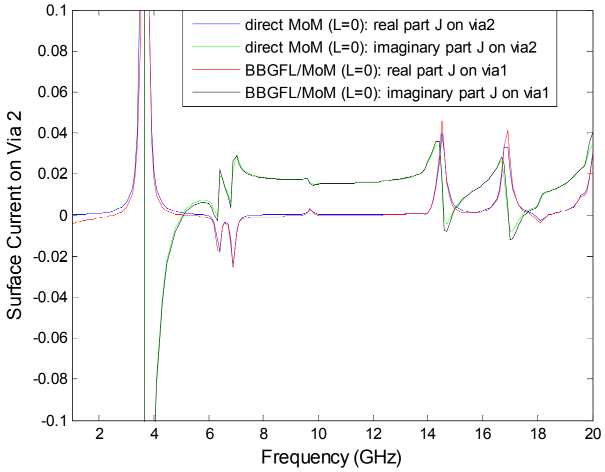

(b) Surface Currents on Via 2

Figure 4.4 Comparison of BBGFL/MoM and MoM for surface currents on vias from simulations with Figure 4.3: Red – real part of surface currents by BBGFL/MoM, Black – imaginary part of surface currents by BBGFL/MoM, Blue – real part of surface currents by direct MoM, Green – imaginary part of surface currents by direct MoM.

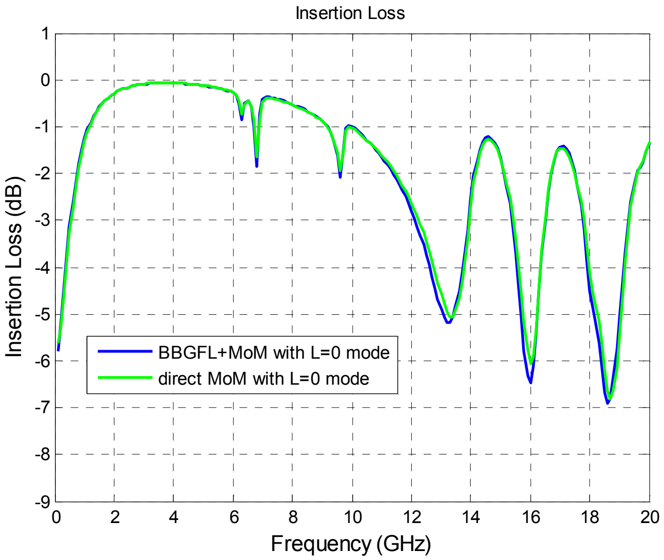

(a) Insertion Loss

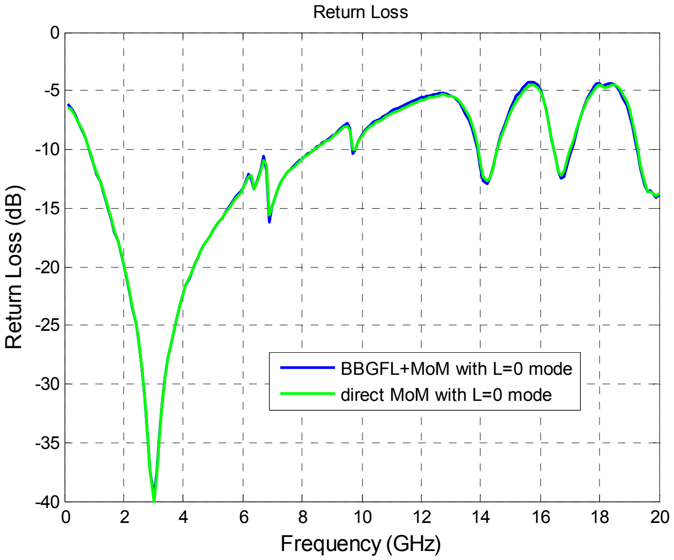

(b) Return Loss

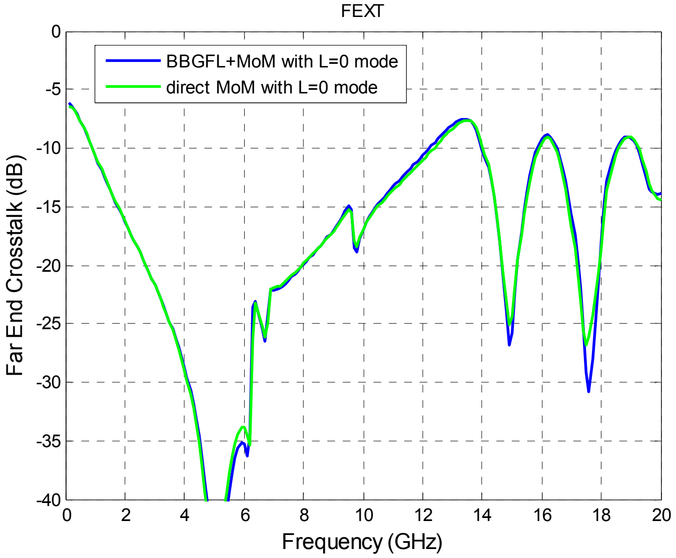

(c) Far End Crosstalk

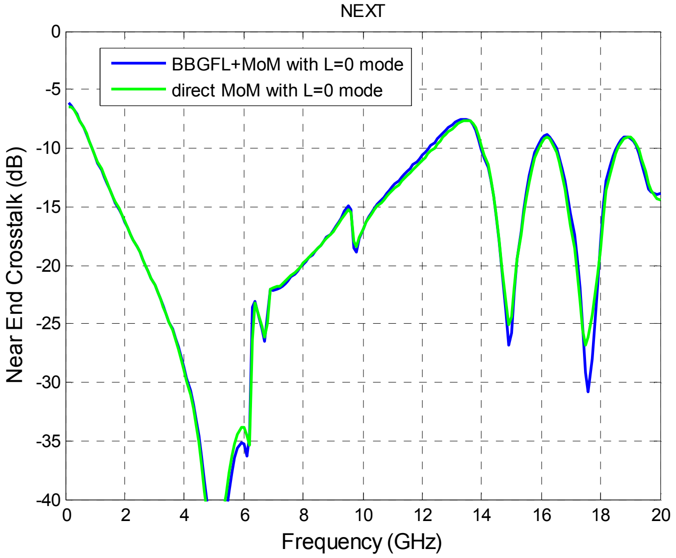

(d) Near End Crosstalk

Figure 4.5 Comparison of BBGFL and different methods for s-parameters from simulations with Figure 4.3: Blue – combine BBGFL and MoM with L=0 mode, Green – direct MoM with L=0 mode.

4.4.1.2 Modeling of Two Signal Vias and Two Shorting Vias in a Rectangular Power/Power (or Ground/Ground) Plane Pair with Large Cut Out

Consider a power/power or ground/ground plane pair with two signal vias and two shorting as shown in Figure 4.6. Lx=Ly=500mils, L1=200mils, W1=100mils. The relative permittivity $\varepsilon_r = 3.4(1 - j0.02)$. Thickness d=20mils. Via 1 and Via 2 are signal vias, and they are located at (-25, 0) mil and (25, 0) mil respectively. Two shorting vias are located at (0, -25) mil and (0, 25) mil, respectively. The via radius is 6.75 mils, and the antipad radius is 20 mils.

In Figure 4.7, we compare the results of BBGFL/MoM and direct MoM for the surface currents on the Via 1 and Via 2. The red/black curves are the real/imaginary part of surface currents obtained by the method combining BBGFL and MoM with ℓ =0 mode respectively. The blue/green curves are the real/imaginary part of surface currents obtained by direct MoM with ℓ =0 mode respectively. Figure 4.7a show the currents on Via 1, and Figure 4.7b show the currents on Via 2. The excitation is on Via 1. The BBGFL/MoM and direct MoM have good agreement.

In Figure 4.8, we compare the results of the 4 methods for the s-parameters of insertion loss, return loss, near end crosstalk (NEXT), and far end crosstalk (FEXT). The blue curves are results obtained by the hybrid method combining BBGFL and MoM with ℓ =0 mode. The green curves are results from direct MoM solution, with ℓ =0 mode. Direct MoM means solving, at every frequency, the surface integral equation of arbitrary ground plane and vias formulated with free space Green's function. The results of BBGFL/MoM (blue) are in good agreement direct MoM (green). It can be seen that two methods capture the resonance frequencies, which are caused by the reflections by the PMC walls of the finite power/ground plane.

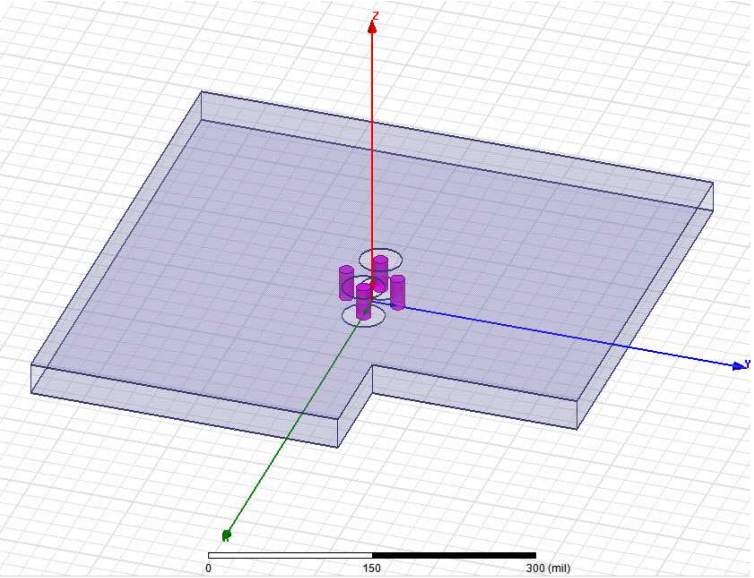

Figure 4.6 3D geometry of the simulation with 2 signal vias and 2 shorting vias in an irregular shaped plate pair with large cut out.

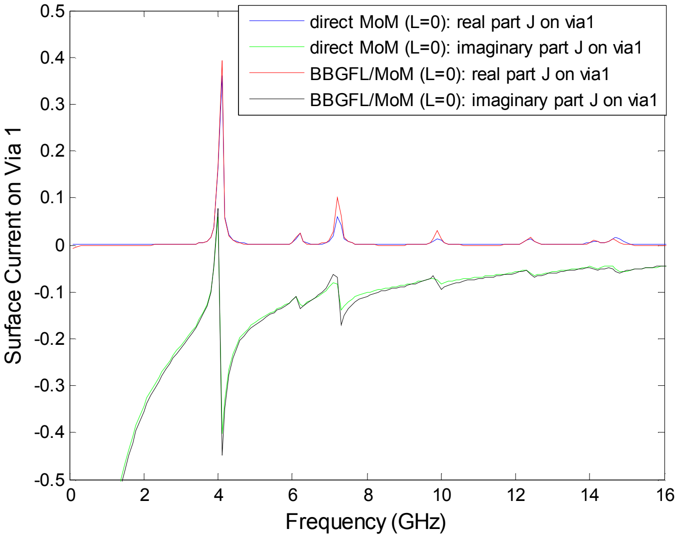

(a) Surface Currents on Via 1

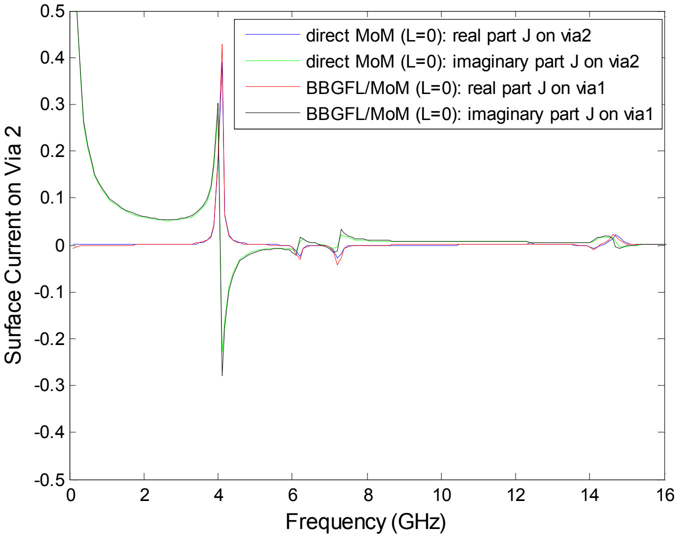

(b) Surface Currents on Via 2

Figure 4.7 Comparison of BBGFL/MoM and MoM for surface currents on vias from simulations with Figure 4.6: Red – real part of surface currents by BBGFL/MoM, Black – imaginary part of surface currents by BBGFL/MoM, Blue – real part of surface currents by direct MoM, Green – imaginary part of surface currents by direct MoM.

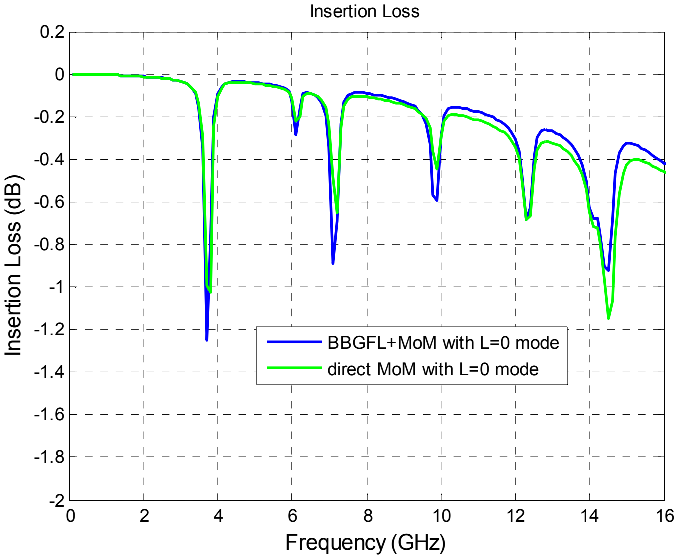

(a) Insertion Loss

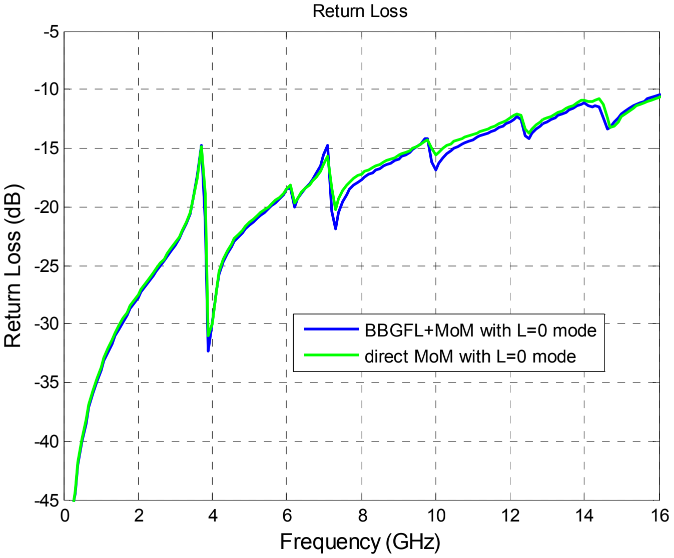

(b) Return Loss

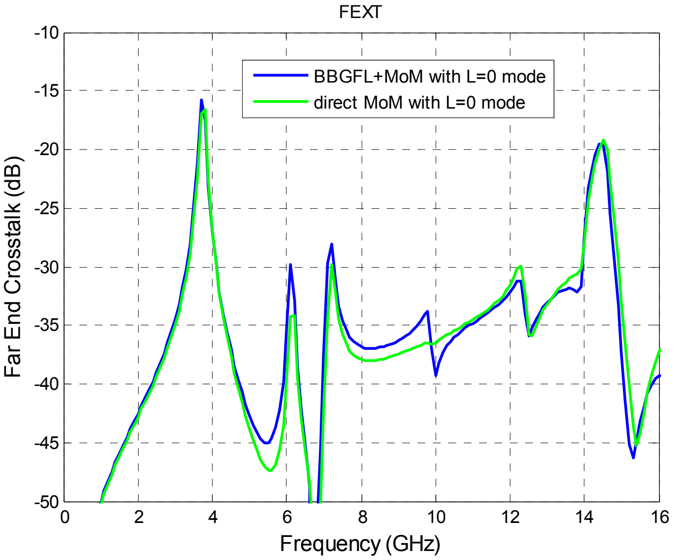

(c) Far End Crosstalk

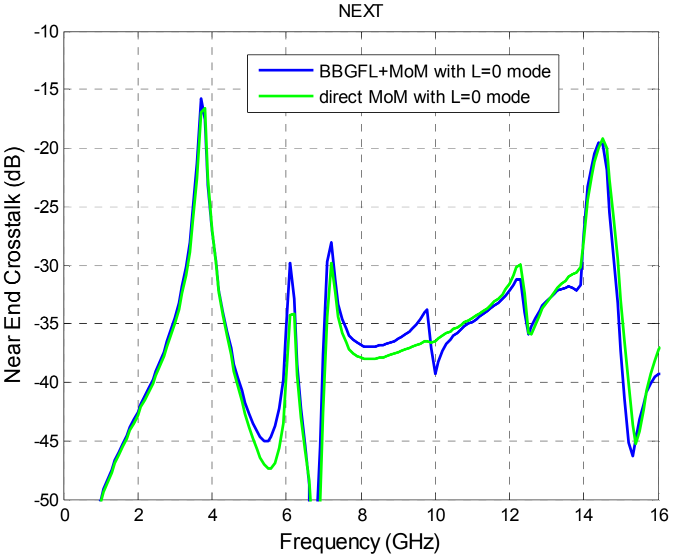

(d) Near End Crosstalk

Figure 4.8 Comparison of BBGFL and different methods for s-parameters from simulations with Figure 4.6: Blue – combine BBGFL and MoM with L=0 mode, Green – direct MoM with L=0 mode, Red - HFSS.

4.4.2 3D Problem of Multiple Vias in the Arbitrary Waveguide and Comparison with HFSS Including All $\ell \geq 0$ Modes

We next perform broadband simulations for the 3D problem of multiple vias in the L-shaped PCB power/ground plane and compare with HFSS.

4.4.2.1 Modeling of Two Signal Vias in a Rectangular Power/Ground Plane Pair with Large Cut Out

Consider a power/ground plane pair with two signal vias as showed in Figure 4.3. Lx=Ly=500mils, L1=100mils, W1=200mils. The relative permittivity is $\varepsilon_r = 3.4(1 - j0.02)$. Thickness d=30mils. Via 1 and Via 2 are located at (-25,

0) mil and (25, 0) mil, respectively. The via radius is 6.75 mils, and the antipad radius is 20 mils.

In Figure 4.9, BBGFL is compared with three different methods. The results of the s-parameters of insertion loss, return loss, near end crosstalk (NEXT), and far end crosstalk (FEXT) are shown. The blue curves are results obtained by the method combining BBGFL and MoM with ℓ =0 mode. The green curves are results from direct MoM solution, with ℓ =0 mode. The magenta curves are results by BBGFL/MoM with ℓ =0 mode and Foldy Lax with $\ell > 0$ modes. The black curves are results by direct MoM with ℓ =0 mode and Foldy Lax with $\ell > 0$ modes. The red curves are results from HFSS. The results of BBGFL/MoM (L=0) and Foldy Lax (L>0) (blue), direct MoM (L=0) and Foldy Lax (L>0) (black), and HFSS are in good agreement. It can be seen that all the methods capture the resonance frequencies, which are caused by the reflections by the PMC walls of the finite power/ground plane.

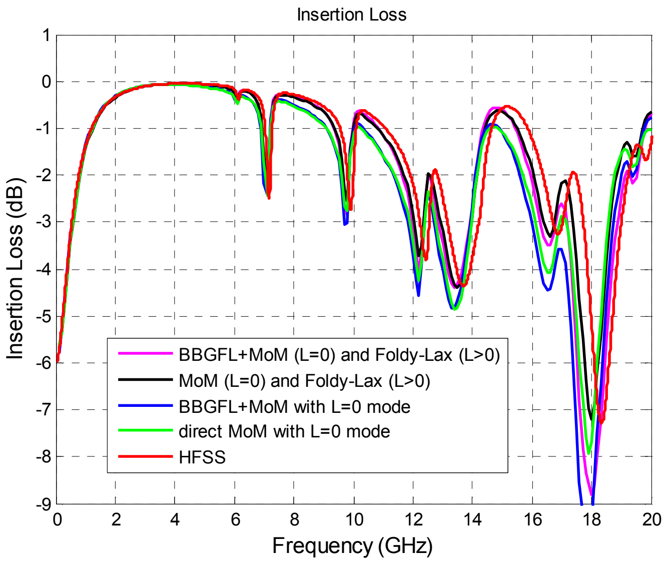

(a) Insertion Loss

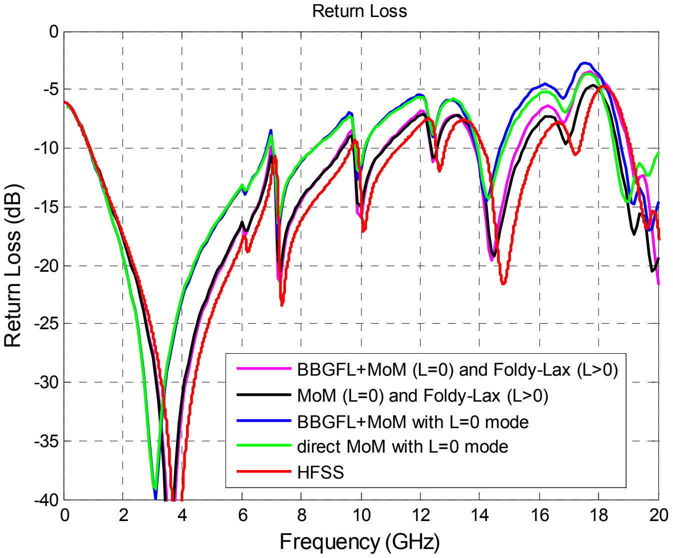

(b) Return Loss

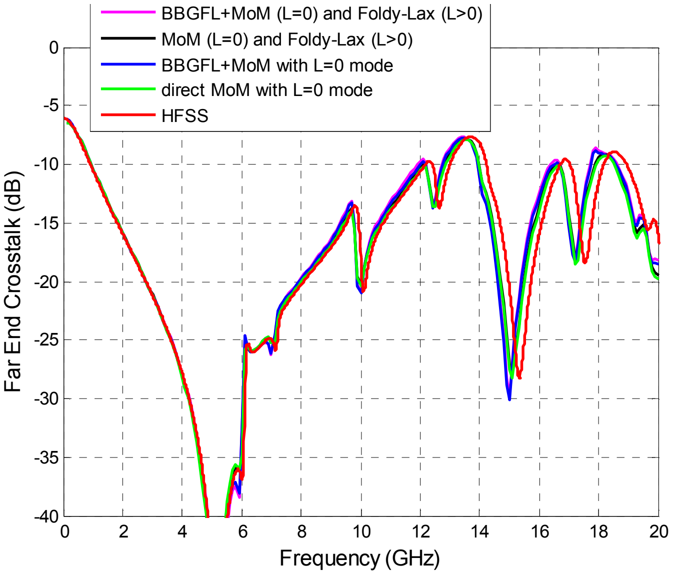

(c) Far End Crosstalk

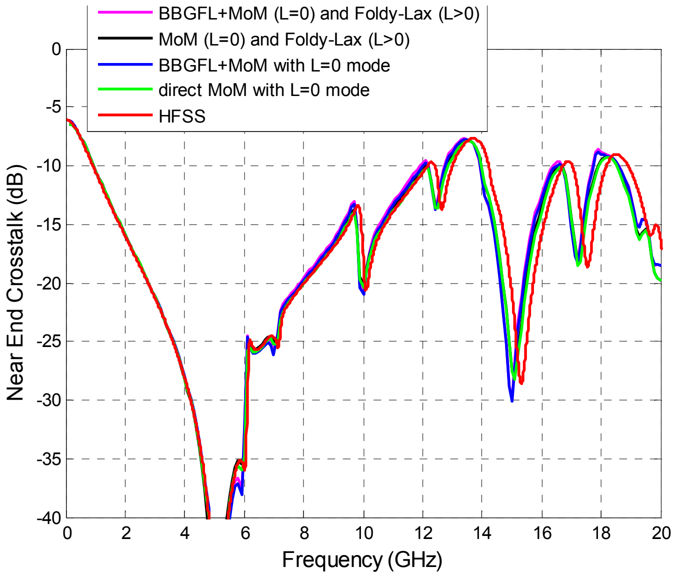

(d) Near End Crosstalk

Figure 4.9 Comparison of BBGFL and different methods for s-parameters: Blue – combine BBGFL and MoM with L=0 mode, Green – direct MoM with L=0 mode, Magenta – BBGFL/MoM with L=0 mode and Foldy Lax with L>0 modes, Black – direct MoM with L=0 mode and Foldy Lax with L>0 modes, Red - HFSS.

4.4.2.2 Modeling of 8 Vias: Four Signal Vias and Four Shorting Vias in a Rectangular Power/Power (or Ground/Ground) Plane Pair with Large Cut Out

Consider a power/power or ground/ground plane pair with 4 signal vias and 4 shorting as showed in Figure 10. Lx=Ly=500mils, L1=200mils, W1=100mils. The relative permittivity$\varepsilon_r = 3.4(1 - j0.02)$. Thickness d=20mils. Signal Vias 1, 2, 3 and 4 are located at (-25, 50), (25, 50), (-25, -50), and (25, 50) mils, respectively. Shorting vias are located at (0, 75), (0, 25), (0,-25), and (0,-75) mils, respectively. Two shorting vias are located at (0, -25) mil and (0, 25) mil, respectively. The via radius is 6.75 mils, and the antipad radius is 20 mils. The results are shown in Figure 4.11.

The results from the various methods are in good agreement.

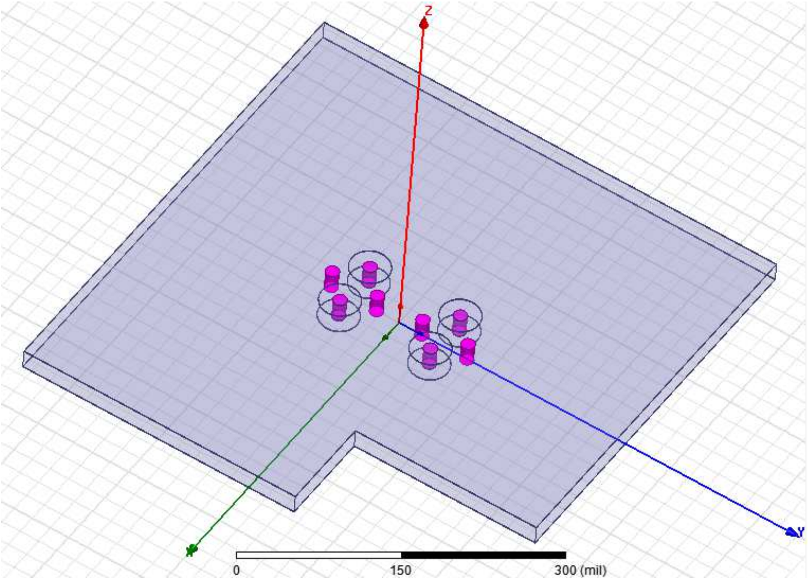

Figure 4.10 3D geometry of the simulation with 4 signal vias and 4 shorting vias in an irregular shaped plate pair with large cut out.

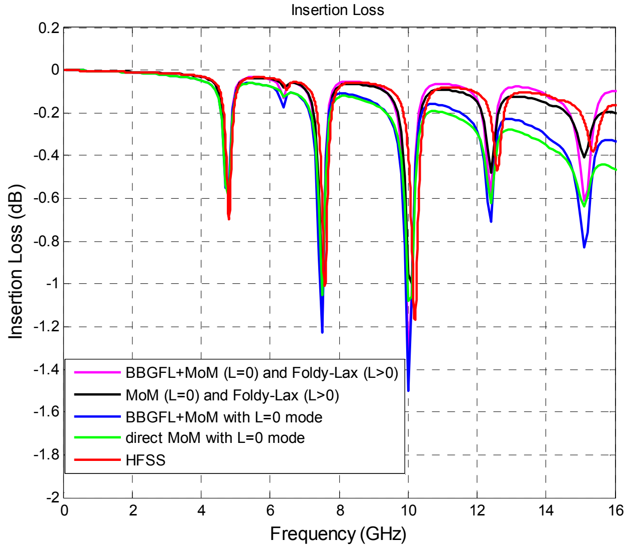

(a) Insertion Loss

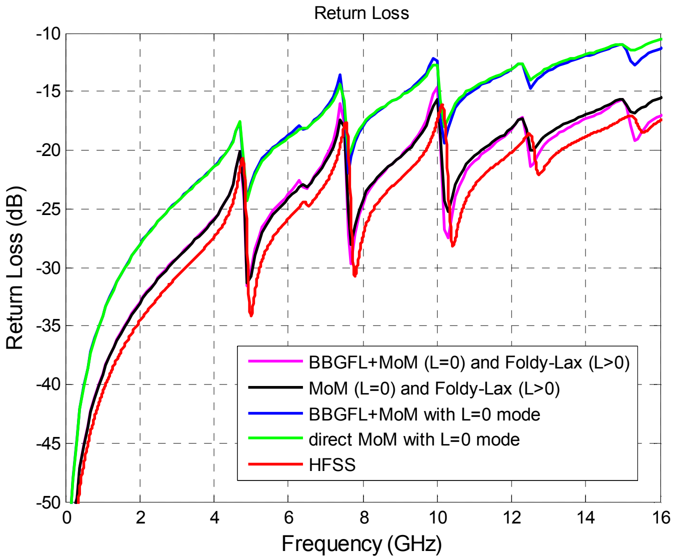

(b) Return Loss

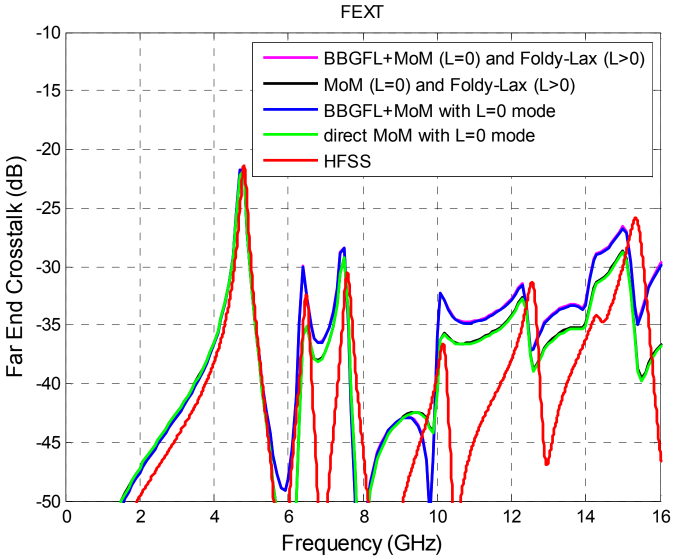

(c) Far End Crosstalk

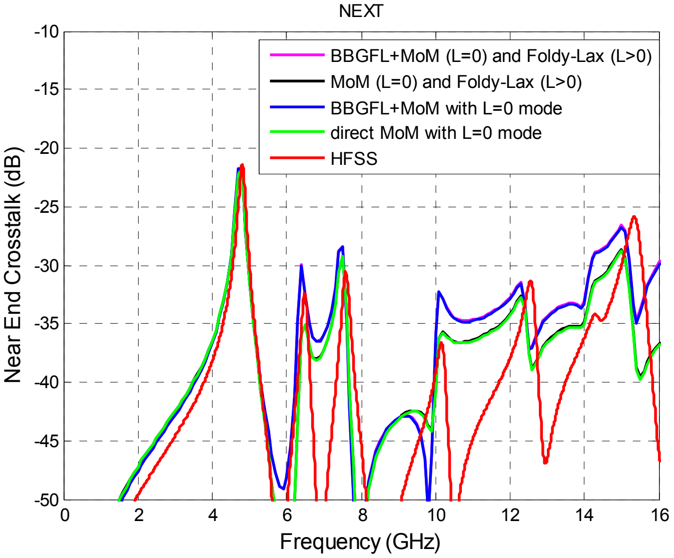

(d) Near End Crosstalk

Figure 4.11 Comparison of BBGFL and different methods for s-parameters from simulations with Figure 4.10: Blue – combine BBGFL and MoM with L=0 mode, Green – direct MoM with L=0 mode, Magenta – BBGFL/MoM with L=0 mode and Foldy Lax with L>0 modes, Black – direct MoM with L=0 mode and Foldy Lax with L>0 modes, Red - HFSS.

4.4.3 Comparison of CPU Time for Vias Simulations

In Table 4-1, we compare the CPU time used in the simulations of Figure 4. In the comparison, the input parameters are: the discretization spacing is 4 mils for both MoM and BBGFL, the BBGFL uses $M_o = 20$ for both kxm and kyn. For BBGFL, the CPU time consists three parts. The first part is for computation of eigenfunctions and values. The second part is for creating response Green's function with the computed eigenfunctions and values. The third part is solve internal vias problem using MoM with the response Green's function. We show the sum of the 3 parts. The CPU time of HFSS contains two parts. The first part is for simulation setup (CAD meshing, etc) which is done only once, and the second part is for FEM simulation which needs to be repeated for all frequency points. For the simulation of 1000 frequency points, BBGFL/MoM takes 4.7 seconds for first part, 2 seconds for the second part, and 25 seconds for the third part. For total CPU time used for 100 frequency points, the proposed method is 44 times faster than direct MoM, and is 76 times faster than HFSS. For total CPU time used for 1000 frequency points, the proposed method is 107 times faster than direct MoM, and is 176 times faster than HFSS. This shows that the BBGFL, combined with MoM, is much more efficient than direct MoM and HFSS for broadband simulations. It is to be noted that large number of frequency points are necessary for multiple resonances for the cavity.

Table 4-1 Comparison of CPU times using different methods: BBGFL/Foldy-Lax, direct MoM, and HFSS.

Methods	1 frequency point	10 frequency points	100 frequency points	1000 frequency points
BBGFL/MOM	4.7 + 0.002+0.025 =4.727 sec	4.7 + 0.002*10+0.025*10 =4.952 sec	4.7 + 0.002*100+0.025*100 =7.2 sec	4.7 + 0.002*1000+0.025*1000 =29.7 sec
Direct MoM	3.2 sec	3.2*10 =32 sec	3.2*100 =320 sec	3.2*1000 =3200 sec
HFSS	35+5.2 =40.2 sec	35+5.2*10 =87 sec	35+5.2*100 =555 sec	35+5.2*1000 =5235 sec

4.5 Conclusion

In this chapter, we combine BBGFL and MoM for fast full wave modeling and simulations of scattering in arbitrarily shaped waveguide. The method is applied to solve the problem of vias in side PCB power/ground plane waveguide. We compare the BBGFL/MoM technique with conventional direct MoM solution and HFSS. Results show BBGFL/MoM are in good agreement with direct MoM and

HFSS. Numerical experiments indicate that BBGFL/MoM is several hundred times faster than MoM and HFSS for fast electromagnetic modeling and simulations of vias in finite arbitrary power/ground plane.

Chapter 5 Broadband Green's Function with Low Frequency Extraction Method for Arbitrary Shaped Waveguides: TM case

5.1 Summery

In this chapter we extend the method of broadband Green's function with low frequency extraction (BBGFL) for the transverse magnetic (TM) case with Dirichlet boundary conditions. Small patch integrated Green's function is introduced to accelerate the convergence of modal expansion. The BBGFL is applied to fast modeling of Dirichlet boundary value problems, such as the boundary of an arbitrarily shaped conducting waveguide. The broadband Green's function consists of modal expansion of modes that are frequency independent. To accelerate convergence of the Green's function, two low frequency extractions are performed. The first low frequency extraction is done by integrating the Green's function over small patch, which has two advantages: (1) in many applications, the integrated Green's function defined at small patch is needed, not the point Green's function; (2) the convergence of integrated Green's function is one order faster than that of conventional point Green's function. In model expansion series, the terms for source are independent with the terms for observation. In addition, all the terms are frequency independent. Thus, the model expansion series terms are pre-computed once, and used for all points and all frequencies. The second low frequency extraction is performed by calculating the final Green's function for arbitrarily shaped waveguide at a single low frequency using MoM. The singularity of the Green's function is extracted by such low frequency extraction. These are readily computed once and used for all frequencies. Computation results are presented for TM case. Results show BBGLF and direct MoM are in good agreement. The substantial improvement in computational efficiency enables the BBGFL for fast computer-aided design (CAD) in applications of TM case.

5.2 Introduction

The effects of waveguide structures are critical for the electrical performance of electronic devices and components in wireless communication systems and digital electronic systems. In radio frequency (RF) and microwave circuits and components, the functional operation may rely on the resonant modes of the waveguide structures. Moreover, harmful electromagnetic signal noises or interferences are also usually generated and amplified at the resonant frequencies due to the waveguide structures in electronic devices. The issue deteriorates when the electronic devices or systems operate at higher frequency or faster speed, which have been the trend in industry.

In design and application of RF and microwave components and circuits, fast and accurate modeling technique is desired for broadband simulations. Various methods have been developed to calculate the resonant frequencies and modes of the waveguide structures with Dirichlet boundary condition. For example, analytical method is developed for rectangular structure [1] and boundary integral resonant mode method (BI-RME) [2] was developed for arbitrarily shaped waveguide structures. However, in practical electronic design and application, it usually needs to characterize not only the conducting waveguides, but also the structures within the waveguide boundary. 3D commercial tools such as HFSS provide solutions for accurate analysis the complex coupling problem. But, existing 3D full wave simulators need too much CPU times and memory, they may not be suited for fast broadband analysis.

Green's function has played a critical role in various techniques used in modeling electronic devices and components. For example, boundary integral equation method with free space Green's function is used to model the power/ground planes in printed circuit boards (PCBs) [3] [4] [5] [6] [31] [32] [30]. One key advantage of Green's functions is it can be used for compute the complex structures including waveguide/cavity, vias, and other components in PCB. But, conventional Green's function needs separate computation for different frequencies points. This is a fundamental restriction in broadband modeling and simulations. Hence, it is desired to develop fast techniques for computing the Green's function.

In [31] we presented the broadband Green's function with low frequency extraction (BBGFL) for TE case. In this chapter the broadband Green's function with low frequency extraction (BBGFL), is extended for the transverse magnetic (TM) case with Dirichlet boundary condition. It is applied to fast and accurate modeling of electronic devices and components with arbitrarily shaped conducting waveguide/cavity structures. Integrated Green's function defined at small patch is introduced to accelerate the convergence of modal expansion series. The broadband Green's function consists of modal expansion of modes that are frequency independent. To accelerate convergence of the Green's function, two low frequency extractions are performed. The first low frequency extraction is done by integrating the modal expansion series of Green's function for the rectangular waveguide over small patches. There are two motivations to introduce the integrated Green's function: (1) in many applications, the integrated Green's function defined at small patch is needed, not the point Green's function; (2) the convergence of integrated Green's function is one order faster than that of conventional point Green's function. In model expansion series, the terms of source are independent with those of observation. In addition, all the terms are frequency independent. Thus, the model expansion series terms are simply pre-computed once, and used for all points and all frequencies. In the second low frequency extraction, we calculate the final Green's function for arbitrarily shaped waveguide at a single low frequency using MoM. The singularity of the Green's function is extracted by such low frequency extraction. These are readily computed once and used for all frequencies. Computation results are presented for TM case. Results show BBGLF and direct MoM are in good agreement. The substantial improvement in computational efficiency enables the BBGFL for fast computer-aided design (CAD) in applications of TM case.

The major contributions of this chapter are: (1) to extend the BBGLF to TM case, (2) to propose the integrated Green's function defined at small patch.

The chapter is organized as follows. In Section II, we present the methodology for the proposed method. In Section III, we show the simulation results. In Section IV, we make conclusion on this work.

5.3 Methodology

In this section, we describe the theorem and derive the equations for the presented BBGFL technique.

5.3.1 Broadband Green's Function Based on Low Frequency Extraction

5.3.1.1 Green's Function Expressed Using Modal Expansion

Consider an arbitrary shaped waveguide in Figure 5.1, $g^s(\bar{\rho}, \bar{\rho}', k)$ refers the Green's Function for the waveguide, with observation point $\bar{\rho}$, source point $\bar{\rho}'$, and wavenumber k. Lx, Ly, L1, L2, W1, and W2 are the dimensions of its edges. Given a frequency f, the corresponding k can be computed $k = 2\pi f\sqrt{\varepsilon\mu}$, with ε

and μ are permittivity and permeability of the medium inside the waveguide. For transverse magnetic (TM) modes, $g^s(\bar{\rho}, \bar{\rho}', k)$ satisfies Dirichlet boundary condition.

Using eigenfunction expansion, $g^s(\bar{\rho}, \bar{\rho}', k)$ is written as

$$g^s(\bar{\rho}, \bar{\rho}', k) = \sum_\beta \frac{\psi_\beta^s(\bar{\rho})\psi_\beta^s(\bar{\rho}\prime)}{k_\beta^2 - k^2} \tag{5.1}$$

where $\psi_\beta^s(\bar{\rho})$ and k_β represent the modes and the resonant frequencies in physics. In mathematics, $\psi_\beta^s(\bar{\rho})$ and k_β correspond to the eigenfunction and the eigenvalue for the eigen problem of the waveguide.

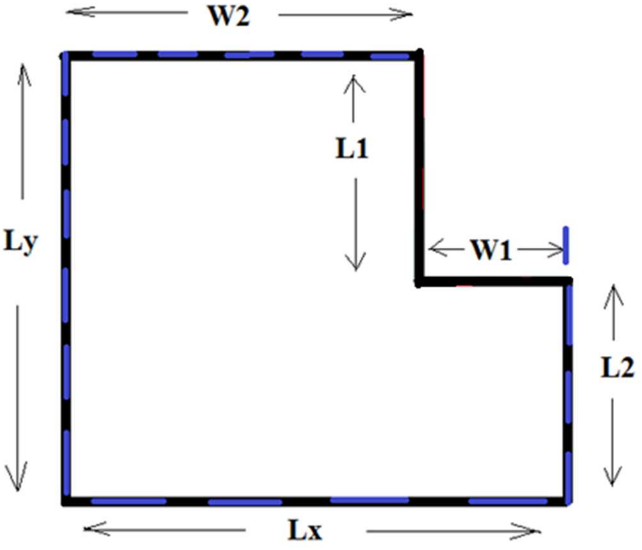

Figure 5.1 Cross-section of an arbitrary shaped waveguide

5.3.1.2 Concept of broadband Green's function

Direct calculation of $g^s(\bar{\rho}, \bar{\rho}', k)$ using conventional methods is time consuming. However, based on expression (1), if $\psi_\beta^s(\bar{\rho})$ and k_β^2 are known parameters, the Green's function can be calculated for the k at arbitrary frequency with negligible CPU resource. Hence, one can construct a broadband Green's function for arbitrary shaped waveguide problems through pre-computing $\psi_\beta^s(\bar{\rho})$ and k_β^2 of resonant modes. Once the $\psi_\beta^s(\bar{\rho})$ and k_β^2 are calculated out, the broadband Green's function can be used to fast derive results at all frequencies of interest.

$\psi_\beta^s(\bar{\rho})$ and k_β^2 can be computed using different methods, for examples, the BI-RME method [2], the finite element method (FEM) [39], method of moment (MoM) [37] [38] [15] [26]. In this chapter, we use BI-RME to find $\psi_\beta^s(\bar{\rho})$ and k_β^2. The broadband Green's Functions are constructed for TE and TM cases, respectively.

5.3.1.3 Low Frequency Extraction to Accelerate Convergence of Broadband Green's Function

The convergence of broadband Green's function in expression (5.1) is on second order of k_β, as $\mathrm{o}\left(k_\beta^2\right)$. Particularly, the convergence can be very slow around $\bar{\rho} = \bar{\rho}'$, where the singularity occurs in the Green's function. In this work, we present a method for accelerating the convergence by using low frequency extraction.

$$g^s(\bar{\rho},\bar{\rho}',k) = [g^s(\bar{\rho},\bar{\rho}',k) - g_L^s(\bar{\rho},\bar{\rho}',k_L)] + g_L^s(\bar{\rho},\bar{\rho}',k_L) \qquad (5.2)$$

where $g_L^s(\bar{\rho},\bar{\rho}',k_L)$ is the Green's function at a single low frequency f_L with $k_L = 2\pi f_L\sqrt{\varepsilon\mu}$. Then $g_L^s(\bar{\rho},\bar{\rho}',k_L)$ can be rewritten using modal expansion

$$g_L^s(\bar{\rho},\bar{\rho}',k_L) = \sum_\beta \frac{\psi_\beta^s(\bar{\rho})\psi_\beta^s(\bar{\rho}')}{k_\beta^2 - k_L^2} \qquad (5.3)$$

Substitute (5.1) and (5.3) into (5.2), yields

$$g^s(\bar{\rho},\bar{\rho}',k) = \sum_\beta \frac{\psi_\beta^s(\bar{\rho})\psi_\beta^s(\bar{\rho}\prime)(k^2-k_L^2)}{(k_\beta^2-k^2)(k_\beta^2-k_L^2)} + g_L^s(\bar{\rho},\bar{\rho}',k_L) \tag{5.4}$$

where $g_L^s(\bar{\rho},\bar{\rho}',k_L)$ can be solved using appropriate rigorous methods, e.g. MoM, for only one time, and then stored in core memory. Note, with $g_L^s(\bar{\rho},\bar{\rho}',k_L)$ in place, the convergence speed of $g^s(\bar{\rho},\bar{\rho}',k)$ increases from second order in (1) to fourth order of k_β, as $o(k_\beta^4)$. This further improves the overall computational efficiency of proposed BBGFL technique.

5.3.2 Broadband Green's Function of TM Case

Consider a waveguide with arbitrary shape, as showed in Figure 5.2. Let boundary ∂s (black curve) refers to the original waveguide, $\partial\Omega$ (blue curve) refers to the extended rectangular waveguide, and σ_o (red curve) refers to the cut out boundary. Hence, $\partial s = (\partial s - \sigma_v) + \sigma_v$, and $(\partial s - \sigma_v) \subset \partial\Omega$. The Green's function ψ_H^s of the original waveguide obey Helmholtz equation,

$$\nabla_{\mathrm{t}}^2\psi_E^s + k^2\psi_E^s = 0 \tag{5.5}$$

In TM case, ψ_E^s satisfy Dirichlet boundary condition $\psi_E^s(\bar{\rho}) = 0$ at boundary ∂s and σ_v. Let g_E^Ω refers to the Green's function for the rectangular waveguide, then g_E^Ω obeys Dirichlet boundary condition at $\partial\Omega$.

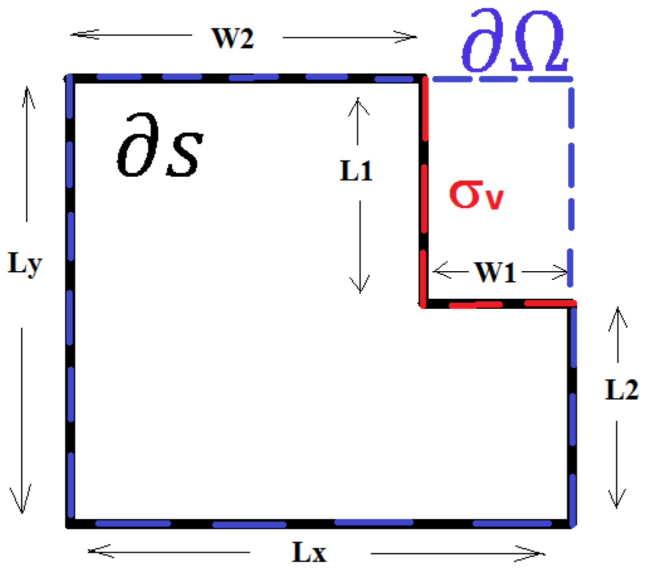

Figure 5.2 Arbitrary shaped waveguide with Dirichlet boundary condition

5.3.2.1 Integral Equation from Green's Theorem

Based on Green's theory,

$$\iint_A dxdy\left(\psi_E^s(\bar{\rho})\nabla_t^2 g_E^\Omega(\bar{\rho},\bar{\rho}') - g_E^\Omega(\bar{\rho},\bar{\rho}')\nabla_t^2\psi_E^s(\bar{\rho})\right)$$

$$= \int_{\partial s} dl\left(\psi_E^s(\bar{\rho})\hat{n}\cdot\nabla_{\mathrm{t}} g_E^\Omega(\bar{\rho},\bar{\rho}') - g_E^\Omega(\bar{\rho},\bar{\rho}')\hat{n}\cdot\nabla_{\mathrm{t}}\psi_E^s(\bar{\rho})\right) \tag{5.6}$$

with the Dirichlet boundary condition $\psi_E^s(\bar{\rho}) = 0$, we have the integral as

$$\int_{\sigma_v} dl'\left(g_E^\Omega(\bar{\rho},\bar{\rho}')J(\bar{\rho}')\right) = 0 \tag{5.7}$$

where $J(\bar{\rho}') = -\hat{n}'\cdot\nabla_{\mathrm{t}}'\psi_E^s(\bar{\rho}')$ are the unknown electric charge on the boundary σ_v. For rectangular waveguide, $g_H^\Omega(\bar{\rho},\bar{\rho}')$.

5.3.2.2 Broadband Green's Function for TM Case

The rectangular waveguide Green's function with Neumann boundary condition can be calculated out using hybrid modal analysis and MoM low frequency extraction

$$g_E^{\Omega}(k) = g_E^{\Omega\mathrm{L}}(k_L) + \sum_\alpha \frac{k^2-k_L^2}{(k_\alpha^2-k^2)(k_\alpha^2-k_L^2)} \Psi_\alpha(\bar{\rho})\Psi_\alpha(\bar{\rho}') \tag{5.8}$$

where index $\alpha = (m,n)$, $m',n' = 1,2,\cdots$. Eigenfunctions $\Psi_{m'n'}(\bar{\rho}) = \mathrm{A}_{\mathrm{m'n'}} \sin \mathrm{k}_{\mathrm{xm'}} \left(\mathrm{x}+\frac{\mathrm{a}}{2}\right) \sin \mathrm{k}_{\mathrm{yn'}} \left(\mathrm{y}+\frac{\mathrm{b}}{2}\right)$. Eigenvalues $\mathrm{k}_{\mathrm{m'n'}} = \sqrt{(\mathrm{k}_{\mathrm{xm'}})^2 + \left(\mathrm{k}_{\mathrm{yn'}}\right)^2}$, with $\mathrm{k}_{\mathrm{xm'}} = \frac{\mathrm{m'\pi}}{\mathrm{L_x}}$, $\mathrm{k}_{\mathrm{yn'}} = \frac{\mathrm{n'\pi}}{\mathrm{L_y}}$, $\mathrm{A}_{\mathrm{m'n'}} = \frac{2}{\sqrt{\mathrm{L_x L_y}}}$.

Let

$$a_\alpha = \frac{k^2-k_L^2}{k_\alpha^2-k^2} \int_{\sigma_v} dl' \, \Psi_\alpha(\bar{\rho}') J(\bar{\rho}') \tag{5.9}$$

Then,

$$\int_{\sigma_v} dl' \left(g_E^{\Omega\mathrm{L}}(\bar{\rho}_v, \bar{\rho}') \mathrm{J}(\bar{\rho}') \right) + \sum_\alpha a_\alpha \frac{\Psi_\alpha(\bar{\rho}_v)}{k_\alpha^2-k_L^2} = 0 \tag{5.10}$$

for $\bar{\rho}$ be on σ_v. Using pulse basis function, discretizing σ_o with spacing step Δt, and letting current $\psi_E^s(\bar{\rho}') = d_j/\Delta t$ with unknown coefficient d_j, lead to linear equations

$$\sum_\alpha a_\alpha R_{\alpha i} + \sum_j L_{ij}^{vv} c_j = 0 \tag{5.11}$$

With matrix elements

$$R_{i'\alpha} = \frac{\Psi_\alpha(\bar{\rho}_{i'})}{k_\alpha^2-k_L^2} \tag{5.12}$$

and

$$L_{ij}^{vv} = \frac{1}{\Delta t} \left[\int_{\sigma_{vj'}} dl' \left(g_v^{\Omega L}(\bar{\rho}_{oi}, \bar{\rho}'_{oj'}) \right) + \int_{\sigma_{vj'}} dl' \left(\hat{n}' \cdot \nabla' g_{ER}^{\Omega\mathrm{L}}(\bar{\rho}_{oi}, \bar{\rho}'_{oj'}) \right) \right] \tag{5.13}$$

First term is for contribution of free space Green's function $g_o^{\Omega L}$, and the second term is for that of response Green's function $g_{HR}^{\Omega \mathrm{L}}$ from rectangular waveguide boundary. Using pulse basis function and point matching [37], L_{ij}^{vv}, can be calculated

$$-\psi_E^s(\bar{\rho}_o) = \int_{\sigma_v} dl' \left(g_E^{\Omega \mathrm{L}}(\bar{\rho}_o, \bar{\rho}')\mathrm{J}(\bar{\rho}') \right) + \sum_\alpha a_\alpha \frac{\Psi_\alpha(\bar{\rho}_o)}{k_\alpha^2 - k_L^2} \tag{5.14}$$

From (4.1), one can derive the equation

$$D_\alpha a_\alpha + \sum_j U_{\alpha j}^v c_j = \frac{1}{k^2 - k_L^2} a_\alpha \tag{5.15}$$

with matrix elements

$$U_{\alpha j}^v = \frac{\Psi_\alpha(\,\bar{\rho}'_{vj})}{k_\alpha^2 - k_L^2} \tag{5.16}$$

$$D_\alpha = \frac{1}{k_\alpha^2 - k_L^2} \tag{5.17}$$

For the numerical computation, we can truncate the infinite summations. $m', n' = 1,2,\cdots, M_o$, and $\alpha = 1,2,\cdots, M_\alpha$, and $M_\alpha = (1 + M_o) \times (1 + M_o)$.

Combining the equations (5.11) and (5.15) yields

$$\left[[\bar{\bar{D}}] - [\bar{\bar{U}}^v][\bar{\bar{L}}^{vv}]^{-1}[\bar{\bar{R}}^v] \right] [\bar{a}] = \frac{1}{\tilde{k}^2} [\bar{a}] \tag{5.18}$$

with $\tilde{k}^2 = k^2 - k_L^2$. The eigen equation (5.18) can be solved for eigenvalues $\tilde{k}$ and the corresponding eigenvectors $\bar{b}$. Then, the original eigenvalues can be obtained using

$$k^2 = k_L^2 + \tilde{k}^2 \tag{5.19}$$

With k in place, the resonance frequencies f of the original waveguide ∂s can be calculated using $f = k/(2\pi\sqrt{\mu\varepsilon})$.

5.3.2.3 Normalization of Modes for TM Case

Let

$$\tilde{\psi}_E^s(\bar{\rho}) = \sum_\alpha a_\alpha \frac{\Psi_\alpha(\bar{\rho})}{k_\alpha^2 - k_L^2} \tag{5.20}$$

Substitute (5.20) into (5.14), and apply ∇^2 to both sides, yield

$$\nabla^2 \tilde{\psi}_E^s(\bar{\rho}) = -\nabla^2 \psi_E^s(\bar{\rho}) + k_L^2 \int_{\sigma_v} dl'\, g^{\Omega L}(\bar{\rho}, \bar{\rho}') \mathrm{J}(\bar{\rho}') \tag{5.21}$$

then

$$k_\beta^2 \psi_{E\beta}^s(\bar{\rho}) = \sum_\alpha a_\alpha \frac{k_\alpha^2 \Psi_\alpha(\bar{\rho})}{k_\alpha^2 - k_L^2} - k_L^2 [\bar{\xi}][\bar{\mathrm{c}}] \tag{5.22}$$

With

$$[\bar{\mathrm{c}}] = \left[\bar{\bar{L}}^{vv}\right]^{-1} \left[\bar{\bar{R}}^{v}\right][\bar{a}] \tag{5.23}$$

$$\xi_n = \int_{\sigma_{v,j}} dl'\, g^{\Omega L}(\bar{\rho}_j, \bar{\rho}') \tag{5.24}$$

Apply integral $\iint_\Omega dxdy$ on both sides of (5.22), with $\iint_\Omega dxdy \left(\psi_{E\beta}^s\right)^2 = 1$, yields the normalization condition

$$\frac{1}{k_\beta^4} \sum_\alpha \left(\frac{k_\alpha^2}{k_\alpha^2 - k_L^2}\right)^2 a_\alpha^2 + \frac{1}{k_\beta^4} L_x L_y \left(k_L^2 [\bar{\xi}][\bar{\mathrm{c}}]\right)^2 = 1 \tag{5.25}$$

For cases using low frequency extraction $k_L \ll k_\beta$, the normalization condition can be simplified to

$$\frac{1}{k_\beta^4}\sum_\alpha a_\alpha^2 = 1 \tag{5.26}$$

Given the eigenvectors from direct numerical solution are $\tilde{a}$, and they normalized to $\sum_\alpha \tilde{a}_{\alpha\beta}^2 = \mathrm{K}_\beta$, then $a_{\alpha\beta} = a_{\alpha\beta}\frac{k_\beta^2}{\sqrt{\mathrm{K}_\beta}}$, then the eigenfunctions can be computed

$$\psi_{E\beta}^s(\bar{\rho}) = -\sum_\alpha \tilde{a}_{\alpha\beta}\frac{1}{\sqrt{\mathrm{K}_\beta}}\frac{k_\alpha^2\Psi_\alpha(\bar{\rho})}{k_\alpha^2-k_L^2} + \frac{k_L^2}{k_\beta^2}\left[\bar{\xi}\right][\bar{\mathrm{c}}] \tag{5.27}$$

For case using DC extraction $k_L = 0$, we arrive at

$$\psi_{E\beta}^s(\bar{\rho}) = -\sum_\alpha \tilde{a}_{\alpha\beta}\frac{1}{\sqrt{\mathrm{K}_\beta}}\Psi_\alpha(\bar{\rho}) \tag{5.28}$$

Then, the final broadband Green's function for TM case can be computed using

$$g_E^s(\bar{\rho},\bar{\rho}') = \sum_\beta \frac{\psi_{E\beta}^s(\bar{\rho})\psi_{E\beta}^s(\bar{\rho}')}{k_\beta^2+k_L^2-k^2} \tag{5.29}$$

5.3.3 Integrated Green's Function for Rectangular Waveguide

5.3.3.1 Convergence of Point Green's Function for Rectangular Waveguide $\mathbf{g_E^s(k_L,\bar{\rho},\bar{\rho}')}$ for TM Case

Consider a rectangular waveguide with Dirichlet boundary condition showed in Figure 5.4. The conventional point Green's function for rectangular waveguide can be written in modal expansion series as

$$g_E^\Omega(k_L,\bar{\rho},\bar{\rho}') = \sum_{m=1}^\infty\sum_{n=1}^\infty \frac{A_{mn}A_{mn}}{(k_{mn})^2-(k_L)^2}\sin\frac{m\pi}{L_x}\left(x+\frac{L_x}{2}\right)$$

$$\sin\frac{n\pi}{L_y}\left(y+\frac{L_y}{2}\right)\sin\frac{m\pi}{L_x}\left(x'+\frac{L_x}{2}\right)\sin\frac{n\pi}{L_y}\left(y'+\frac{L_y}{2}\right) \tag{5.30}$$

As $(m,n)\to\infty$, then

$$\frac{A_{mn}A_{mn}}{(k_{mn})^2-(k_L)^2} \to \frac{1}{(k_{mn})^2} = \frac{1}{\left(\frac{m\pi}{L_x}\right)^2+\left(\frac{n\pi}{L_y}\right)^2} \tag{5.31}$$

Thus, the series (30) slowly converges when $\bar{\rho} \neq \bar{\rho}'$. How many terms depend on how close $\bar{\rho}$ is close to $\bar{\rho}'$. But it have no convergence when $\bar{\rho} = \bar{\rho}$. Since $g_E^\Omega(k_L, \bar{\rho}, \bar{\rho}') = g_0(k_L, \bar{\rho}, \bar{\rho}') + g_{ER}^\Omega(k_L, \bar{\rho}, \bar{\rho}')$, the free space Green's function $g_0(k_L, \bar{\rho}, \bar{\rho}')$ and response Green's function $g_{ER}^\Omega(k_L, \bar{\rho}, \bar{\rho}')$. Note, $g_0(k_L, \bar{\rho}, \bar{\rho}) = \ln \infty$, which is not that "bad" because $\log \infty$ is a small ∞.

5.3.3.2 Small Patch Integrated Green's Function for Rectangular Waveguide $\int_{\sigma_{oj'}} \mathbf{dl}' \, \mathbf{g}_\mathbf{E}^\Omega(\mathbf{k_L}, \bar{\boldsymbol{\rho}}, \bar{\boldsymbol{\rho}}')$ for TM Case

Apply integrate $\int_{\sigma_{oj'}} dl'$ to (30), yield

$$\int_{\sigma_{oj'}} dl' \, g_E^\Omega(k_L, \bar{\rho}, \bar{\rho}') = \sum_{m=1}^{\infty} \sum_{n=1}^{\infty} \frac{A_{mn} A_{mn}}{(k_{mn})^2 - (k_L)^2} \sin \frac{m\pi}{L_x}\left(x + \frac{L_x}{2}\right) \sin \frac{n\pi}{L_y}\left(y + \frac{L_y}{2}\right)$$

$$\int_{\sigma_{oj'}} dl' \left(\sin \frac{m\pi}{L_x}\left(x' + \frac{L_x}{2}\right) \sin \frac{n\pi}{L_y}\left(y' + \frac{L_y}{2}\right) \right) \tag{5.32}$$

Since $dl = \tau_x dx + \tau_y dy$, the integrand

$$\int_{\sigma_{oj'}} dl' \left(\sin \frac{m\pi}{L_x}\left(x' + \frac{L_x}{2}\right) \sin \frac{n\pi}{L_y}\left(y' + \frac{L_y}{2}\right) \right)$$

$$= -\sin \frac{n\pi}{L_y}\left(y' + \frac{L_y}{2}\right) \frac{\tau_{x'}}{\frac{m\pi}{L_x}} \int_{\sigma_{oj'}} d\left(\cos \frac{m\pi}{L_x}\left(x' + \frac{L_x}{2}\right) \right)$$

$$- \sin \frac{m\pi}{L_x}\left(x' + \frac{L_x}{2}\right) \frac{\tau_{y'}}{\frac{n\pi}{L_y}} \int_{\sigma_{oj'}} d\left(\cos \frac{n\pi}{L_y}\left(y' + \frac{L_y}{2}\right) \right) \tag{5.33}$$

As the small patch $\sigma_{oj'} \to 0$, $\Delta x' = |x_2' - x_1'| \to 0$, and $\Delta y' = |y_2' - y_1'| \to 0$, then

the integrand

$$\int_{\sigma_{oj'}} dl' \left(\sin\frac{m\pi}{L_x}\left(x' + \frac{L_x}{2}\right)\sin\frac{n\pi}{L_y}\left(y' + \frac{L_y}{2}\right)\right)$$

$$= \sin\frac{n\pi}{L_y}\left(y' + \frac{L_y}{2}\right)\frac{\tau_{x'}}{\frac{m\pi}{L_x}} 2\sin\frac{m\pi}{L_x}\left(x' + \frac{L_x}{2}\right)\sin\frac{m\pi}{L_x}\left(\frac{\Delta x'}{2}\right)$$

$$+ \sin\frac{m\pi}{L_x}\left(x' + \frac{L_x}{2}\right)\frac{\tau_{y'}}{\frac{n\pi}{L_y}} 2\sin\frac{n\pi}{L_y}\left(y' + \frac{L_y}{2}\right)\sin\frac{n\pi}{L_y}\left(\frac{\Delta y'}{2}\right) \qquad (5.34)$$

Then the integrated Green's function

$$\int_{\sigma_{oj'}} dl'\, g_E^{\Omega}(k_L, \bar{\rho}, \bar{\rho}')$$

$$= \sum_{m=1}^{\infty}\sum_{n=1}^{\infty} 2\frac{A_{mn}A_{mn}}{(k_{mn})^2 - (k_L)^2}\left[\frac{\tau_{x'}\sin\frac{m\pi}{L_x}\left(\frac{\Delta x'}{2}\right)}{\frac{m\pi}{L_x}} + \frac{\tau_{y'}\sin\frac{n\pi}{L_y}\left(\frac{\Delta y'}{2}\right)}{\frac{n\pi}{L_y}}\right]$$

$$\sin\frac{m\pi}{L_x}\left(x + \frac{L_x}{2}\right)\sin\frac{n\pi}{L_y}\left(y + \frac{L_y}{2}\right)\ \sin\frac{m\pi}{L_x}\left(x' + \frac{L_x}{2}\right)\sin\frac{n\pi}{L_y}\left(y' + \frac{L_y}{2}\right) \qquad (5.35)$$

As $(m, n) \to \infty$, then

$$\frac{A_{mn}A_{mn}}{(k_{mn})^2 - (k_L)^2}\left[\frac{\tau_{x'}\sin\frac{m\pi}{L_x}\left(\frac{\Delta x'}{2}\right)}{\frac{m\pi}{L_x}} + \frac{\tau_{y'}\sin\frac{n\pi}{L_y}\left(\frac{\Delta y'}{2}\right)}{\frac{n\pi}{L_y}}\right] \to \frac{1}{\left(\frac{m\pi}{L_x}\right)^2 + \left(\frac{n\pi}{L_y}\right)^2}\left[\frac{1}{\frac{m\pi}{L_x}} + \frac{1}{\frac{n\pi}{L_y}}\right] \qquad (5.36)$$

Hence, the series (34) fast converges when $\bar{\rho} \neq \bar{\rho}'$. And slowly but still converges when $\bar{\rho} = \bar{\rho}'$. Overall, patch integrated Green's function (5.36) is one order faster than point Green's function (5.30) on convergence.

With pre-computed $\int_{\sigma_{oj'}} dl'\, g_E^{\Omega}(k_L, \bar{\rho}, \bar{\rho}')$ in place, the point Green's function $g_E^{\Omega}(k_L, \bar{\rho}, \bar{\rho}')$ can be calculated from small patch integrated Green's function using

$$g_E^{\Omega}(k_L,\bar{\rho},\bar{\rho}') = \frac{\int_{\sigma_{oj'}} dl' g_E^{\Omega}(k_L,\bar{\rho},\bar{\rho}')}{\Delta l} \tag{5.37}$$

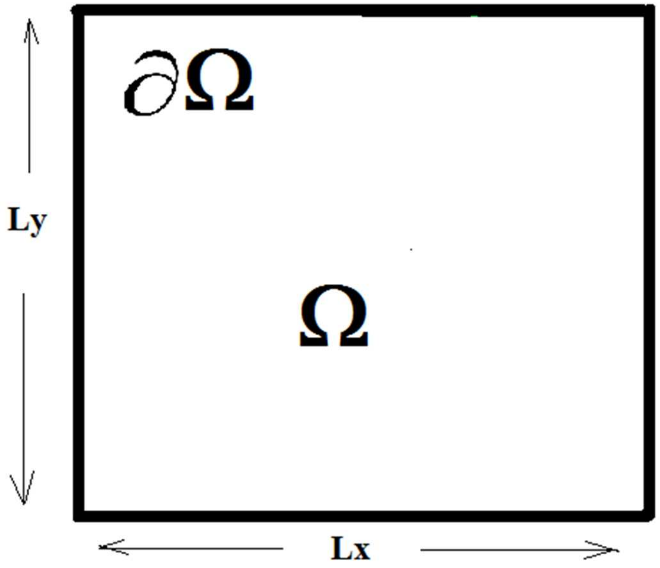

Figure 5.3 Rectangular waveguide with Dirichlet boundary condition

5.4 Simulations

In this section, we present the simulation results of green functions computed for TM case.

5.4.1 Green's Functions for Rectangular Waveguide

In Figure 5.4 (a)-(d), we compare direct integrated Green's function and MoM for point Green's function at different frequencies. Rectangular waveguide with width and length both = 500mils. Relative permittivity inside the waveguide is $\varepsilon_r = 4.4$. In calculating the broadband Green's function, the source point is located at (25mils, 20mils), and the observation points are located at y=20mils, x=[-245mils, 245mils]. Both MoM and BBGFL use same discretization step of 2mils in the simulation. MoM and BBGFL are in good agreement. Red curves are obtained using small patch integrated Green's function with 100 modes; blue are obtained using small patch integrated Green's function with 300 modes; green are obtained using small patch integrated Green's function with 500 modes; black are obtained using MoM. The results show integrated Green's function has good convergence.

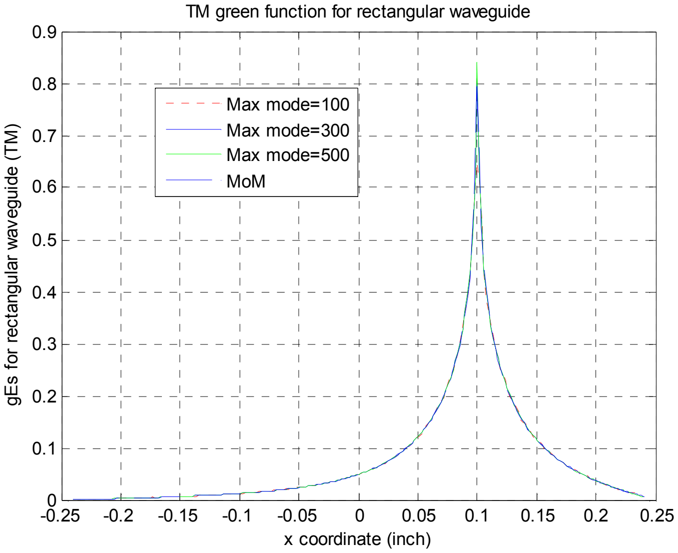

(a) TE g_E^{Ω} at 0.5GHz

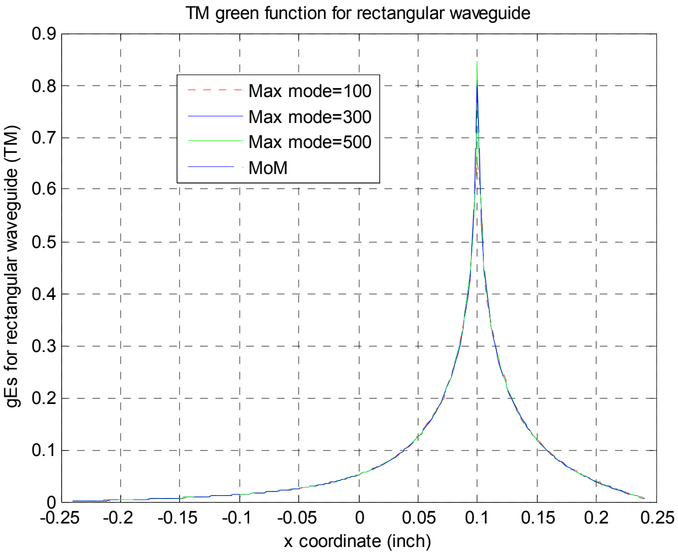

(b) TE g_E^{Ω} at 5 GHz

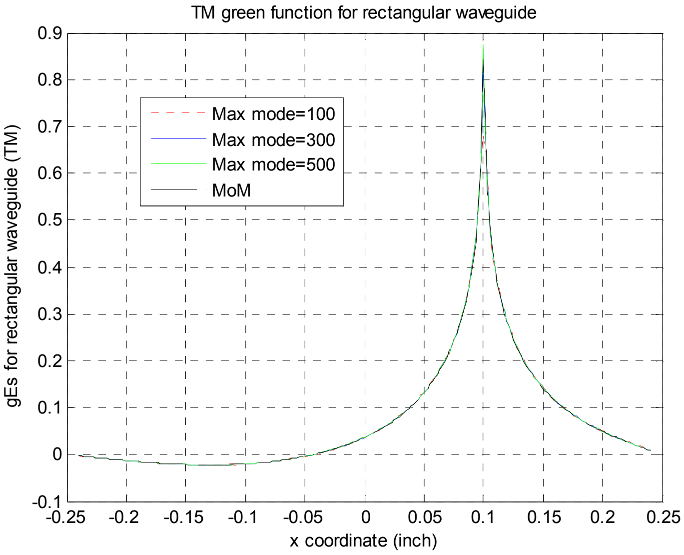

(c) TE g_E^{Ω} at 20 GHz

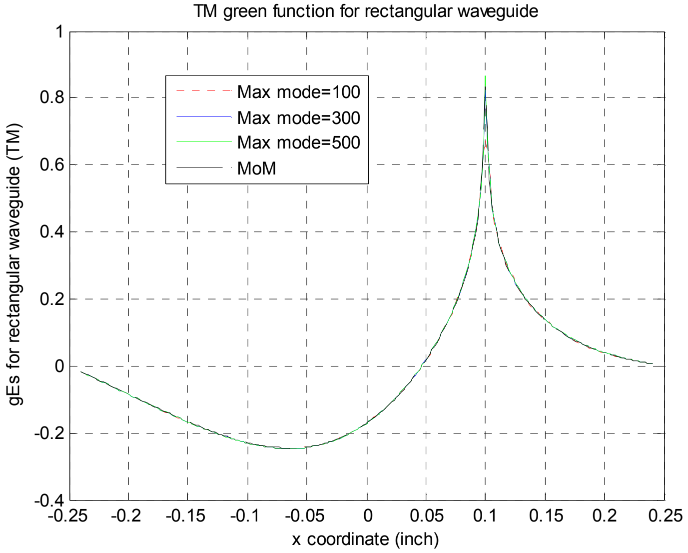

(d) TE gHs at 40GHz

Figure 5.4 Point Green's function of rectangular waveguide. Red – computed using small patch integrated Green's function with 100 modes; blue – computed using small patch integrated Green's function with 300 modes; green – computed using small patch integrated Green's function with 500 modes; black – computed using MoM.

5.4.2 Computation of Green's Functions for L-shape Waveguide

The arbitrary shaped waveguide in Figure 5.2 is used for simulations. The dimension parameters are: Lx=Ly=500mils, L1=250mils, and W1=100mils. Relative permittivity inside the waveguide is $\varepsilon_r = 4.4$. In calculating the broadband Green's function, the source point is located at (25mils, 20mils), and the observation points are located at y=20mils, x=[-245mils, 245mils]. Both MoM and BBGFL use same discretization step of 2mils in the simulation.

5.4.2.1 Resonant Frequency Comparison for L-shape Waveguide

In Table 5.1, we compare the direct MoM and BBGFL for resonant frequencies of TM case. The first 10 physical modes are compared. MoM and BBGFL are in good agreement. There is no nonphysical mode in the BBGFL results of first 10 modes. BBGFL may have nonphysical modes in higher order solutions. However, the nonphysical modes can be identified and removed for TM case, based on the criteria that eigenfunction is zero outside the original solution boundary.

Table 5-1 Compare resonant frequencies of MoM and Broadband Green for TM case

MoM Mode Number	MoM Resonant Frequency (GHz)	BBGFL Mode Number	BBGFL Resonant Frequency (GHz)
1	8.73	1	8.716
2	12.83	2	12.814
3	14.29	3	14.273
4	16.87	4	16.860
5	18.22	5	18.203
6	19.58	6	19.564
7	21.49	7	21.466
8	22.60	8	22.583
9	23.46	9	23.441
10	24.73	10	24.714

5.4.2.2 Eigenfunction Comparison for TM Case

In Figure 5.5 (a)-(m), we compare direct MoM and BBGFL for resonant modes (eigenfunctions) of TM case at different frequencies. The eigenfunctions from MoM are normalized to the same scale as BBGFL. Results show BBGFL has good agreement with MoM. Note, the imaginary parts of eigenfunctions should be zero, since $\varepsilon_r = 4.4$ is real in the simulation. MoM solution has non-zero imaginary parts, which are due to the Hankel function used in direct MoM solution. The BBGFL gives more accurate results, except there are nonphysical modes. The nonphysical modes can be identified and removed for TM case, by the criteria that eigenfunction is zero outside the original solution boundary.

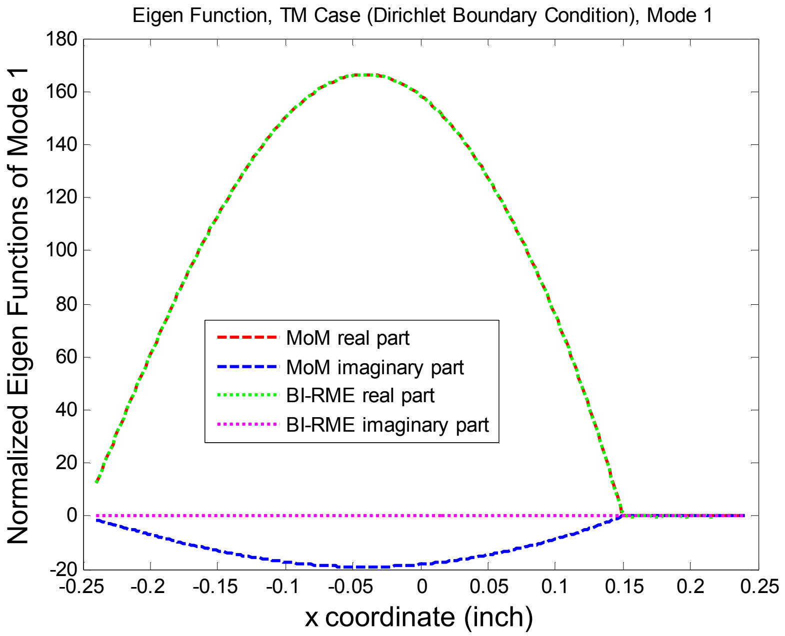

(a) Mode #1 at 8.715GHz

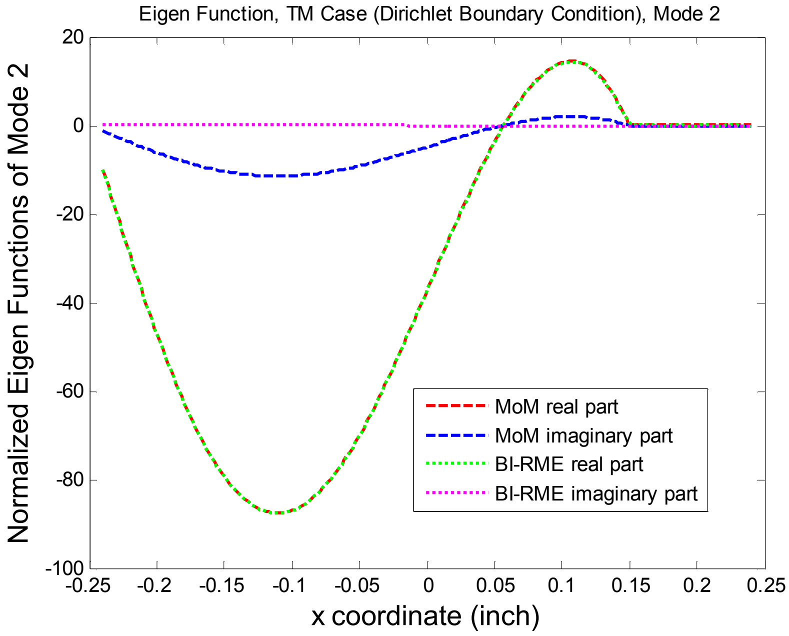

(b) Mode #2 at 12.814GHz

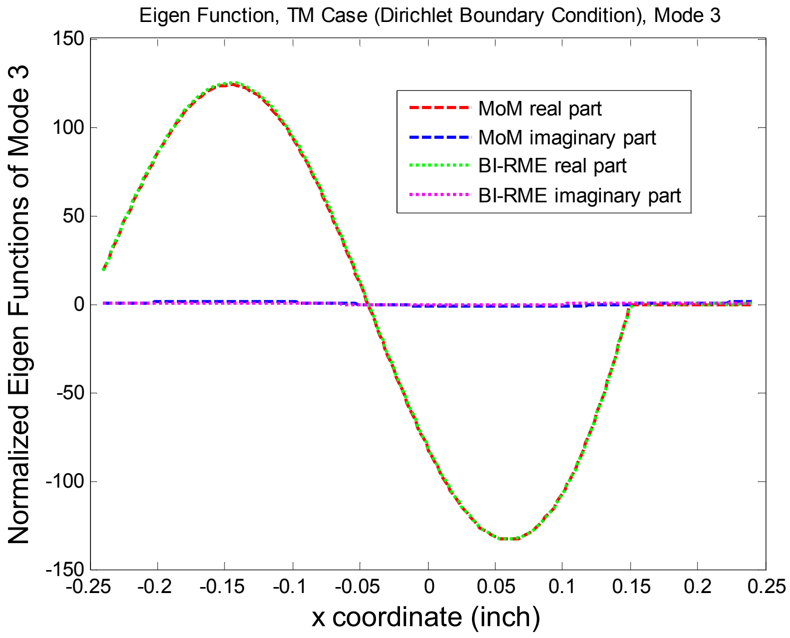

(c) Mode #3 at 14.273GHz

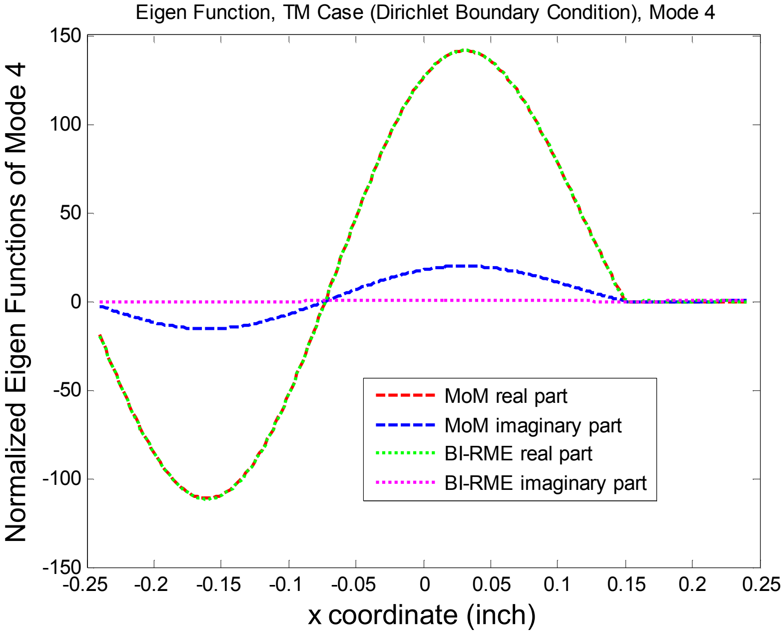

(d) Mode #4 at 16.860GHz

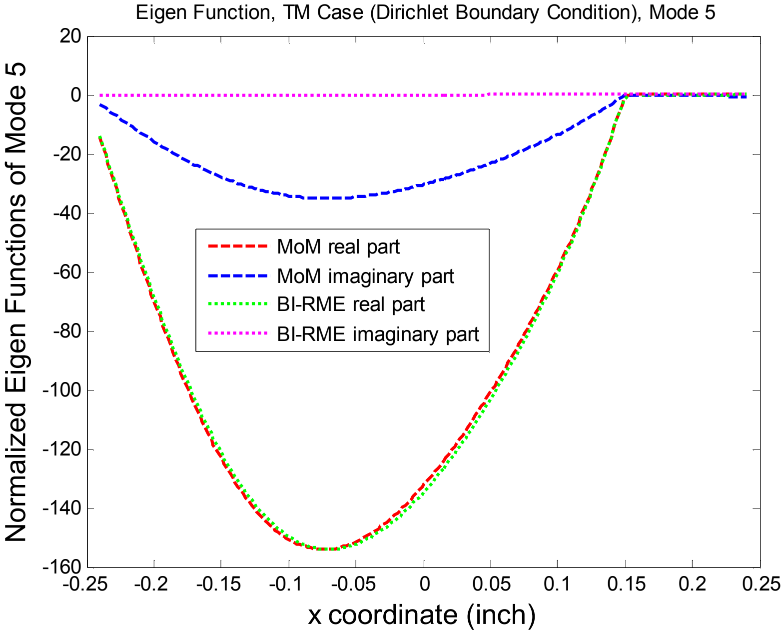

(e) Mode #5 at 18.203GHz

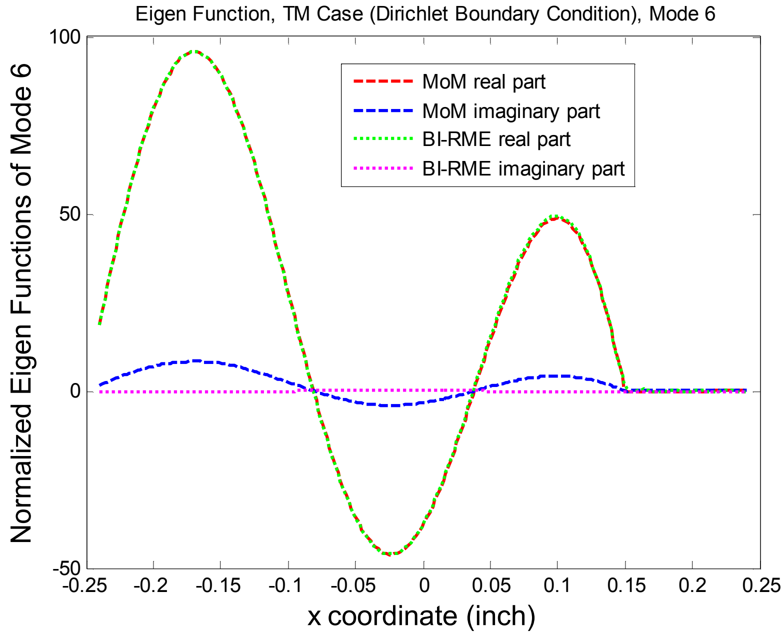

(f) Mode #6 at 19.564GHz

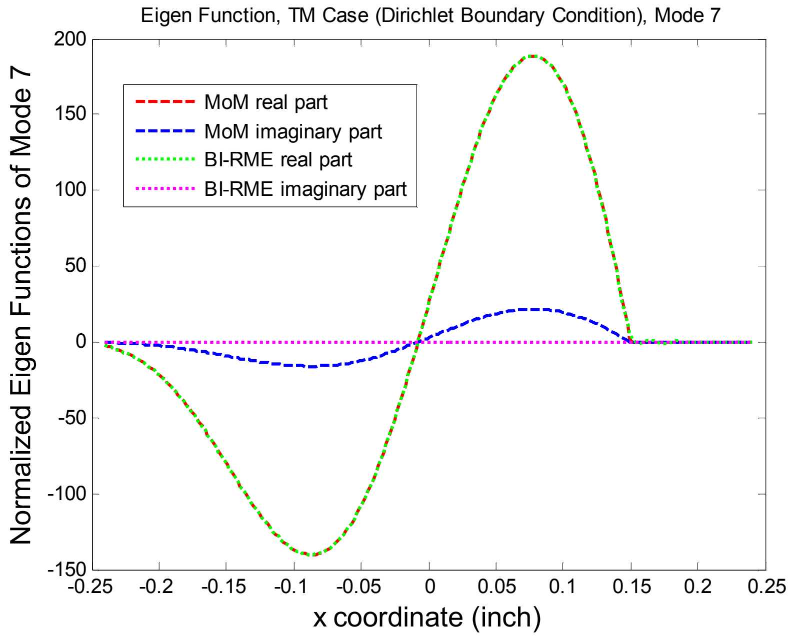

(g) Mode #7 at 21.466GHz

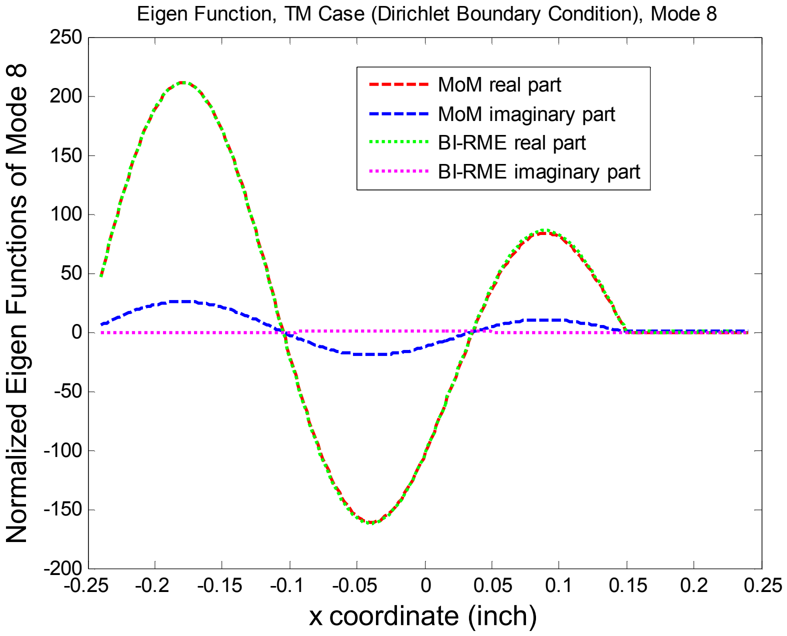

(h) Mode #8 at 22.583GHz

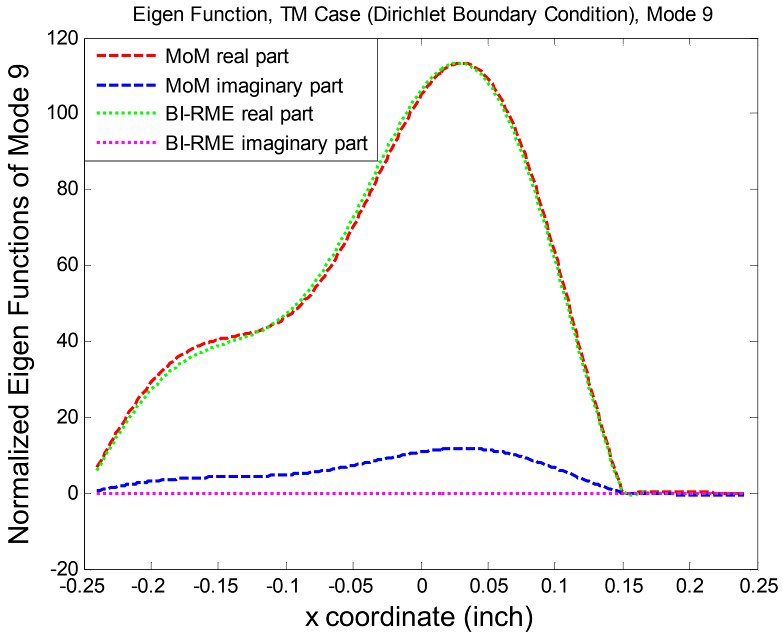

(l) Mode #9 at 23.441GHz

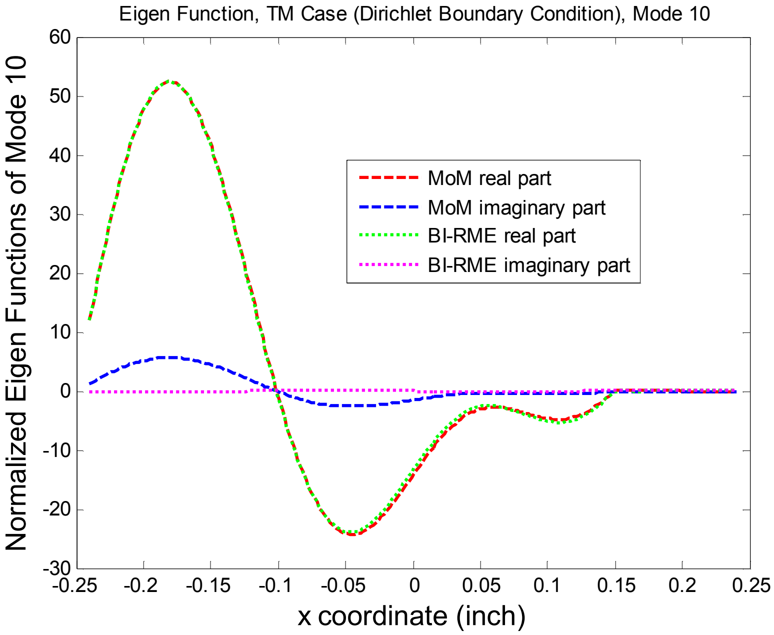

(m) Mode #10 at 24.714GHz

Figure 5.5 Comparison between MoM and BBGFL for final total Green's function of TE case.

5.4.3 Comparison of Final Response Green Function gEs for L-shape Waveguide

In Figure 5.6 (a)-(m), we compare the final response Green's function between direct MoM and BBGFL at different frequencies. MoM and BBGFL are in good agreement.

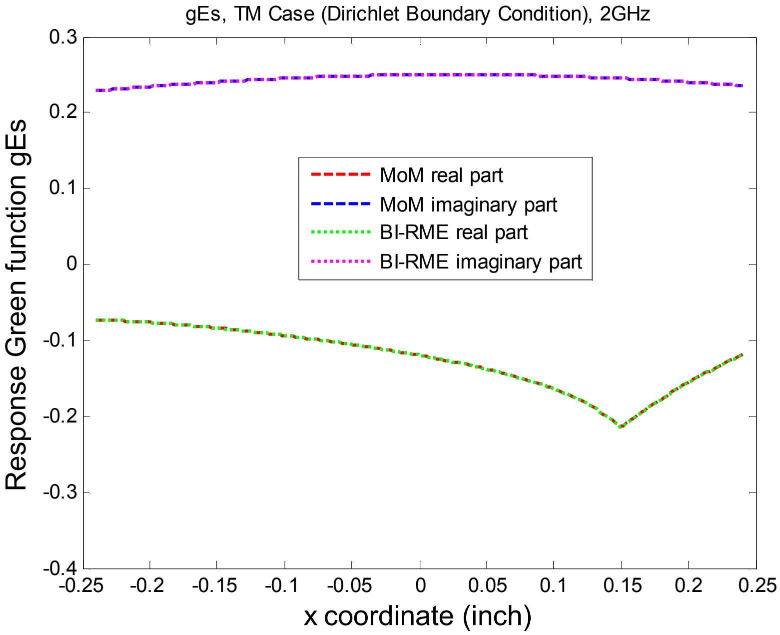

(a) TM response gEs at 2GHz

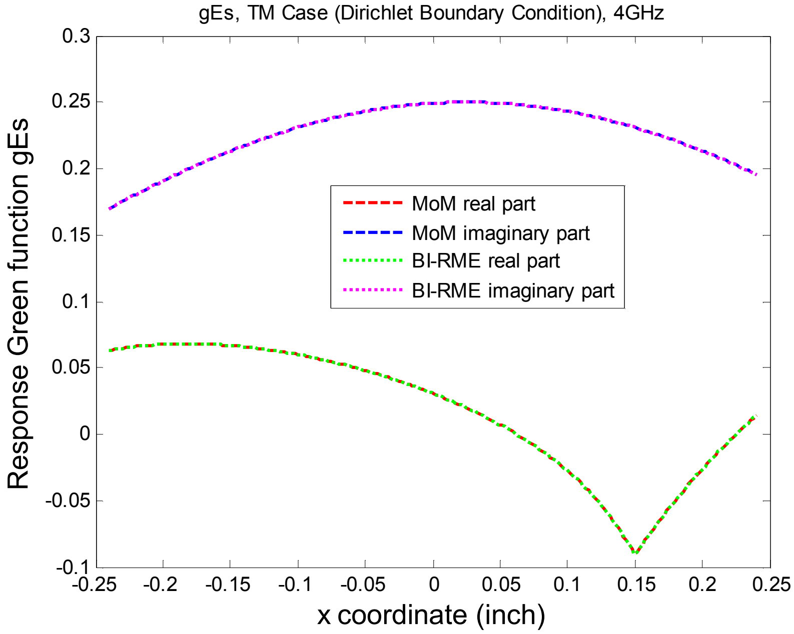

(b) TM response gEs at 4GHz

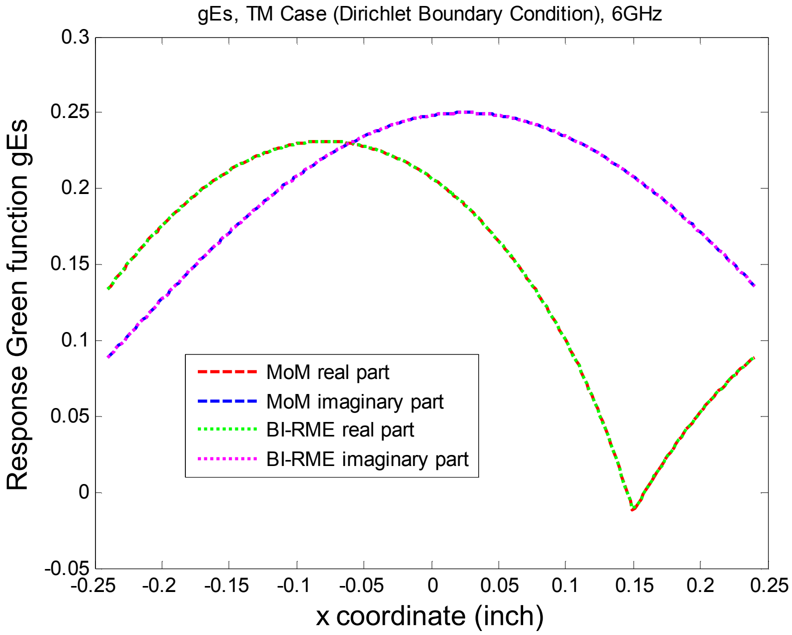

(c) TM response gEs at 6GHz

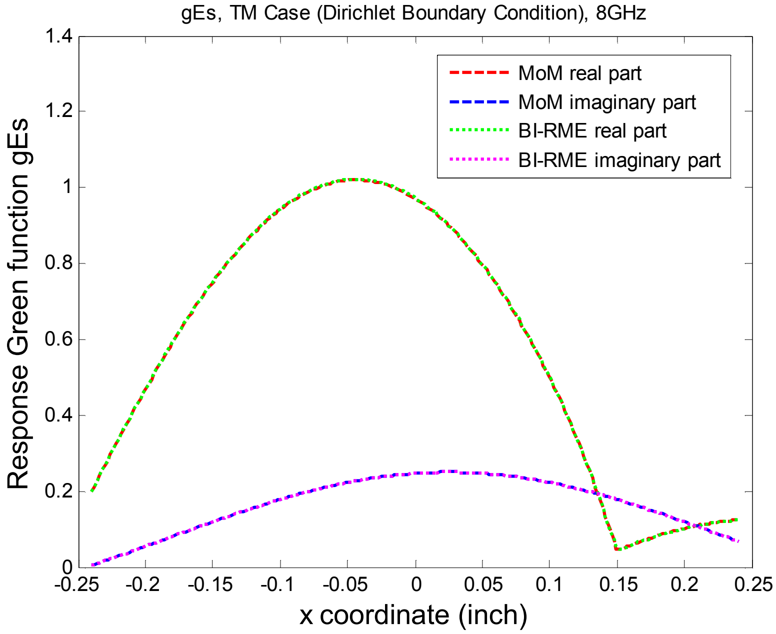

(d) TM response gEs at 8GHz

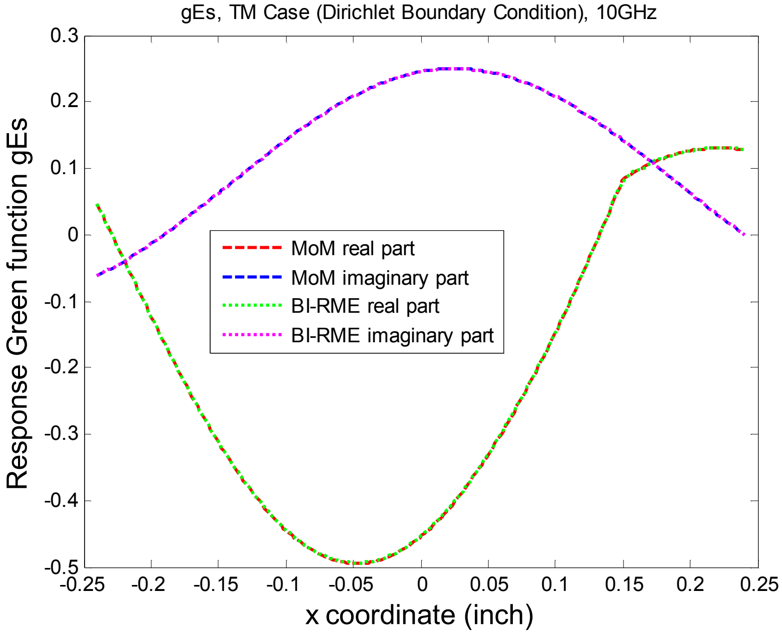

(e) TM response gEs at 10GHz

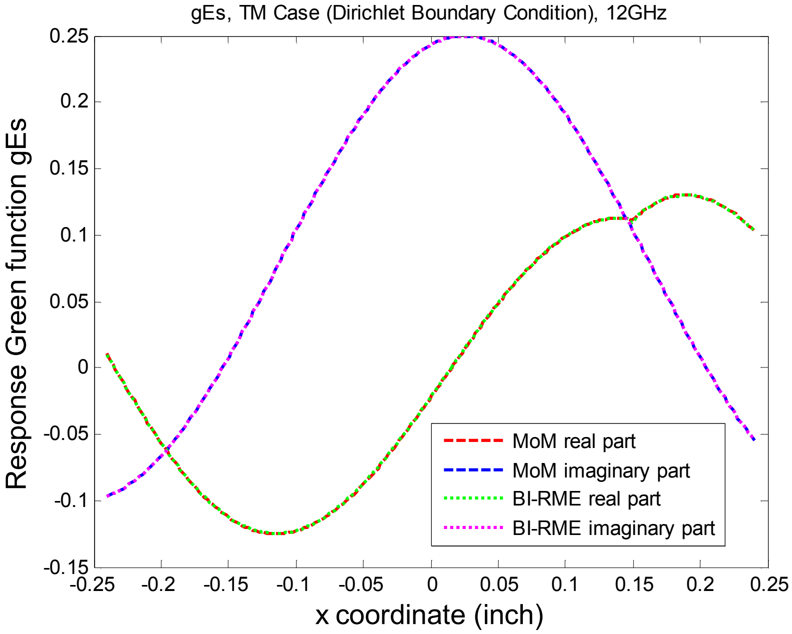

(f) TM response gEs at 12GHz

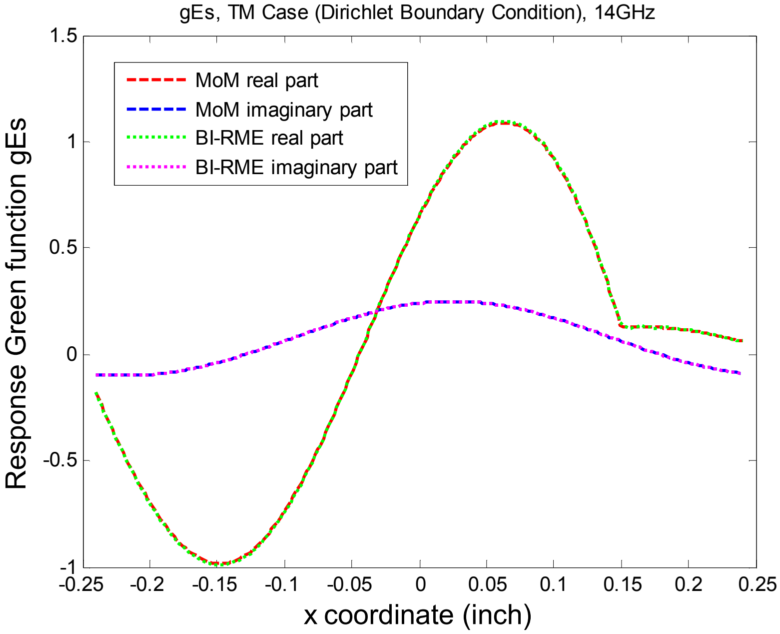

(g) TM response gEs at 14GHz

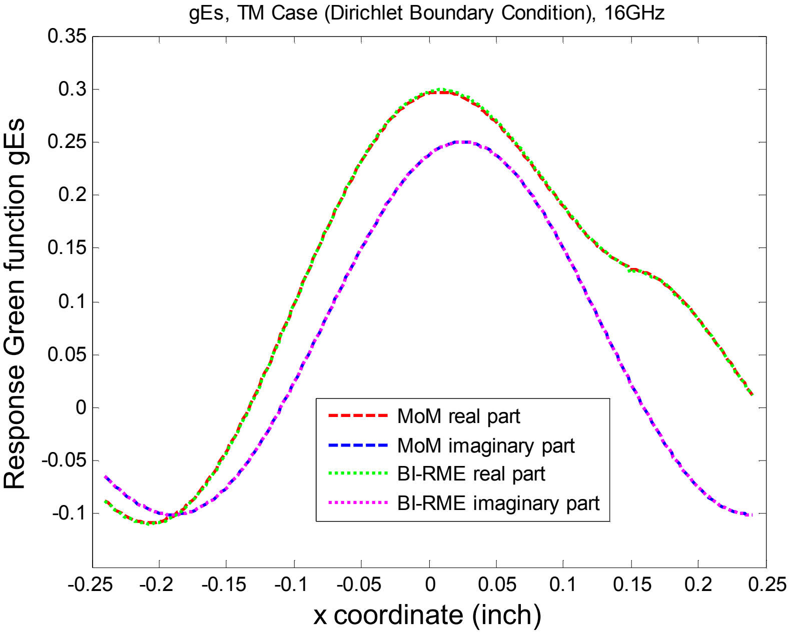

(h) TM response gEs at 16GHz

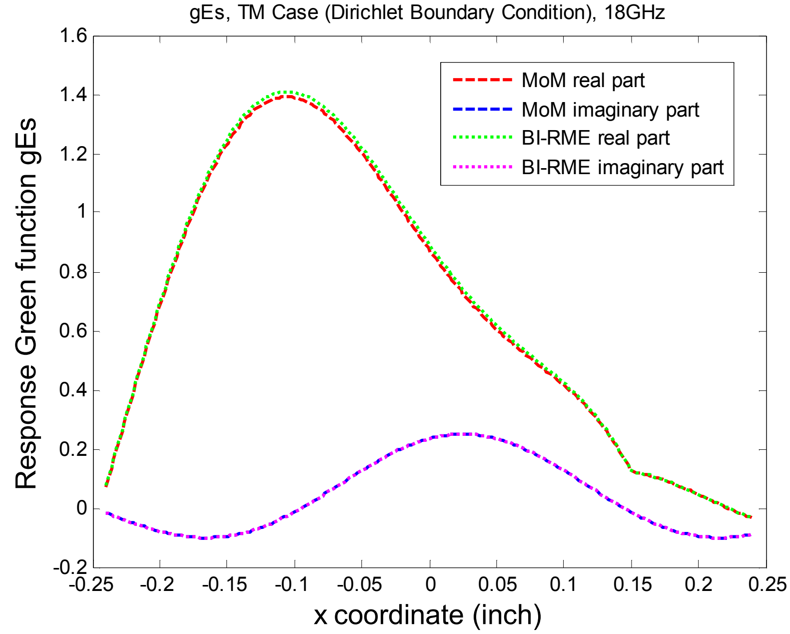

(*l*) TM response gEs at 18GHz

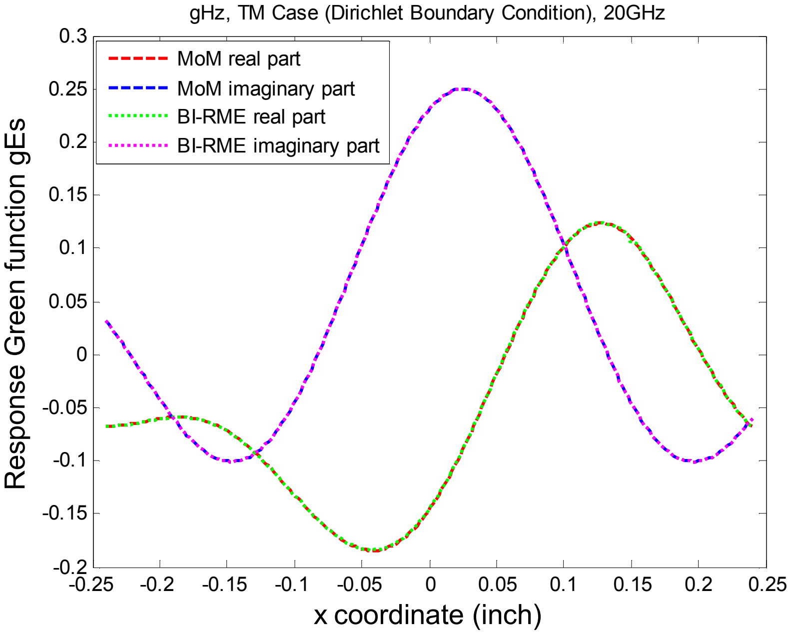

(m) TM response gEs at 20GHz

Figure 5.6 Comparison of final response Green's function of TM case between direct MoM and BBGFL.

5.4.4 Final Green Function gEs Comparison for L-shape Waveguide

In Figure 5.7 (a)-(m), we compare final total Green's function of TM case between direct MoM and BBGFL at different frequencies. MoM and BBGFL are in good agreement.

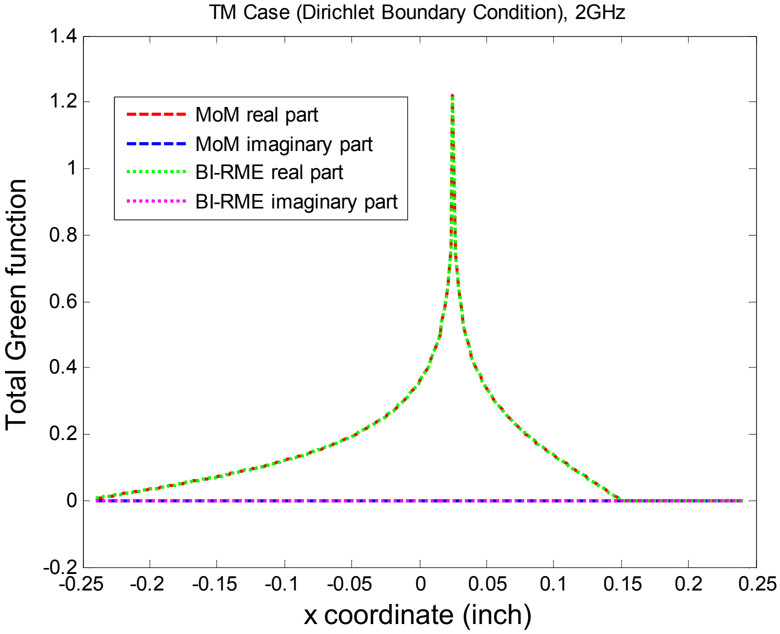

(a) TM total Green's function at 2GHz

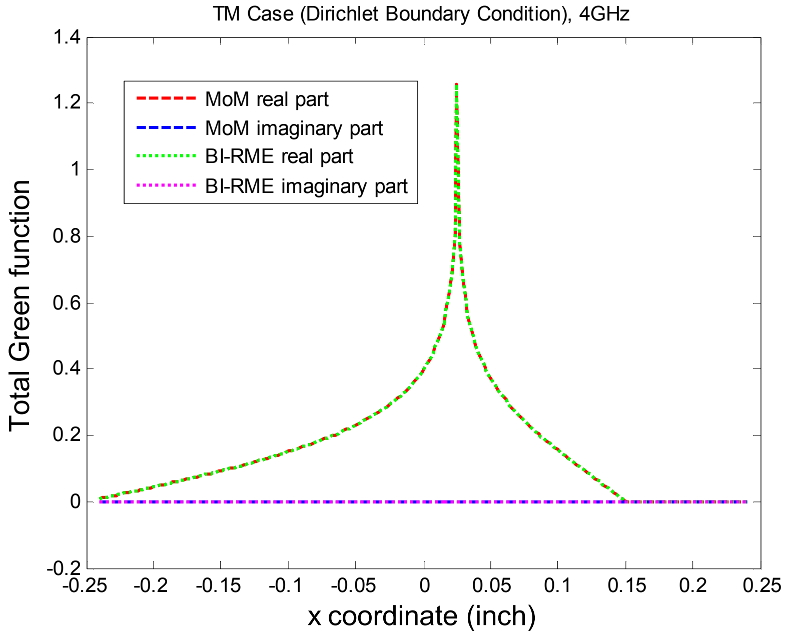

(b) TM total Green's function at 4GHz

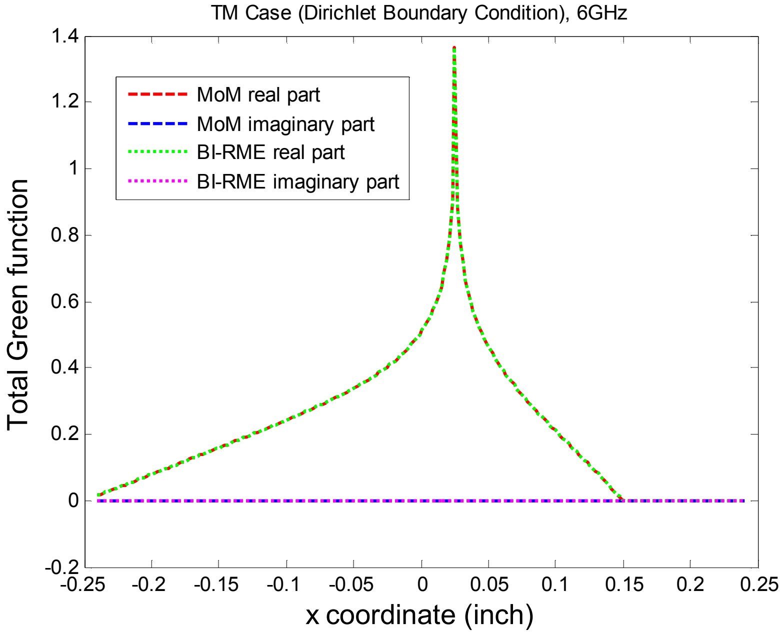

(c) TM total Green's function at 6GHz

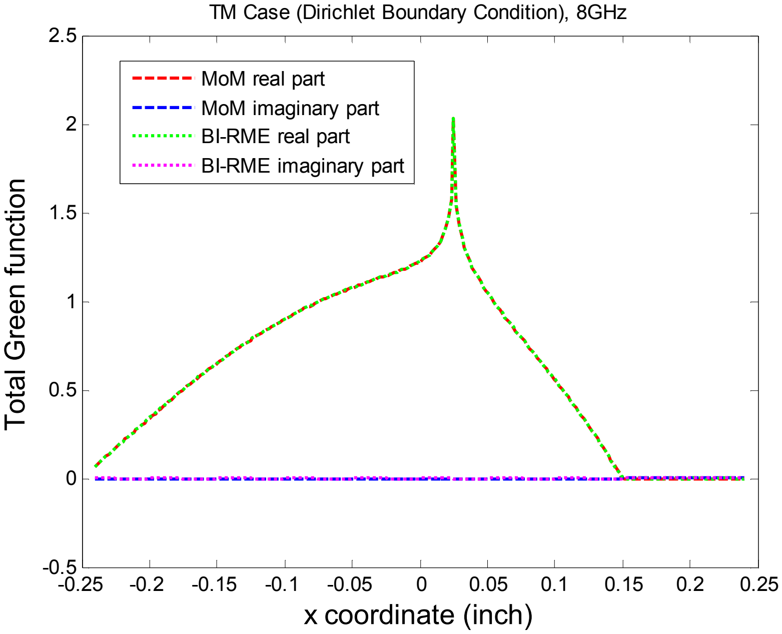

(d) TM total Green’s function at 8GHz

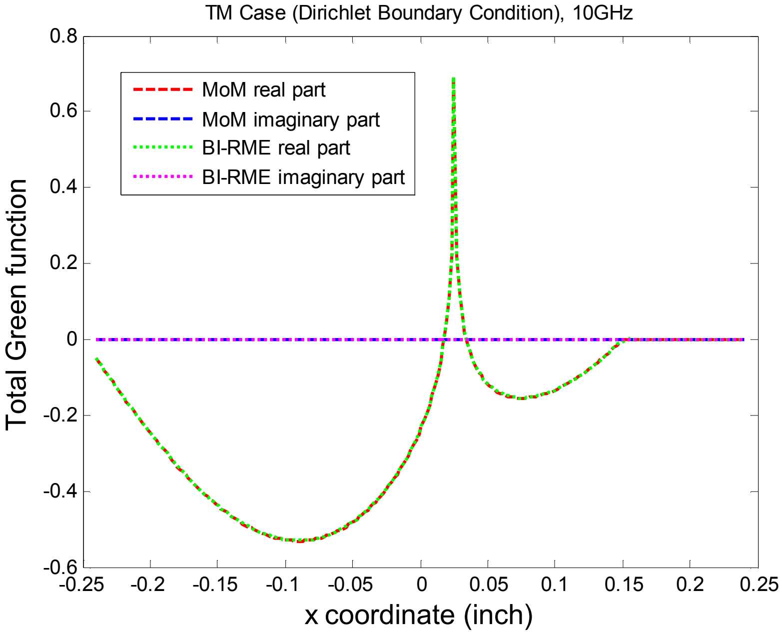

(e) TM total Green’s function at 10GHz

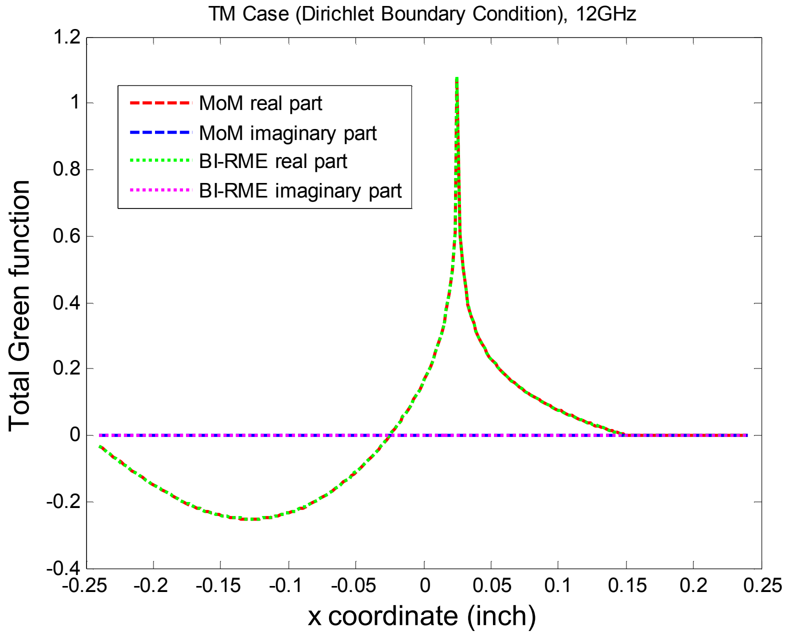

(f) TM total Green’s function at 12GHz

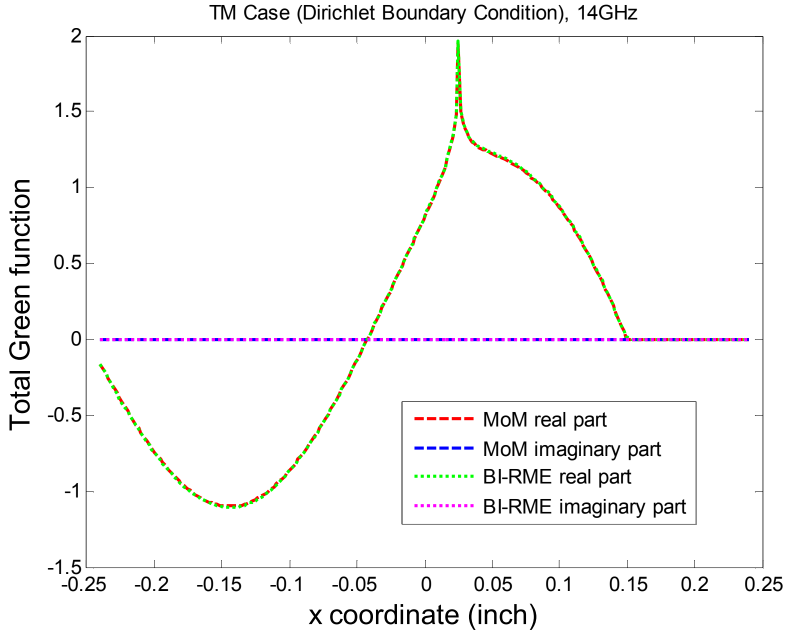

(g) TM total Green’s function at 14GHz

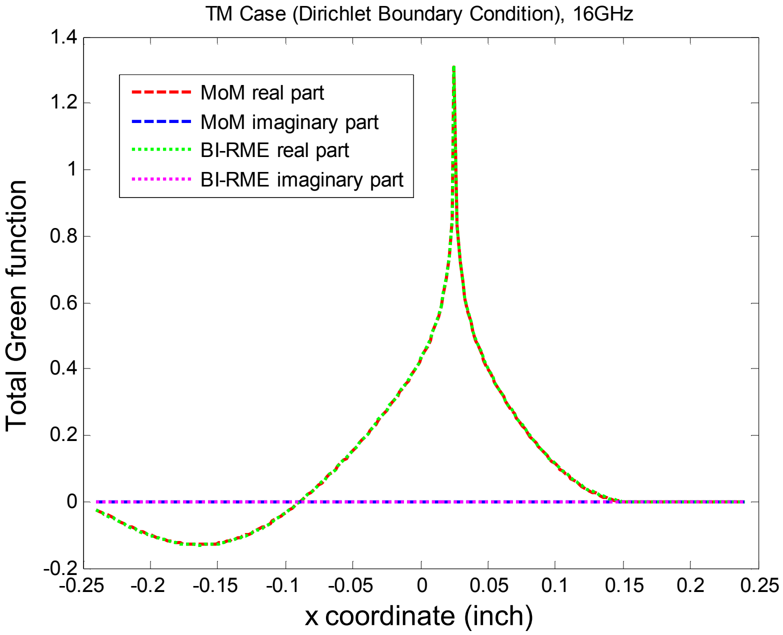

(h) TM total Green's function at 16GHz

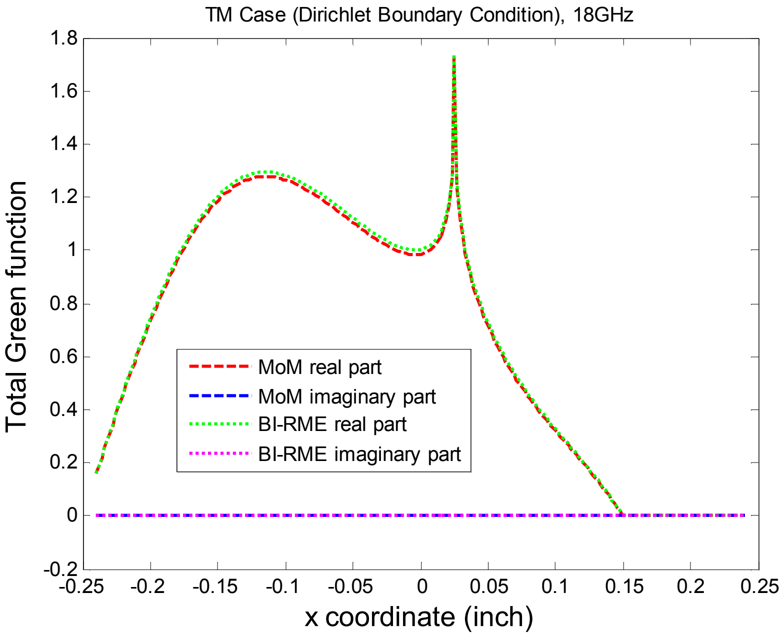

(*l*) TM total Green's function at 18GHz

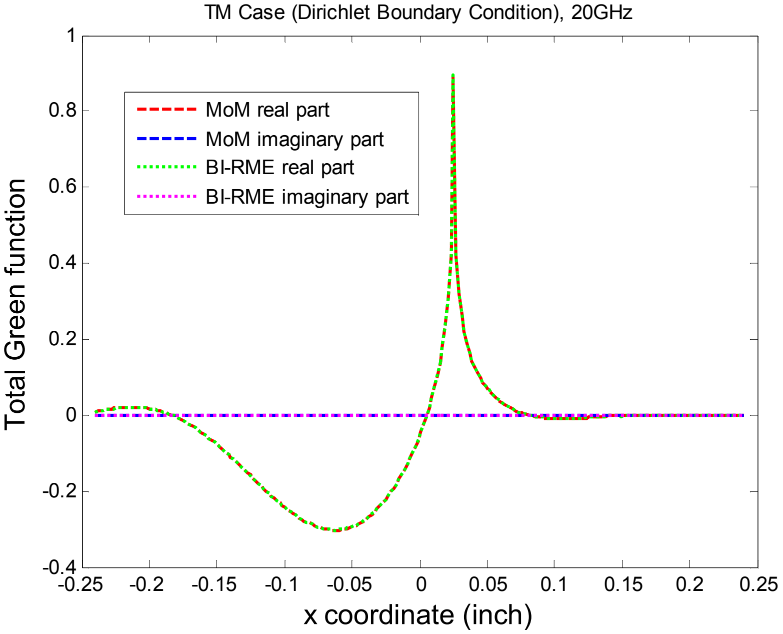

(m) TM total Green's function at 20GHz

Figure 5.7 Comparison of final total Green's function of TM case between direct MoM and BBGFL.

5.4.5 **Comparison of CPU Times for L-shape Waveguide**

In Table 5-2. we compare BBGFL with direct MoM for the CPU time taken in computing the final Green's function. In the comparison, the input parameters are: the discretization spacing is 2mils for both MoM and BBGFL, the BBGFL uses Mo=30 for both kxm and kyn with total Mα=(1+Mo)×(1+Mo)=900 modes. For 1 frequency point, the Green's functions are calculated with 1 source point and 240 observation points. For BBGFL, the CPU time consists two parts, the first part is for computation of eigenfunctions and eigenvalues, and second part is for creating final Green's function with the pre-computed eigenfunctions and eigenvalues. In the Table II, for 1000 frequency points, the first part takes 23.93 seconds, while the second part needs only 180 seconds for computing the final gHs of 240 observation points. Again, this indicates that, even for computation of

240 observation points, the second part is still negligible. For broadband modeling with 1000 frequency points, the proposed method is more than 104 times faster than direct MoM.

Table 5-2 Comparison of BBGFL and direct MoM for CPU times

Methods	1 frequency point	10 frequency points	100 frequency points	1000 frequency points
BBGFL	23.93 + 0.18 =24.11 sec	23.93 + 0.18*10 =25.73 sec	23.93 + 0.18*100 =41.93 sec	23.93 + 0.18*1000 =203.93 sec
Direct MoM	21.31 sec	21.31*10 =213.1 sec	21.31*100 =2131 sec	21.31*1000 =21310 sec

5.5 Conclusion

In this chapter, we extend BBGFL for fast broadband modeling and simulation of electronic devices and components with arbitrarily shaped waveguides of Dirichlet boundary condition. The methodology is derived for TM case. Simulations are done to compare the BBGFL technique with conventional direct MoM solution. Results show BBGFL and direct MoM are in good agreement on resonance frequencies, modes, and final Green's function for the TM case. The integrated Green's function derived at small patch is introduced to accelerate the convergence of modal expansion. Numerical experiments indicate that BBGFL is several hundred times faster than MoM for broadband simulation of arbitrarily shaped conducting waveguides.

Chapter 6 Application of Broadband Green's function to Fast Modeling of Power/Ground Planes with Traces and Vias

6.1 Summary

In this chapter, the proposed Broadband Green's function with low wavenumber extraction (BBGFL) is applied to modeling of traces connecting vias in printed circuit boards, particularly arbitrarily shaped power/ground planes. The proposed method is a hybrid technique based on mode decomposition: BBGFL is used to fast compute the vias in power/ground planes, MoM is used to calculate the impedance matrix of the traces, and then physical circuit model is applied to cascade the vias and traces in the power/ground planes. The present method is compared to method of moment (MoM) and commercial tool HFSS. Results show the present technique has good agreement with MoM and HFSS on the radiated emissions from printed circuit board (PCB) power/ground planes. But it is several hundred times faster than HFSS in CPU time for broadband simulations. The technique provides a fast technique for system level high speed interconnect design and applications.

6.2 Introduction

In practical PCB and package design and applications, there are transmission line routing as horizontal interconnect [34] [35] [40] [41] [42] [43] [44] [45] [46]. We refer transmission line in PCB or package as "trace" in this chapter. A trace inside internal layers is called stripline, which is for horizontal transition connecting vias. A typical point-to-point high speed signal link includes both vias and trace.

In previous papers, Broadband Green's function is proposed and different applications are investigated [32] [31] [30] [36] [47]. In [31] [30], Broadband Green’s function is used to solve the scattering in arbitrarily shaped waveguides and vias in finite power/ground plane. In [47], Broadband Green’s function is combined with method of moment (MoM) for arbitrary waveguides. In [36], Broadband Green’s function is applied in fast full wave modeling and simulations of radiated emissions from PCBs.

In this chapter, the Broadband Green’s function is used to modeling of arbitrarily shaped power/ground plane with both traces and vias for system level high-speed interconnect design and applications. A hybrid technique is proposed by combining, (1) the Foldy-Lax solution of vias with power/ground plane cavity effects using broadband Green's function; (2) 2D full wave modeling of traces, which includes the crosstalk between adjacent traces; and (3) circuit model which has been widely used in the industry. This will provide fast full wave solution of interconnects including the cavity resonance effects of power/ground planes.

We compare the present technique with different methods including MoM and commercial tool HFSS. Results show that the method agrees with MoM and HFSS on the S-parameters, but it is several hundred times faster than MoM and HFSS in CPU for broadband simulations.

6.3 Methodology

6.3.1 Circuit Model Cascading the Vias/Traces in Power/Ground Plane Cavity

We propose to use circuit model in [42] [43] to cascades the vias and traces for system level modeling and simulations.

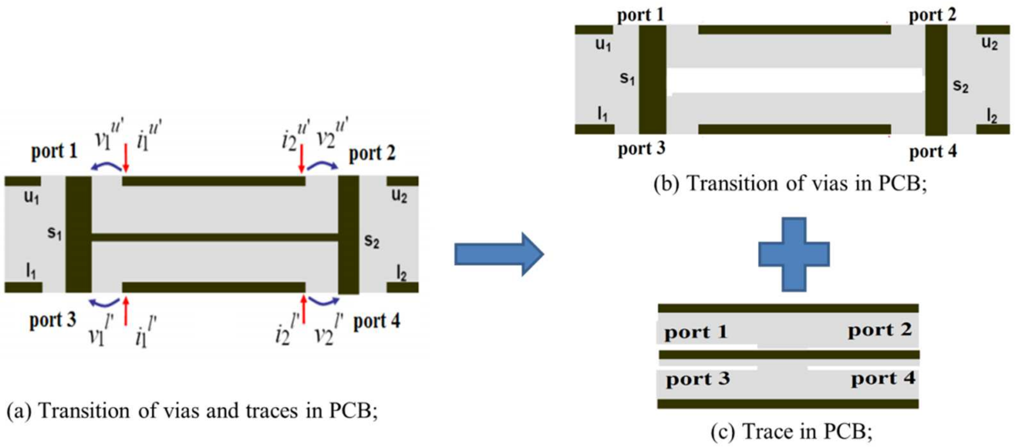

(a) Transition of vias and traces in PCB;

(b) Transition of vias in PCB;

(c) Trace in PCB;

Figure 6.1 (a) Transition of vias and traces in PCB, which is decomposed into two parts: (b) the transition of vias in PCB, and (c) the transition of trace in PCB.

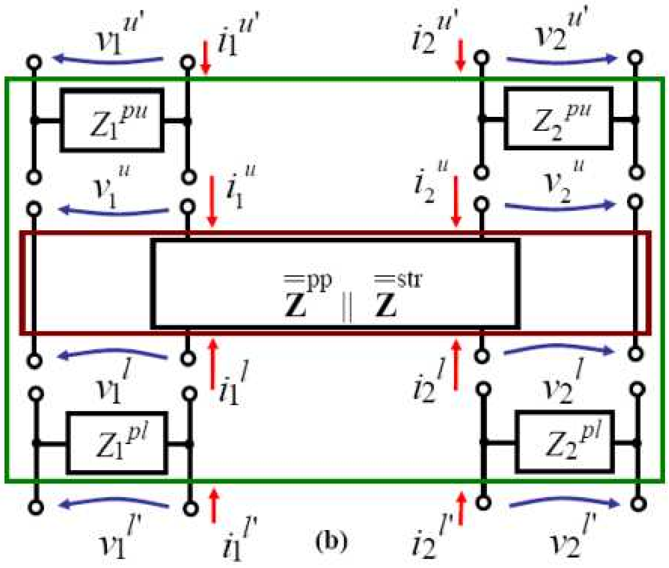

Figure 6.2 Equivalent electrical model of the PCB model in Figure 6.1 (a).

The circuit model used to cascade the vias and traces can be written in terms of Y-matrix as follow

$$\begin{pmatrix} i_1^u \\ i_2^u \\ i_1^d \\ i_2^d \end{pmatrix} = \begin{pmatrix} k^2\bar{\bar{Y}}^{str} + \bar{\bar{Y}}^{uu} & (-k^2 - k)\bar{\bar{Y}}^{str} - \bar{\bar{Y}}^{ud} \\ (-k^2 - k)\bar{\bar{Y}}^{str} - \bar{\bar{Y}}^{du} & (k^2 + 2k + 1)\bar{\bar{Y}}^{str} + \bar{\bar{Y}}^{dd} \end{pmatrix} \cdot \begin{pmatrix} v_1^u \\ v_2^u \\ v_1^d \\ v_2^d \end{pmatrix} \quad (6.1)$$

Where $\bar{\bar{Y}}^{str}$ refers to the admittance matrix of stripline; $\bar{\bar{Y}}^{PP}$ refers to the admittance matrix of the parallel-plate (power/ground planes); v_i^u and v_i^l are the terminal voltages for ports on up plate (e.g. power plane) and down plate (e.g. ground plane), respectively; i_i^u and i_i^l are the terminal current for ports on up plate (e.g. power plane) and down plate (e.g. ground plane), respectively; k is the ratio of dielectric heights as $k = -\frac{h_i^d}{h_i^u + h_i^d}$.

6.3.2 Modeling of Vias in Power/Ground Plane Cavity Using Broadband Green's Function

We propose to leverage the Broadband Green's function method described in previous chapter to analyze the vias in the power/ground plane cavity. The effects of open via stub will be investigated.

6.3.3 Modeling of Internal Trace (Stripline) Using Method of Moments

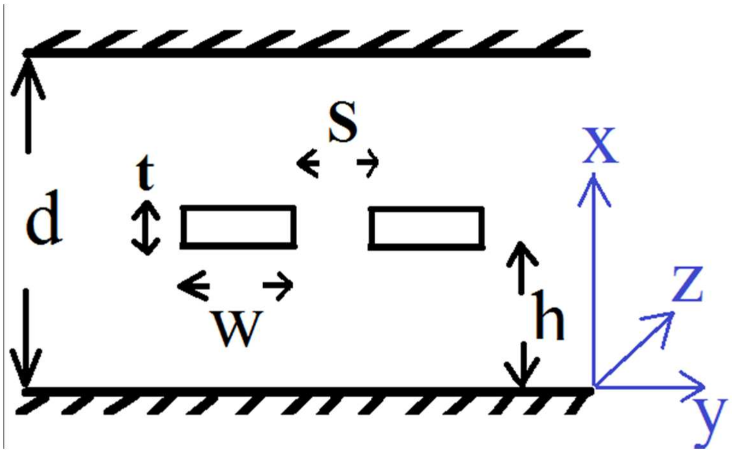

Figure 6.3 Coupled striplines in PCB

We propose to use 2D Method of Moment to analyze the multi-line structures for striplines.

The surface integral equation for electrostatic case (DC with wavenumber k=0) can be written as

$$\int_{\partial s} dl' \left(g_0(\bar{\rho}', \bar{\rho}) \sigma_s(\bar{\rho}') \right) = \psi(\bar{\rho}) \tag{6.2}$$

Where $\psi(\bar{\rho})$ is the potential, and $\sigma_s(\bar{\rho}')$ is the unknown electric charge on the boundary, and $g_0(\bar{\rho}', \bar{\rho})$ is free space Green's function at DC (electrostatic)

$$g_0(\bar{\rho}', \bar{\rho}) = -\frac{1}{2\pi} \ln|\bar{\rho}' - \bar{\rho}| \tag{6.3}$$

$$\nabla_t^2 \, g_0(\bar{\rho}', \bar{\rho}) = -\delta(\bar{\rho}' - \bar{\rho}) \tag{6.4}$$

Discretize ∂S into patches Δt, with number of N_v patches on σ_v. Let points on σ_v be labeled i, j. Use point matching at the center of the patch.

Let σ_{vi} be patch i, $\bar{\rho}$ be on σ_v,

$$\sum_j \left[\int_{\sigma_{vj}} dl' \left(g_0(\bar{\rho}_{vi}, \bar{\rho}'_{vj}) \sigma_j(\bar{\rho}'_{vj}) \right) \right] = \psi(\bar{\rho}_{vi}) \tag{6.5}$$

Let

$$\sigma_j(\bar{\rho}'_{vj'}) = \frac{a_{j'}}{\Delta t} \tag{6.6}$$

Then

$$\sum_j \left[\int_{\sigma_{vj}} dl' \left(g_0(\bar{\rho}_{vi}, \bar{\rho}'_{vj}) \frac{a_j}{\Delta t} \right) \right] = \psi(\bar{\rho}_{vi}) \tag{6.7}$$

Define matrix elements

$$L_{ij}^{vv} = \frac{1}{\Delta t}\left[\int_{\sigma_{vj}} dl' \left(g_0\left(\bar{\rho}_{vi}, \bar{\rho}'_{vj}\right)\right)\right] \tag{6.8}$$

$$\sum_j L_{ij}^{vv} a_j = -g_0(\bar{\rho}_{vi}, \bar{\rho}'') \tag{6.9}$$

Let $B_i = \psi(\bar{\rho}_{vi})$

Write into matrix form:

$$\left[\bar{\bar{L}}^{vv}\right][\bar{a}] = [\bar{B}] \tag{6.10}$$

Impedance matrix has dimension of $\bar{\bar{L}}^{vv} = N_v \times N_v$, and matrix elements expression:

$$L_{ij}^{vv} = \frac{1}{\Delta t}\left[\int_{\sigma_{vj}} dl' \left(g_0\left(\bar{\rho}_{vi}, \bar{\rho}'_{vj}\right)\right)\right] \tag{6.11}$$

Apply point matching and pulse basis function, yields

$$L_{ij}^{vv} = g_0\left(\bar{\rho}_{vi}, \bar{\rho}'_{vj}\right) \tag{6.12}$$

for $i \neq j$;

$$L_{ij}^{vv} = -\frac{1}{2\pi}\ln\left(\frac{\Delta t}{2e}\right) \tag{6.13}$$

for $i \neq j$.

The MoM solution provide the characterization impedance matrix Z_0, then the admittance matrix is given by [48],

$$\bar{\bar{Y}} = \begin{bmatrix} \frac{-j}{Z_0 tanh(\gamma L)} & \frac{j}{Z_0 sinh(\gamma L)} \\ \frac{j}{Z_0 sinh(\gamma L)} & \frac{-j}{Z_0 tanh(\gamma L)} \end{bmatrix} \tag{6.14}$$

With γ is the complex propagation constant and L is the trace length.

6.4 Simulation

6.4.1 Case 1: Via and Balanced Stripline in Irregular Shaped Cavity

The first case used to check the proposed technique is a model with 4 signal vias and a pair of balanced striplines in irregular shaped power/ground cavity. The stripline is balanced configuration with d1=d2 = 10 mils.

6.4.1.1 Broadband Green's Function for Irregular Shaped Waveguide

In this section, we present the simulation results of green functions computed for TE case. The arbitrary shaped waveguide in Figure 6.4 is used for TE simulation. The dimension parameters are: Lx=500mils, Ly=1000mils, L1=700mils, and W1=100mils.

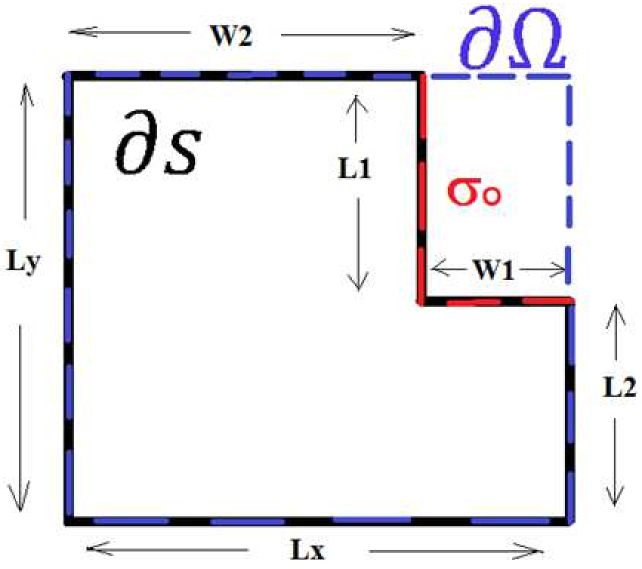

Figure 6.4 Arbitrary shaped waveguide with Neumann boundary condition

6.4.1.1.1 Resonant Frequency Comparison for TE Case

In Table 6.1 – 6.4, we compare the direct MoM and BBGFL for the resonant frequencies of TE case with different permittivities. The first 10 physical modes are compared. Results indicate MoM and BBGFL are in good agreement.

Table 6-1: Comparison of MoM and BBGFL for resonant frequencies of TE case; Relative permittivity inside the waveguide is $\varepsilon_r = 3.4$.

MoM Mode Number	MoM Resonant Frequency (GHz)	BBGFL Mode Number Total/physical	BBGFL Resonant Frequency (GHz)
0 (constant mode)	0.08	0 (constant mode)	0
1	3.06	1	3.05
2	6.33	2	6.22
3	7.03	3	7.02
4	8.27	4	8.31
5	9.66	5	9.66
6	10.04	6	10.05
7	12.17	7	12.16
8	12.57	8	12.57
9	13.18	9	13.18
10	14.36	10	14.36

11	15.83	11	15.83

Table 6-2 Comparison of MoM and BBGFL for resonant frequencies of TE case; Relative permittivity inside the waveguide is $\varepsilon_r = 3.4 * (1 - j * 0.02)$.

MoM Mode Number	MoM Resonant Frequency (GHz)	BBGFL Mode Number Total/physical	BBGFL Resonant Frequency (GHz)
0 (constant mode)	0.08	0 (constant mode)	0
1	3.06	1	3.05
2	6.33	2	6.22
3	7.03	3	7.02
4	8.27	4	8.31
5	9.66	5	9.65
6	10.04	6	10.05
7	12.17	7	12.16
8	12.57	8	12.57
9	13.18	9	13.18
10	14.36	10	14.36

11	15.83	11	15.83

Table 6-3 Comparison of MoM and BBGFL for resonant frequencies of TE case; Relative permittivity inside the waveguide is $\varepsilon_r = 4.4$.

MoM Mode Number	MoM Resonant Frequency (GHz)	BBGFL Mode Number Total/physical	BBGFL Resonant Frequency (GHz)
0 (constant mode)	0.07	0 (constant mode)	0
1	2.69	1	2.68
2	5.48	2	5.47
3	6.18	3	6.17
4	7.30	4	7.30
5	8.49	5	8.49
6	8.83	6	8.84
7	10.71	7	10.69
8	11.05	8	11.05
9	11.59	9	11.58
10	12.63	10	12.62
11	13.91	11	13.92

Table 6-4 Comparison of MoM and BBGFL for resonant frequencies of TE case; Relative permittivity inside the waveguide is $\varepsilon_r = 4.4 * (1 - j * 0.02)$.

MoM Mode Number	MoM Resonant Frequency (GHz)	BBGFL Mode Number Total/physical	BBGFL Resonant Frequency (GHz)
0 (constant mode)	0.07	0 (constant mode)	0
1	2.69	1	2.68
2	5.48	2	5.47
3	6.18	3	6.17
4	7.29	4	7.31
5	8.51	5	8.49
6	8.80	6	8.83
7	10.74	7	10.69
8	11.03	8	11.05
9	11.57	9	11.58
10	12.64	10	12.62
11	14.16	11	13.91

6.4.1.1.2 Comparison of BBGFL and MoM for Response Green's Functions

Consider a plate pair as showed in Figure 6.4, with Lx= 500mils, Ly= 1000mils, L1=100mils, W1=700mils. Via 1 and Via 2 are located at (-25, 0) mil and (25, 0) mil, respectively.

Figure 6.5 show the results for the case with PCB dielectric substrate has relative permittivity εr=4.4. We compare both the real and imaginary parts of response Green's function coefficients. Results show the BBGFL matches well with MoM solution for real part. The imaginary parts are also in good agreement, except that MoM has some peaks in the imaginary part. Note, given εr=4.4, the response Green's function Gw physically should be zero. The none zero imaginary part of Gw is caused by the Hankel function.

Figure 6.6 show the results for the case with PCB dielectric substrate has relative permittivity ε_r=4.4*(1-0.02*j). BBGFL and MoM are in good agreement for both real and imaginary parts of response Green's function.

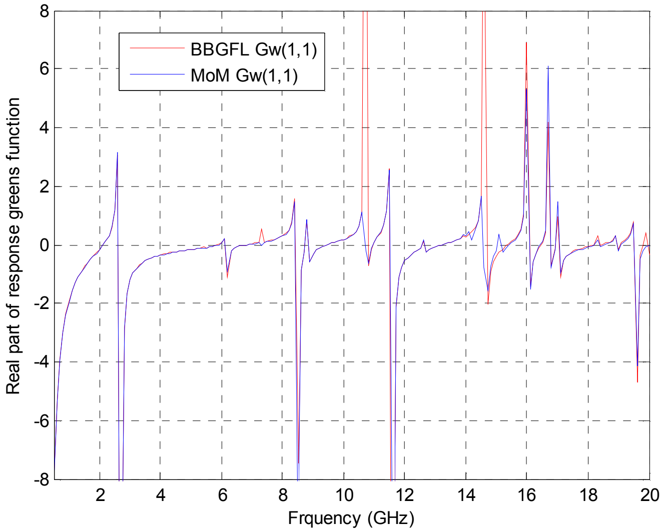

(a) Real part of Gw(1,1)

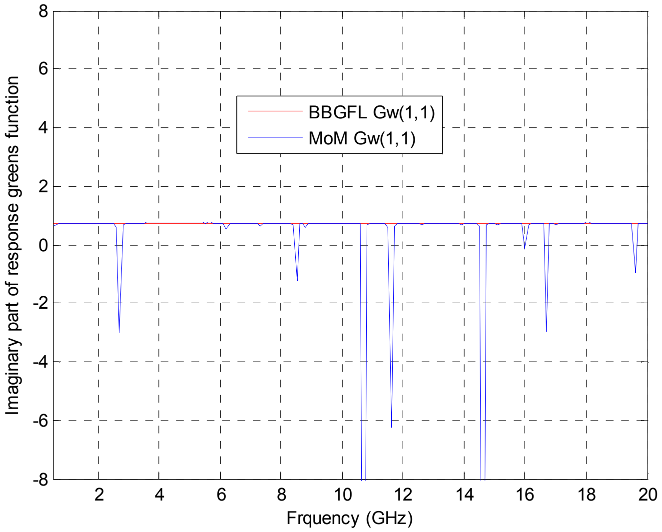

(b) Imaginary part of Gw(1,1)

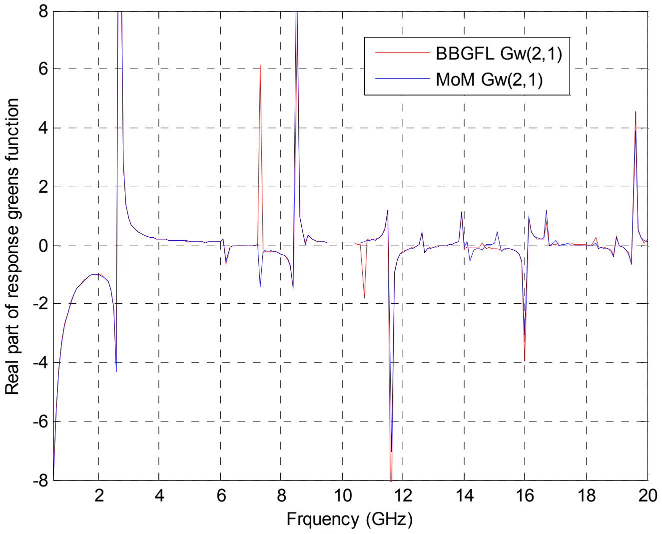

(c) Real part of Gw(2,1)

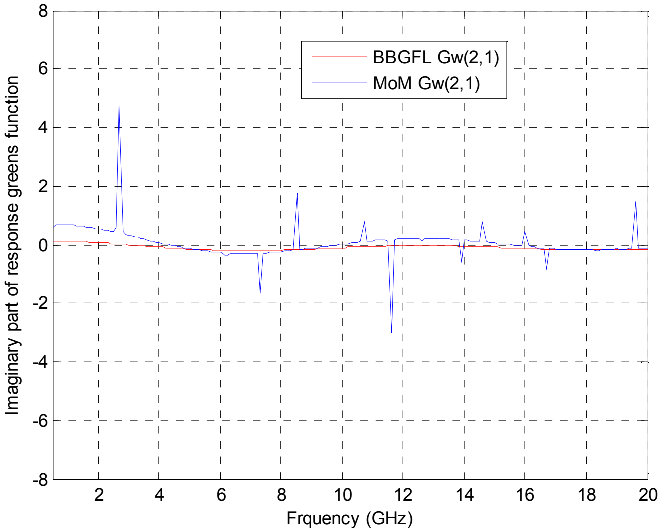

(d) Imaginary part of Gw(2,1)

Figure 6.5 Comparison of MoM and BBGFL for response Green's function Gw. Gw(1,1) refer to the response Green's function from via 1 to via 1. Gw(2,1) refer to the response Green's function from via 1 to via 2. Dielectric substrate has relative permittivity εr = 4.4.

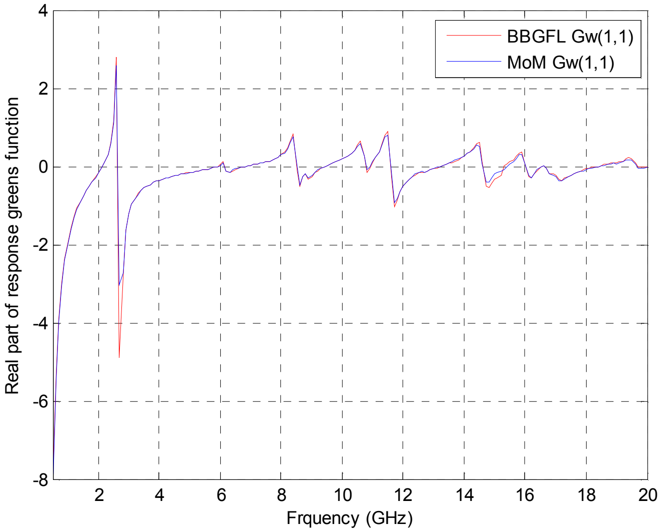

(a) Real part of Gw(1,1)

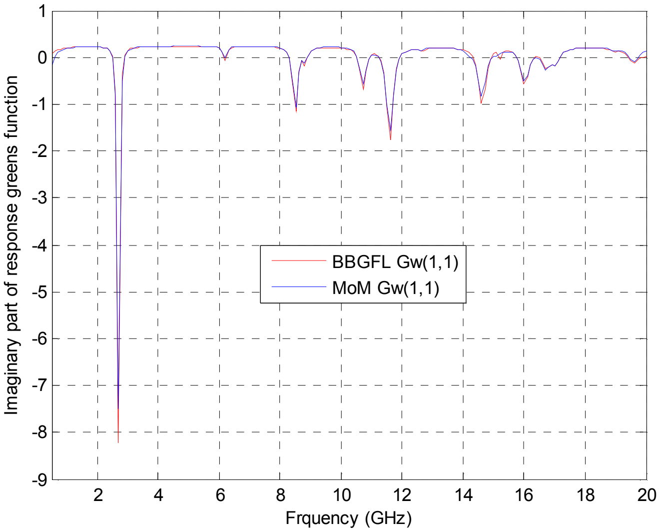

(b) Imaginary part of Gw(1,1)

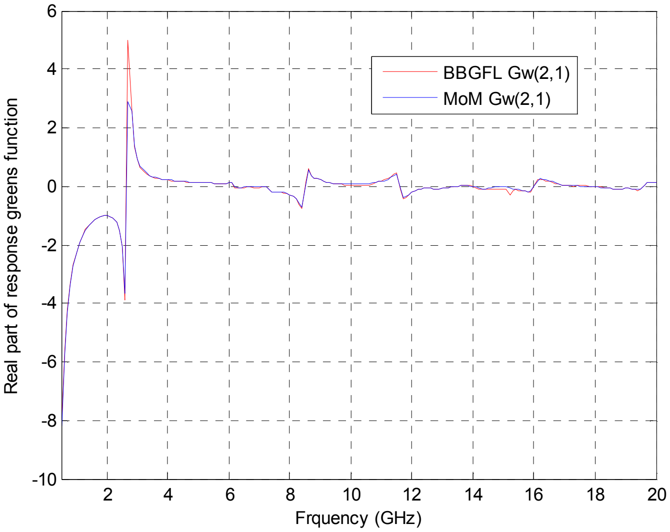

(c) Real part of Gw(2,1)

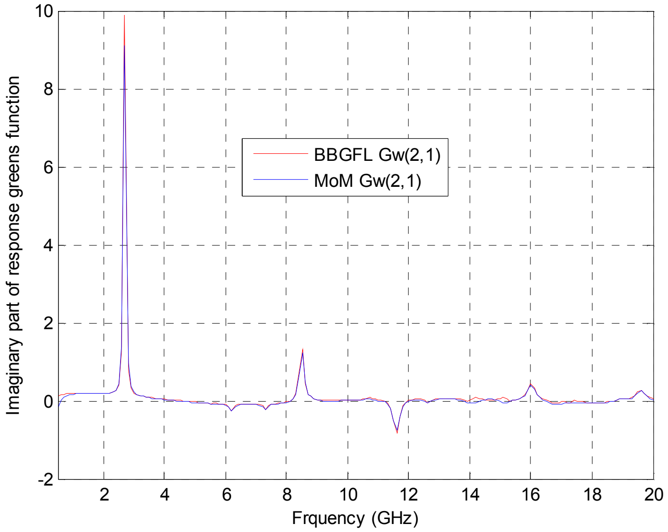

(d) Imaginary part of Gw(2,1)

Figure 6.6 Comparison of MoM and BBGFL for response Green's function Gw. Gw(1,1) refer to the response Green's function from via 1 to via 1. Gw(2,1) refer to the response Green's function from via 1 to via 2. Dielectric substrate has relative permittivity εr = 4.4*(1-j*0.02).

6.4.1.2 Via in Irregular Shaped Cavity

Consider a power/ground plane pair with two signal vias as showed in Figure 6.7. Lx=Ly=500mils, L1=100mils, W1=200mils. The dielectric thickness is 30 mils, and the relative permittivity εr=4.4*(1-j*0.02). Via 1, Via 2, Via 3, Via 4 are located at (-25, 0), (25, 0), (-25, 500), and (25, 500) mil, respectively. The barrel radius is 6.75 mils, and the antipad radius is 20 mils.

In Figure 6.8, BBGFL is compared with three different methods for the s-parameters of insertion loss, return loss, near end crosstalk (NEXT), and far end crosstalk (FEXT). The red curves are results obtained by using BBGFL with Foldy-Lax, which is described in Section II.4 of chapter 2. The blue curves are results from HFSS. The green curves are results from direct MoM solution of the mix problem with signal vias and plane pair, with L=0 mode. Note, direct MoM has include all anisotropic mode (m,n)>(0,0) in the solution for L=0 mode. The black curves are results combining direct MoM solution with L=0 mode, and Foldy-Lax solution with L>0 modes. Overall, BBGFL/Foldy-Lax (red) is in good agreement with HFSS (blue) and MoM/Foldy-Lax (black). It can be seem that all the methods can capture the resonance frequencies, which are caused by the finite plane edges. This indicates that it is sufficient to truncate up to $G_{W0}^{pq}(0,0)$ to capture the resonant frequencies of finite plane edges. However, the green results with only L=0 has large difference compared to other methods. This means the L>0 modes are important for the coupling effects caused by the dense vias (small pitch between two vias).

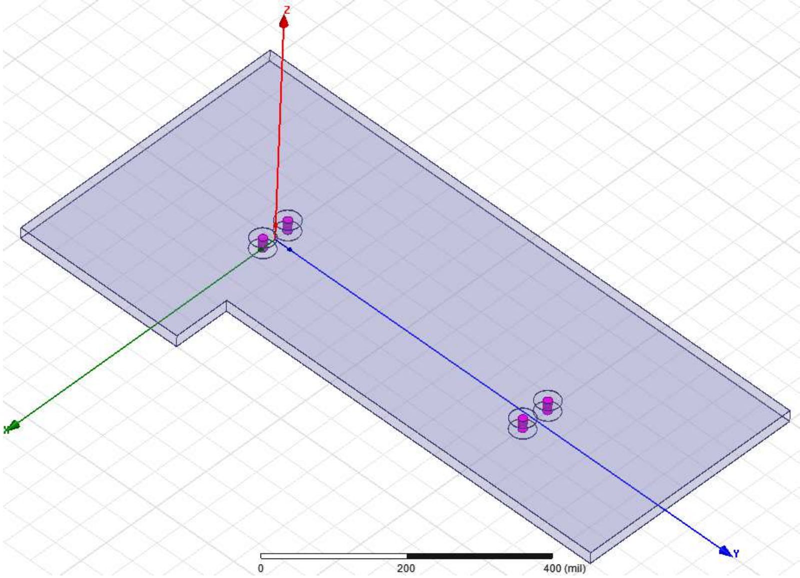

Figure 6.7 3D geometry of the simulation with 2 signal vias in an irregular shaped plate pair.

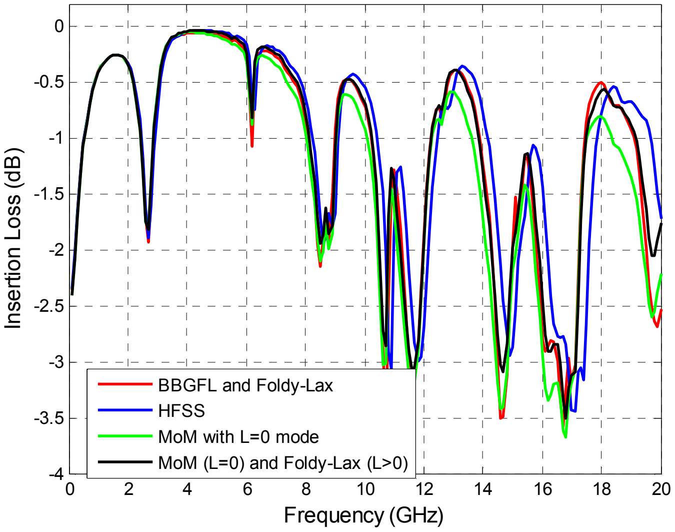

(a) Insertion Loss

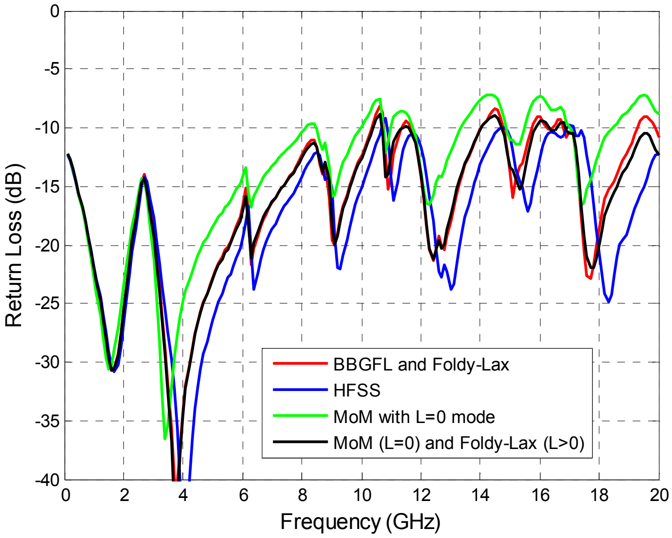

(b) Return Loss

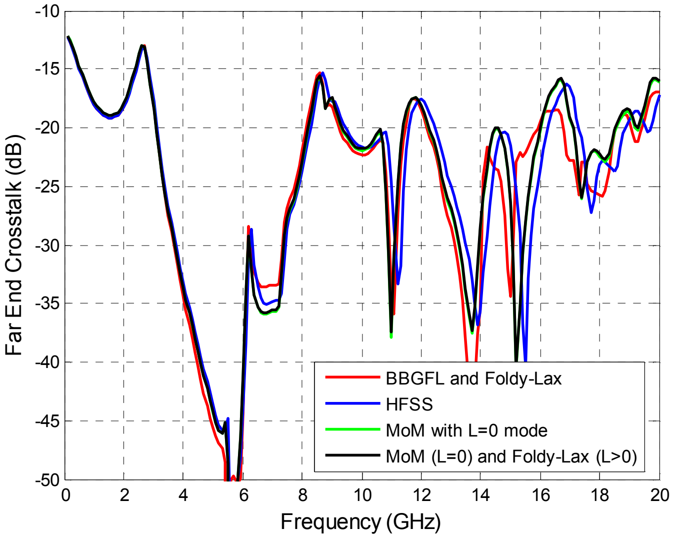

(c) Far End Crosstalk

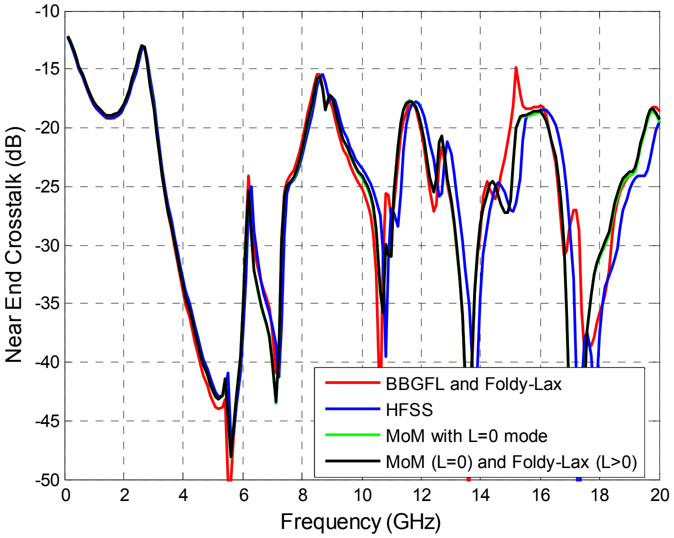

(d) Near End Crosstalk

Figure 6.8 Comparison of BBGFL and different methods for s-parameters from simulations with Figure 6.7: Red –BBGFL/Foldy-Lax, Blue – HFSS, Green –

direct MoM with L=0 mode, Black - combine direct MoM with L=0 mode and Foldy-Lax with L>0 modes.

6.4.1.3 Traces in Internal Layers

Consider a pair of striplines as showed in Figure 6.9. Since it is internal routing with homogeneous dielectric substrate, the odd mode and even mode have same velocity, thus the far end crosstalk should be close to zero [30]. And the near end crosstalk should be small. In Figure 6.10 (a) and (b), we compare 3D HFSS and 2D MoM solution for the magnitude and phase of insertion loss, respectively. In Figure 6.11 (a) and (b), we compare 3D HFSS and 2D MoM solution for the magnitude and phase of return loss, respectively. Results show 2D MoM and 3D HFSS are in good agreement.

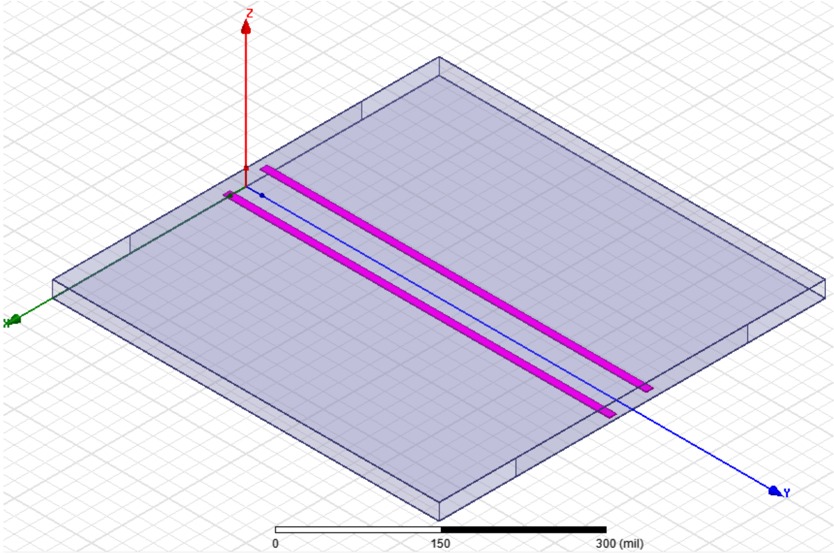

Figure 6.9 3D geometry of a pair of striplines in an irregular shaped power/ground plane cavity. Trace length = 500 mils.

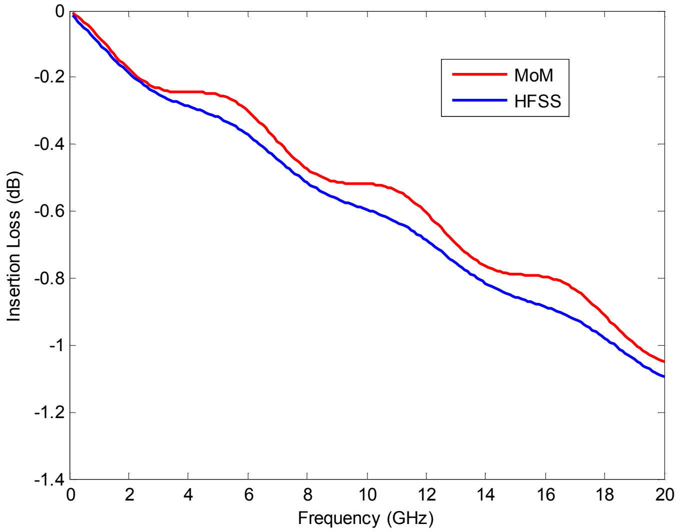

(a) Insertion loss of stripline in dB scale

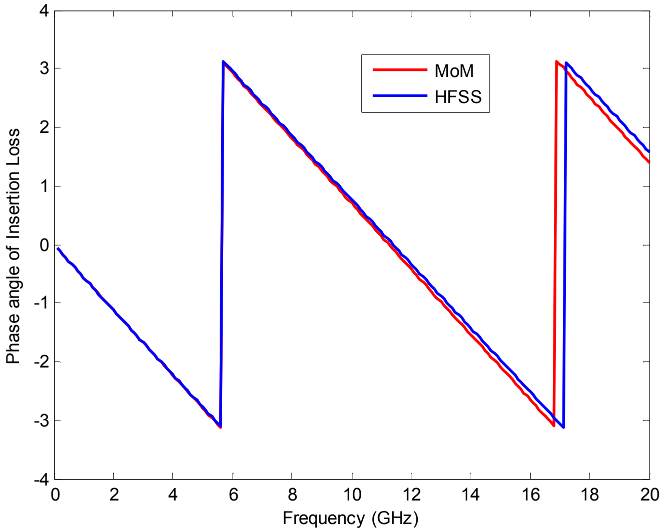

(b) Phase of insertion loss of stripline

Figure 6.10 Comparison of Insertion loss for a pair of striplines in Figure 6.9.

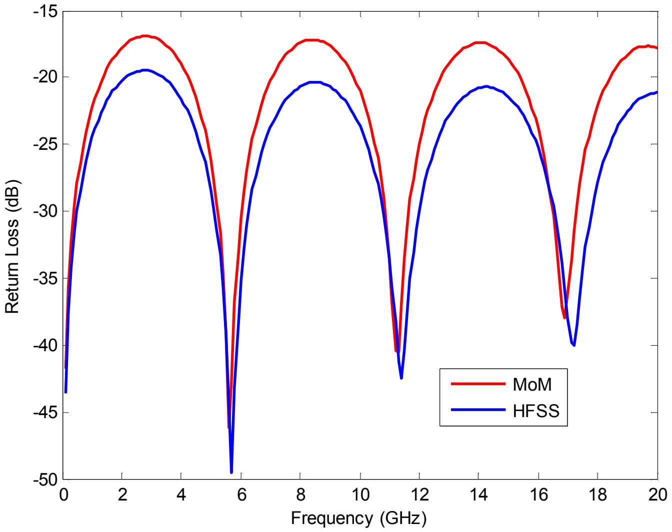

(a) Return loss in dB scale

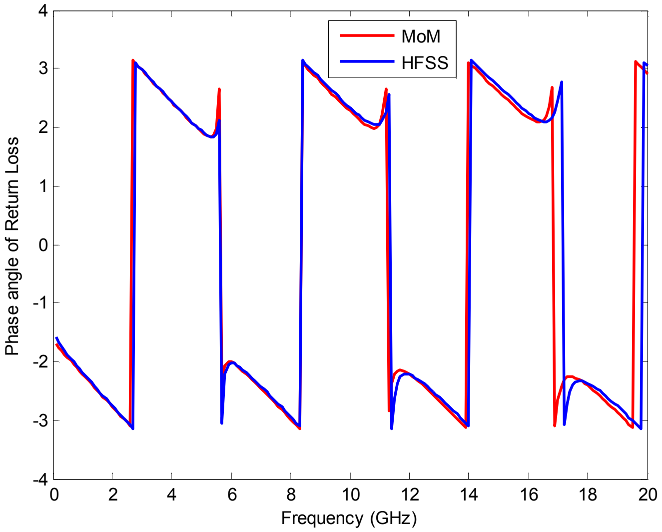

(b) Phase of return loss of stripline

Figure 6.11 Comparison of Return loss for a pair of striplines in Figure 6.9.

6.4.1.4 Via and Balanced Stripline in Irregular Shaped Cavity

Figure 6.12 show the 3D geometry of the first case used to check the hybrid model proposed in this chapter. The cavity is consists of a power plane and a ground plane, with 4 signal vias and 2 traces. The stripline is balanced configuration with d1=d2 = 10 mils. The substrate has no dielectric loss with relative permittivity = 4.4*(1-j*0.02).

Figure 6.13 show the comparison for 4 different methods: Method 1 - direct HFSS solving entire structures with both vias and traces; Method 2 – HFSS solving vias in power/ground planes, and HFSS solving traces, then cascade using circuit model described in section 6.2.1; Method 3 - HFSS solving vias in power/ground planes, and MoM solving traces, then cascade using circuit model described in section 6.2.1; Method 4 - BBGFL solving vias in power/ground planes, and HFSS solving traces, then cascade using circuit model described in section 6.2.1. Overall, Method 4 agrees with Method 1, 2, 3. It should be pointed out that the circuit model works pretty well.

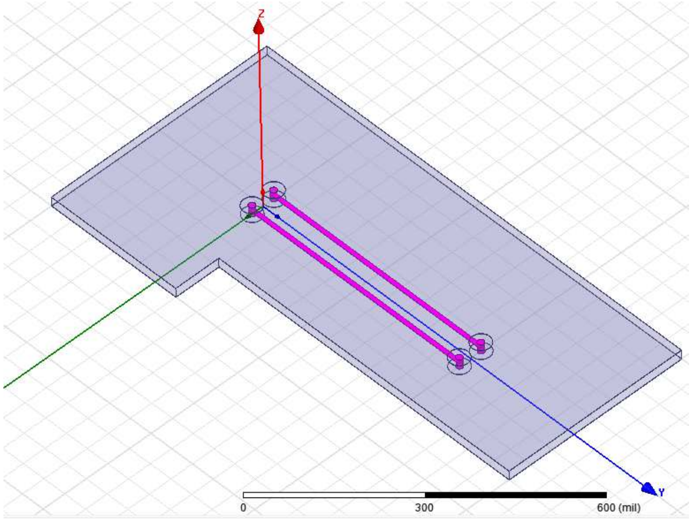

(a) 3D View

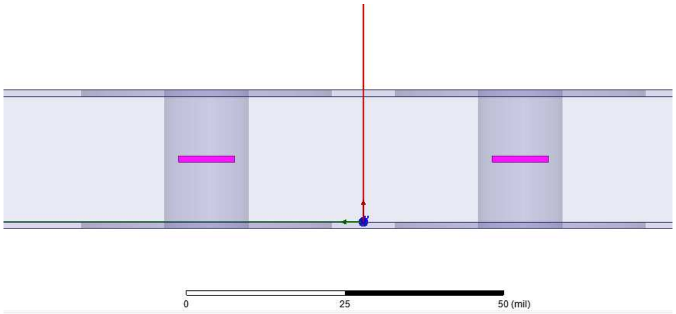

(b) Side View

Figure 6.12 3D geometry of an irregular shaped power/ground plane cavity with 4 signal vias and two balanced traces. (a) 3D view; (b) side view.

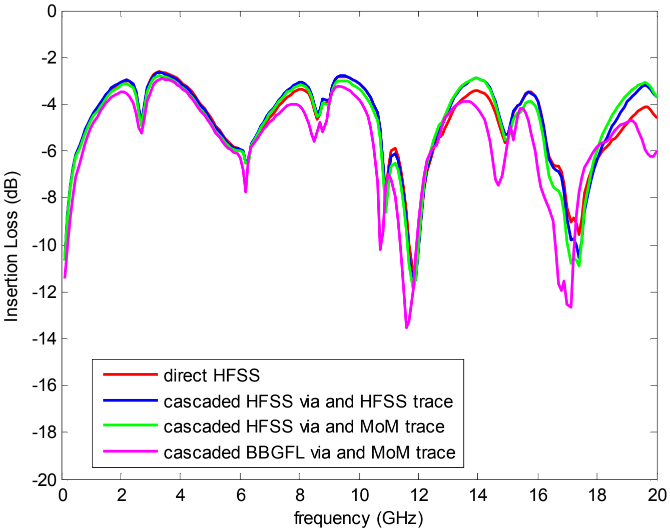

(a) Insertion Loss

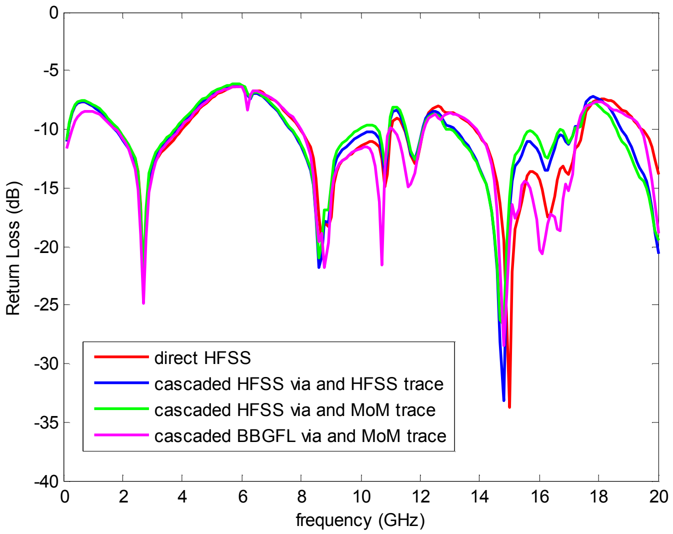

(b) Return Loss

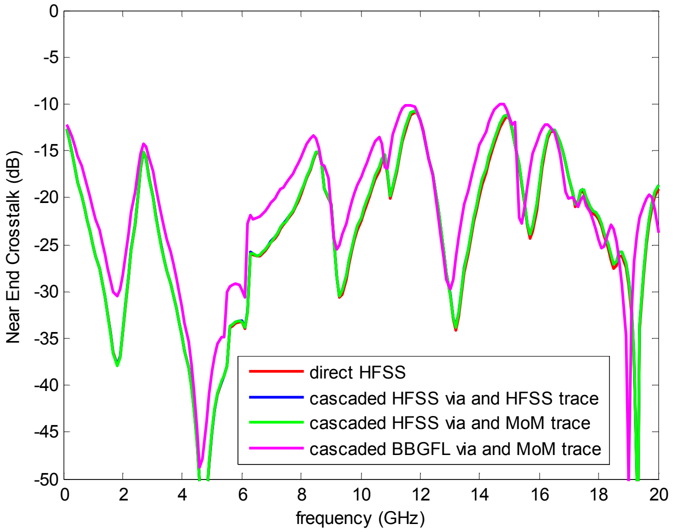

(c) Near End Crosstalk

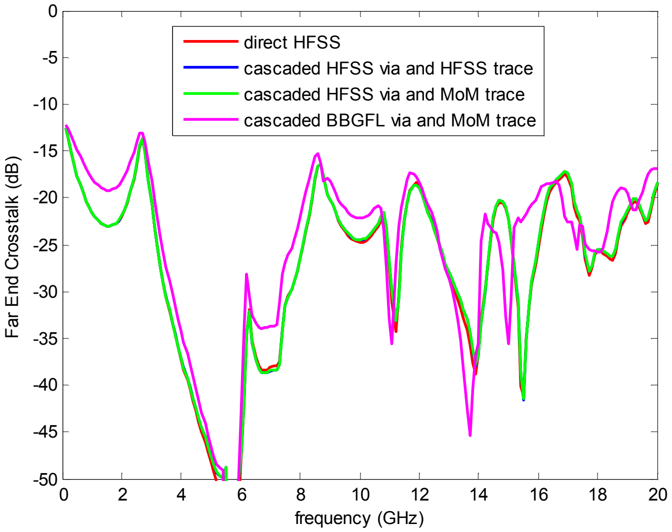

(d) Far End Crosstalk

Figure 6.13 S-parameters for the model in Figure 6.12.

6.4.2 Case 2: Unbalanced Stripline in Irregular Shaped Power/Ground Plane Cavity with Vias

Figure 6.14 show the 3D geometry of the second case used to check the hybrid model proposed in this chapter. The cavity is consists of a power plane and a ground plane, with 4 signal vias and 2 traces. The stripline is an unbalanced configuration with upper dielectric height d_1=15mis and downside dielectric height d_2 = 5 mils. The substrate has no dielectric loss with relative permittivity = 4.4*(1-j*0.02).

Figure 6.15 show the comparison for 4 different methods: Method 1 - direct HFSS solving entire structures with both vias and traces; Method 2 – HFSS solving vias in power/ground planes, and HFSS solving traces, then cascade using circuit model described in section 6.2.1; Method 3 - HFSS solving vias in power/ground planes, and MoM solving traces, then cascade using circuit model described in section 6.2.1; Method 4 - BBGFL solving vias in power/ground planes, and HFSS solving traces, then cascade using circuit model described in section 6.2.1. Overall, Method 4 agrees with Method 1, 2, 3. It should be pointed out that the circuit model works pretty well.

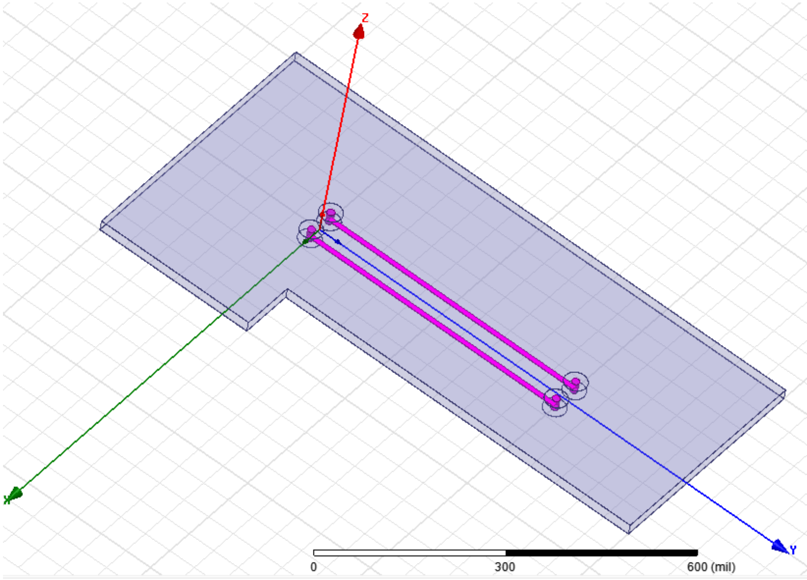

(a) 3D View

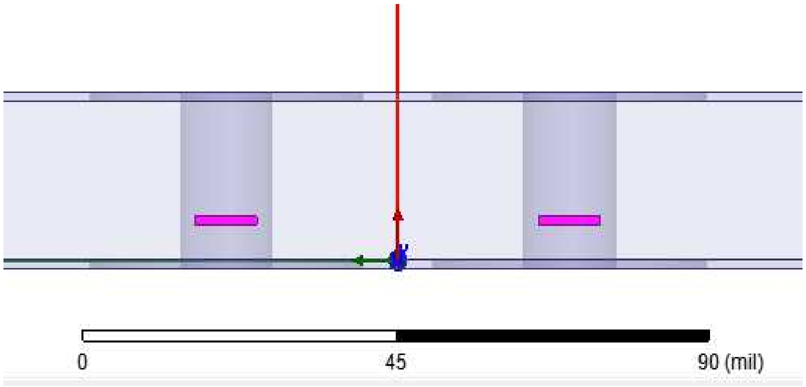

(b) Side View

Figure 6.14 3D geometry of an irregular shaped power/ground plane cavity with 4 signal vias and two unbalanced traces. (a) 3D view; (b) side view.

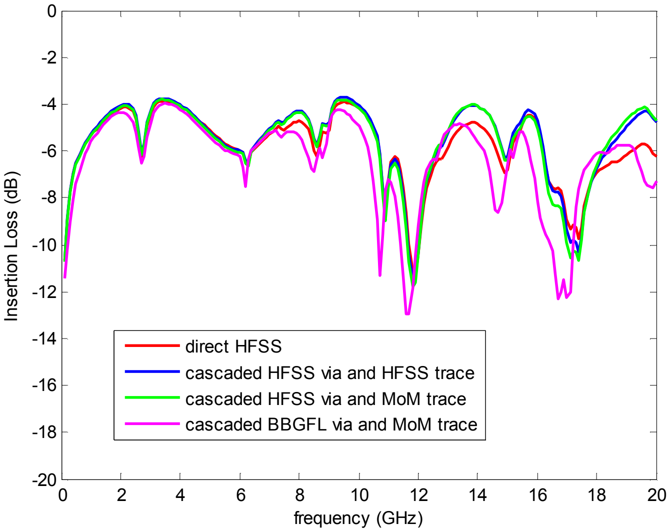

(a) Insertion Loss

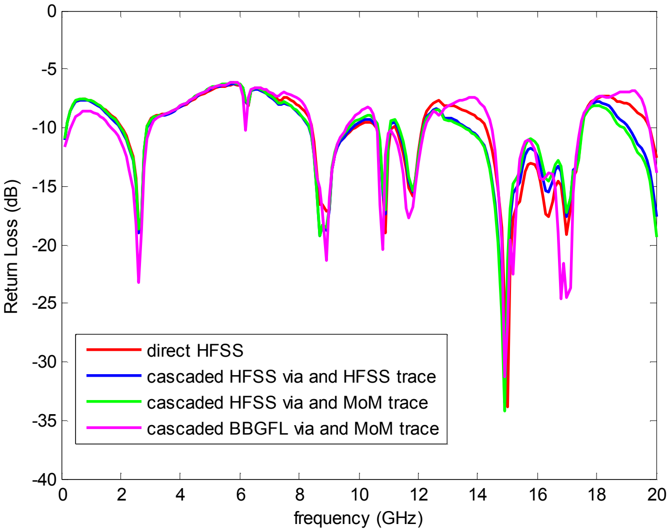

(b) Return Loss

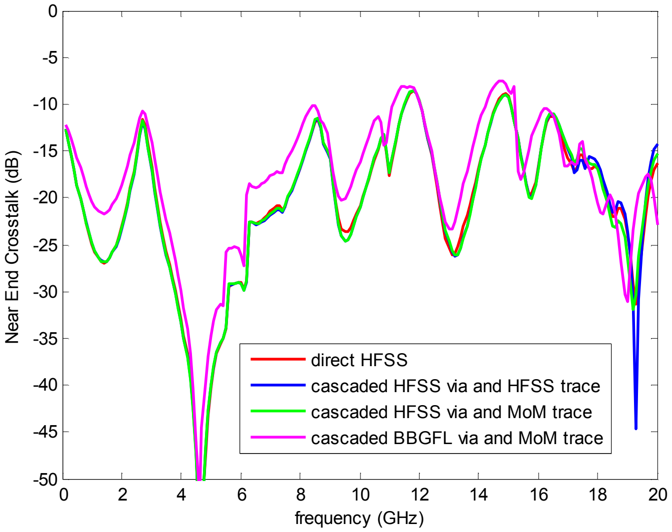

(c) Near End Crosstalk

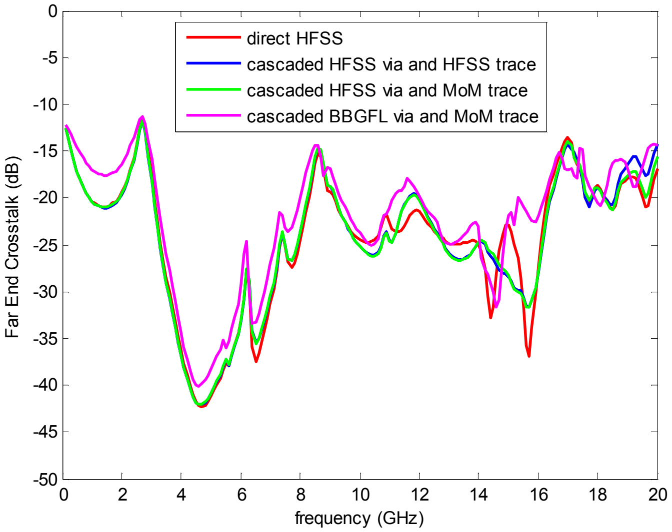

(d) Far End Crosstalk

Figure 6.15 S-parameters for the model in Figure 6.14.

6.4.3 **Comparison of CPU time**

In Table 6-5, we compare BBGFL with MoM and HFSS for the CPU time used in the simulations of Figure 6.9. In the comparison, the input parameters are: the discretization spacing is 10mils for both MoM and BBGFL, the BBGFL uses $M_o = 20$ for both kxm and kyn.

Five different modeling methodologies are compared:

1) For Cascaded “BBGFL via” + “MoM trace”: the CPU time consists four parts, the first part is for computation of eigenfunctions and values, and second part is for creating response Green’s function with the pre-computed eigenfunctions and values, the third part is solve the Foldy-Lax equations with the pre-computed response Green’s function, the fourth part is 2D MoM solution of traces. The circuit cascading is negligible.

2) For Cascaded “MoM via” + “MoM trace”: the CPU time consists three parts, the first part is for computation of response Green’s function using MoM, the second part is solve the Foldy-Lax equations with the pre-computed response Green’s function, the third part is 2D MoM solution of traces. The circuit cascading is negligible.

3) For Cascaded “HFSS via” + “MoM trace”: the CPU time consists three parts, the first part is for computation of response Green’s function using HFSS, the second part is solve the Foldy-Lax equations with the pre-computed response Green’s function, the third part is 2D MoM solution of traces. The circuit cascading is negligible.

4) For Cascaded “HFSS via” + “HFSS trace”: the CPU time consists three parts, the first part is for computation of response Green’s function using HFSS, the

second part is solve the Foldy-Lax equations with the pre-computed response Green's function, the third part is 3D HFSS solution of traces. The circuit cascading is negligible.

5) For direct HFSS: the CPU time consists one part using 3D HFSS solution of entire structures with both vias and traces in power/ground planes.

For the simulation of 100 frequency points, the method of Cascaded "BBGFL via" + "MoM trace" is about 44 times faster than the method of Cascaded "MoM via" + "MoM trace", and is about 130 times faster than the method of direct HFSS. For the simulation of 1000 frequency points, the method of Cascaded "BBGFL via" + "MoM trace" is about 165 times faster than the method of Cascaded "MoM via" + "MoM trace", and is about 449 times faster than the method of direct HFSS.

Table 6-5 Comparison of CPU times using different methods: BBGFL/Foldy-Lax, direct MoM, and HFSS.

Methods	1 frequency point	10 frequency points	100 frequency points	1000 frequency points
Cascaded "BBGFL via" + "MoM trace"	10.3 (BBGFL setup) + 0.006*1 (BBGFL)+0.02*1 (Foldy-Lax) + 0.004*1 (2D MoM) =10.3 sec	10.3+ 0.006*10+0.02*10 + 0.004*10 =10.6 sec	10.3+ 0.006*1000+0.02*1000 + 0.004*1000 =13.3 sec	10.3+ 0.006*1000+0.02*1000 + 0.004*1000 =36.3 sec
Cascaded "MoM via" + "MoM trace"	6.00*1 (MoM)+0.02*1 (Foldy-Lax) + 0.004*1 (2D MoM) =10.3 sec	6.00*10+0.02*10 + 0.004*10 =60.24 sec	6.00*10+0.02*10 + 0.004*10 =602.4 sec	6.00*10+0.02*10 + 0.004*10 =6024 sec

Cascaded “HFSS via” + “MoM trace”	110.0 (HFSS setup) + 13.5*1 (HFSS) + 0.004*1 (2D MoM) =10.3 sec	110.0 + 13.5*10 + 0.004*10 =245.04 sec	110.0 + 13.5*100 + 0.004*100 =1460.4 sec	110.0 + 13.5*1000 + 0.004*1000 =14604 sec
Cascaded “HFSS via” + “HFSS trace”	110.0 (HFSS via setup) + 13.5*1 (HFSS via) + 42 (HFSS trace setup) + 8.5*1 (HFSS via) =10.3 sec	110.0 + 13.5*10 + 42.0 + 8.5*10 =372 sec	110.0 + 13.5*100 + 42.0 + 8.5*100 =2352 sec	110.0 + 13.5*1000 + 42.0 + 8.5*1000 =22152 sec
Direct HFSS	123 (HFSS setup) + 16.2*1 (HFSS) = 139.2 sec	123 + 16.2*10 = 285 sec	123 + 16.2*100 = 1743 sec	123 + 16.2*1000 = 16323 sec

Note:

“sec” refers to second, and “fp” refers to frequency point.

1) Cpu time for a trace of 0.5 inch using 2D MoM: 0.0037 sec/fp
2) Cpu time for a trace of 0.5 inch using 3D Hfss: 42 sec (set up) + 8.5 sec/fp
3) Cpu time for 4 vias in 0.5inchX1inch with 0.1inchX0.7inch cutout using Hfss with PMC boundary: 31 sec (set up) + 2.01sec/fp
4) Cpu time for 4 vias and trace in 0.5inchX1inch with 0.1inchX0.7inch cutout using Hfss with PMC boundary: 227 sec (set up) + 14.39sec/fp
5) Cpu time for 4 vias in 0.5inchX1inch with 0.1inchX0.7inch cutout using Hfss with radiation boundary: 110sec (set up) + 13.5sec/fp

6) Cpu time for 4 vias and trace in 0.5inchX1inch with 0.1inchX0.7inch cutout using Hfss with radiation boundary: 123sec (set up) + 16.17sec/fp
7) Cpu time for 4 vias using Foldy-Lax with L=5 and M=3: 0.02 sec/fp
8) Cpu time for 4 vias in 0.5inchX1inch with 0.1inchX0.7inch cutout using BBGFL:
9) 10.3 sec (set up) + 0.006sec/fp

6.5 Conclusion

In this chapter, we present a hybrid technique based on BBGFL, for fast broadband modeling and simulation of traces and vias in power/ground planes. Simulations are done to compare the BBGFL technique with conventional direct conventional hybrid MoM techniques and hybrid or direct HFSS solutions. Results show BBGFL and direct HFSS are in good agreement. Numerical experiments indicate that BBGFL is several hundred times faster than MoM and HFSS for broadband simulation of high-speed interconnects with vias and traces in arbitrarily shaped power/ground planes.

Bibliography

[1] M. Leone, "The radiation of a rectangular power-bus structure at multiple cavity-mode resonances," *IEEE Trans. Microw. Theory Tech.,* vol. 45, no. 3, p. 486–492, 1 August 2003.

[2] G. Conciauro, G. Marco and S. Roberto, Advanced Modal Analysis: CAD Techniques for Waveguide Components and Filters, NY, USA: Wiley, 2002.

[3] L. Tsang and D. Miller, "Coupling of vias in electronic packaging and printed circuit board structures with finite ground plane," *IEEE Trans. Advanced Packaging.,* vol. 26, no. 4, pp. 375-384, Nov. 2003.

[4] Y. –. Zhang and J. Fan, "A generalized multiple scattering method for dense vias with axially-anisotropic modes in an arbitrarily-shaped plate pair," *IEEE Trans. Microw. Theory Tech.,* vol. 60, no. 7, p. 2035–2045, Jul. 2012.

[5] L. Tsang and X. Chang, "Modeling of Vias Sharing the Same Antipad in Planar Waveguide with Boundary Integral Equation and Group T Matrix Method," *IEEE Trans. Compon. Packag. Manuf. Technol.,* vol. 3, no. 2, p. 315–327, Feb. 2013.

[6] X. Chang and L. Tsang, "Fast and broadband modeling method for multiple vias with irregular antipad in arbitrarily shaped power/ground planes in 3-D IC and packaging based on generalized Foldy–Lax equations," *IEEE Trans. Compon. Packag. Manuf. Technol.,* vol. 4, no. 4, p. 685–696, Apr. 2014.

[7] G. Conciauro, M. Bressan and C. Zuffada, "Waveguide modes via an integral equation leading to a linear matrix eigenvalue problem," *IEEE Trans. Microw. Theory Tech.,* vol. 32, no. 11, pp. 1495-1504, Nov. 1984.

[8] P. Arcioni, M. Bozzi, M. Bressan, G. Conciauro and L. Perregrini, "The BI-RME method: An historical overview," in *2014 International Conference on Numerical Electromagnetic Modeling and Optimization for RF, Microwave, and Terahertz Applications (NEMO)*, Aula Foscolo, Italy, 2014.

[9] C. Carceller, F. J. Perez, J. Gil, C. Vicente, V. E. Boria, B. Gimeno and M. Guglielmi, "A commercial EM solver using the BI-RME method," in *International Conference on*

Numerical Electromagnetic Modeling and Optimization for RF, Microwave, and Terahertz Applications (NEMO), Aula Foscolo, Italy, 2014.

[10] M. Bozzi, M. Pasian and L. Perregrini, "MoM/BI-RME method for the modeling of frequency selective surfaces and printed circuits," in *International Conference on Numerical Electromagnetic Modeling and Optimization for RF, Microwave, and Terahertz Applications (NEMO)*, Aula Foscolo, Italy, 2014.

[11] M. Taroncher, A. Vidal, V. E. Boria-Esbert, S. Marini, S. Cogollos, J. Gil and B. Gimeno, "CAD of complex passive devices composed of arbitrarily shaped waveguides using Nyström and BI-RME methods," *IEEE Trans. Microw. Theory Tech.,* vol. 53, no. 6, pp. 2153-2163, Jun. 2005.

[12] M. Bozzi, L. Perregrini and K. Wu, "Modeling of conductor, dielectric, and radiation losses in substrate integrated waveguide by the boundary integral-resonant mode expansion method," *IEEE Trans. Microw. Theory Tech.,* vol. 56, no. 12, pp. 3153-3161, Dec. 2008.

[13] Y. –J. Zhang, G. Feng and J. Fan, "A novel impedance definition of a parallel plate pair for an intrinsic via circuit model," *IEEE Trans. Microw. Theory Tech.,* vol. 58, no. 12, pp. 3780-3789, Dec. 2010.

[14] A. Ishimaru, Electromagnetic wave propagation, radiation, and scattering, New Jersey: Prentice-Hall, 1991.

[15] L. Tsang, J. A. Kong, K. H. Ding and C. Ao, Scattering of Electromagnetic waves, volume 2 Numerical simulations, New York: Wiley, 2001.

[16] L. Tsang, H. Chen, C. Huang and V. Jandhyala, "Modeling of multiple scattering among vias in planar waveguides using Foldy-Lax Equations," *Microw. Opt. Tech. Lett.,* vol. 31, no. 3, pp. 201-208, Nov. 2001.

[17] H. Chen, Q. Li, L. Tsang, C. Huang and V. Jandhyala, "Analysis of large number of vias and differential signaling in multi-layered structures," *IEEE Trans. on Microw. Theory and Tech.,* vol. 51, no. 3, pp. 818-829, Mar. 2008.

[18] X. Gu, B. Wu, C. Baks and L. Tsang, "Fast full wave analysis of PCB via arrays with model-to-hardware correlation," in *IEEE 18th Conference on Electrical Performance*

of Electronic Packaging and Systems (EPEPS'09), 2009.

[19] B. Wu and L. Tsang, "Modeling multiple vias with arbitrary shape of antipads and pads in high speed interconnect circuits," *IEEE Microwave and Wireless Comp. Lett.,* vol. 19, no. 1, pp. 12-14, 2009.

[20] H.-W. Shim and T. H. Hubing, "A closed-form expression for estimating radiated emissions from the power planes in a populated printed circuit board," *IEEE Trans. Electromagn. Compat.,* vol. 48, no. 1, pp. 74-81, Feb. 2006.

[21] M. Stumpf and M. Leone, "Efficient 2-D integral equation approach for the analysis of power bus structures with arbitrary shape," *IEEE Trans. Electromagn. Compat.,* vol. 51, no. 1, pp. 38-45, Feb. 2009.

[22] B. Archambeault and C. C. S. Brench, "Review of printed-circuit-board level EMI/EMC issues and tools," *IEEE Trans. Electromagn. Compat.,* vol. 52, no. 2, pp. 455-461, May 2010.

[23] X. Duan, R. Rimolo-Donadio, H.-D. Bruns and C. Schuster, "A combined method for fast analysis of signal propagation, ground noise, and radiated emission of multilayer printed circuit boards," *IEEE Trans. Electromagn. Compat.,* vol. 52, no. 2, pp. 487-495, May 2010.

[24] G.-T. Lei, R. W. Techentin and B. K. Gilbert, "High-frequency characterization of power/ground-plane strucures," *IEEE Trans. Microw. Theory Tech.,* vol. 47, no. 5, 562-569 May 1999.

[25] J. Fan, J. L. Drewniak, H. Shi and J. L. Knighten, "DC power-bus modeling and design with a mixed-potential integral-equation formulation and circuit extraction," *IEEE Trans. Electromagn. Compat.,* vol. 43, no. 4, p. 426–436, Nov. 2001.

[26] L. Tsang, D. Chen and Q. Li, "Fast solution of integral equations representing wave propagation". U.S. Patent 7,359,929, Apr. 2008.

[27] B. Archambeault and A. Ruehli, "Analysis of power/ground-plane EMI decoupling performance using the partial-element equivalent circuit technique," *IEEE Trans. Electromagn. Compat.,* vol. 43, no. 4, p. 437–445, 2001.

[28] X. Ye, M. Y. Koledintseva, M. Li and J. L. Drewniak, "DC power-bus design using FDTD modeling with dispersive media and surface mount technology components," *IEEE Trans. Electromagn. Compat.,* vol. 43, no. 4, p. 579–587, 2001.

[29] A. E. Engin, K. Bharath and M. Swaminathan, "Multilayered finite-difference method (MFDM) for modeling of package and printed circuit board planes," *IEEE Trans. Electromagn. Compat.,* vol. 49, no. 2, pp. 441-447, 2007.

[30] S. Huang and L. Tsang, "Broadband Bounded Medium Green's Function and Applications to Fast Electromagnetic Modeling of High Speed Interconnects," in *IEEE International Symposium on Antennas and Propagation*, Vancouver, BC, Canada, 2015.

[31] L. Tsang and S. Huang, "Broadband Green's Function with Low Wavenumber Extraction for Arbitrary Shaped Waveguide and Modeling of Vias in Finite Power/Ground Plane," *IEEE Trans. Microw. Theory Tech.,* p. 1, 1 under review 2015.

[32] L. Tsang and S. Huang, "Full Wave Modeling and Simulations of The Waveguide Behavior of Printed Circuit Boards Using A Broadband Green's Function Technique". U.S. Patent 62/152.702, Apr. 2015.

[33] C. A. Balanis, Advanced engineering electromagnetics, New York: Wiley, 1989.

[34] M. Swaminathan, D. Chung, S. Grivet-Talocia, K. Bharath, V. Laddha and J. Xie, "Designing and modeling for power integrity," *IEEE Trans. Electromagn. Compat.,* vol. 52, no. 2, pp. 288-310, 2010.

[35] E. P. Li, X. C. Wei, A. C. Cangellaris, E. X. Liu, Y. J. Zhang, M. D'Amore, J. Kim and T. Sudo, "Progress review of electromagnetic compatibility analysis technologies for packages, printed circuit boards, and novel interconnects," *IEEE Trans. Electromagn. Compat.,* vol. 52, no. 2, pp. 248-265, 2010.

[36] S. Huang and L. Tsang, "Fast Electromagnetic Analysis of Emissions from Printed Circuit Board Using Broadband Green's Function," *IEEE Trans. Microw. Theory Tech.,* p. 1, 2015.

[37] R. F. Harrington and J. L. Harrington, Field Computation by Moment Methods,

Oxford, UK: Oxford University Press, 1996.

[38] L. Tsang, J. A. Kong and R. Shin, Theory of Microwave Remote Sensing., New York, USA: Interscience, 1985.

[39] J.-M. Jin, The Finite Element Method in Electromagnetics, New York, USA: Wiley, 2002.

[40] E. Engin, W. John, G. Sommer, W. Mathis and H. Reichl, "Modeling of striplines between a power and a ground plane," *IEEE Trans. Adv. Packag.,* vol. 29, no. 3, pp. 415-426, Aug. 2006.

[41] G. Heinrich and S. Dickmann, "On the coupling between the signal layers and the power-bus on multilayered PCBs," in *Proc. Int. Symp. Electromag. Compat.*, 2009.

[42] R. Rimolo-Donadio, H. Bruns and C. Schuster, "Including stripline connections into network parameter based via models for fast simulation of interconnects," in *Proc. Int. Zurich Symp. Electromag. Compat.*, 2009.

[43] R. Rimolo-Donadio, X. Gu, Y. H. Kwark, M. B. Ritter, B. Archambeault, F. D. Paulis, Y. Zhang, J. Fan, H. Bruns and C. Schuster, "Physics-based via and trace models for efficient link simulation on multilayer structures up to 40 GHz," *IEEE Trans. Microw. Theory Tech.,* vol. 57, no. 8, pp. 2072-2083, Aug. 2009.

[44] S. Pan, J. Zhang, Q. B. Chen and J. Fan, "Equivalent transmission-line model for vias connected to striplines in multilayer print circuit boards," in *Proc. Int. Symp. Electromag. Compat.*, 2010.

[45] J. Fan, A. Hardock, R. Rimolo-Donadio, S. Muller, Y. H. Kwark and C. Schuster, "Signal integrity: Efficient, physics-based via modeling: Return path, impedance, and stub effect control," *IEEE Electromag. Compat. Magazine,* pp. 76-84, 2014.

[46] S. Pan and J. Fan, "Characterization of via structures in multilayer printed circuit boards with an equivalent transmission-line model," *IEEE Trans. Electromagn. Compat.,* vol. 54, no. 5, pp. 1077-1086, Oct. 2012.

[47] L. Tsang and S. Huang, "Combining Broadband Green's Function with Low Wavenumber Extraction and Method of Moment for Fast Broadband Simulations of

Scattering in Arbitrary Shaped W aveguides," *IEEE Trans. Components, Packaging, and Manufacturing Techniques,* p. 1, 2015.

[48] D. M. Pozar, Microwave Engineering, John Wiley & Sons, 2009.

[49] L. Tsang, J. A. Kong, K. H. Ding and C. Ao, Scattering of Electromagnetic Wave, vol. 2, New York: Wiley, 2001.

VITA

Shaowu Huang received B.S. degree in Physics Science from Sun Yat-Sen University in 2004 and the M.S. degree in Electrical Engineering from Peking University in 2008. He was a research assistant with Peking University from 2015 to 2008. In 2008, he began his doctoral work under supervisory of Professor Leung Tsang, earning the Ph.D. in electrical engineering from University of Washington, Seattle, in 2015. He was a research assistant with University of Washington from 2008 to 2012. His Ph.D. research is focused on development of innovative fast electromagnetic simulation algorithms and tools for modeling and simulations of various problems (1) Signal Integrity, Power Integrity, EMC/EMI; (2) Optics, Photonics; (3) Microwave Remote Sensing.

In 2012 he joined Intel Corporation as a signal integrity engineer, with emphasis on research and development of signal integrity and hardware design for data center and server platform products.

He published 17 journal articles and 29 international conference papers, filed 7 US non-provisional patents (all 1st inventor) and 1 US provisional patent (2nd inventor).

He received 4 paper awards in IEEE conferences, an Intel High-5 Award (A special honorarium awarded to an inventor for every five new non-provisional patent applications filed in his/her name within a rolling 52-week basis), and an Intel Distinguished Invention Award (for an outstanding invention selected to be kept as trade secret rather than filing as patent application for more valuable to Intel).

He is member of TC-9 committee of IEEE Electromagnetic Compatibility Society. He was the co-chair of “High Speed Link Design II” session in IEEE International Symposium on Electromagnetic Compatibility and Signal Integrity, Santa Clara, CA, March 15-20, 2015.

Awards

- Intel High 5 Award: A special honorarium awarded to an inventor for every five new non-provisional patent applications filed in his/her name within a rolling 52-week basis (2014).

- Intel Distinguished Invention Award: An outstanding invention is selected to be kept as trade secret rather than filing as patent application for more valuable to Intel (2014).

- "Subwavelength Imaging Enhancement through 3-Dimensional Plasmon Superlens with Rough Surface," published in *Optics Letters*, was recognized by Optical Society of America (OSA) among the "Best in Imaging Systems from OSA's Journals," 2012.

- Honorable Mention Paper Prize and Travel Grant Award in 2015 IEEE International Symposium on Antennas and Propagation and USNC/URSI National Radio Science Meeting, Vancouver, BC, Canada, July 19-24, 2015.

- Honorable Mention Paper Prize and Travel Grant Award in 2012 IEEE International Symposium on Antennas and Propagation and USNC/URSI National Radio Science Meeting, Chicago, IL, USA, July 8-14, 2012.

- Finalist at Student Paper Competition and Travel Grant Award in 2011 IEEE International Symposium on Antennas and Propagation and USNC/URSI National Radio Science Meeting, Spokane, WA, USA, July 3-8, 2011.

- Finalist at Student Paper Competition and Travel Grant Award in 2010 IEEE International Geoscience and Remote Sensing Symposium, Hawaii, USA, July 25-30, 2010.

- Travel Grant Award in 11th Specialist Meeting on Microwave Radiometry and Remote Sensing of Environment, Washington D. C., USA, March 1-4, 2010.

- 2009 Annual Highlighted Research by Electrical Engineering Kaleidoscope, University of Washington.

LIST OF PUBLICATIONS

Journal Papers

1. S. Huang and L. Tsang, "Fast Electromagnetic Modeling of Traces Connecting Vias in Printed Circuit Boards Using Broadband Green's Function," *IEEE Transaction on Electromagnetic Compatibility*, to publish.
2. S. Huang and L. Tsang, "Broadband Green's Function with Low Frequency Extraction Method for Arbitrary Shaped Waveguides: TM case," *IEEE Transaction on Components, Packaging and Manufacturing Technology*, to publish.
3. L. Tsang and S. Huang, "Combining Broadband Green's Function with Low Wavenumber Extraction and Method of Moment for Fast Broadband Simulations of Scattering in Arbitrary Shaped Waveguides," *IEEE Transaction on Components, Packaging and Manufacturing Technology*, under review.
4. S. Huang and L. Tsang, "Fast Electromagnetic Analysis of Emissions from Printed Circuit Boards Using Broadband Green's Function," *IEEE Transactions on Microwave Theorem and Techniques*, under review.
5. L. Tsang and S. Huang, "Broadband Green's Function with Low Wavenumber Extraction for Arbitrary Shaped Waveguide and Applications to Modeling of Vias in finite Power/Ground Plane," *IEEE Transactions on Microwave Theorem and Techniques*, under review.
6. T. Liao, L. Tsang, S. Huang, S. Tanelli, N. Niamsuwan, S. Jaruwatanadilok, S. Kim, and H. Ren and KL Chen, "Co-polarized and Cross polarized Backscattering from Random Rough Soil Surfaces from L-band to Ku-band Using Numerical Solutions of Maxwell's Equations with Near Field Precondition," *IEEE Transactions on Geoscience and Remote Sensing*, accepted for publication, 2015.

7. S. Huang and L. Tsang, “Interpolation Extended Boundary Condition Method for 3-Dimensional Electromagnetic Scattering from Rough Surfaces,” *Journal of the Optical Society of America A*, to publish.
8. L. Tsang, I. Koh, T. Liao, S. Huang, X. Xu, E.G. Njoku, and Y. Kerr, “Omega-Tau model with Rough Surface Boundary Conditions from NMM3D and Applying Data Cubes to Both Active and Passive Remote Sensing”, *IEEE Journal of Selected Topics in Applied Earth Observations and Remote Sensing,* vol. 6, pp. 1698-1709 , 2013.
9. L. Tsang, K. H. Ding, S. Huang, and X. Xu, “Electromagnetic Computation in Scattering of Electromagnetic Waves by Random Rough Surface and Dense Media in Microwave Remote Sensing of Land Surfaces,” *Proceedings of the IEEE*, Special Issue on “Large Scale Electromagnetic Computation for Modeling and Applications,” vol. 101, pp. 255-279 , 2013.
10. S. Huang and L. Tsang, “Electromagnetic Scattering of Randomly Rough Soil Surfaces Based on Numerical Solutions of Maxwell Equations in 3-Dimensional Simulations Using a Hybrid UV/PBTG/SMCG Method,” *IEEE Transactions on Geoscience and Remote Sensing,* vol. 50, no.10, pp.4025-4035, 2012.
11. H. Wang, L. Tsang, and S. Huang, “The Loss and Back-Coupling Effects on Subwavelength Imaging of 3-Dimensional Superlens,” *Optics Letters*, vol. 37, no.12, pp.2262-2264, 2012.
12. S. Huang, H. Wang, K. H. Ding, and L. Tsang, “Subwavelength Imaging Enhancement through 3-Dimensional Plasmon Superlens with Rough Surface,” *Optics Letters*, vol. 37, no. 8, pp.1295-1297, 2012.
13. S. Kim, L. Tsang, J. T. Johnson, S. Huang, J. J. van Zyl, and E. G. Njoku, “Soil moisture retrieval using time-series radar observations over bare surfaces,” *IEEE Transactions on Geoscience and Remote Sensing*, vol.50, no.5, pp.1853-1863, 2012.
14. H. Wang, J. Q. Bagley, L. Tsang, S. Huang, K. H. Ding, and A. Ishimaru, “Image Enhancement for Flat and Rough Film Plasmon Superlenses by Adding Loss,” *Journal of the Optical Society of America B*, vol. 28, no. 10, pp. 2499-2509, 2011.
15. S. Huang, L. Tsang, Njoku, E.G., K. S. Chen, “Backscattering Coefficients, Coherent Reflectivities, and Emissivities of Randomly Rough Soil Surfaces at L-Band for

SMAP Applications Based on Numerical Solutions of Maxwell Equations in Three-Dimensional Simulations," *IEEE Transactions on Geoscience and Remote Sensing*, vol.48, no.6, pp.2557-2568, June 2010.

16. S. Huang, "scattering and emission of rough surface in Microwave remote sensing of soil Moisture," 2009 Electrical Engineering Kaleidoscope, University of Washington. (UW EE research highlight magazine)
17. S. Huang, G. Zhang, M. Xia, and C. H. Chan, "Numerical Analysis of Scattering by Dielectric Random Rough Surfaces Using Modified SMCG Scheme and Curvilinear RWG Basis Functions," *IEEE Transactions on Antennas and Propagation*, vol. 57, no. 10, pp. 3392-3397, Oct., 2009.
18. S. Huang and M. Xia, "A modified scheme of sparse-matrix canonical grid method with Chebyshev interpolating Green's function," *Microwave and Optical Technology Letters*, vol. 50, no. 7, pp. 1844-1848, Jul., 2008.

Conference Papers

1. S. Huang and L. Tsang, "Broadband Bounded Medium Green's Function and Applications to Fast Electromagnetic Modeling of High Speed Interconnects," *IEEE International Symposium on Antennas and Propagation*, Vancouver, BC, Canada, July 19-25, 2015, accepted for presentation.
2. L. Tsang, I. Koh, T. H. Liao, and S. Huang, "Passive Microwave Remote Sensing Using Omega-tau Model with Rough Surface Boundary Conditions from NMM3D," *Progress In Electromagnetics Research Symposium*, Moscow, Russia, August 19-23, 2012.
3. S. Huang, and L. Tsang, "Subwavelength Imaging of Plasmon Superlens with 3-Dimensional Small Surface Roughness", *IEEE International Symposium on Antennas and Propagation and USNC/URSI National Radio Science Meeting*, Chicago, IL, USA, July 8-14, 2012.
4. S. Huang, L. Tsang, J. Johnson, and K. S. Chen, "Backscattering and Emissivity in Microwave Remote Sensing of Soil Moisture at L-Band based on 3-D Full Wave

Simulations", *IEEE International Symposium on Antennas and Propagation and USNC/URSI National Radio Science Meeting*, Chicago, IL, USA, July 8-14, 2012.

5. S. Huang, P. Xu, L. Tsang, J. Shi, E. Njoku, and Y. Kerr, "Combined Active and Passive Microwave Remote Sensing of Bare Soils at L-band Based on Numerical Maxwell Model in 3-Dimensional Simulations (NMM3D) ", *IEEE International Geoscience and Remote Sensing Symposium*, Munich, Germany, July 22-27, 2012.
6. X. Xu, L. Tsang, T. H. Liao, S. Huang, and S. Kim, Physical Forward Models and Data Cubes for Radar Remote Sensing at L-band for SMAP Applications, *Progress In Electromagnetics Research Symposium*, Kuala Lumpur, Maylaysia, on 27-30 March, 2012.
7. S. Huang, X. Duan, J. Ouellette, X. Xu, T.H. Liao, J. Johnson, M. Moghaddam, L. Tsang, "Like polarization and Cross polarization of Radar remote sensing of soil moisture at L band: 3D numerical simulations of Maxwell equations, Analytical models, and Retrieval Performance in Soil Moisture Retrieval", *IEEE International Geoscience and Remote Sensing Symposium*, Vancouver, Canada, July 24-29, 2011.
8. S. Kim, S. Huang, L. Tsang, J. Johnson, Njoku, E.G., "Soil Moisture retrieval over bare surfaces using time-series radar observations and a lookup table representation of forward scattering," *IEEE International Geoscience and Remote Sensing Symposium*, Vancouver, Canada, July 24-29, 2011.
9. S. Huang and L. Tsang, "Analysis of 3D Electromagnetic Scattering of Multilayer Dielectric Random Rough Surfaces Using Interpolation Extended Boundary Condition Method", *IEEE International Symposium on Antennas and Propagation and USNC/URSI National Radio Science Meeting*, Spokane, WA, USA, July 3-8, 2011.
10. S. Huang and L. Tsang, "Hybrid UV/PBTG/SMCG Method Based on NMM3D for 3D Electromagnetic Scattering of Random Rough Surfaces", *IEEE International Symposium on Antennas and Propagation and USNC/URSI National Radio Science Meeting*, Spokane, WA, USA, July 3-8, 2011.
11. X. Xu, T. H. Liao, L. Tsang, S. Huang, J. C. Shi, and K. S. Chen, Forward Models and Retrieval of Soil Moisture of Radar Remote Sensing of Bare Soil at L Band

Based on 3D Numerical Simulations of Maxwell Equations Using both Like Polarization and Cross Polarization, *Progress In Electromagnetics Research Symposium*, Marrakesh, MOROCCO, on 20-23 March, 2011.

12. S. Huang and L. Tsang, "Bistatic Scattering, Backscattering and Emissivities of Randomly Rough Soil Surfaces at L Band Based on Numerical Solutions of Maxwell Equations of 3 Dimensional Simulations", *IEEE International Geoscience and Remote Sensing Symposium*, Hawaii, USA, July 25-30, 2010.
13. X. Xu, S. Huang, L. Tsang, S. Kim, E. G. Njoku, " Data Cube Representation of Vegetated Surfaces Based on Physical Scattering Model for SMAP mission", *IEEE International Geoscience and Remote Sensing Symposium*, Hawaii, USA, July 25-30, 2010.
14. X. Xu, S. Huang, L. Tsang, S. Kim, E. G. Njoku, "Data Cube Representation of Vegetated Surfaces Based on Physical Scattering Model for SMAP Mission", *Progress In Electromagnetics Research Symposium*, Cambridge, USA, July 5-8, 2010.
15. S. Huang, L. Tsang, E. Gerald Njoku, and Kun-Shan Chen,Analysis of Electromagnetic Scattering by Random Rough Soil Surfaces at L Band Using Numerical Solutions of Maxwell Equations of 3 Dimensional Simulations (NMM3D), *Progress In Electromagnetics Research Symposium*, Xi'an, CHINA, on 22-26 March, 2010.
16. X. Xu, L. Tsang, S. Huang, and E. G. Njoku, Microwave Scattering Model of Vegetated Surfaces for Applications in SMAP Mission, *Progress In Electromagnetics Research Symposium*, Xi'an, CHINA, on 22-26 March, 2010.
17. S. Huang, L. Tsang, and E. Njoku, "Emissivities and Backscattering of Randomly Rough Soil Surfaces at L band Based on Numerical Solutions of Maxwell Equations of 3 Dimensional Simulations", *11th Specialist Meeting on Microwave Radiometry and Remote Sensing of Environment*, Washington D. C., USA, March 1-4, 2010.
18. S. Huang, G. Charles, K. Xiao, B. Lee, G. Ouyang, H. Zhang, "Suppression of Cavity Resonance In Printed Circuit Board and Packages Using Absorbing Materials along

the Edge", *IEEE International Symposium on Electromagnetic Compatibility*, Santa Clara, CA, March 15-20, 2015.

19. S. Huang, B. Lee, X. Ye, K. Xiao, "Rigorous One-Port Measurement Method for the Characterization of On-chip Pad Response", *IEEE International Symposium on Electromagnetic Compatibility*, Santa Clara, CA, March 15-20, 2015.
20. S. Huang, O. Oluwafemi, G. Brist, "Microstrip Improvement by Using Dielectric Film", *IEEE International Symposium on Electromagnetic Compatibility*, Santa Clara, CA, March 15-20, 2015.
21. S. Huang, "Method to Improve the Accuracy of Mixed -mode S-parameters Derived from Single-Ended Results and Application to Shorter Test Coupon Design", *IEEE International Symposium on Electromagnetic Compatibility*, Santa Clara, CA, March 15-20, 2015.
22. B. Wu, S. Huang, "Integrated Power Supply Packaging Technique with Reduced Parasitic Inductance for On-die Voltage Regulator Design and Application", *IEEE International Symposium on Electromagnetic Compatibility*, Santa Clara, CA, March 15-20, 2015.
23. S. Huang, J. Loyer, R. Kunze, B. Wu, "Method to reduce coupon lengths for transmission line S-parameter measurements through elimination of guided-wave multiple reflections", session on High Speed Interconnects for High Performance Computing, *Progress in Electromagnetics Research Symposium (PIERS)*, Aug 25-28, 2014, Guangzhou, China.
24. S. Huang, J. Loyer, R. Kunze, B. Wu, "Method to Reduce Coupon Length for S-parameter Measurements", *DesignCon 2015*, Jan 27-30, Santa Clara, CA, USA.
25. S. Huang and M. Xia, "Analysis of Scattering by Ocean-like Surfaces Using an Augmented SMCG Scheme with Curvilinear Modeling," *Progress in Electromagnetics Research Symposium*, Beijing, China, March 23-27, 2009.
26. S. Huang and M. Xia, "Parametric geometric modeling using piecewise interpolation functions for solutions of electromagnetic integral equations," *Asia-Pacific Microwave Conference*, Hong Kong, December 16-20, 2008.

27. S. Huang and M. Xia, “Simulation of Scattering from Dielectric Random Rough Surfaces Using SMCG Method with Curvilinear RWG Basis Functions,” *International Conference on Microwave and Millimeter Wave Technology*, Nanjing, China, April 21-24, 2008.
28. S. Huang and M. Xia, “Analysis of Random Rough Surface Scattering Using Sparse-Matrix Canonical-Grid Method with Chebyshev Interpolating Green's Function,” *2007 Cross Strait Tri-regional Radio Science and Wireless Technology Conference*, Hefei, China, August 23-27, 2007.
29. M. Xia, S. Huang and G. H. Zhang, “A Modified Scheme of Sparse-matrix Canonical-grid Method for Rough Surface Scattering Using Interpolating Green’s Function,” *Progress in Electromagnetics Research Symposium*, Beijing, China, March 26-30, 2007.

Patent (from Ph.D research)

Leung Tsang, and Shaowu Huang, “Full Wave Modeling and Simulations of The Waveguide Behavior of Printed Circuit Boards Using A Broadband Green’s Function Technique”, U.S. Patent No. 62/152.702, Apr. 24, 2015, pending.